REPORT DOCUMENTATION PAGE

The public reporting burden for this collection of information is estimated to average 1 hour per response, including the time for reviewing instructions, searching existing data sources, gathering and maintaining the data needed, and completing and reviewing the collection of information. Send comments regarding this burden estimate or any other aspect of this collection of information, including suggestions for reducing the burden, to the Department of Defense, Executive Services and Communications Directorate (0704-0188). Respondents should be aware that notwithstanding any other provision of law, no person shall be subject to any penalty for failing to comply with a collection of information if it does not display a currently valid OMB control number.
PLEASE DO NOT RETURN YOUR FORM TO THE ABOVE ORGANIZATION.

1. REPORT DATE *(DD-MM-YYYY)*	2. REPORT TYPE	3. DATES COVERED *(From - To)*

4. TITLE AND SUBTITLE

	5a. CONTRACT NUMBER
	5b. GRANT NUMBER
	5c. PROGRAM ELEMENT NUMBER

6. AUTHOR(S)

	5d. PROJECT NUMBER
	5e. TASK NUMBER
	5f. WORK UNIT NUMBER

7. PERFORMING ORGANIZATION NAME(S) AND ADDRESS(ES)	8. PERFORMING ORGANIZATION REPORT NUMBER

9. SPONSORING/MONITORING AGENCY NAME(S) AND ADDRESS(ES)	10. SPONSOR/MONITOR'S ACRONYM(S)
	11. SPONSOR/MONITOR'S REPORT NUMBER(S)

12. DISTRIBUTION/AVAILABILITY STATEMENT

13. SUPPLEMENTARY NOTES

14. ABSTRACT

15. SUBJECT TERMS

16. SECURITY CLASSIFICATION OF:			17. LIMITATION OF ABSTRACT	18. NUMBER OF PAGES	19a. NAME OF RESPONSIBLE PERSON
a. REPORT	b. ABSTRACT	c. THIS PAGE			
					19b. TELEPHONE NUMBER *(Include area code)*

Massachusetts Institute of Technology

Final Technical Report

AFOSR Grant FA9550-05-1-0380
(06.01.05-11.30.07)

Advanced Electrodynamic Tether Systems:

Modeling of Scattering
and
Unsteady Effects

PI:　　　**Manuel Martinez-Sanchez**
Professor of Aeronautics and Astronautics
Massachusetts Institute of Technology
Cambridge, MA 02139, USA
mmart@mit.edu

Co-I:　　**Oleg Batishchev, Ph.D.**
Principal Research Scientist
batish@mit.edu

-- Cambridge, June 2008 --

TABLE OF CONTENTS

Motivation

This work addresses the needs for advanced computational tools and theoretical models devoted to the study of two interrelated topics of interest to the Air Force: Radiation Belt Remediation (RBR) and potential use of tethers as low frequency oscillators/radiators. Both problems stretch the capabilities of existing numerical methods, while connecting with a body of previous work on probe theory, spacecraft-plasma interactions and electrodynamic tether propulsion. The Electrostatic RBR application would typically require MV-level potentials and complex, multi-strand wire arrangements. The high voltages imply extreme disparity of length scales, as well as relativistic conditions in some cases. The geometrical complexity and driving physical processes may require 3D capabilities, particularly when magnetic effects cannot be ignored. For its part, the study of sheath ion or electron oscillations in the vicinity of a high power radiating tether requires tracking of a time-dependent sheath boundary and use of boundary conditions that allow radiation escape while denying spurious reflections.

Our studies also addressed the engineering integration aspects of these two problems. The detailed kinetic code, which is required for accurate and consistent modeling of the physics is expected to be ill-suited for parametric studies that aim at design and optimization of an actual RBR or broadcasting system. For this reason, we also developed reduced order models that retain the main scaling and performance capabilities while drastically reducing computational effort. The applications are in principle physically different, so we developed separate models for the electrostatic and for the wave-driven cases. These models can be ultimately used to guide the selection of parameters for detailed simulations, as well as for a future systems study that will produce recommendations regarding system configuration and project power, mass and other global metrics for each application.

Background

The RBR problem arises from the possibility of man-made intensification of the already dangerous levels of high-energy particle populations trapped by the geomagnetic field in the altitude range of 1,000-15,000 km. These particles, typically protons and electrons, have pitch angles with respect to the magnetic field high enough to induce repeated reflections above the dense atmosphere altitude. Any intervention that can reduce this pitch angle can ultimately lead to absorption of the particle as it dips farther into the atmosphere near magnetic poles. Among the possible mechanisms that have been proposed for this purpose, two deserve mention here:

(a) injection of whistler waves into the magnetospheric cavity to mimic the particle-scattering action of ionospheric hiss or lightning, which are some of the natural decay mechanisms for the trapped particles, and

(b) scattering by some high potential structure (a metallic tether or combination of tethers has been suggested) that will send a fraction of the protons into the loss cone for their magnetic line.

Our study addresses both of these mechanisms. In addition to the direct interest for this RBR application, our studies will have applicability to probe theory, electrodynamic tether propulsion and power generation, and spacecraft-plasma interactions.

The study of RBR tether operation can be attempted at two levels of accuracy. For design studies, where multiple parametric trials need to be evaluated, a simple model can be developed that uses an approximate analytical potential distribution around the tether, evaluates the scattering cross-section for particle removal, and uses it to calculated total loss rate. On the other hand, for a clear understanding of he physical issues and for numerical precision, one needs to resort to a detailed kinetic simulation capable of including magnetic effects, relativistic corrections and complicated geometries.

For the scattering approach, a good example of the simplified approach is the original study of Danilov et al [1]. Their work can be used to establish some of the main parameters of a typical RBR system, and this can then guide our discussion of the numerical issues for the kinetic simulation. Danilov pointed out that a pair of tethers biased in a double-probe arrangement could be used, with most of the potential deviation from the background being taken up by the negative tether, which then becomes the active scattering center. Since the trapped proton energy is up to 1 MeV, the bias must also be of this order. The electron temperature in the background magnetospheric plasma is of the order of 100 eV, and the plasma density at the high altitudes considered can be as low as 10^8 m-3, for a Debye length of nearly 25 m. The radius of the sheath formed around the negative tether can be estimated [Ref 2] from the implicit formula

$$\frac{eV}{kT_e} = 2.554 (\frac{r_s}{d_D})^{1.325} \ln \frac{r_s}{R} \tag{1}$$

where V is the tether potential, T_e the electron temperature, r_s the sheath radius, R the tether radius, and d_D the Debye length. For the conditions quoted above, with a 1MV potential, the sheath radius ranges from 1,400 m when the tether radius is 0.01 mm to 1,900 m when the tether radius is 10 mm. The ratio of sheath to tether radii is then from 1.4×10^8 to 1.9×10^5. The energetic particle density is much smaller than the background density, which sets the Debye length and, together with the tether radius, determines the current capture rate by the two tethers, and hence the power required by the system.

Numerical work towards the RBR problem has been carried out by Choiniere and Gilchrist [2] as well as by Minor, of Tethers Unlimited (Ref.[3]). The result expressed by Eq (1) is a correlation of the numerical results of Ref. [2], and has since been confirmed through analytical work of Sanmartin et al. [4]. References [2,3] have used an axisymmetric steady state model in which the potential is gradually adjusted as a result of a large number of charged particle trajectories that are computed at each stage in the iteration. This procedure, analogous to that used in the classical probe studies of Laframboise [5], accelerates convergence at the cost of ignoring the transient dynamics. In addition to its direct importance for oscillator studies, this transient behavior may also be relevant to the scattering problem if, as suggested by our electron capture result [6], it results in the long-term trapping of a significant population around the attracting tether. The use of an electrostatic tether as a combination resonator-antenna for broadcasting of VLF or ELF signals appears to have received comparatively less attention than the RBR

application, although Refs. [17-19] have studied the physical basis and considered the injection of whistlers from antennas in orbiting spacecraft. Scaling arguments were advanced by NRL researchers (Ref. [7]), who pointed out that ion oscillations in the sheath of a negative tether would have frequencies in the range of interest. Whether these oscillations can become self-sustained, or, on the contrary, will require steady excitation power, is at this time unclear. Transients in the TSS-1 space experiment were described by Bilen et al. (Ref. [8]) and an experimental and numerical study of the possibility of enhancing electron current collection by the scattering effect of forced sheath potential fluctuations was reported by Choiniere et al. (Ref. [9]). The effect was indeed positive, especially near resonance (somewhat below plasma frequency), but the driving power was also very high at that frequency. Current enhancement per unit power peaked well below resonance.

One of the most likely sources of oscillation is the trapped population of ions that can develop around a negatively biased tether. The possibility of these trapped populations in potential wells has been long recognized (Ref [10]). Gurevich [11] analyzed their development though adiabatic potential changes in one-dimensional geometries, and derived the resulting energy distribution of the trapped particles. He also recognized that fast transients could result in very similar distributions as well. Sanmartin et al [12] generalized Gurevich's analysis to axisymmetric geometries and explained through the presence of trapped electrons the paradox that arises in the frontal pre-sheath region of a positively biased tether in a hypersonic flow: the retarded ions tend to pile up and overshoot the upstream plasma density, while the untrapped electron density cannot exceed that upstream density [13]. In our electron capture PIC simulations [5], we have observed large-scale trapping of electrons inside the sheath around a positive tether, as well as weaker trapping in the pre-sheath. Their origin is clearly the potential transient at tether turn-on, but we have also noticed that there is a sort of electrostatic feedback tending to restore that population when scattering or artificial removal is used in the simulation to reduce it.

Given the presence of a charge population orbiting a biased tether, it is not difficult to conceive the possibility of "sloshing" modes of this charge, and we have occasionally noticed these modes in simulations (probably triggered by numerical events). Their frequency is of the order of, but lower than the plasma frequency of the trapped type of particles. This is supported by the following simplified argument: it can be easily shown that the frequency of a harmonic oscillator in which the peak potential energy U_{max} occurs at maximum deflection x_{max} is given by $\omega = \sqrt{\dfrac{2U_{max}}{mx^2_{max}}}$. For the particles trapped inside the sheath, the potential energy is a sizeable fraction of eV, while the amplitude of the oscillation can be a similar fraction of r_s, the sheath radius. Equation (1) shows an approximate scaling of r_s as $(eV/kT_e)^{3/4}$. Combining these expressions, one can show that

$$\omega \approx \frac{\omega_p}{(eV/kT_e)^{1/4}} \tag{2}$$

where ω_p is the plasma frequency of the oscillating particle (ions in the case of present interest).

RBR Research Requirements

The discussion in previous section can serve as a basis for identification of the research needs and challenges in this area. Some of these have been addressed and resolved in our work, while others remain as challenges for future research. Regarding the high-voltage tether option, the very large sheath radius makes it difficult to devise a numerical scheme that can resolve both, the thin tether neighborhood, and the sheath edge, which because of its large local potential gradients, may significantly influence scattering. A possible compromise would involve the use of an "analytical inner domain", as in the work of Onishi [14], dynamically coupled to the coarser outer grid. The inner domain is essentially Coulombic and axisymmetric, while the outer domain needs to account for the relative plasma flow and the geomagnetic field, and has to be at least two-dimensional, with 3D vector quantities. Since many of the promising designs include multiple tethers, these outer domains need to include more than one sheath, and the numerical domain will have to extend for several hundred Debye lengths. Because the spatial grid for solution of the Poisson equation needs to resolve the Debye length, one further difficulty accrues in that a very large number of grid nodes will be necessary even for these outer regions alone. A possible approach that can be envisioned is a transition to a quasi-neutral fluid model of the electrons at some distance from each tether; the Poisson equation then degenerates to quasineutrality, $n_e = n_i$, and the grid restriction to Debye size disappears. We have experience with this approach in the plasma plume area (Ref. [15]).

For the oscillator problem, one faces the need to resolve a shifting sheath boundary, probably requiring the use of an adaptive grid scheme. Also, since the emphasis is now on a consistent rendering of the oscillatory motions, the boundary conditions used at the edges of the computational domain will need to be of the radiation type, allowing outgoing waves, but not incoming waves to cross. This is a familiar problem in CFD and acoustics computations, where only one simple type of wave exists. For magnetized plasma, care will have to be exerted to accommodate all the wave modes of interest. Our analytical work on Whistler emission (Appendix 4) can be used for this task. One additional requirement for this type of computation is the accurate determination of the trapped particle population, for which not much numerical experience exists as yet. At a minimum, the numerical scheme will need to conserve energy over the full computational time, rather than just the passage time of a non-trapped particle, as is more usually the case. Perhaps the feedback mechanism referred to above, if fully confirmed, can be relied on to preserve the trapped population even in the presence of long-term numerical error accumulation

Reported Results

During the period of this Grant work was done along several paths: collection and review of experimental data, reduced order model studies of the electrostatic RBR problem, theoretical work on remediation using plasma waves, and development of relativistic adaptive numerical model for MV-tethers, ambient plasma dynamics with self-consistent description of wave-plasma interactions, and analytical modeling of the radiation pattern from a long tether acting as a VLF antenna. This work is described below in summary form, and additional details are available in the Appendices.

Task 1. Environment Parameters for RBR

Initial analysis included review of Radiation Belts composition data from 20+ US and Russian sources, which are partially included in the reference list at the bottom of this document, with additional details in **Appendix 1**. Charge and neutral particle concentrations and energy spectra have been identified for various spatial-temporal conditions, etc.

Next a comparison of natural Van-Allen belts conditions with artificial ionic and electron belts was performed to better characterize the space environment to be remediated with high-voltage tethers and RF-waves. Characterization of plasma collisionality, Debye shielding, thermal conditions has been performed.

Finally, the analysis of bare tethers erosion loses in orbit was done using available sputtering data. In short, the conclusion is that this effect can be neglected for the tether's operational parameters currently envisioned for electrostatic RBR.

Task 2. Study of electrostatic scattering by a tether as an RBR system

The systems model for radiation belt remediation is the development of work we had initiated prior to this work [16]. The model assumes a purely Coulombic potential around a negative tether, extending to zero value at the radius r_s of the sheath. The tether is assumed to be in a circular equatorial orbit, directed vertically (see Fig.1). Magnetic effects are ignored during the scattering interaction, but a background magnetic field is assumed, with its dipole axis coincident with the Geographic NS axis.

A classical scattering formulation furnishes a relationship between the incoming particle "miss distance" in the equatorial plane and its angular deflection by the electrostatic potential field. Analytical conditions are derived to test whether the leaving direction falls within the Loss Cone at the location of the interaction (defined as the angular range around the magnetic direction that will allow penetration of the particle below 110 km in either polar region), and an integration is performed over all velocities belonging to a "hollow cone" Maxwellian distribution and over all miss distances

consistent with entering the Loss Cone. The calculations are only partially done analytically, the rest being performed as a series of nested numerical quadratures.
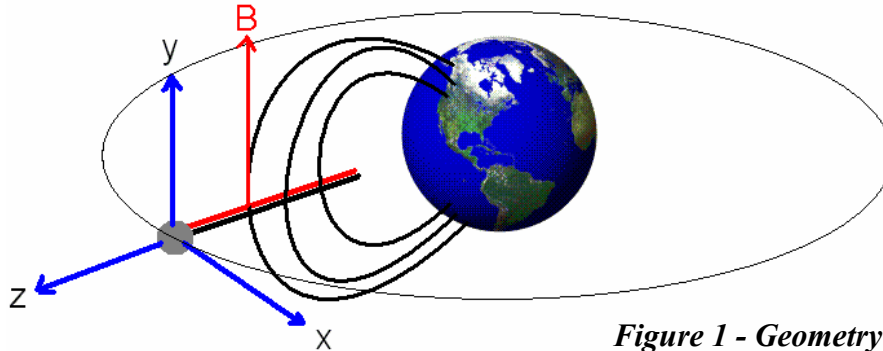
***Figure 1 - Geometry of RBR setup
used for reduced order model analysis***

The program embodying the above formulation has been coded and tested. Extensions are added to calculate the current collected by either polarity tether, hence the DC power required to sustain the potential. The OML formulation is used for this purpose. This tool was exercised to postulate and evaluate a number of system configurations (orbital parameters, number of tethers, tether dimensions, system mass, expected life, cost, etc). These are applied to assess against the system's performance, namely, the time to reduce the initial RB energetic particle population by a desired percentage. Natural as well as enhanced initial conditions are considered in the model, and the competition of the natural capture rate of cosmic radiation is an input to the calculations. A detailed description of the reduced model can be found in MS thesis by Chris Zeineh [16], which is incorporated here as **Appendix 2**. A useful presentation version of this work is also given in **Appendix 5.**

Task 3. Study of the Wave-Based RBR

3.1 General discussion

The loss mechanisms for the natural population of energetic particles in the Van Allen belts have been discussed quantitatively by Abel and Thorpe [17,18], and later examined in relation with the Radiation Belt Remediation concept by Inan, Bell and Bortnik [19]. Abel and Thorpe concluded that, except for the lowest altitudes, where Coulomb scattering dominates, natural and artificially injected waves of the Whistler family are responsible for most of the precipitation of trapped particles. The mechanism by which a fraction of the trapped particles gradually lose pitch angle and eventually enter the loss cone appears to be the accumulation of short periods of resonant interaction between a given trapped particle and the ducted radiation that propagates along the same magnetic tube. This mechanism is represented as a diffusion in pitch angle space, and the authors present a quasi-linear formulation to calculate the corresponding diffusivities due to the various resonant orders, including 0'th order (Landau resonance), first order

(cyclotron resonance) and, at the higher energies, second and higher orders as well. The frequency range that dominates precipitation depends on particle energy and altitude (*L*-shell); in particular, for the inner belt (*L*<2.6), the major contributor was found to be the near-monochromatic radiation from a small number of identifiable VLF antennas operating around the globe. This finding lends credence to the possibility of a deliberate intervention that could strongly reduce the mean life of these particles, possibly well below the roughly 100 days that apply to the inner radiation peak.

Inan, Bell and Bortnik, in their later work [19], discussed several parametric changes that would lead to further acceleration of the pitch angle diffusion. Thus, it was shown that VLF/ELF frequencies of only a few kHz, rather than the roughly *20 kHz* accounted for in the Abel and Thorpe study, would accelerate the effect by factors of the order of 30. Additional amplification should occur through the efficient accumulation of whistler wave energy in the magnetospheric cavity.

As Inan et al. point out, an electrical dipole antenna radiates most intensely at a frequency for which the wavelength is twice the antenna length ($L \approx c/(2nf)$), where n is the index of refraction at a frequency *f* and at the particular wave direction ψ with respect to the basic B field. Except for large ψ angles, near the resonance angle (ie, near 90°), n is of the order of 15, so that a choice *f=2.5 kHz*, as proposed by Inan el al. implies an antenna length of about 4 km. It seems clear that conventional satellite-based antennae, limited as they would be to *L* of the order of 100m, would force the use of much higher frequencies, with the attendant lower scattering effectiveness. To circumvent this problem, Inan et al. propose injection angles near the resonance angle, for which the index of refraction can be as high as 1000 (limited by thermal effects). If instead one used a fraction of the length of a multi-km gravity-gradient stabilized tether, the length of the antenna could be easily selected to match any desired frequency, down to below 1kHz, as well as any convenient wave angle. Concepts using several tethers segments as independent dipoles could offer additional flexibility, including the possibility of phasing arrangements that would help focus the radiated power.

3.2 Pitch scattering by Whistlers

We have pursued modeling work along the lines of Ref. [17] in order to create a tool for rapid evaluation of a variety of radiating tether concepts. Our model incorporates the effect of the $n \neq 0$ interaction modes and their bounce-averaged contributions to the pitch diffusivity as a function of the electron pitch and energy. The preliminary result, see Fig. 2, agrees well with those reported in Ref [17]. A more detailed account of this work is given in our **Appendix 3,** and in presentation form in **Appendix 5.**
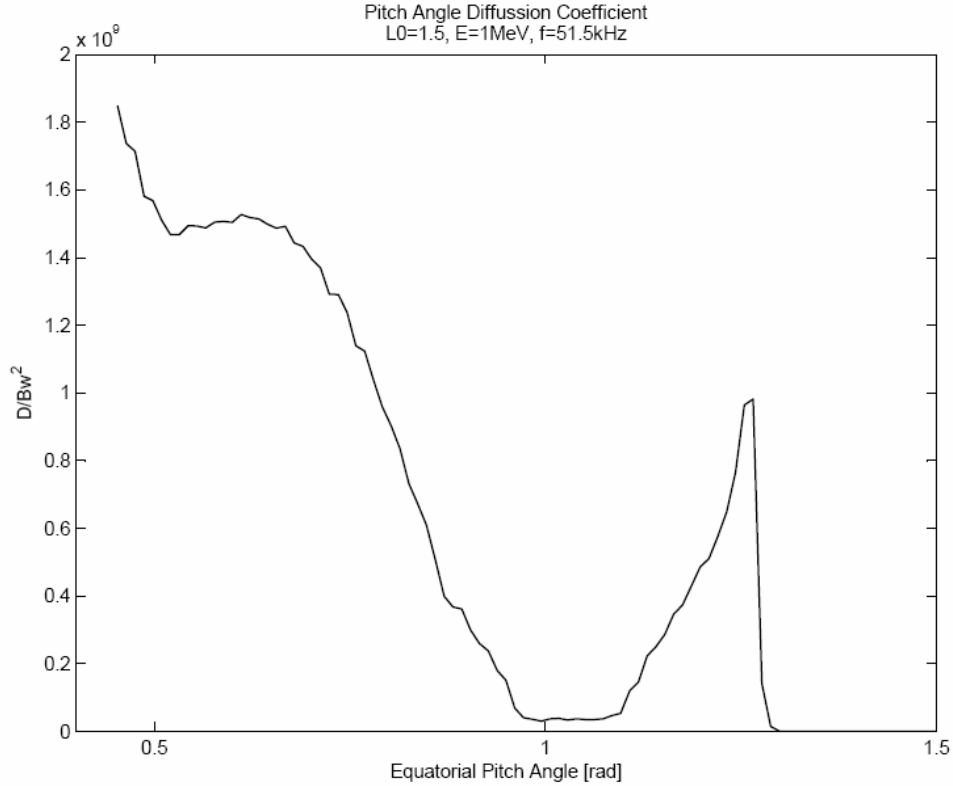
***Figure 2 – Calculated pitch-angle diffusion
coefficient for the quasi-linear model***

3.3 Whistler radiation from a tether

Future work on the spatial integration for a given L-shell requires as inputs the angular antenna pattern and a measure of the local wave intensity, such as the wave **B** field amplitude. This was initially attempted by using the results by Wang and Bell [20,21] for cold and warm magneto-plasmas, but it was thought important to develop our own detailed model, still within the cold plasma linear approximation, so that generalizations to other wave bands or other geometries could later be easily accommodated. This work is nearing completion now, as the MS Thesis for Mr. Yu Takiguchi, and its current status is described in detail in **Appendix 4** (and in presentation form in **Appendix 5)**. Refinements will be later introduced based on our numerical code (see the following sections). The Thesis is expected by September 2008, and it will contain a complete theoretical analysis of the radiation pattern as a function of antenna (tether) size and orientation, plus a full discussion of the electron dynamics as driven by the wave, for use in further pitch diffusion calculations. Numerical results will be shown for parameter ranges of interest to RBR. Beyond this, we intend to apply the same methodology to the lower frequency ion band, which is the one likely to be of use for removal of protons and other positive ions from the Belts. In addition, our numerical methods will be used to include nonlinear near-tether effects and complex geometries.

Task 4. Development of an Adaptive Numerical Model for RBR

The several orders of magnitude difference in spatial and temporal scales in the RBR electrostatic tether problem, and the smaller, but still large variation of scales for the low frequency driven electromagnetic tether, makes impossible the direct modeling of such systems using traditional kinetic approaches, e.g. a regular particle-in-cell method.

Indeed, for the plasma of interest the ratio of Debye length to the tether diameter could be on the order of 10^4 and more. Unlike common electrodynamic tethers, with sheaths sizes comparable to the radius of the wire and to the Debye length, the mega-volt electrostatic tethers have sheath sizes in the excess of hundreds of meters, comprising hundreds of Debye lengths. At the same time accurate calculation of small-scale phenomena are required, for instance:
  i) current collection by thin tether (exact trajectory intersection with surface);
  ii) parameters of the scattering cross-sections, affected by space charge near wire.

The simulation domain to capture the important pre-sheath region has to be at least several sheath lengths, 10 if possible. Thus we easily arrive at a billion required cell grids, making simulations impractical if a mostly uniform grid is retained, because 10-100 particles are required per cell to assure ~10% statistical accuracy of calculating transient regimes. This problem can be alleviated by either by:
  i) analytical integration of the trajectories near a high-voltage tether, as was first proposed by Onishi [14], or
  ii) numerical integration of trajectories in the high potential gradient region at a much finer scale [25].

Because the singular regions amount to about 1% of the entire simulation domain, both procedures are acceptable from the computational standpoint. However, the purely analytical approach does not allow potential variations, e.g. due to trapped particle space-charge, while the numerical approach may require tiny sub-stepping near the wire.

A significant acceleration of computations could be obtained by using a variation of FFT technique that allows internal boundaries. It was implemented in for the 2D case in [25], and used for detailed studies of current collection by tethers in different configurations [27,28], including multiple tether interaction. But this method, though used in many cases, still relies on the fact that the grid is uniform, and therefore, has a limited potential to study tethers with dimensions much smaller than Debye length, and with sophisticated shapes.

For practical engineering purposes, an additional important requirement is the ability to simulate complex geometries of the tethers, especially when we are talking about predictive modeling of tether arrays, systems with multiple elements as VLF antennas with complex cross-sections, etc. Partial patches, as shown in Fig. 3, can be used in a limited number of cases, because in the general case these cross-sections are not square or circular, and it is impossible to match an arbitrary shape with a combination of fixed

elements. Moreover, tethers can move mutually, excluding fixed grids as candidates for the universal approach.

Thus, despite the possibility of using some of the partial remedies so far discussed, it becomes obvious that the best way to proceed with multi-scale modeling of systems with complex geometries is the use of non-uniform grids. These are most desirable if they have an additional ability of conforming automatically to the arbitrarily shaped collecting surfaces. One of such possibility is illustrated in Fig. 4, where a circular tether is approximated using uniform structured and non-uniform unstructured grids.
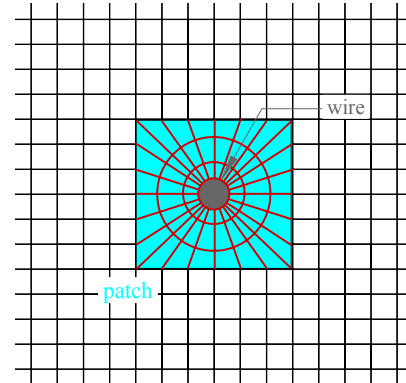

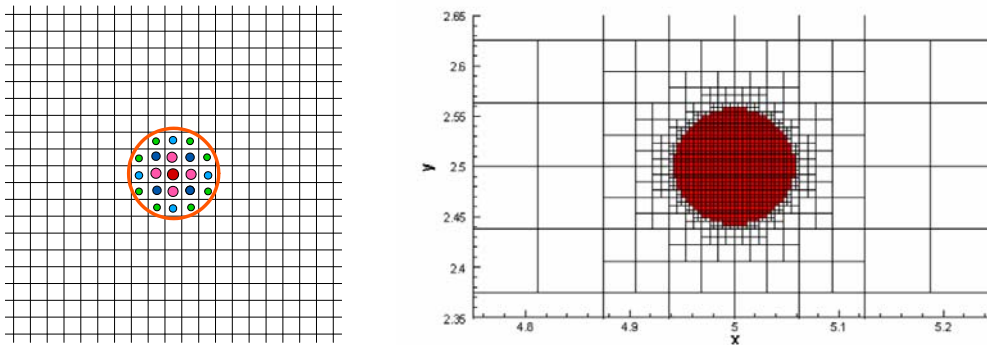*Figure 3 - Square-to-round patch for uniform grid near the tether [14]*

Figure 4 - Tether shape approximation using uniform structured (left) and non-uniform unstructured grid (right panel)

Modeling on non-uniform grids allows capturing of the tethered RBR and VLF problems with just millions of cells, instead of billions. Moreover, the adaptive approach opens the possibility to study interference of several tethers without doubling the amount of calculation. Indeed, a non-uniform adaptive mesh is capable of refining the mesh near the wire, leaving the majority of the nodes large. As a result, the total number of nodes is increased by a few percent. The computational grid in the tethers' vicinity is refined, as could be seen from Fig. 5, where an example of a two-tether system is
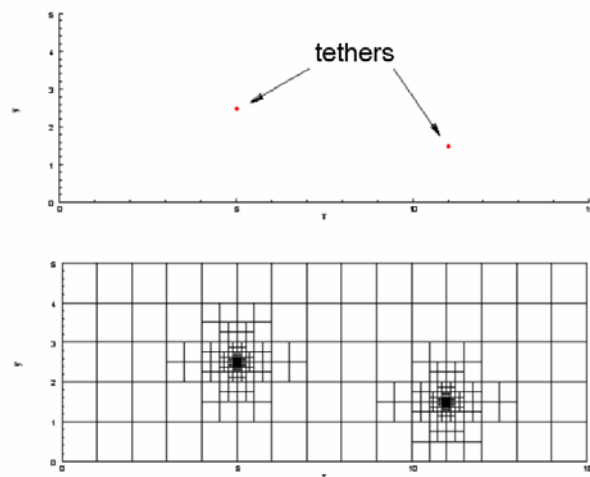

Figure 5 - Example of an adaptive grid local refinement for a 2-wire system

presented. It is clear that vast exterior region of the simulated domain remains unmodified. Doubling resolution just near a single pole requires adding only 4 extra cells. To reduce resolution by 10^6 (~2^{20}) only 160 extra nodes will be required.

We can easily match any spatial dimension through the exponential subdivision of cells: just 14 divisions are required to reduce cell size in excess of 4 orders of magnitude. Estimates show that simultaneous capturing on, say, 10x10km domain, and a tether with 1mm radius will require about 0.5 million cells, and about 20 millions of particles. Such simulation could be easily carried out on a desktop PC.

The adaptive grid approach allows not only flexible internal, but also external boundaries. Usually calculations are performed in a rectangular domain, which is not always the best choice. For instance, a circular domain allows cutting the number of required cells by a quarter, as could be seen from Fig. 7, in which contours of electrostatic potential are presented for regions with two different shapes. Also it shows initial grids, and meshes, after they automatically adapted to the structure of the potential.
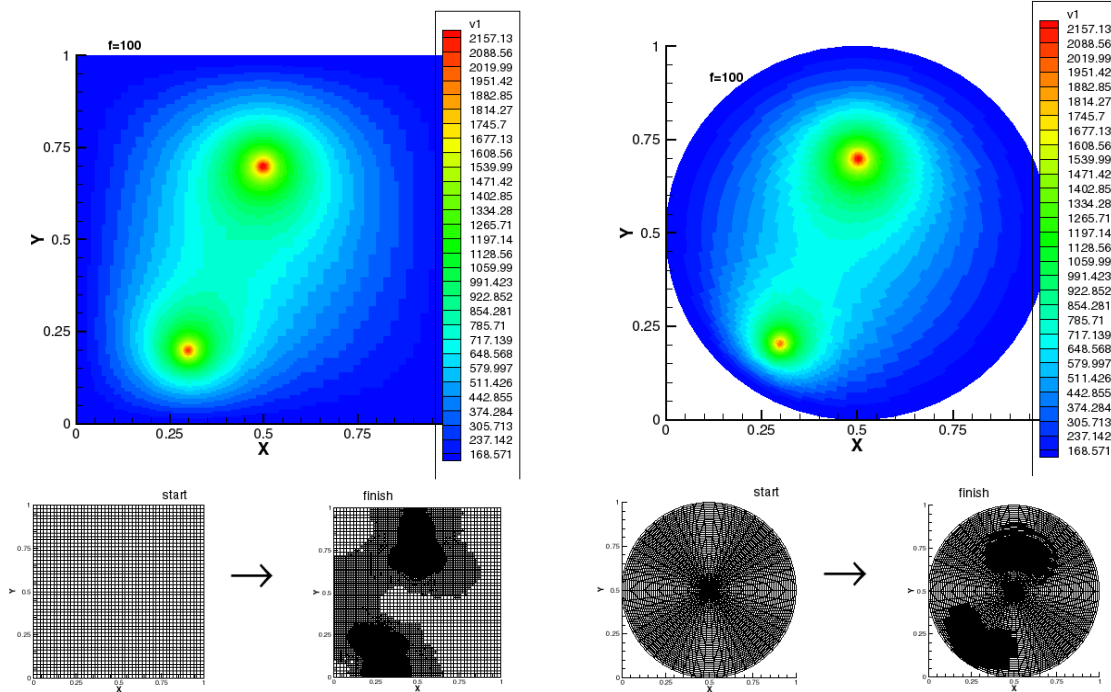

Figure 7 - Comparison of two electrostatic tether problem in a rectangular and in a circular domain

We also consider the introduction of other computational techniques to speed-up calculations. As an important example, since most of the computational cells may be located in smoothly varying distant pre-sheath regions, we will evaluate the use of hybrid methods, where a fluid description for electrons is applied for these quasi-neutral parts of the domain. These regions of hybrid simulation will dynamically be matched to those where the full Poisson equation needs to be solved, as we did in Ref. [15]. The boundary is adjusted by evaluating the degree on non-neutrality implied by the quasi-neutral

solution in its vicinity. The potential derived from the quasi-neutral side becomes a Dirichlet condition for the Poisson side, and an electron injection scheme has to be implemented on the kinetic side of the boundary. The results of these hybrid methods are being verified against fully kinetic modeling for selected test cases. The development of the latter becomes the top priority for the project, because they will be needed at a minimum for verification of the faster hybrid algorithms.

The key elements of the 2D adaptive grid RRC method [24] have been developed and applied to various problems [25-26] in 2D2V approximation. To allow arbitrary direction of the tether orientation to Earth's magnetic field it has to be expanded to 2D3V. Another important extension is an addition of fixed potential, current absorption and corrected algorithm for mesh refinement near the tethers' surface. If the potential will approach the MV level, then the relativistic equations of motion will have to be added (at least to electrons) to replace current classical trajectories.

For the VLF generation studies we are developing a Maxwell equation solver. It will have to take into account both antenna currents and currents induced in the plasma. To avoid possible time step limitations we will look whether the so-called Darwin model [29], which in effect suppresses EM-wave propagation by eliminating transversal displacement currents, is beneficial to such studies from physical and computational standpoints.

Another avenue, which we are exploiting, is the introduction of an artificial permittivity of the medium in the vast region beyond sheath and pre-sheath:

$$\varepsilon \operatorname{div} \vec{E}_S = e \int (f_i - f_e) d\vec{v} \qquad (3)$$

This transformation will decrease the magnitude of the polarization field, and will increase Debye length and thus reduce grid requirements by an order of magnitude. Unlike the sheath, remote areas remain always quasi-neutral, and charge separation does not seem to affect physics of the important processes that occur in there. To maintain undisturbed Maxwell plasma distribution in the periphery of a simulation domain we will apply either collisonless technique [22] of continuous distribution function adjustment, or, following continuous non-Monte-Carlo method [24-26], we will introduce effective collisions.

4.1 Features of the Kinetic Model. Benchmarking

The most important pieces of model: particle trajectory integrator and electro-magnetic solver have been developed in 2D2V approximation. In the electrostatic limit the dynamics of plasma species is described with set of kinetic equations for distribution function of plasma species – electrons and ions, if neutral dynamics is not important:

$$\frac{\partial f_\alpha}{\partial t} + \vec{v}\frac{\partial f_\alpha}{\partial \vec{x}} + \frac{(\vec{E}_{EXT} + \vec{E} + \vec{v}\times\vec{B}_{EXT})}{m_\alpha c}\frac{\partial f_\alpha}{\partial \vec{v}} = S_\alpha, \quad \alpha = e,i \quad (4)$$

here the self-consistent electric field is described by Poisson's equation depending on the spatial distribution of charges as given by Eq. (3), while the external electric (tether potential) and (Earth's) magnetic fields are fixed. The right-hand side describes particle sources and sinks inside the domain (capture) and at the boundary (orbital motion).

Trajectory integration

For orbit integration instead of finite differences approximation of Newton's equations of motion, we use partial analytical solutions. For example, in the simplest 2D2V planar case (*B* is normal to velocity) Eq. (4) reduces to:

$$\frac{\partial f_e}{\partial t} + v_x\frac{\partial f_e}{\partial x} + v_y\frac{\partial f_e}{\partial y} - (E_x + v_y B_z)\frac{\partial f_e}{\partial p_x} - (E_y - v_x B_z)\frac{\partial f_e}{\partial p_y} = S_e \quad (5)$$

immediately giving four equations for trajectories:

$$\begin{cases} \dfrac{dx}{dt} = v_x; & \dfrac{dv_x}{dt} = E_x + v_y B_z \\[2mm] \dfrac{dy}{dt} = v_y; & \dfrac{dv_y}{dt} = E_y - v_x B_z \end{cases} \quad (6)$$

which could be analytically integrated:

$$\frac{d^2(v_x - \frac{E_y}{B_z})}{dt^2} = \frac{dv_y}{dt}B_z = -B_z^2(v_x - \frac{E_y}{B_z}) \;\rightarrow\; v_x = \frac{E_y}{B_z} + (v_x^0 - \frac{E_y}{B_z})\, e^{-iB_z t} \quad (7)$$

Thus, we obtain an unconditionally stable algorithm, which guarantees that a particle will remain on a helical trajectory for arbitrary time steps and electro-magnetic field magnitudes. A few examples of the calculated particle trajectories in the laboratory (plasma) frame and in the flying tether frame are collected in the following Fig. 8.
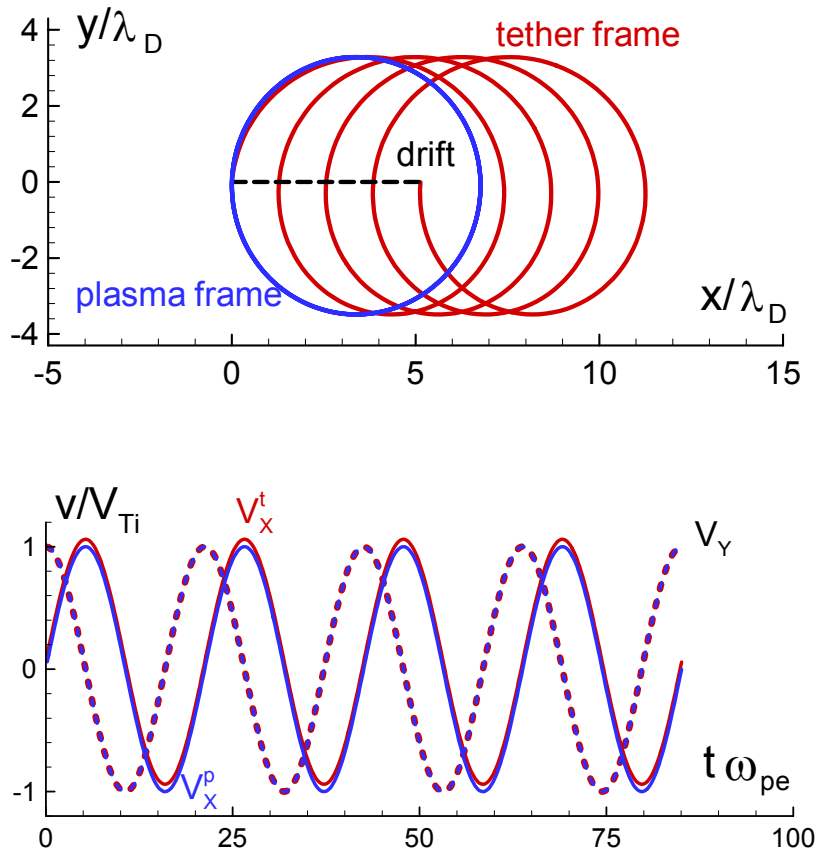
***Figure 8 - The same particle orbit calculated in the laboratory
frame (blue) and moving frame (red)***

To correctly describe particle trajectory in the moving tether frame one has to take into account simultaneously two factors:

i) particles have extra velocity V_parallel* = V_parallel + V_orbit
ii) particles drift across B with "external" electric field E_normal = V_orbit × B

As follows from Fig. 8 these guarantee that the Larmor radii and velocity magnitudes are preserved in both systems.

Another important observation is the need of actual electron/ion mass ratio for the predictive simulations. In the following two Fig.9 we present calculated ion trajectories for commonly used artificial mass ration M/m=100 and for the actual ratio for oxygen ions.
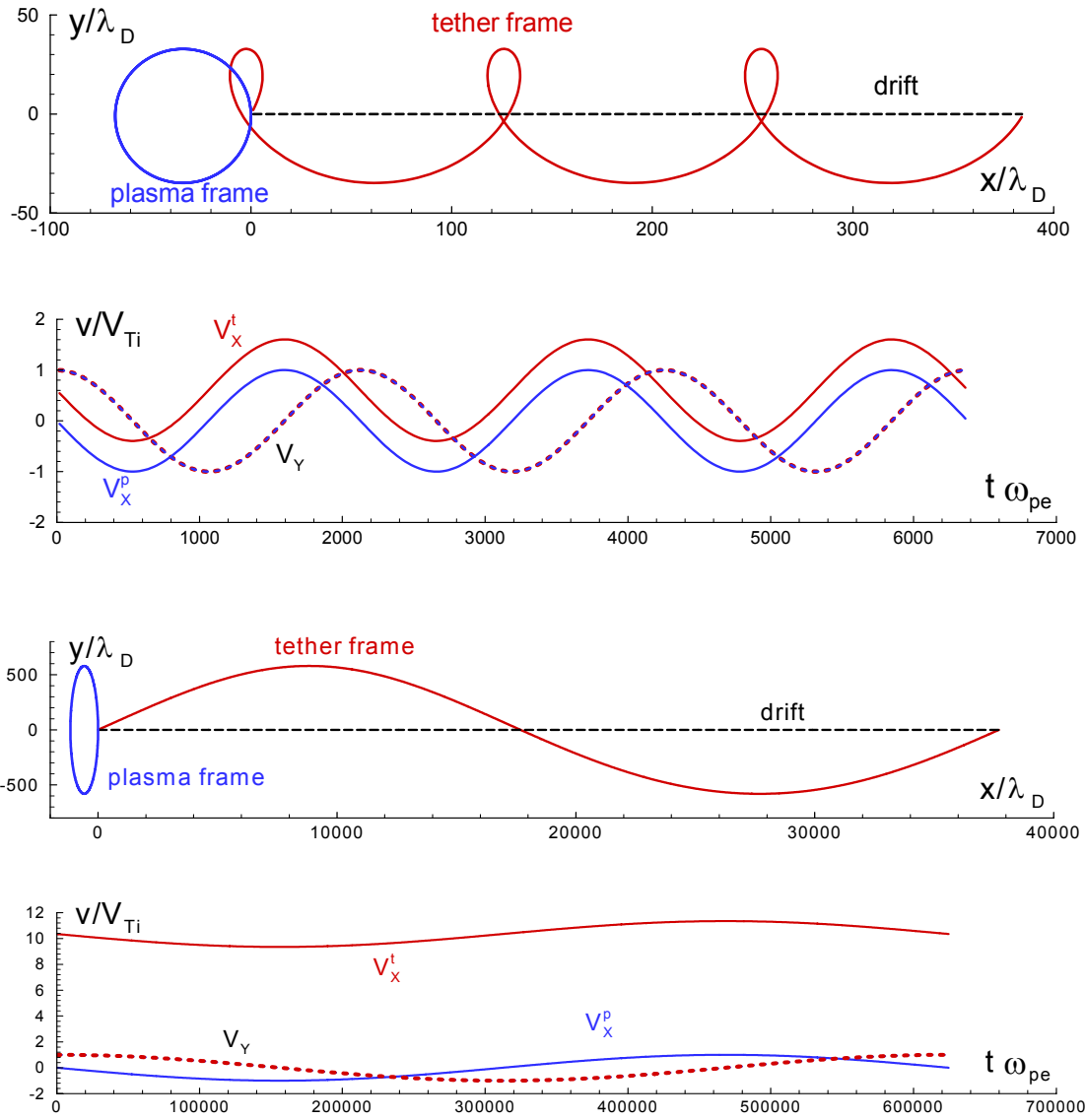
Figure 9 – Particle trajectory and velocity plot (two upper panels) for artificial mass ratio, and (two lower panels) – the same for actual oxygen ions

As one can see there is a part of a trajectory when ion moves in the negative axial direction, breaking the strong meso-thermal character of orbital motion ($M_i \sim 10$).

Electrostatic field solver

For Poisson solver on a structured mesh we deploy a fast FFT-based solver, while an SOR-based solver is used in the general unstructured grid case. In the latter case the benchmarking problem was chosen to be a field created by a uniformly charged wire. The results of comparison of the calculated and analytical potentials are given in Fig.10
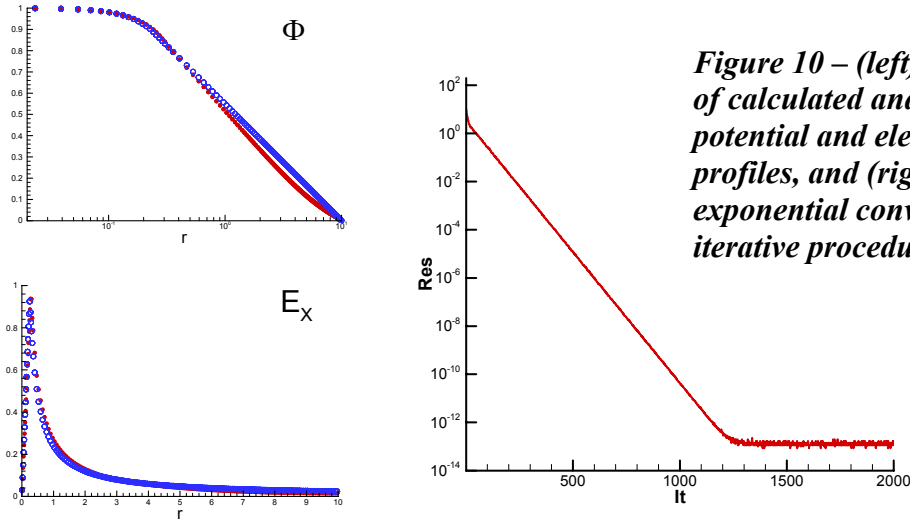
Figure 10 – (left) – comparison of calculated and analytical potential and electric field profiles, and (right) – exponential convergence of iterative procedure

The overall temporal resolution and conservations properties of the coupled kinetic solver and field solver are benchmarked on a plasma blob oscillations in a large simulation domain. Electrons are initially displaced from the heavy ion core. As follows from Fig. 11 the period of Langmuir plasma oscillations and the integral kinetic + potential energy are maintained within 1% accuracy.
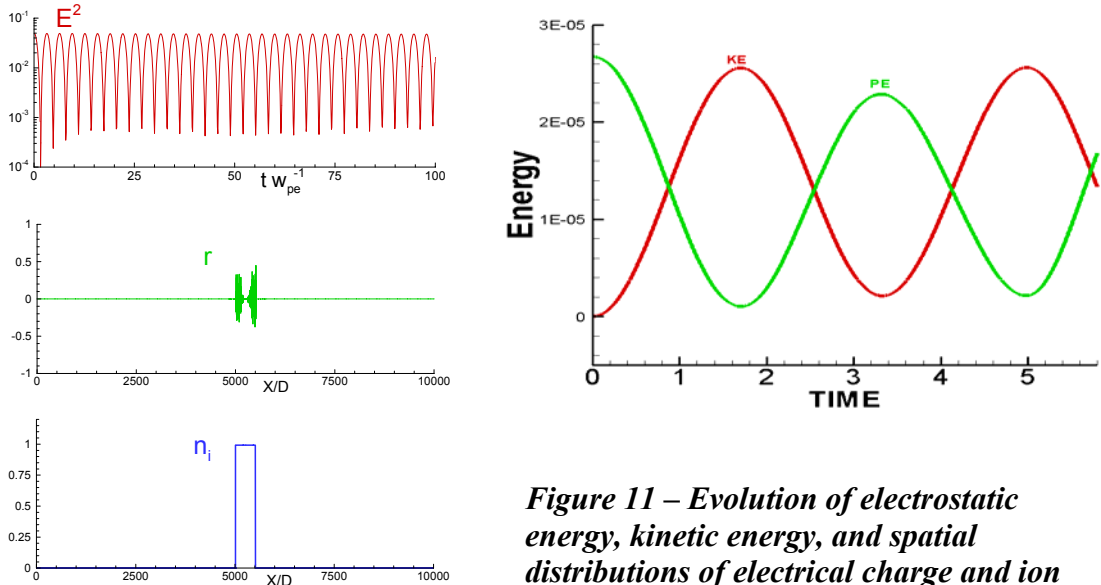

Figure 11 – Evolution of electrostatic energy, kinetic energy, and spatial distributions of electrical charge and ion density in the test

4.2 Single Tether Simulation

First simulations in a large domain on a structured grid involving the region of influence of a tether with relatively low potential ~100V indicate that i) the region of influence stretches as far as several meters from the wire, ii) a separatrix between open plasma streamlines and trapped plasma is formed, iii) there is a large void region formed behind the wire and a pre-cursor structure in front of it. These features are demonstrated by the following Fig. 12.
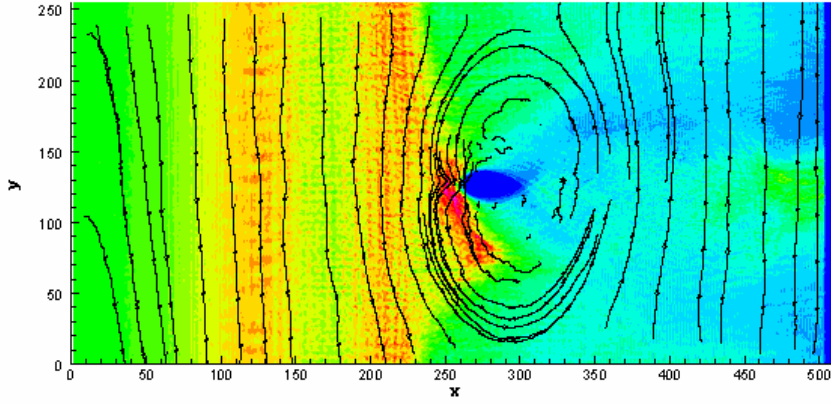
18

Figure 12 – Quasi-stationary flow around positively biased bare tether in a large simulation domain

4.3 Simulation of Multiple Tethers

First simulations of two equally biased bare tethers (on a structured 2D grid indicate the complex non-linear nature of the plasma flow interaction. In Fig. 13 we present contours of electrostatic potential (top) and ion density for initial and steady-state flows. Formation of initial vortices, density voids and interference of the two frontal shock-like structures is clearly visible.
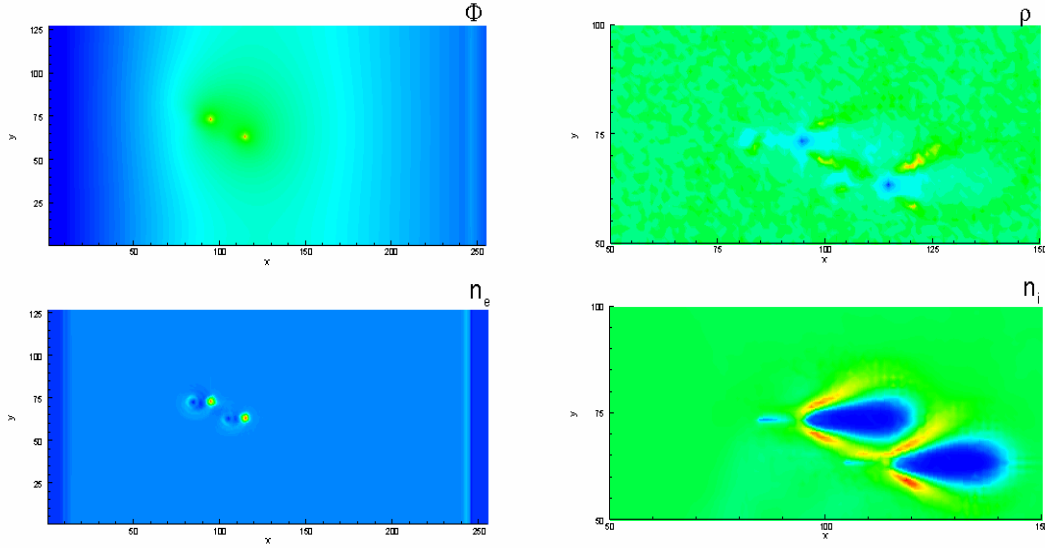

Figure 13 – (top) – contours of electrostatic potential, and (bottom) – contours of ion species density during the initial transient (left) and near-steady-state regimes (right)

4.4 Tethers with Negative Potential

A possibility of kinetic modeling of a couple of negatively biased tethers that can be used for scattering of the electron RB is presented in Fig. 14. The formation of a gigantic void in the plasma density can be clearly seen.
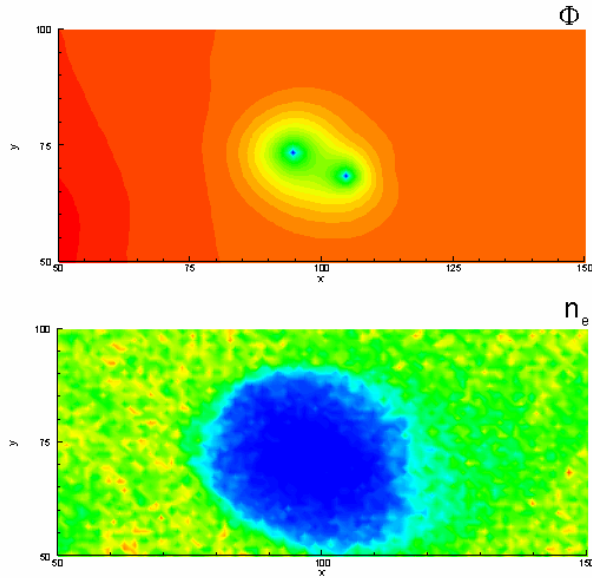

Figure 14 – (top) contour of electrostatic potential around negatively biased tethers and (bottom) – of the plasma density

4.5 Example of Adaptive Grid Simulation

Adaptive grid simulation of a single tether (Fig. 15) shows much finer detail of the flow structure, which appears to be more "turbulent" compared to the coarser uniform mesh results presented in Fig. 13. The edaptive branch is being actively tested.
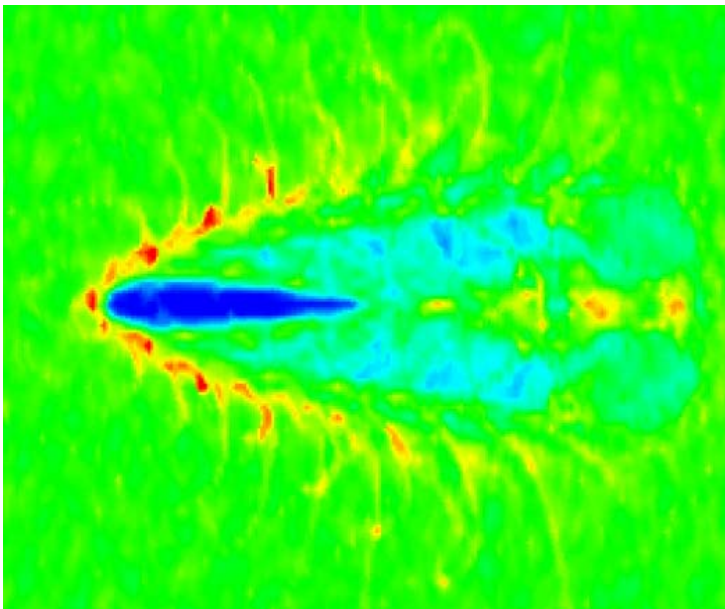

Figure 15 – contours of plasma density obtained in the adaptive grid simulations that automatically follow gradients of the numerical solution

4.6 Further developments

The focus of current kinetic model development is the addition of an arbitrary direction of the magnetic field with respect to x-y plane. This requires introduction of 3D velocity space, which substantially slows computational speed, roughly by one order. This makes parallelization of the code using MPI [23] the next priority.

The following step will include addition of a Maxwell set solver for EM-response to the self-generated currents in plasma:

$$\begin{cases} \dfrac{1}{c}\dfrac{\partial \vec{E}}{\partial t} = rot\vec{B} - \dfrac{4\pi}{c}\vec{j} = rot\vec{B} - \dfrac{4\pi}{c}\sum_{\alpha} q_{\alpha}\int f_{\alpha}\vec{v}d\vec{v} \\[2mm] \dfrac{1}{c}\dfrac{\partial \vec{B}}{\partial t} = -rot\vec{E} \\[2mm] div\vec{E} = 4\pi\rho = 4\pi\sum_{\alpha} q_{\alpha}\int f_{\alpha}d\vec{v} \\[2mm] div\vec{B} = 0 \end{cases} \qquad (8)$$

here index $\alpha = e,i$ represents plasma species. Neutral gas species can be included into the

Ultimately, 3D3V capability will be very desirable, but will require serious efforts, well beyond original plans.

Extension to 3D

However, two-dimensional Recursive Refinement and Coarsening adaptive grid was expanded to 3D dimensions using the following data format:

3D initial mesh (static):
To describe initial mesh we need two numbers – number of basic elements = *elements_base* and number of vertices = *vertices_base*. Also we need to specify connectivity *list(6,elements_base)*, and provide coordinates of vertices *x_vertices(vertices_base), y_vertices(vertices_base), z_vertices(vertices_base)*

3D adaptive mesh (dynamic):
elements – actual number of elements
value(V,element) – cell-centered values of total *V* unknowns
level(element) - subdivision level of elements, zero means the element
belongs to the base mesh.
index (level,element) – index (history) of the element as follows
index(0,element) – pointer to parent on the base mesh   Y
index(0<I<level+1,element) = 1,…,8 in accordance with   3 4
adopted sub-cells numeration: 1 2 X
neighbor(1:24,element) – list of neighborhood, with the following   7 8
assumption: 1-4 E, 5-8 W, 9-12 N, 13-16 S, 17-20 Up, 21-24 Down   5 6
neighbor(1,5,9,13,17,21;element) always non-zero;   Z
neighbor(2,6,10,14;18,22;element)=0 means just 1 in the direction

neighbor(1,5,9,13,17,21;element) < 0 means there is a boundary
3D *Class-function*:
XYZ(element) returns coordinates of 8 corners of the element and of its center

Full algorithm includes local refinement, which was implemented and tested up to 3 levels of subdivision, see example in Fig.16.

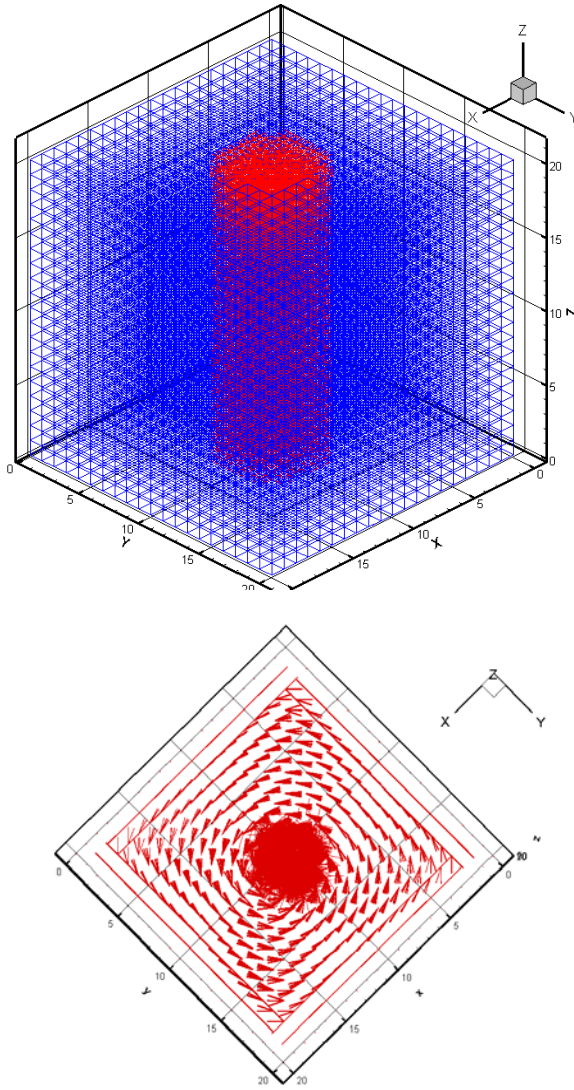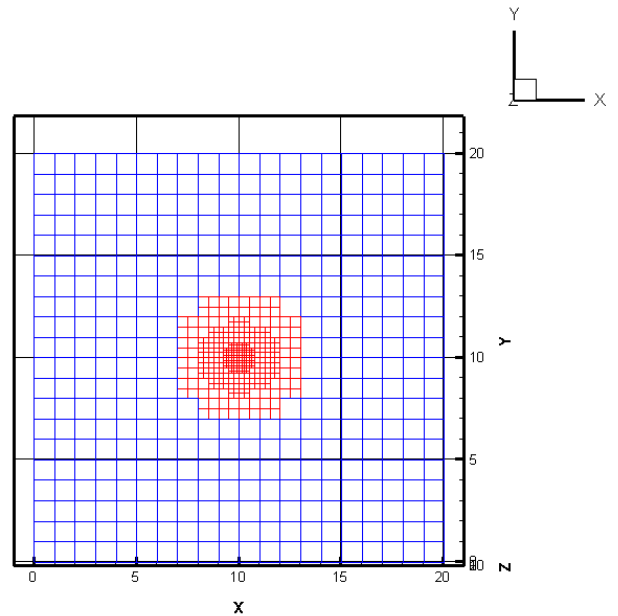***Figure 16: Mesh adapted to the 3-D current in the thin wire; 3 levels of subdivision are seen from 2D projections on X-Y plane; also shown is vector field of the calculated B-field***

Current effort includes:

i)   Testing automatic, up to 12 levels, mesh refinement;
ii)   Development of the reversed function – unstructured mesh coarsening;
iii) Optimization of the data base and two-way algorithms.

These steps are the cornerstone of current work. Methodologically they are similar to the 2D case. However, the complexly of the code is one order higher. The main reason is algebraic increase in the number of immediate neighbors, and topological complexity due to the need of finding neighbors of neighbors of neighbors, one level more than in the 2D case.

Another major problem is continuous tracking of the particles. For efficient particle locating on the unstructured grid particles are spatially-ordered with the stored relative coordinate with respect to the element they belong to. Tracking particle algorithm is substantially more complicated in three dimensions. It is being debugged in the general case, including the most complicated with 1:8 variations of the ratios of linear elements' sizes along cell corners. In 2D case only 1:4 corresponding ratio was possible.

Relativistic orbits

The system of Boltzmann equations (4) in the relativistic 3D3P formulation is normalized using natural units for the RBR problem:

Elementary charge: $e = 1.6022 \times 10^{-19} C$

Proton mass: $m_p = 1.6726 \times 10^{-27} kg$

Length unit: $1\, meter$

Speed of light in vacuum: $c = 2.9979 \times 10^8\, m/\sec$

From these primary units we derive secondary units for time, EM-fields, kinetic and potential energies, etc. For instance, the dimensionless equations of motion of individual particles read:

$$\begin{cases} \dfrac{d\vec{r}_i}{dt} = \vec{v}_i = \dfrac{\vec{p}_i}{\sqrt{m_{0i}^2 + p_i^2}} \\ \dfrac{d\vec{p}_i}{dt} = q_i\, (\vec{E}(\vec{r}_i) + \vec{v}_i \times \vec{B}(\vec{r}_i)) \end{cases} \qquad i = \overline{1, N} \qquad (9)$$

here $\vec{p}_i = m_{0i} \gamma_i \vec{v}_i$ is the relativistic momentum of the i-th particle, m_{0i} is its mass at rest, q_i is the integer (normalized) charge and normalized relativistic factor $\gamma_i = \sqrt{\dfrac{1}{1 - v_i^2}} = \sqrt{1 + \dfrac{p_i^2}{m_{0i}^2}}$.

Equations (9) are solved using semi-analytical approach similar to [26]. On-going benchmarking includes calculation of orbits is analytical configurations and fields calculated by the solvers for static EM-fields.

Student involvement

During this project several students received training.

Graduate Student Christopher Zeineh (USA), M.S. '05, submitted in the end of 2005 his Master of Science thesis entitled "***Application of an Electrostatic High-Voltage Tether to Radiation Belt Remediation***".

Undergraduate Student Nicholas Edelman (USA), B.S. '07 was involved through the MIT UROP program. His report entitled "***Research of the Environment Parameters for Radiation Belt Remediation with a High Voltage Tether***" is attached to this report.

Visiting Summer Student Jose Manuel Zorrilla-Matilla, (to graduate from Supaero, Toulouse and from the Polytechnical U. of Madrid, Spain in 2007) has developed the model for wave-based RBR.

Graduate student Yu Takiguchi, from Japan, has been working on the emission of Whistler waves by a tether, and intends to submit this work as his MS Thesis in September 2008.

References

1. V.V. Danilov, B.A. Elgin, O.S. Grafodatsky and V.V. Mirnov, "High voltage satellite tethers for active experiments in space". 6th Spacecraft Charging Conference, AFRL-VS-TR-20001578, 1 Sep. 2000.
2. E. Choiniere and B. Gilchrist, presentation at the MIT Tethers Workshop, Sep. 29, 2004.
3. Bryan M. Minor, TUI/Science Ops. Report to DARPA, 24 Sep. 2003, App. H
4. J. R. Sanmartin, "Bare tether sheath and current: Comparison of asymptotic theory and kinetic simulations in a stationary plasma" To appear in the IEEE… .
5. Laframboise, J. G. "Theory of spherical and cylindrical Langmuir probes in a collisionless Maxwellian plasma at rest", Rep. 100, Institute for Aerospace Studies, Univ. of Toronto, Ontario, Canada, 1966.
6. Jean-Marie Deux, "Advanced Kinetic Model of Ionospheric Tethers", Master of Science Thesis, MIT, Department of Aeronautics/Astronautics, December 2005.
7. David Cooke, personal communication
8. S. G. Bilen, B. E. Gilchrist, C. Bonifaci, E. Melchioni, "Transient response of an electrodynamic tether system in the ionosphere: TSS-1 first results". Radio Science, 1519, 1535, (1995).
9. E. Choiniere, B. E. Gilchrist and S. G. Bilen, "Enhancement of electrodynamic tether electron current collection using radio frequency power".
10. I. B. Bernstein, J.M. Green and M.D. Kruskal, Phys. Rev. 108, 546 (1957)
11. A. V. Gurevich, "Distribution of captured particles in a potential well in the absence of collisions", Soviet Physics JETP, Volume 26, No. 3, March 1968.
12. T. Onishi, M. Martinez-Sanchez, D. L. Cooke and J.R. Sanmartin, "PIC computation of electron current collection to a moving bare tether in the mesothermal

condition". Paper IEPC-01-245, 27th International Electric Propulsion Conference, Pasadena, CA, Oct 2001.

13. J.G. Laframboise and L. W. Parker, Probe design for orbit-limited current collection", Physics of Fluids, 16, 629, 1973.

14. T. Onishi, Numerical Study of Current Collection by an Orbiting Bare Tether, PhD Thesis, MIT, August 2002.

15. M. Santi, S. Cheng, M. Celik, M. Martinez-Sanchez and J. Peraire, "Further development and preliminary results of the AQUILA Hall thruster plume model". Paper AIAA-2003-4873, 39th Joint Propulsion Conference, Huntsville, AL, July 2003.

16. C.Zeineh, Application of an Electrostatic High-Voltage Tether to Radiation Belt Remediation, M.S. Thesis, MIT, 2005

17. Bob Abel and Richard M. Thorpe, "Electron scattering loss in the Earths inner magnetosphere. 1 Dominant physical processes". J of Geoph. Res., V. 103, No. A2, pp 2385-2396, Feb. 1 1998.

18. Bob Abel and Richard M. Thorpe, "Electron scattering loss in the Earths inner magnetosphere.2. Sensitivity to model parameters". J of Geoph. Res., V. 103, No. A2, pp 2397-23XX, Feb. 1 1998.

19. U.S. Inan, T.F. Bell and J. Bortnik, "Controlled precipitation of radiation belt electrons". J of Geoph. Res., V.108, No. A5, pp 1186-1197, Jan. 2002.

20. T.N.C. Wang and T.F. Bell, "VLF/ELF radiation patterns of arbitrarily oriented electric and magnetic dipoles in cold, lossless multi-component magneto-plasma". J of Geoph. Res., V.77, No. 7, pp 1174-1189, March 1972

21. T.N.C. Wang and T.F. Bell, "Electric dipole radiation at VLF in a uniform warm magneto-plasma". Revue de Physsique Appliquee, Tome 7, Mars 1972, page 11.

22. J. B. Ferry and M. Martinez-Sanchez, "Electron collection by a tether at high potential in a magnetized plasma", Paper AIAA-03-4948, 39th Joint Propulsion Conference, Huntsville, AL, July 2003.

23. Justin Fox. "Parallelization of a Particle-in-cell Simulation Modeling Hall-effect Thrusters". Master of Science Thesis, MIT, Department of Aeronautics/Astronautics, January 2005.

24. A.A.Batishcheva, O.V.Batishchev, "RRC Adaptive Grid Method For Magnetized Plasma", Proceedings of the 17th Int. conference on the Numerical Simulation of Plasmas, Banff, Canada, May 22–24, 2000, p.29–32

25. O. Batishchev and M. Martinez-Sanchez, "Adaptive Mesh PIC and PIC-Vlasov Hybrid Methods for Space Electrodynamic Tether and Anomalous Transport Modeling", p.391, 18th ICNSP, Cape Cod, 7-10 September, 2003.

26. Alla Batishcheva, Oleg Batishchev, "Adaptive Kinetic Simulation of Plasma Propulsion by Laser Ablation", APS Bulletin 49 (8) 260, November 2004.

27. J.-M. Deux, O.V. Batishchev, M. Martinez-Sanchez, "Advanced Kinetic Model for Electrodynamic Space Tether", Proc. 4th Intl. Space Prop. Conf., Cagliari, Italy, June 2-4, 2004.

28. Jean-Marie Deux, Oleg Batishchev, Manuel Martinez-Sanchez, "Space tether current collection: an advanced kinetic model", APS Bulletin 49 (8) 299, Nov. 2004.

29. C.K. Birdsall, A.B. Langdon, Plasma Physics via Computer Simulation, McGraw-Hill, 1985.

APPENDIX 1: THE RBR ENVIRONMENTAL BACKGROUND

Nicholas Edelman, January 10, 2006

i) Environment Parameters for Radiation Belt

ii) Possible remediation with a High Voltage Tether

1. Background Information

The earths magnetic field traps high energy charged particles in the magnetosphere, forming an inner proton belt and an outer electron belt. High energy particle fluxes lead to radiation damage and degradation of spacecraft and satellites. A high altitude nuclear detonation would likely create a new high energy electron belt and increase the radiation risk to spacecraft and satellites. To mitigate the effects of this new belt, a high voltage tether system has been suggested as a method for accelerating the deflection of high energy particles into their loss cone. On July 9, 1962, the United States detonated 1.4 Megaton nuclear warhead code-named "Starfish" at an altitude of 400km (L = 1.12) above Johnson Island in the Pacific Ocean. The explosion released high energy neutrons and fission fragments and ionized large quantities of neutral atmospheric gases. This created an artificial electron radiation belt centered at L = 1.5 [9] within the naturally occurring inner Van Allen proton belt (Appendix II contains a more detailed description of the particles processes involved after the explosion). In addition, the explosion created a thin region of very high energy electrons near L = 1.2 [6]. On October 28, 1962, the U.S.S.R. detonated a submegaton nuclear weapon at L = 2, and as with the Starfish explosion, the trapped radiation belt formed close to the L-value of detonation [15]. As expected, the electron distribution best resembles the fission spectrum near the L-value of detonation (Figure 1.1). Although many altitudes are suitable for simulation, I propose a study at an altitude of 3000km (L = 1.5) centered on the equatorial magnetic latitude. The lower atmosphere (a few hundred kilometers altitude) would not be a suitable simulation zone, because the decay times are in the order of days and thus are not a primary concern. L = 1.5 is in a region of substantial high energy proton flux and is at a similar L-value to the trapped radiation belts created by the Soviet and U.S. nuclear detonations.
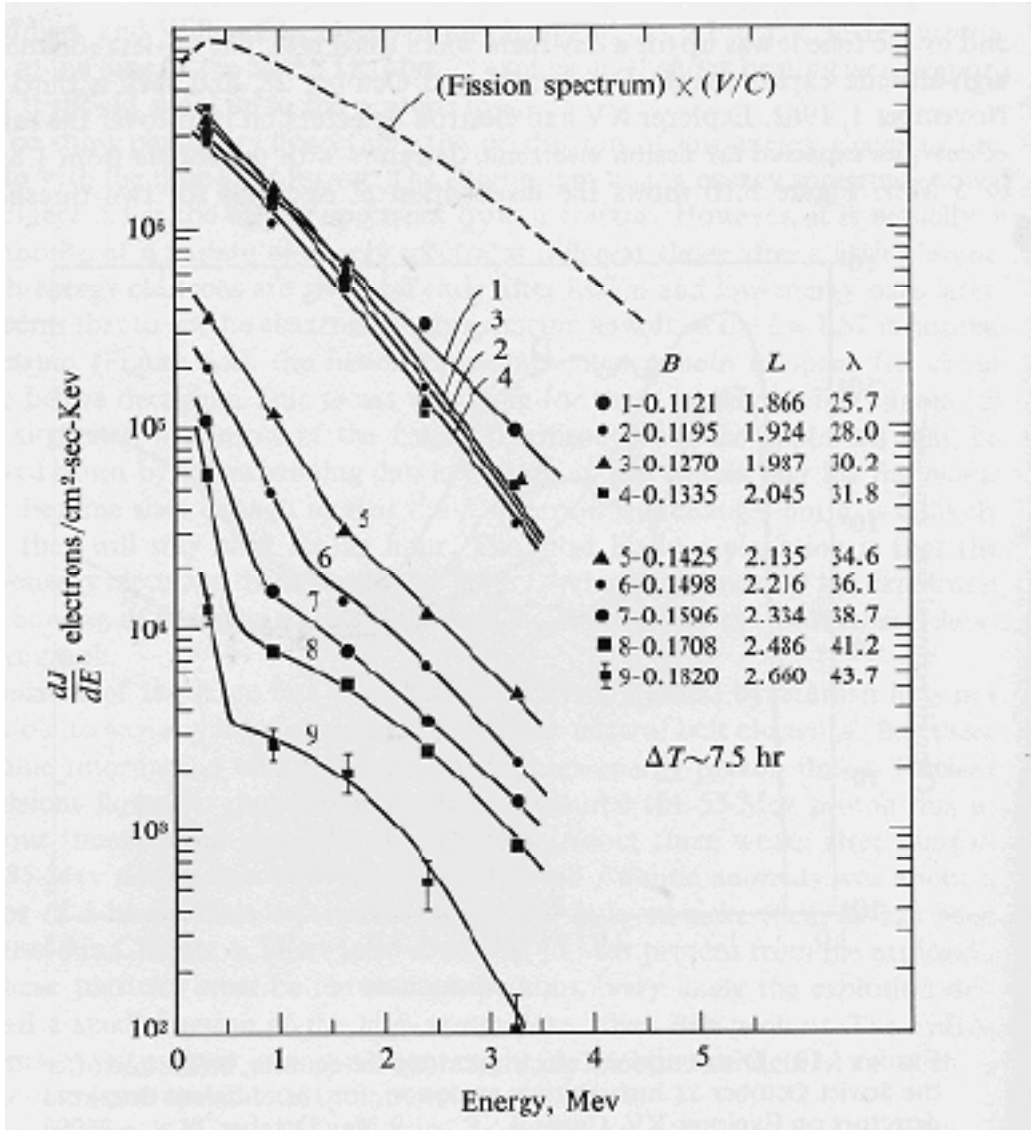
Figure 1.1: Trapped electron spectrum at various L-values following the October 28, 1962 Soviet nuclear detonation [15].

2. Inner Van Allen Plasma Environment

The inner Van Allen belt extends from approximately $L = 1.2$ to $L = 2$ and naturally traps high energy protons. In the event of a nuclear detonation, the region would become heavily populated with high energy electrons. For the purposes of this analysis, the tether assumed to be operating at $L = 1.5$ at equatorial magnetic latitude ($\lambda = 0$), or approximately an altitude of 3000km.

Table 2.1 summarizes the characteristics of the natural plasma environment.

Characteristics of Natural Plasma Environment	
Magnetic Field	$B = 9.815 \times 10^{-2}$ Gauss
Plasma temperature (daytime)	$T = 0.4$ eV
Plasma temperature nighttime	$T = 0.2$ eV
Plasma density	$n = 10^4 \text{cm}^{-3}$
Ion composition	$H^+ = 5 \times 10^3 \text{cm}^{-3}$ $He^+ = 10^3 \text{cm}^{-3}$ $O^+ = 10^2 \text{cm}^{-3}$
Neutral density	$n = 10^4 \text{cm}^{-3}$
Neutral composition	$H = 10^4 \text{cm}^{-3}$ $He = 10^4 \text{cm}^{-3}$ $O = 10^3 \text{cm}^{-3}$
Larmor Radius	$r_e = 15.3 \text{cm}$ $r_i = 6.57 \times 10^2 \text{cm}$
Debye Length	$\lambda_D = 4.70 \text{cm}$
Collisionality (mean free path)	$\lambda_e = 135 \text{km}$ $\lambda_i = 192 \text{km}$

Table 2.1: Environment Parameters

2.1 Particle Energies

The dominant space plasma environment in inner Van Allen Belt consists of a relatively cool, low density background plasma (see Figures 2.1 and 2.2). Extrapolating from the data in Figure 2.2, the natural plasma temperatures at an altitude of 3000km and =0 are approximately:

$$\text{Plasma temperature(daytime)} = 0.4\text{eV}$$

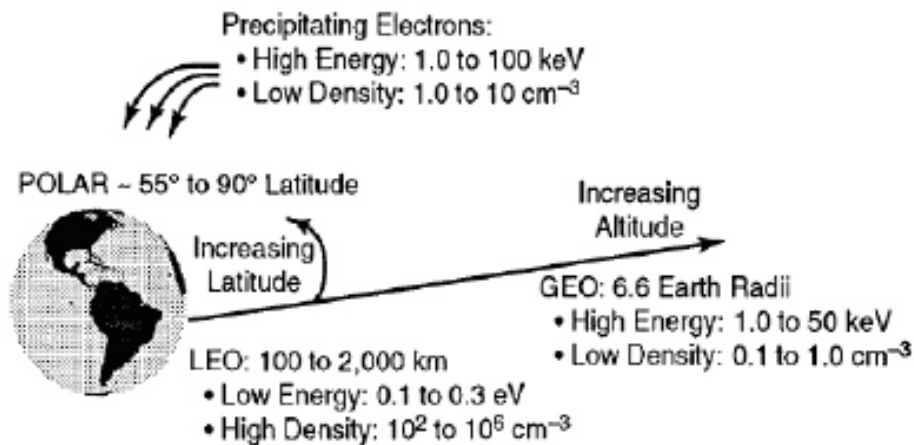$$\text{Plasma temperature(nighttime)} = 0.2\text{eV}$$

Figure 2.1: Properties of the natural space plasma as reported in a NASA report on spacecraft charging [2].
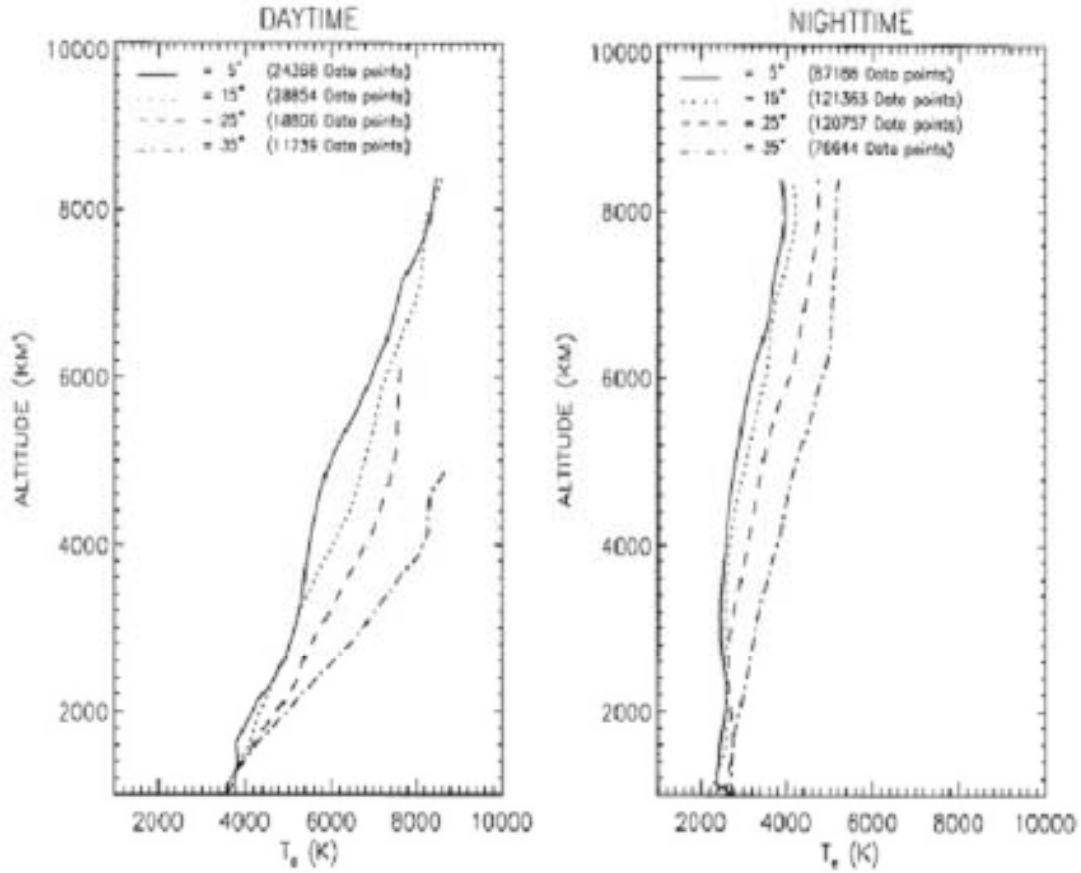
Figure 2.2: Variation of electron temperature with altitude and magnetic latitude. The data depicts the average temperatures from 1989 to 1995 recorded by the thermal electron distribution instrument on the EXOS-D satellite [10].

2.1.1 High Energy Particle Fluxes

In addition to the average particle populations, the natural space plasma environment is characterized by high energy particle fluxes, which are of particular interest for studying radiation belt remediation applications. These fluxes are illustrated in Figures 2.3 and 2.4.
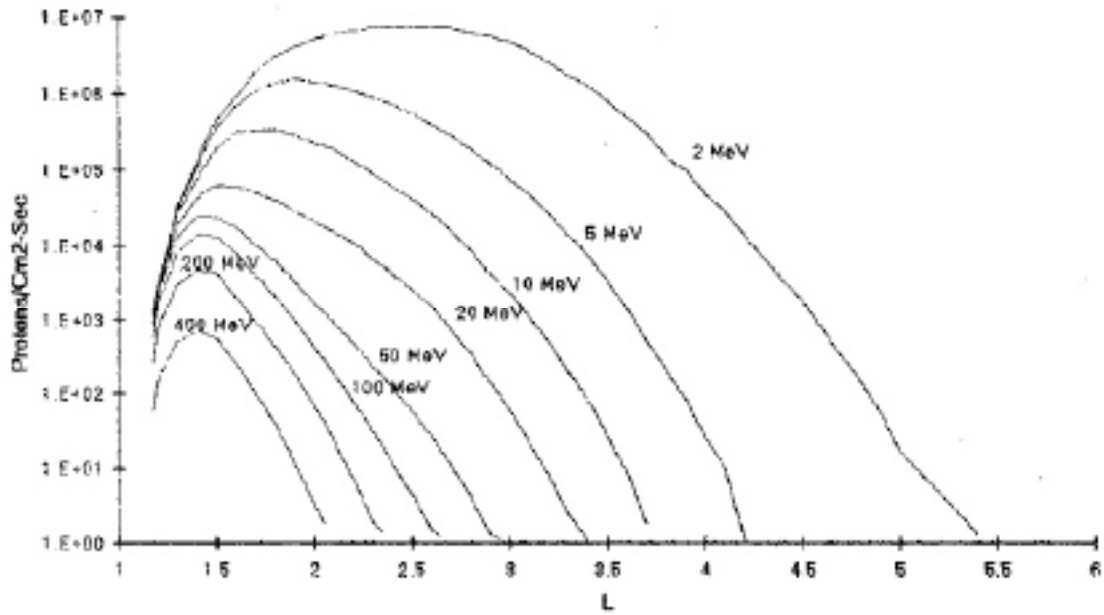
Figure 2.3: High energy proton fluxes and energies as a function of L-value from the AP8MIN model [3].

2.2 Particle Densities

At the high altitude of the inner Van Allen Belt region, the environment is characterized by a relatively low plasma density. Near L=1.5 at an equatorial magnetic latitude, Figures 2.5 and 2.6 contain an ambient density n = 10^4 cm $^{-3}$.
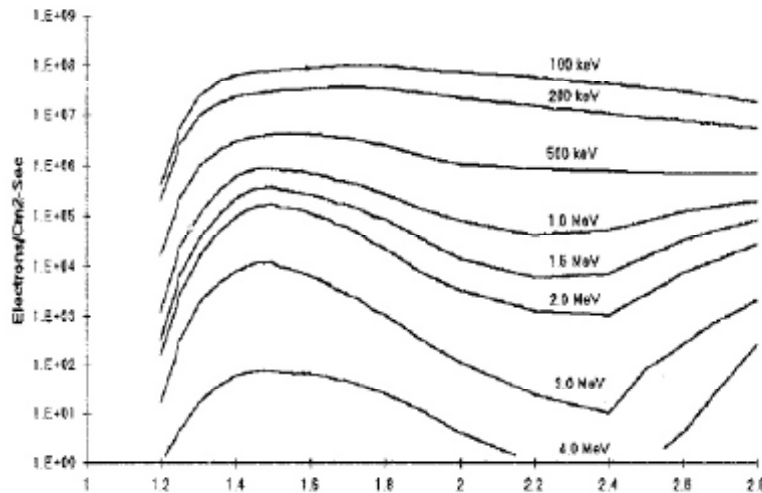

Figure 2.4: High energy electron fluxes and energies as a function of L-value. The data reflects Vampola's update of the AE-8 model using data from the Combined Release and Radiation Effects Satellite (CRRES) [3].
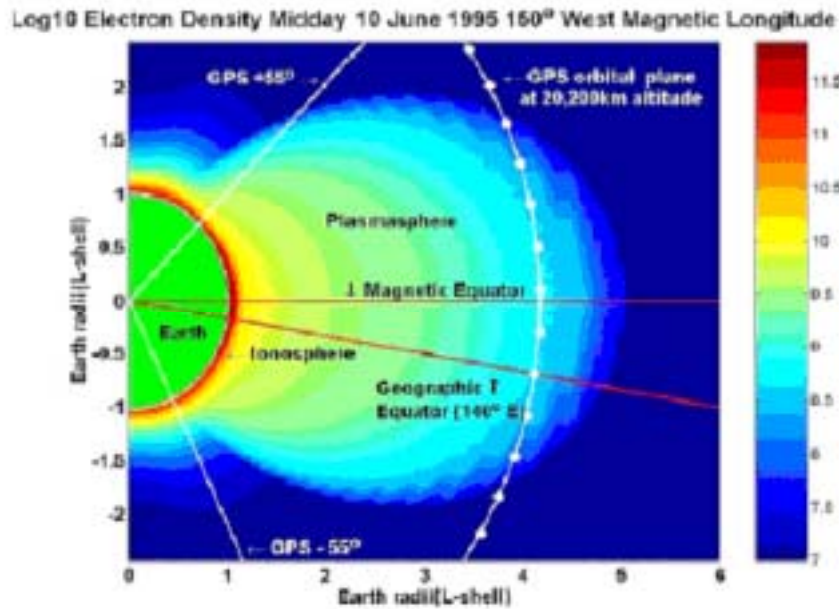
Figure 2.5: Electron densities (m₋₃) described as a function of distance from the earth. Densities were calculated by the Global Plasmasphere Ionosphere Density (GPID) model [4].

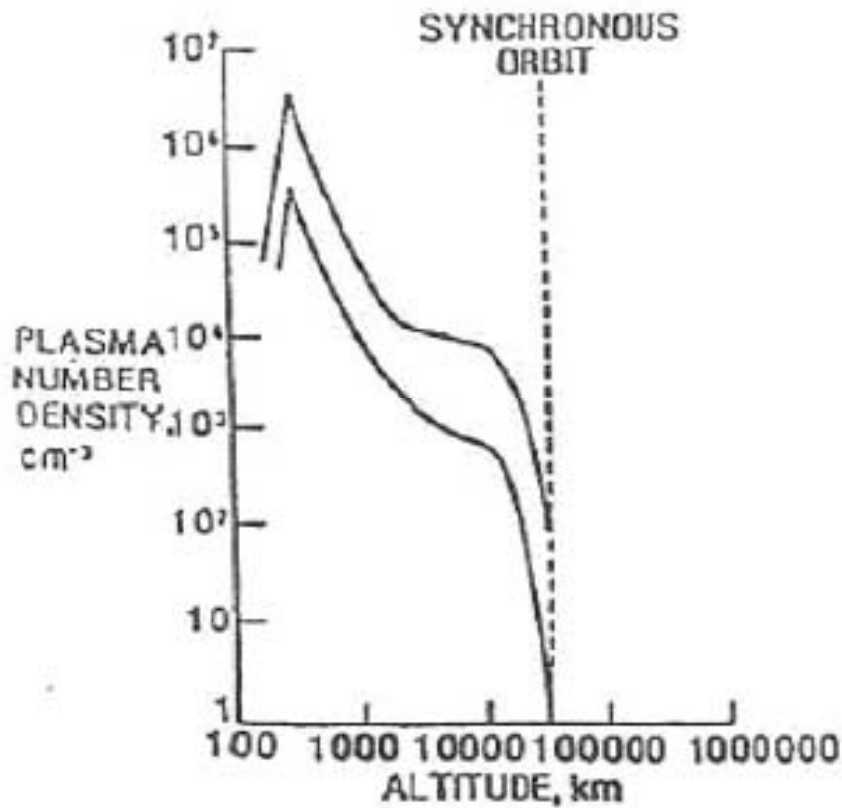

Figure 2.6: Variation of electron density with altitude at the magnetic equatorial latitude [12].

2.2.1 Neutral Densities

The neutral particles from Figures 2.7, 2.8(a), 2.8(b), and 2.9 supports the fact that the high altitude space plasma is a weakly ionized plasma with neutral density approximately equal to the plasma density. From the data, it can be seen that the neutral particles density is $n_{neutral} = 10^4$ cm^{-3}. The data indicates that the neutral density composition is as follows:

$H = 10^4$ cm^{-3}
$He = 10^4$ cm^{-3}
$O = 10^3$ cm^{-3}

2.2.2 Ion Composition

From Figure 2.10, it can be seen that the inner Van Allen belt ions are dominated by low energy protons. The region contains the following ion densities:

$H^+ = 5 \times 10^3$ cm^{-3}
$He^+ = 10^3$ cm^{-3}
$O^+ = 10^2$ cm^{-3}
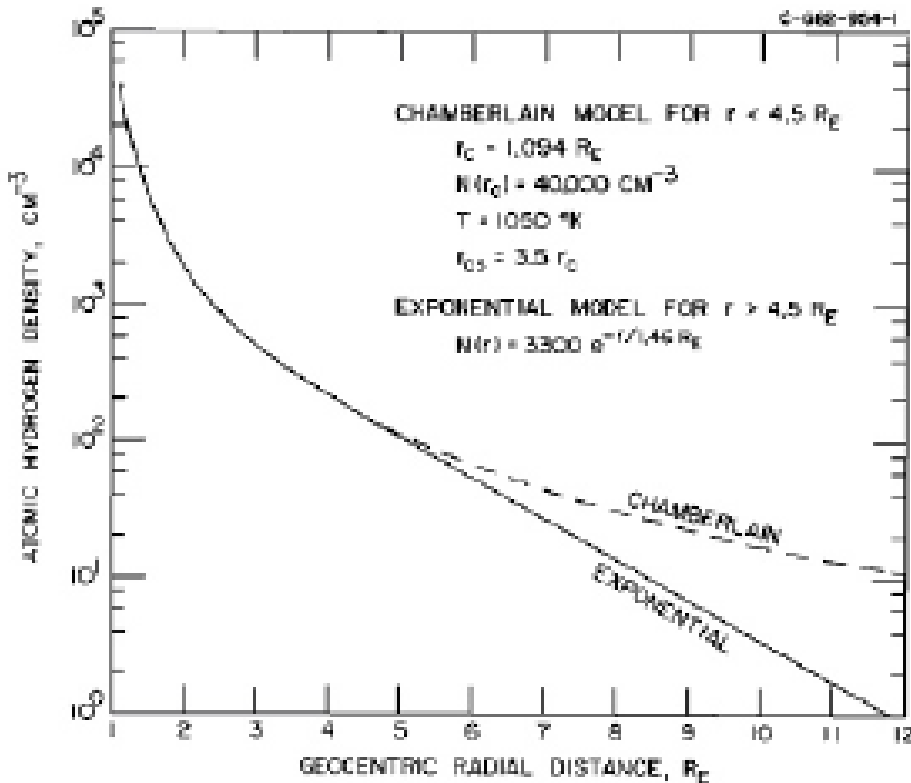
Figure 2.7: Density profile of atomic hydrogen with altitude as measured by the Dynamic Explorer (DE-1) satellite [14].
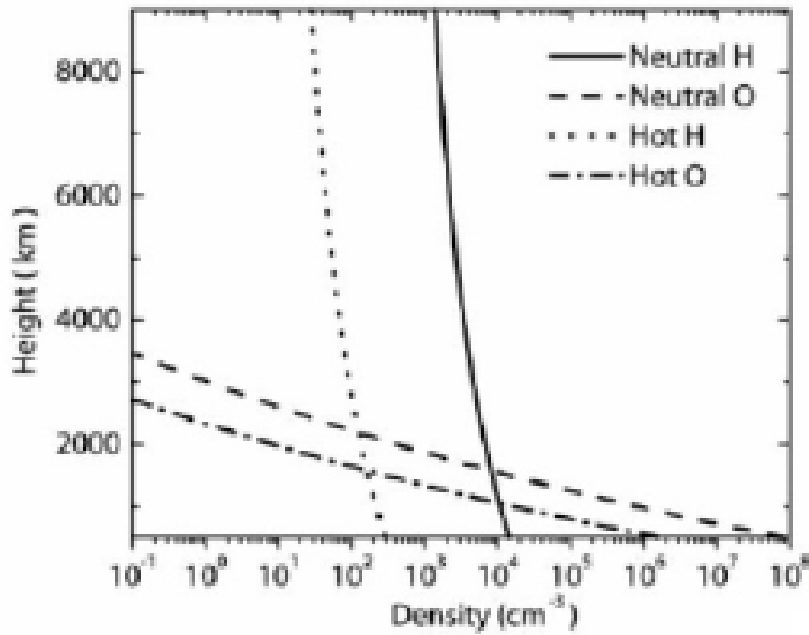
(a) Solar maximum conditions
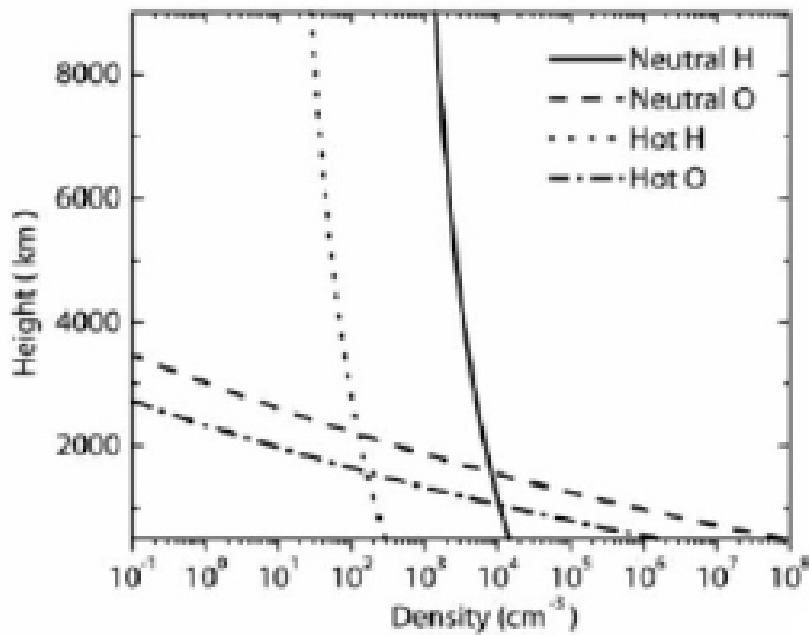
(b) Solar minimum conditions

Figure 2.8: Density profile of neutral hydrogen and oxygen during solar maximum and solar minimum conditions. The data presents the output from the Mass-Spectrometer-Incoherent-Scatter (MSIS) model [16].
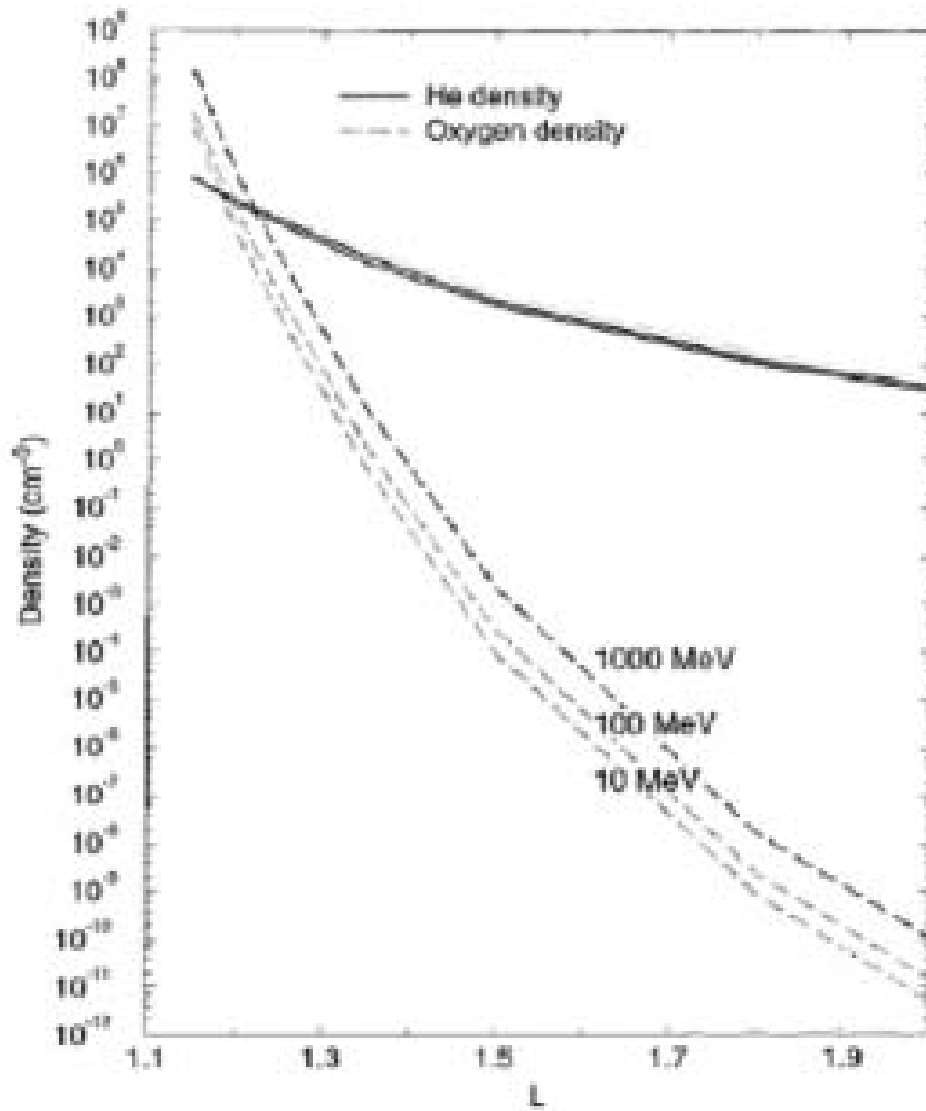
Figure 2.9: Dependence of neutral helium and oxygen densities on L-values as obtained by data from the MSIS model and the IGRF-95 geomagnetic field model [17].
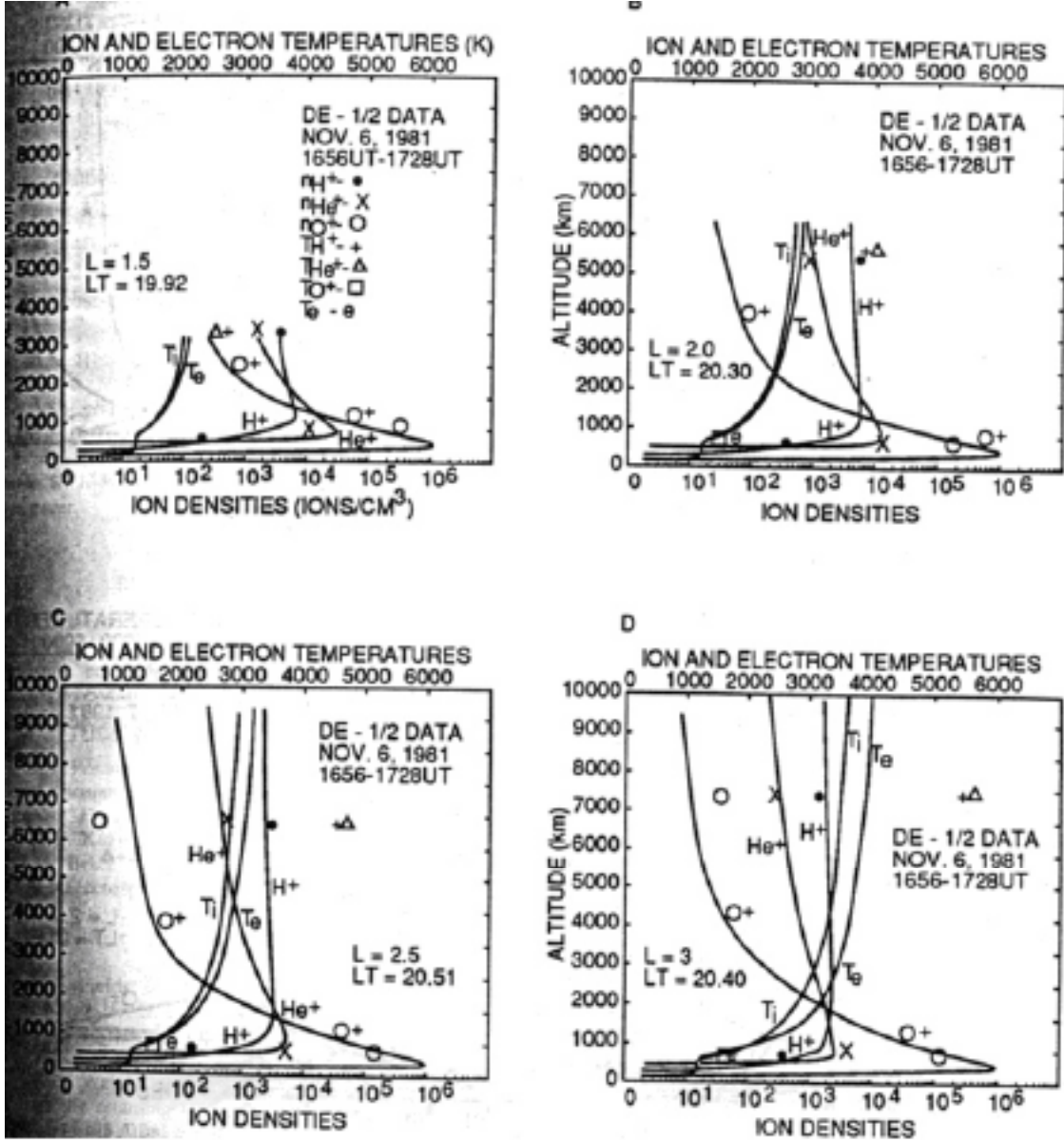
Figure 2.10: Dependence of various ion densities on altitude from the field-line interhemispheric plasma (FLIP) model [17].

2.3 Earth's Magnetic Field

The earth's magnetic field can be approximated to first order by a magnetic dipole centered at the earth's core and tilted 11° from the rotation axis.

$$B = B_E \left(\frac{R_E}{R}\right)^3 \frac{[4 - 3\cos^2\lambda]}{\cos^6\lambda}$$

(2.1)

At $R = R_E + 3000$km and $\lambda = 0$, The strength of earth's magnetic field is approximately, 9.815×10^{-2} Gauss

2.4 Nuclear Detonation in Space [15]

Assumption: A one megaton thermonuclear bomb is detonated an altitude of a few hundred kilometers.

• Immediately after detonation, massive radiation bursts ionized nearby gases. Because of the Earth's magnetic field and the particles in the local plasma, most of this newly formed plasma is trapped and reaches lower energies quickly through atmospheric interactions.
• A nuclear explosion yields approximately 10^{23} neutrons per kiloton. The neutrons ejected away from the earth travel with such a high velocity that most escape the magnetosphere before decaying. However, when neutrons are ejected towards the earth, many are reflected by the atmospheric. Because of interactions with atmospheric particles, a substantial percentage of the neutrons decay in the magnetosphere. Although protons are produced during – decay, the additional flux increase is negligible in comparison to the ambient high energy proton flux of the inner Van Allen region.
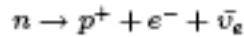• The predominant source of particles arises from the beta decay of fission fragments. The fission fragments undergo – decay in the following reaction:

$$n \rightarrow p^{+} + e^{-} + \bar{v}_{e}$$

This reaction converts a neutron to a proton in the nucleus and ejects high energy electrons and antineutrinos. Combined with the decay of the free neutrons, this reaction combines to create an artificial electron belt.

2.4.1 Decay of Starfish Electrons

After the 1962 "Starfish" space nuclear detonation, high energy electron fluxes bombarded the inner Van Allen region for mainly months. As a result of these high energy electron fluxes, many satellites in the region suffered extensive radiation damage that led to the failure of several US and Russian satellites. The decay of the Starfish electrons is depicted in Figures 2.11, 2.12, and 2.13.
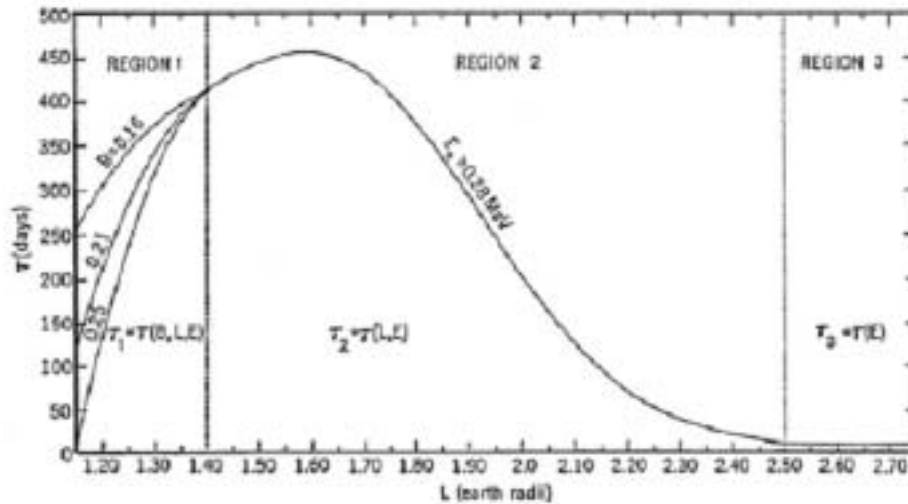

Figure 2.11: Average decay lifetimes of Starfish electrons (E > 0.28MeV)
from the analysis of 1963-38C satellite data [9].

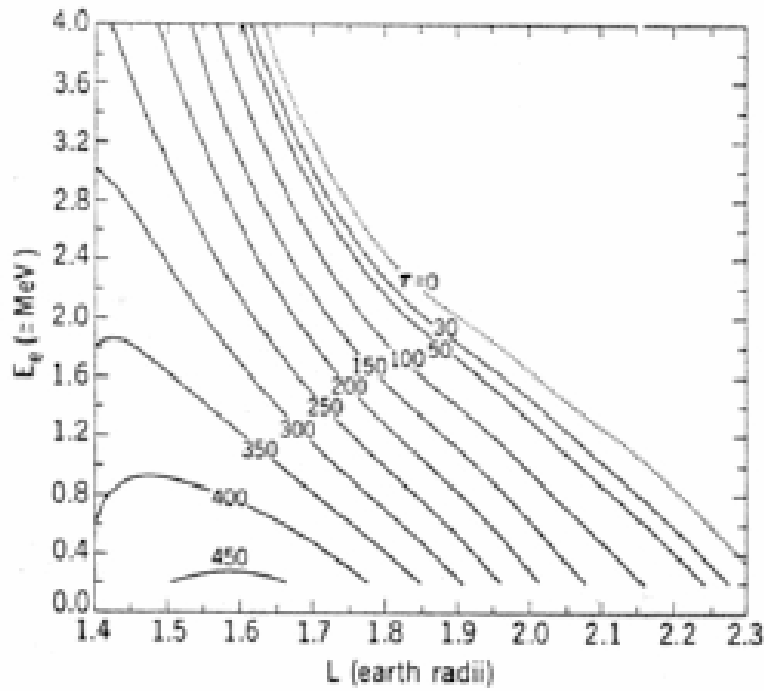*Figure 2.12: Decay lifetimes (days) for Starfish electrons (E > 0.2MeV) as determined by the data from the 1963-38C satellite [9].*
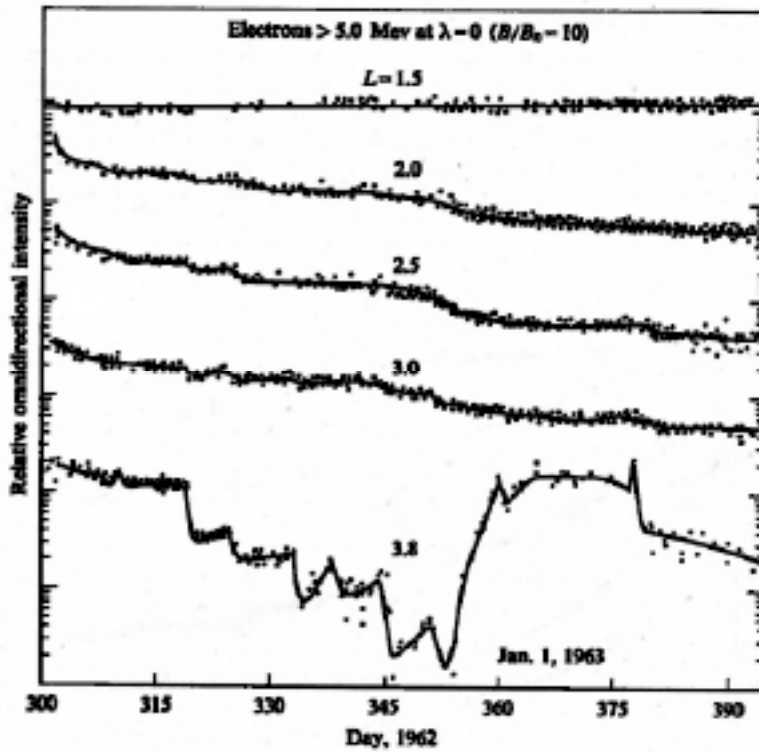
Figure 2.13: Relative flux decrease of Starfish electrons (E > 5MeV) with time [15]

2.5 Sputtering Yield

In the inner Van Allen radiation belt, the tether is subject to high energy fluxes of particles. When high energy ions bombard the surface of the material, the impact energy causes the dislodging of surface particle from the bulk material. As can be seen in Figures 3.1(a) and 3.1(b), the sputtering yield does not increase monotonically with energy. As energy increases, the ions are able to penetrate deeper into the bulk of the material and less of their energy is transferred to atoms on the surface. Smaller ions begin experiencing decay in sputtering yields at a lower level than larger ions due to their smaller atomic cross section.
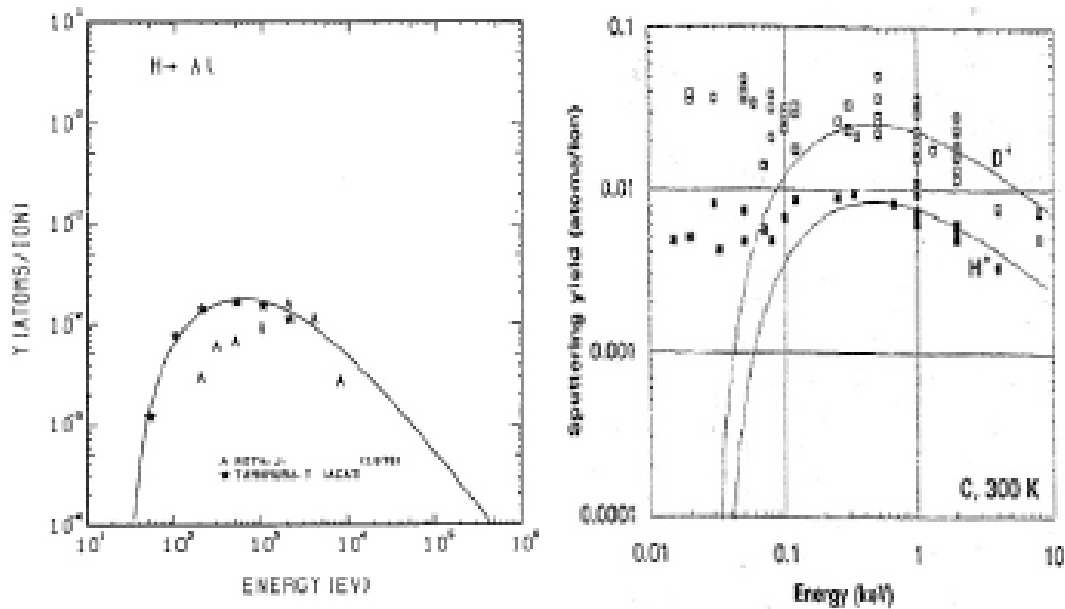
(a) Dependence of sputtering yield on energy for aluminum bombardment with hydrogen ions [13].

(b) Sputtering yield of carbon with deuterium and hydrogen ions. The graph exhibits similar shape and magnitude to the sputtering of copper by hydrogen [19].

Figure 3.1: Sputtering yield for materials of interest in electrodynamic tether implementations.

Materials suggested for use in an electrodynamic tether system include aluminum for its high conductivity to mass ratio and carbon nanotubes for their high strength. Figures 3.1(a) and 3.1(b) present empirical sputtering yields for aluminum and carbon bombardment by hydrogen. For an upper bound calculation of the depth loss rate due to sputtering, the following assumptions are made:

• Energy spectrum consisting of 1KeV protons (the corresponding maximum sputtering yield for aluminum, the weaker of the two materials)
• Proton flux of 10^{10} cm^{-2} s^{-1} (higher than observed fluxes at any energy level)

• For simplicity, the aluminum is represented as an infinite planar surface.

Using the above assumptions the sputtering yield of aluminum by hydrogen ions can be

$$Y(E) \approx 10^{-1} \frac{\text{atoms Al}}{\text{H}^+}$$

calculated.1. At 1KeV, the sputtering yield is (an upper limit chosen from the data in Figure 3.1(a)). This produces a loss rate of 10^9 atoms of Al/H$^+$, or 3.14x10^{16} atoms of Al per cm^2, per year. Knowing the density of aluminum to be 2.70 g/cm^3, the aluminum structure contains 6.026x10^{22} atoms of Al per cm^3. The depth loss rate with time in years can be expressed as dL/dt=5.21x10^{-5} mm/yr. Thus, it would take 1.92x105 years to sputter a depth loss of 1mm.

Despite choosing upper bound parameters to increase the sputtering yield, the sputtering of aluminum by hydrogen did not have a substantial impact. The ineffectiveness of this sputtering clearly demonstrates that sputtering will have a negligible impact on a space tether implementation.

Bibliography

[1] A.S. Jursa, Handbook of Geophysics and the Space Environment, US Air Force Geophysics Laboratory, 1985, p. 5-1.

[2] M.B. Alexander and R.D Leach, Failures and Anomalies Attributed to Spacecraft Charging, tech. report RP-1375, Marshall Space Flight Center, 1995.

[3] A.L. Vampola, "The Hazardous Space Particle Environment," IEEE Transactions on Plasma Science, vol. 28, no. 6, Dec. 2000.

[4] P.A. Webb, Electron Density Measurements of the Plasmasphere — experimental observations and modeling studies, tech. report, Cooperative Research Centre for Satellite Systems, La Trobe Univ., 2000.

[5] J.D. Huba, 2004 Revised NRL Plasma Formulary, The Office of Naval Research, 2004.

[6] W.L. Brown, W.N. Hess, J.A. Van Allen, "Introduction to Collected Papers on the Artificial Radiation Belt from the July 8, 1962, Nuclear Detonation," Journal of Geophysical Research, vol. 68, no. 3, February 1963, pp. 605-606.

[7] H. Hoerlin, United States High-Altitude Test Experiences: A Review Emphasizing the Impact on the Environment, tech. report LA-6405, Los Alamos Scientific Laboratory, 1976.

[8] Eric Choiniere, Theory and Experimental Evaluation of a Consistent Stead-State Kinetic Model for 2-D Conductive Structures in Ionospheric Plasmas with Application to Bare Electrodynamic Tethers in Space, doctoral thesis, Dept. of Electrical Engineering, University of Michigan, 2004.

[9] E.G. Stassinopoulos and P. Verzariu, "General Formula for Decay Lifetimes of Starfish Electrons," Journal of Geophysical Research, vol. 76, no. 7, March 1971.

[10] M.H. Denton, G.J. Bailey, Y.Z. Su, K.I. Oyama, T. Abe, "High altitude observations of electron temperature and a possible north-south asymmetry," Journal of Atmospheric and Solar-Terrestrial Physics, vol. 61, 1999, pp. 775-788.

[11] F. F. Chen, Introduction to Plasma Physics and Controlled Fusion, Plenum Press, 1984, p. 181.

[12] C.K. Purvis, Overview from a Systems Perspective in The Behaviour of Systems in

the Space Environment, Proc. NATO Advanced Study Institute 245, Kluwer Academic Publishers, R. N. DeWitt et al. (eds.), pp. 23-44, 1993.

[13] Y. Yamamura and H. Tawara, "Energy Dependence of Ion-Induced Sputtering Yields from Monatomic Solids at Normal Incidence," Atomic and Nuclear Data Tables, National Institute of Fusion Science, Chigusaku, 1996, pp. 149-253.

[14] M. Gruntman, "Energetic Neutral Imaging of Space Plasmas," Review of Scientific Instruments, vol. 68, October 1997, pp. 3617-3656.

[15] W. H. Hess, The Radiation Belt and Magnetosphere, Blaisdell Publishing Company, 1986, pp. 69-106, 155-205.

[16] L.C. Gardner and R.W. Schunk, "Neutral Polar Wind," Journal of Geophysical Research, vol. 109, 2004.

[17] G.I. Pugacheva, W.N. Spjeldvik, A.A. Gusev, I.M. Martin, and N.M. Sobolevsky, "Hydrogen and helium isotope inner radiation belts in the Earth's magnetosphere," Annales Geophysicae, vol. 16, 1998, pp. 931-939.

[18] I.L. Horwitz et. al., "Plasamsphere-Ionosphere Coupling 2. Ion Composition Measurements at Plasmaspheric and Ionospheric Altitudes and Comparison with Modeling Results," Journal of Geophysical Research, vol. 95, no. A6, June 1990, pp. 7949-7959.

[19] J. Roth and C. Garcia-Rosales, "Analytic Description of the Chemical Erosion of Graphite by Hydrogen Ions," Nuclear Fusion, vol. 36, no. 12, 1996.

[20] J.M Deux, Kinetic Modeling of Electrodynamic Space Tethers, master's thesis, Dept. Aeronautics and Astronautics, Massachusetts Institute of Technology, 2004.

[21] J.E. Allen, "Probe Theory - The Orbital Motion Limited Approach," Physica Scripta, vol. 45, 1992, pp. 497-503.

[22] G. V. Khazanov, N. H. Stone, E. N. Krivorutsky, K. V. Gamayunov, and M.H. Liemohn, "Current-induced magnetic field effects on bare tether current collection: A parametric study," Journal of Geophysical Research, vol. 106, no. A6, June 2001, pp. 10565-10579.

[23] J.R. Sanmartn and R.D. Estes, "Magnetic self-field effects on current collection by an ionospheric bare tether," Journal of Geophysical Research, vol. 107, no. A11, 2002.

[24] "Nuclear Reactors in Space," Briefing Paper #82, Uranium Information Center, Melbourne, 2004; http://www.uic.com.au/nip82.htm.

APPENDIX 2: ANALYSIS OF RBR THROUGH ELECTROSTATIC TETHER SCATTERING

**Applications of an Electrostatic High-Voltage Tether
to Radiation Belt Remediation**

by

Christopher F. Zeineh

Submitted to the Department of Aeronautics and Astronautics
on August 19, 2005 in Partial Fulfillment of the Requirements
for the Degree of Master of Science in Aeronautics and Astronautics

Abstract

A computational algorithm is developed and executed to calculate the rate of depletion of magnetospheric ions by an electrostatic tether at various altitudes. This computation relies upon past studies in the OML regime of charged tethers to determine the deflection angles incurred upon incoming ions at any given incident velocity. Calculated depletion rates are used to computationally estimate the time required to deplete a given range of the magnetosphere.

Chapter 1

Background

The Earth's magnetosphere is defined as the region within which phenomena are dominated by the Earth's magnetic field and extends to roughly 10 earth radii at the equator. Collisions among incoming cosmic neutrons produce mass amounts of charged particles which in turn have the tendency to travel along magnetic field lines, and populate the magnetosphere. Many such particles follow the field lines into one of the Earth's poles and thus exit the magnetosphere, but many are repelled by the increasing magnetic field and thus become trapped within the magnetosphere for long periods of time. Satellites passing through or orbiting within the magnetosphere require expensive shielding against high-velocity trapped ions, particularly those whose energies exist near or above the order of 1 MeV, and we can minimize the amount of damage incurred if we artificially reduce the magnetospheric populations with electrostatic tether satellites. Furthermore, in the event of a nuclear warhead detonating at high-altitude, the saturation of the magnetosphere may be further exacerbated, in which case a tether satellite can assist in expediting the natural remediation process.

1.1   Magnetic Mirrors

A magnetic mirror is defined as a magnetic field configuration in which the field strength changes along the field lines in such a way that charged particles tend to reverse direction once in the high-field region. Such a configuration usually consists of parallel magnetic field lines constricting and intensifying along a given axis. The Earth's magnetic field produces a similar phenomenon near either magnetic pole, near which the Earth's magnetic field lines constrict.

If a charged particle is traveling along a magnetic field line within a uniform magnetic field and no electric field, then the field exerts no forces upon the particle beyond those contributing to Larmor gyrations. Thus, particles in uniform magnetic fields free of electric fields travel with constant velocity perpendicular to the field line and with constant radial speed. However, if the magnetic field lines begin to converge, a new force is introduced parallel to the field line.
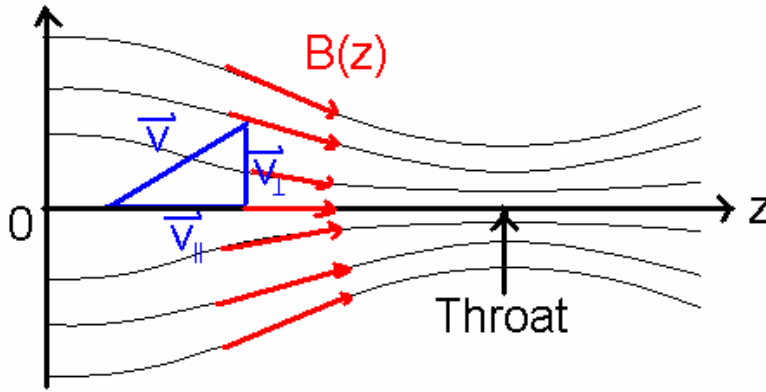
Figure 1-1: Particle approaching a magnetic throat.

Define a particle of charge q and velocity **v** traveling along a magnetic field line **B**. At a given point along the line, an adjacent field line of similar magnitude converges towards it and lies at distance r_L. The force on the particle in the direction parallel to its initial velocity is expressed:

$$< F_\parallel > = -|q\mathbf{v} \times \mathbf{B}| \sin \alpha = -|q|v_\perp B \sin \alpha \qquad (1.1)$$

$$\sin \alpha = \frac{-B_r}{B}$$

To simplify:

$$< F_\parallel > = |q|v_\perp B_r \qquad (1.2)$$

Calculate the gradient of B to obtain B_r as a function of B_z:

$$\nabla \cdot \mathbf{B} = \frac{1}{r}\frac{\partial}{\partial r}(rB_r) + \frac{\partial}{\partial z}B_z = 0 \qquad (1.3)$$

Integrate to obtain:

$$rB_r = -\int r \frac{\partial B_z}{\partial z} dr \qquad (1.4)$$

Suppose the radius of the curvature of the lines is small enough that $\dfrac{\partial B_z}{\partial z}$ is constant:

$$\left[rB_r \right]_0^{r_L} \cong -\int_0^{r_L} r\,dr \frac{\partial B_z}{\partial z} = -\frac{1}{2} r^2 \frac{\partial B_z}{\partial z}$$

$$B_r(r_L) \cong -\frac{1}{2} r_L \frac{\partial B_z}{\partial z}$$

$$(1.4)$$

Substituting this expression back into the parallel force yields:

$$< F_\| > = -\left|q\right| \frac{v_\perp r_L}{2} \frac{\partial B_z}{\partial z} = -\frac{\frac{1}{2} m v_\perp^{\,2}}{B} \frac{\partial B_z}{\partial z}$$

$$(1.5)$$

We define μ as the magnetic moment such that

$$\mu = \frac{\frac{1}{2} m v_\perp^{\,2}}{B} \qquad (1.6)$$

$$< F_\| > = -\mu \frac{\partial B_z}{\partial z} = \mu \cdot \nabla_\| \mathbf{B}$$

$$(1.7)$$

As a particle enters a region where the magnetic field lines converge, it experiences a net parallel retarding force. Depending on the particle's velocity and the magnetic field, the particle may be reflected back entirely. Suppose that such a particle does get reflected. Define a series of magnetic field lines constricted on two sides. Now define a particle at the center, where the field lines are parallel, as having velocity $\mathbf{v}_0 = \langle v_{\perp 0}, v_{\|0} \rangle$. At the point of deflection, the velocity in the direction parallel to the magnetic field is zero, so $\mathbf{v}_r = \langle v_{\perp r}, 0 \rangle$. First we employ energy conservation:

$$\frac{1}{2} m \left(v_{\|r}^{\,2} + v_{\|0}^{\,2} \right) = \frac{1}{2} m v_{\perp r}^{\,2} \qquad (1.8)$$

Then μ conservation:

$$\frac{1}{2}\frac{mv_{\perp 0}{}^2}{B_0} = \frac{1}{2}\frac{mv_{\perp r}{}^2}{B_r} \qquad (1.9)$$

Thus:

$$\frac{B_r}{B_0} = 1 + \left(\frac{v_{0,\parallel}}{v_{0,\perp}}\right)^2 = \frac{1}{\sin^2(\theta_0)}$$

$$\theta_0 \leq \sin^{-1}\sqrt{\frac{B_r}{B_0}}$$

$$(1.10)$$

Thus, if the particle's velocity vector lies at too great an angle from the magnetic field line along which it travels, the particle will reverse direction and be reflected backwards.

1.1.1 Magnetic Mirrors and the Van Allen Belts

Just as the magnetic field lines in our mirror example expand and contract, so do the Earth's magnetic field lines, which converge towards the magnetic poles and expand near the equator. A particle traveling along one of these lines may have its velocity oriented insufficiently along the line to overcome the mirror forces incurred upon approaching a pole. Approximating symmetry of the earth's magnetic field lines across the equator, a particle deflected close to one pole will maintain its parallel speed and thus be similarly deflected upon approaching the opposite pole. Thus, a charged particle with insufficient speed to overcome the earth's mirror effect along a given magnetic field line will be trapped along that field line.

The magnetic field lines along which this phenomenon is particularly prevalent are called the Van Allen Belts, or radiation belts. The high-energy charged particles which heavily populate the radiation belts prove hazardous to satellites attempting to pass through these ranges of space, and sufficiently protecting these satellites against the radiation is terribly costly, so depleting the radiation belts by a given magnitude will cut costs on satellite protection in future launches.

Another concern pertaining to the radiation belts lies in the possibility of nuclear intercontinental ballistic missiles, launched either in error or intentionally, being intercepted and detonated in mid-flight. Nuclear clean-up efforts close to the surface of the Earth take many years already, but the radioactive debris emitted to the ionosphere and magnetosphere by a high-altitude nuclear detonation is trapped in the radiation belts

by the mirror effect. In such an event, man-made satellites could help expedite the radiation belt remediation, thus reducing any possible ecological ramifications.

1.1.2 The Loss Cone

For a particle with a given velocity vector traveling along a given magnetic field line, we define the range of velocities for which the particle can escape as the "loss cone." The angle of this cone is defined by the limits in (1.10) We illustrate this cone in velocity space. For future reference, we establish axes for a particle in the ionosphere.

x: east (x>0)
y: north (y>0)
z: away from the earth, "up" (z>0)

Since this loss cone applies to all particles traveling along this magnetic field line, we can assume that all such particles whose velocities fall into the loss cone have already exited the radiation belts. Our objective is to deflect the remaining particles such that their post-deflection velocities do fall into the loss cone, and to that end we employ a dual-tether satellite.

1.1.3 Solution via Electrostatic Tethers

If we attach an electromagnetic bare tether to a satellite in the magnetosphere, we can induce a potential difference between the tether and the ambient plasma. This would induce an electrodynamic force upon the plasma, including the trapped radiation, and either collect the charged particles or deflect them at various angles. Theoretically, we can use such a tether to deflect trapped radiation belt particles such that their post-deflection velocities would fall into the loss cone. Much research has been conducted on the behavior of tether satellites with regards to collecting charge, and much of this research can be used to analyze its deflecting properties as well.

1.2 Previous Research

Much prior research has been conducted on the behavior of electrodynamic tethers in plasma, including computational, theoretical, and experimental. Since this thesis is focused upon theoretical trajectories of charged particles in the vicinity of the tether, I will review some of the most pertinent theoretical publications and their most useful equations. Computational and experimental research projects are also utilized to establish the proper parameters for our calculations and will be sourced as they warrant.

1.2.1 Langmuir and Mott-Smith - 1926

Langmuir and Mott-Smith pioneered the study of current collection by spherical and cylindrical probes, from which they derived the collection limits for thin and thick cylinders, named the Orbital Motion Limit and Langmuir Limit, respectively. Electrons sense the presence of the tether only within an imaginary cylindrical barrier called a

sheath (beyond which the potential difference is negligible) and their trajectories are deflected toward the tether as they approach. In the OML limit, whether or not it is captured depends upon its angular momentum. In the Langmuir Limit, the sheath can be regarded as totally flat, so that attracted particles that enter the sheath are all collected. Per unit of collecting body area, the OML limit gives the highest current possible.

We use this expression to determine the tether architecture.

1.2.2 Sanmartìn and Estes - 1999

Taking the Maxwellian distribution for the particle distribution function, Sanmartin and Estes calculated not only the limit of the probe radius for the current collection to be within the OML regime, but also an approximation of the collected current once the tether is within the OML regime. The latter is used to approximate the current collected by the tether in the magnetosphere, which we use to determine the tether architecture.

$$I_{OML} \approx 2RLen_{\infty} \sqrt{\frac{2e\Phi_{Tether}}{m_e}} \tag{1.9}$$

1.2.3 B.M. Minor, Tethers Unlimited, Inc. - 2003

Minor calculated the scattering rates of electrons by an electrostatic tether composed of several tethers bound together in a cylindrical alignment, parallel to one another. Employing analytical calculations for the two-dimensional cross-section of the tether cluster, Minor calculates the potential of the tether and the electron flux rates for various energy levels. The electron results lie outside the scope of this thesis, which will focus solely on ion fluxes, yet the analytical methods employed, specifically those pertaining to the 2-dimensional quantifying of tether potential and particle trajectory, bear direct application to theoretical electrodynamic research.

1.3 Thesis Outline

First and foremost, we will have to determine what sort of tether we wish to employ. Many sorts of tether designs have been theorized, including single and dual tethers, yet each of them exhibits its own strengths and weaknesses when faced with the task of deflecting particles in the magnetosphere. We need to determine the best design, or perhaps develop one of our own.

Once we settle on our tether's architecture, we will need to determine the theoretical scattering properties of the tether with respect to incoming particles. Approximation methods for extreme cases will also be useful.

After determining the theoretical deflection properties, we can calculate the rate at which the tether will scatter particles into the loss cone when immersed in plasma with a given distribution of particle velocities and energies. This rate will determine the amount of time required for a tether satellite to depopulate a given region of the Van Allen Belts by a given factor.

Chapter 2

Tether Design

2.1   Tether Orientation

For a base case, we assume an equatorial, circular orbit. In order to maximize the tether's effectiveness, we want to orient the tether such that the maximum fraction of the particles which interact with the tether can be redirected such that their velocities fall into the loss cone. We are utilizing a tether that is much longer than its sheath is wide, so in analyzing its electromagnetic effects on a charged particle, we can assume that the tether is infinitely long. Thus, a charged particle approaching the tether will not undergo any change in velocity in the direction parallel to the tether.

Next we must determine the ideal orientation of the tether with respect to the Earth. If we orient the tether directly parallel to the magnetic field at the equator (i.e. in the y-direction), the only change in velocity will occur in the v_x-v_z plane of velocity space. Since the tether is so much more massive than any incoming particle, we assume their interaction to ultimately result in only a change in the x-z component of the particle's momentum, not a change in its magnitude. Thus, for a particle interacting with a tether oriented in the y-direction, the particle's velocity vector can only be rotated about the y-axis and not altered in any other way. The loss cone is radially symmetric about the y-axis, so if a particle's velocity vector lies outside the loss cone before interacting with the y-oriented tether, the velocity vector cannot be redirected into the loss cone. Thus, a y-oriented tether cannot scatter trapped particles into the loss cone and is inadequate for our design. The tether must ideally lie anywhere within the xz-plane, or equatorial plane, for maximum scattering effect.

Within the equatorial plane, the tether's orientation angle has no effect on its ability to scatter particles since we are assuming the loss cone and particle density to be radially symmetric. However, if the tether is parallel to neither the z-axis nor the x-axis, the earth's gravitational field will exert a greater force on the end closer to the earth, resulting in a torque on the tether. Orienting the satellite parallel to the z-axis, as proposed by TUI, thus results in an unstable equilibrium. On the other hand, if the tether experiences no other forces of similar or greater magnitude, stable equilibrium is maintained by aligning the tether parallel to the z-axis so that it points towards the earth, as in Figure 2-1.
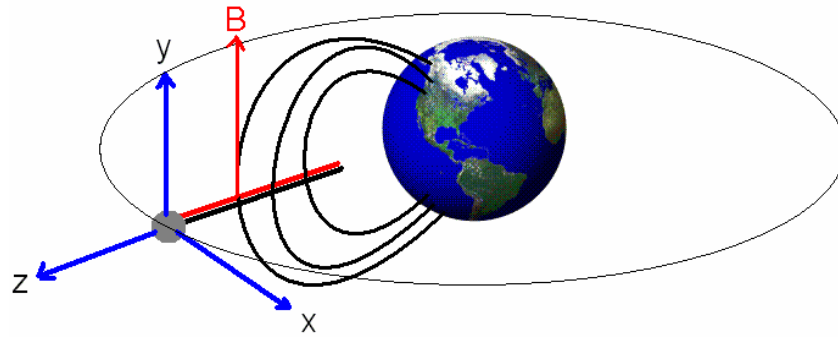
Figure 2-1: Tether Orbital Alignment

2.2 Tether Architecture

2.2.1 Single-Tether Designs

The simplest tether design is a single bare tether attached to a power supply such that the surface of the tether is potentially biased with respect to its surrounding plasma. Since charge cannot accumulate on the tether, a second "electrode" is needed to collect the opposite polarity particles, so a "single tether" design is unphysical.

If the tether is biased positive, the excess charge can be eliminated by affixing a cathode (which must itself be biased negatively) to disperse it out of the end of the tether. Unfortunately, this produces a net current within the tether, and since we have already established that our tether must lie perpendicular to the Earth's magnetic field, the tether succumbs to a Lorentz force constantly accelerating or decelerating the satellite, depending on orientation.
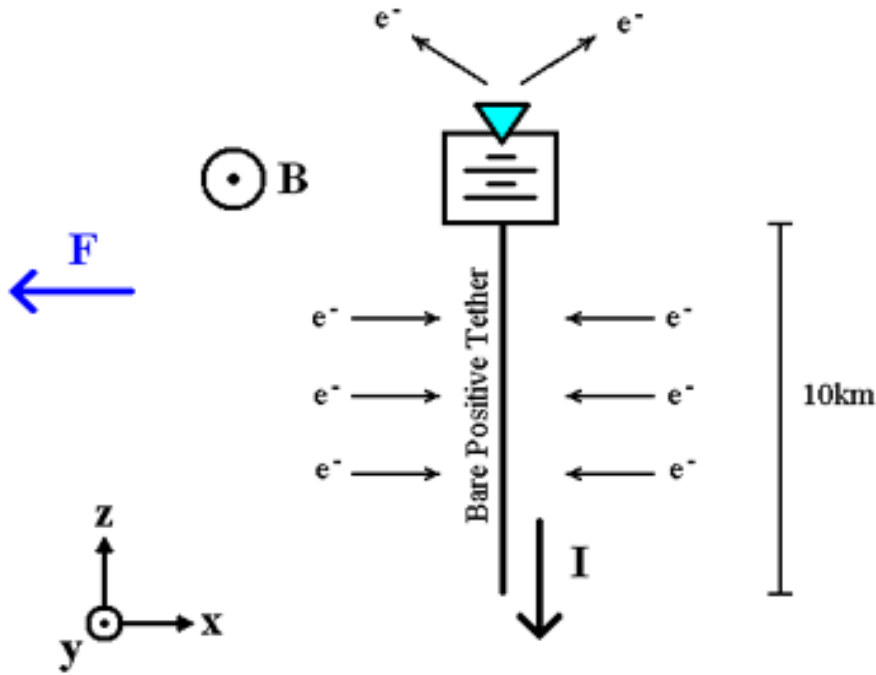
Figure 2-2: Single Bare Positive Tether with Cathode

On the other hand, affixing a cathode either in the center of the tether or onto each end would split the current into two equal and opposite directions. Rather than induce linear acceleration, the Lorentz force would now induce a net torque, which could be countered by the gravitational gradient between the lower and higher cathodes when some equilibrium angle to the vertical is reached.

While such a system would be dynamically stable up to some current, attracting electrons with such a high-voltage tether produces a very high current which must be rejected by the cathodes. Sanmartín and Estes give the current collected by an electromagnetic tether as by the following equations [1], where j is an index for each of the N different types of ions present in the radiation belts.

$$\text{Positive Tether}: \quad I_e = 2r_T e n_\infty L \sqrt{\frac{2e\Phi_T{}^+}{m_e}}$$

(2.1)

$$\text{Negative Tether}: \quad I_i = \sum_{j=1}^{N} 2r_T e n_\infty L \sqrt{\frac{-2e\Phi_T{}^-}{m_j}}$$

(2.2)
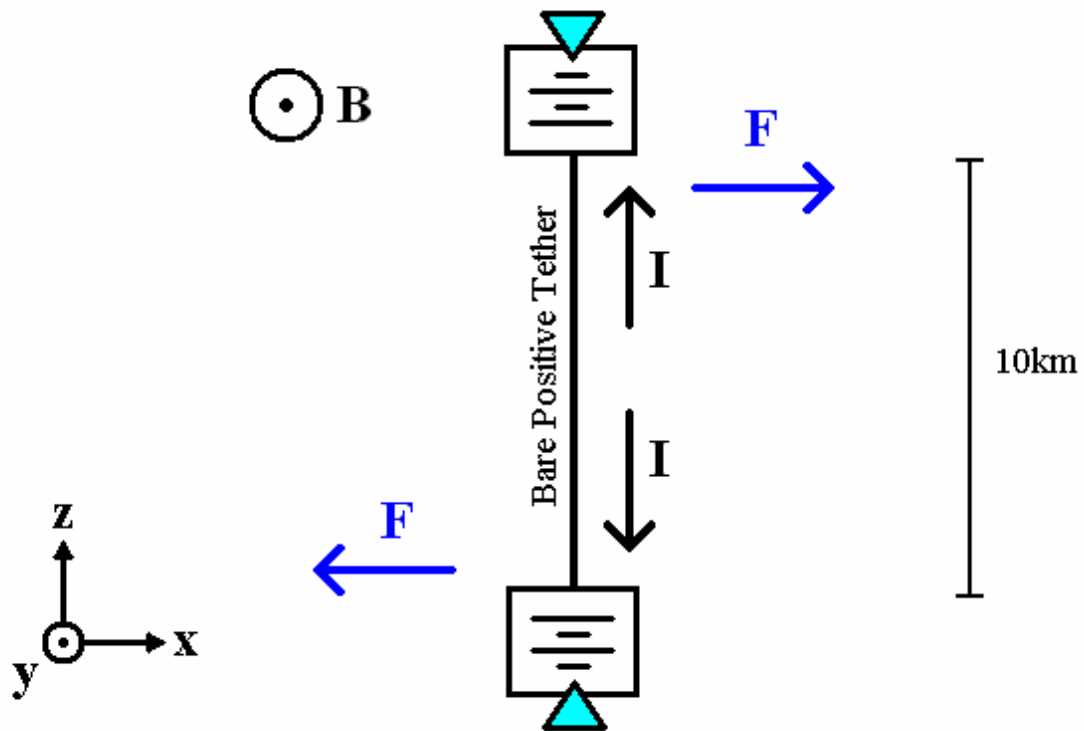
Figure 2-3: Single Bare Positive Tether, Two Cathodes and Power Supplies
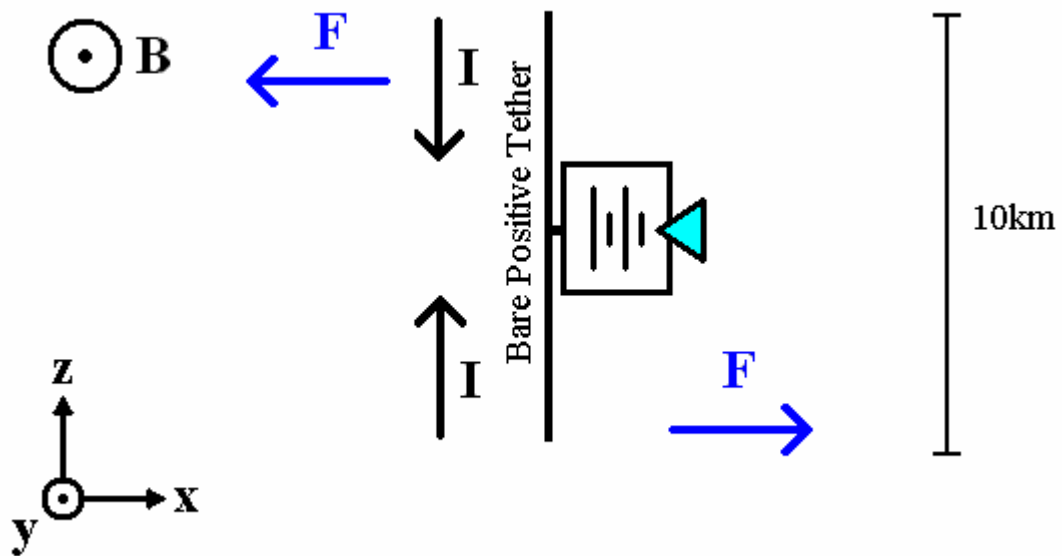
Figure 2-4: Single Bare Positive Tether, Central Cathode and Power Supply

Due to the high voltage of the tether and the low mass of the electrons, the current from a positive tether becomes strikingly high. A preferable design might utilize a negative tether, whose resulting current would be reduced by two orders of magnitude, thanks to the heavier ions.

2.2.2 Dual-Tether Designs

If a simple tether is biased negative, positive ions would be continuously attracted to the tether and would remain affixed to the surface of the tether until enough electrons are attracted to neutralize it. One remedy for this is to add a power supply to bias one portion of the tether positively and sufficiently so that it can attract enough electrons to neutralize all of the incoming ions. This effectively converts our single tether into an anti-parallel dual-tether. However, the electrons collected by the tether would enter from the positive side, and the collected ions would accumulate on the negative side. Thus, the collected electrons would travel in a single direction to neutralize the collected ions, again inducing a Lorentz force and producing in the satellite unwanted acceleration.

Figure 2-5: Anti-Parallel Dual Tether

V.V. Danilov has proposed constructing a 10-km parallel dual-tether consisting of two oppositely-charged tethers traveling parallel to each other and perpendicular to the Earth's magnetic field. His model connects the two tethers at one end by a power supply, architecturally similar to the anti-parallel tether, only bent in half.
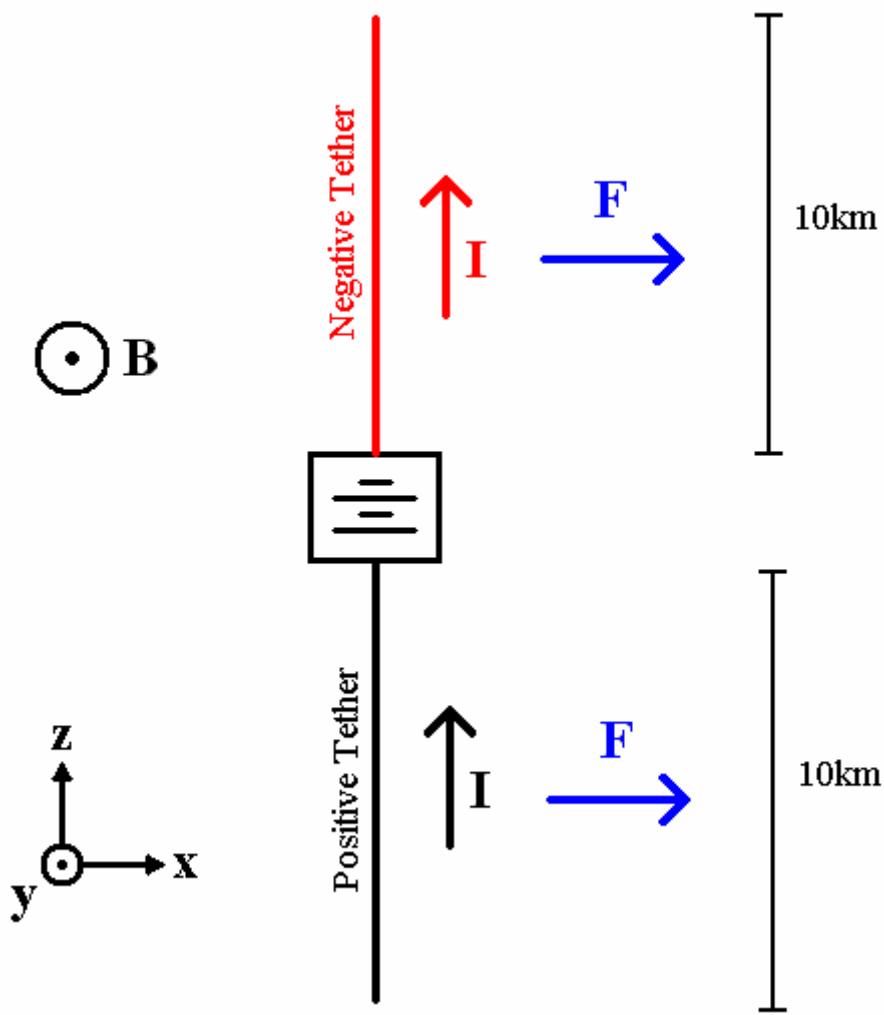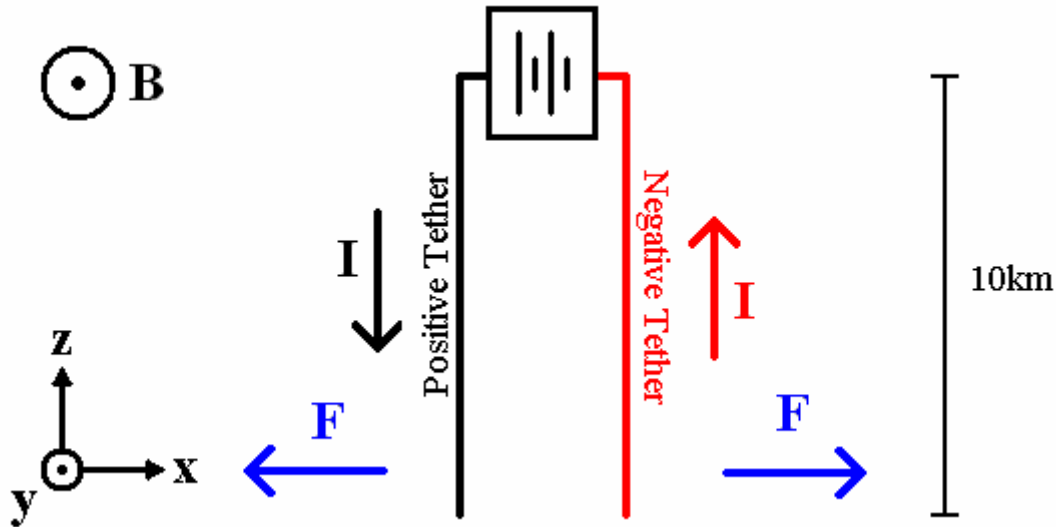

Figure 2-6: Parallel Dual Tether

As electrons reach the positive tether and travel to the negative tether to neutralize its attracted ions, they create a current in each satellite of equal magnitude and opposite direction, producing a Lorentz force in each. These forces cause the tethers to rotate about the power supply. However, while this adjustment eliminates the linear Lorentz acceleration, it requires additional architecture to maintain functionality. For a tether potential of 1 MeV, the sheath radius measures on the order of 10^2 m, so if the two tethers are hooked onto the same satellite and run parallel to each other, their sheaths would intersect, complicating the scattering model and reducing efficiency. Keeping the two tethers outside of each other's sheaths requires the addition of at least one insulated beam no shorter than the sum of the two sheath radii, again on the order of 10^2 m. Even when the tether sheaths no longer directly interfere with one another, their proximity dictates that each tether would "block" a certain angular range of incoming particles from the other. This not only restricts the angular range from which each tether can attract new particles from the plasma, but it also proves inefficient as one tether scatters particles that had already been scattered by the other.

Furthermore, as electrons reach the positive tether and travel to the negative tether to neutralize its attracted ions, they create a current in each satellite of equal magnitude and opposite direction, producing a Lorentz force in each. These forces pull the tether further and further in opposite directions until the entire tether satellite straightens itself out and the Lorentz force becomes linear one again. This can be corrected by once again adding an insulated beam connecting the tethers, this time at the end opposite that of the power

supply, yet we continue to search for a design that is self-correcting and avoids such inefficiencies.

2.2.3 Series Tether Design

We thus propose a tether design which we shall call the "series tether." It consists of a series of three tethers connected by two separate power supplies running current in opposite directions. The central 10-km tether will be positively biased while the two 5-km tethers on either end will be negatively biased, the idea being that each half of the positive tether will attract a sufficient number of electrons to neutralize the ions attracted by the negative tether on its own side. Each half of the tether thus produces an equal amount of current, but in opposite directions. The induced Lorentz forces can be approximated as originating on the center of each half of the total tether, and pointing in opposite directions, resulting in a net torque. However, since two power supplies reside 10 km apart from each other, they induce a substantial gravitational gradient torque in the direction opposite that of the Lorentz torque. The satellite thus reaches a point of stable angular equilibrium at which the two torques negate each other.
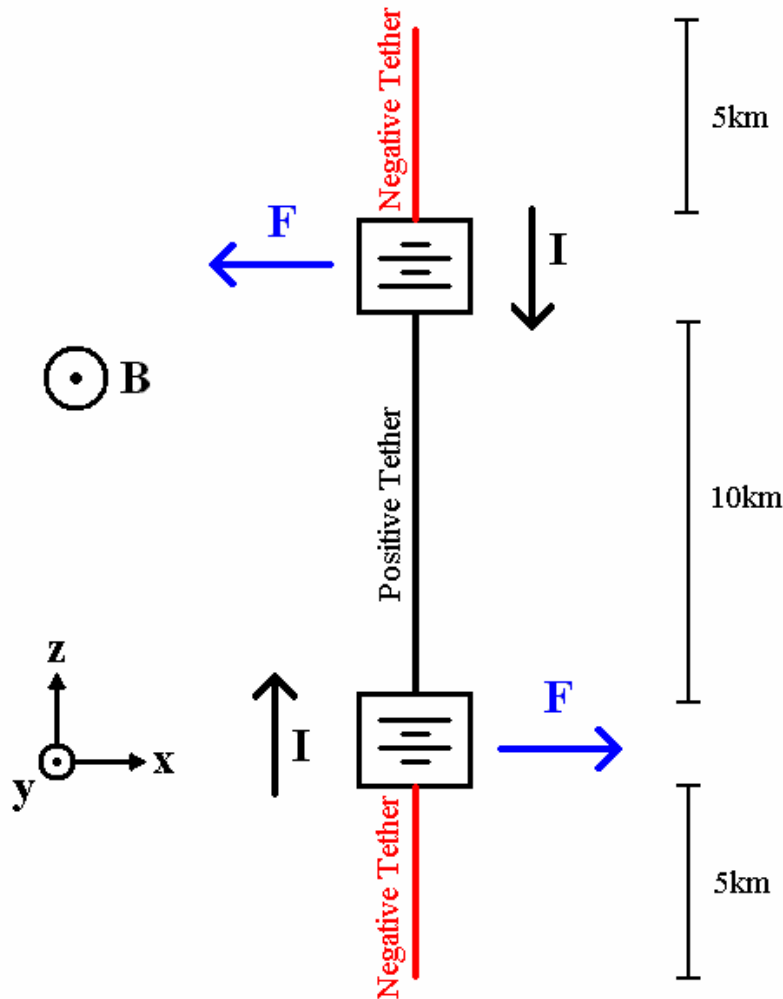

Figure 2-7: Series Tether

2.2.4 Tether Angle

For a tether satellite orbiting the earth, we define the neutral position as when the tether points directly towards and away from the earth. We define θ and ϕ to be the tether's pitch and roll, respectively, such that $X = R\cos\theta$ and $Z = R\sin\theta$, where R is the radius from the satellite's center of mass. Taking R_{orbit} to be the radius of the satellite's orbit measured from the center of the Earth, the total gravitational gradient torque vector is given by:

$$Q_{GG} = 3\Omega^2 \begin{Bmatrix} \left(\int\left(Y^2 - Z^2\right)dm\right)\cos^2\theta\sin\phi\cos\phi \\ \left(\int\left(X^2 - Z^2\right)dm\right)\sin\theta\cos\theta\cos\phi \\ \left(\int\left(Y^2 - X^2\right)dm\right)\sin\theta\cos\theta\sin\phi \end{Bmatrix} \tag{2.3}$$

$$\Omega = \sqrt{\frac{\mu}{R_{orbit}^3}}, \quad \mu = GM_{Earth} = 3.98 \times 10^{14}$$

Since our satellite will retain orbit within the equatorial plane, gravity will induce a torque about only the y-axis, so the only non-zero term in the gravitational gradient torque is the y-component. Furthermore, our tether has no reason to roll, making $\phi=0$, and thus $\cos\phi=1$. The y-component of the torque is thus expressed:

$$\left(Q_{GG}\right)_y = 3\Omega^2 \left(\int\left(X^2 - Z^2\right)dm\right)\sin\theta\cos\theta \tag{2.4}$$

Ignoring the weight of the tether itself for now, we consider only the torque resulting from the power supplies. The integral in the torque expression thus comes to represent what we will approximate as point masses:

$$\int\left(X^2 - Z^2\right)dm = m_1\left(X_1^2 - Z_1^2\right) + m_2\left(X_2^2 - Z_2^2\right) \tag{2.5}$$

The positions of the two power supplies are represented by:

$$\begin{aligned} X_1 &= R\sin\theta & X_2 &= -R\sin\theta \\ Z_1 &= R\cos\theta & Z_2 &= -R\cos\theta \end{aligned} \tag{2.6}$$

Substituting these into the mass integral expansion and assuming the masses of the two power supplies to be equal yields:

$$\int \left(X^2 - Z^2\right)dm = m\left((R\sin\theta)^2 - (R\cos\theta)^2\right) + m\left((R\sin\theta)^2 - (R\cos\theta)^2\right)$$

$$= 2mR^2\left(\sin^2\theta - \cos^2\theta\right) = -2mR^2\cos 2\theta \tag{2.7}$$

Substitute this back into our torque equation (2.4) to get:

$$\left(Q_{GG}\right)_y = 3\Omega^2\left(-2mR^2\cos 2\theta\right)\sin\theta\cos\theta \tag{2.8}$$

$$= -6m\Omega^2 R^2\cos 2\theta\sin 2\theta$$

Assuming the tether pitch to be sufficiently small ($\theta\ll 1$), we can approximate $\cos 2\theta\approx 1$ and $\sin 2\theta\approx 2\theta$. Furthermore, the radius R from the center of the tether to either power supply is simply one quarter the length of the total tether, thus making our torque:

$$\left(Q_{GG}\right)_y = -12m\Omega^2\left(\frac{\ell}{4}\right)^2\theta = -\frac{3}{4}m\Omega^2\ell^2\theta \tag{2.9}$$

Now we pair this against the torque resulting form the Lorentz torque. We first focus on either half of the tether satellite, such that all of the current within our focus travels in a single direction. If we overestimate the half-tether's current to be roughly constant throughout its length, the earth's magnetic field exerts the following Lorentz force:

$$F = \left(\frac{\ell}{2}\right)\vec{I} \times \vec{B} = \frac{I\ell B\sin\psi}{2} \tag{2.10}$$

I = current through either power supply
ℓ = total length of tether
B = magnetic field
ψ = angle between wire and magnetic field

Since we are orienting the tether in the equatorial plane, perpendicular to the magnetic field, $\psi = \pi/2$, and $\sin\psi = 1$. Thus, the Lorentz force on half the tether is simplified to:

$$F = \frac{I\ell B}{2} \tag{2.11}$$

The half-tether Lorentz force can be approximated as being enacted upon the half-tether's center, that is, on its power supply. The distance from the center of the tether satellite to either power supply is, again, one quarter of the length of the entire tether. Thus, the induced torque for either half of the tether is:

$$T_L' = \frac{I\ell B}{2} R = \frac{I\ell^2 B}{8}$$

(2.12)

Since our satellite is both radially and axially symmetric, the torque on either side is equal. The sum of the torques is thus, simply:

$$T_L = \frac{I\ell^2 B}{4}$$

(2.13)

At equilibrium, the torques on the satellite will cancel each other out, and we are left with an expression for the equilibrium pitch angle.

$$\left(Q_{GG}\right)_y + T_L = 0$$

$$-\frac{3}{4} m\Omega^2 \ell^2 \theta + \frac{I\ell^2 B}{4} = 0$$

$$\theta = \frac{IB}{3m\Omega^2}$$

(2.14)

To quantify this expression, we start by squaring our original expression for Ω:

$$\Omega^2 = \frac{\mu}{R_{orbit}^{3}} = \frac{3.98 \times 10^{14}}{R_{orbit}^{3}}$$

(2.15)

Next, we approximate the mass m of the power supplies to be directly proportional to the power requirements, accumulating what we will define as α kilograms per watt of power required. Approximating α to equal roughly 20 kilograms per kilowatt, or 0.02 kilograms per watt, we deduce:

$$m = \alpha P = \alpha I \Phi_{tether} = \alpha I \left(10^6 V\right) = 2.0 \times 10^4 \cdot I$$

(2.16)

For altitudes of less than 10 Earth radii, the geomagnetic field can be approximated as a dipole field:

$$\vec{B} = \frac{\mu_0}{4\pi} \frac{M_E}{R_{orbit}^3} \left(-2\cos\theta, \sin\theta, 0 \right)$$

<div align="right">(2.17)</div>

Where we adopt conventional spherical coordinates aligned with the Earth's dipole moment, whose magnitude is $M_E = 8.05 \times 10^{22}\, Am^2$. The polar angle θ at the equator equals π/2, so the magnetic field lines at the equator all point straight north, as expected. The magnitude of the magnetic field in the equatorial plane is thus expressed as:

$$B = \frac{\mu_0}{4\pi} \frac{M_E}{R_{orbit}^3}$$

<div align="right">(2.18)</div>

Substitute the previous expressions for Ω, m, and B into our angle equation to obtain:

$$\theta = \frac{IB}{3m\Omega^2} = \frac{I\left(\dfrac{\mu_0}{4\pi} \dfrac{M_E}{R_{orbit}^3} \right)}{3\alpha I\Phi_{tether} \left(\dfrac{\mu}{R_{orbit}^3} \right)} = \frac{\mu_0 M_E}{12\pi\mu\alpha\Phi_{tether}}$$

$$\theta = 3.38\cdot 10^{-4}\, rad = 0.019°$$

<div align="right">(2.19)</div>

The equilibrium angle of the tether is not only miniscule, but also independent of altitude and tether length. Thus, we can assert that the Lorentz torque on the satellite is negligible and the tether remains in stable equilibrium parallel to the z-axis, pointing almost directly away from the Earth.

The only concern that results from the Lorentz forces now is satellite deformation resulting from the Lorentz torques pointing in opposite directions. This is a structural concern and lies outside the scope of this thesis, though further study is recommended.

2.3 Tether Potential Magnitude

According to the tether current equations cited earlier, since the total length of negative tether equals the length of its positive counterpart, the magnitudes of the potentials in the positive and negative tethers must be unequal, lest the difference in mass between electrons and ions produce a difference in net current.

We assume that the physical dimensions (total length, radii) of both tethers are equal. Furthermore, for altitudes above 2000 km, hydrogen ions makes up the vast majority of the positive ions, so other ions such as helium and oxygen can be neglected, simplifying the ion current expression to a single term. Since we wish to attract zero net current, we set the two currents equal to each other so they may neutralize one another.

$$I_e = I_i \tag{2.20}$$

$$2r_T e n_\infty L \sqrt{\frac{2e\Phi_T^{+}}{m_e}} = 2r_T e n_\infty L \sqrt{\frac{-2e\Phi_T^{-}}{m_i}}$$

$$\tag{2.21}$$

$$\Phi_T^{+} = -\frac{m_e}{m_i}\Phi_T^{-} \cong -\frac{\Phi_T^{-}}{1840}$$

$$\tag{2.22}$$

We conclude that the potential magnitude of the negative tether is much greater than that of its positive counterpart. This makes sense because electrons travel much faster than the heavier positive ions and using similar tethers of equal and opposite potential would result in the capture of electrons at a far greater rate than that of ion capture.

2.4 Tether Radius and Sheath Radius

2.4.1 Tether Radius

Before we can conduct calculations using our proposed series tether, we must confirm that the tether's radius and sheath radius prove practical. The tether will attract a current proportional to the tether's radius, but it will be limited by the capabilities of the power supplies which will be driving the current. Let us define a power supply with an upper limit of P_{max} watts. When two are attached to the satellite, their maximum current capacity can be deduced thus:

$$P_{max} = I_{max} V_T \qquad (2.23)$$

$$I_{max} = \frac{P_{max}}{V_T} = \frac{P_{max}}{10^6 \, volts} \qquad$$

$$(2.24)$$

Each power supply would be responsible for transporting the current from one half of the central positive tether, so that current must be less than I_{max}. Applying our earlier equations for the current resulting from either half of the positive tether length is thus subjects the radius of the tether to an upper limit. If we assume the negative tether potential to be 10 MV, and if we assume all positive particles are protons, then we calculate:

$$\frac{I_e}{2} = 2r_T e n_\infty \frac{L}{2} \sqrt{\frac{2e\Phi_T^+}{m_e}} = r_T e n_\infty L \sqrt{\frac{2e\Phi_T^+}{m_e}} \leq I_{max}$$

$$r_T \leq \frac{P_{max}}{e n_\infty L \Phi_T^+} \sqrt{\frac{m_e}{2e\Phi_T^+}} = \frac{P_{max}}{e n_\infty L \Phi_T^-} \sqrt{\frac{m_i}{-2e\Phi_T^-}} = \frac{P_{max}}{n_\infty L} \sqrt{\frac{m_i}{-2\left(e\Phi_T^-\right)^3}}$$

$$r_T \leq 90.3 \frac{P_{max}}{n_\infty}$$

$$(2.25)$$

According to Figure 2-8, the total number density of the plasma within the radiation belts numbers on the order of 10^{10} m^{-3} so if we assume the presence of a very strong power supply capable of producing 100kW, the upper limit of the tether radius becomes approximately 1 mm, a feasible radius if our tether is made of tungsten steel. It should be

noted, however, that according to simulations by Jean-Marie Deux in Figure 2-9, the current of the orbiting tether at voltages below 100V can add up to twice the calculated OML current. This differential appears to vanish as the voltage increases, yet stays fairly sizeable around the range of 550V covered by the positive tether. For the sake of conservative calculations, we compensate for this possible phenomenon by halving the tether radius to 0.5 mm.
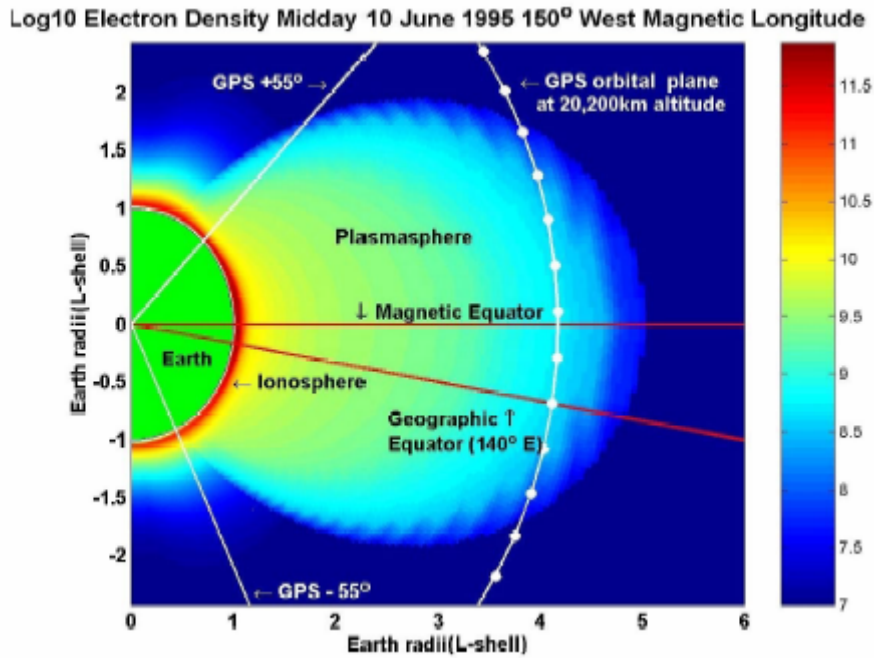
Figure 2-8: Plasma Density as a Function of Altitude [2]

Current collection with orbital velocity : 8 km/s (mesosonic flow)
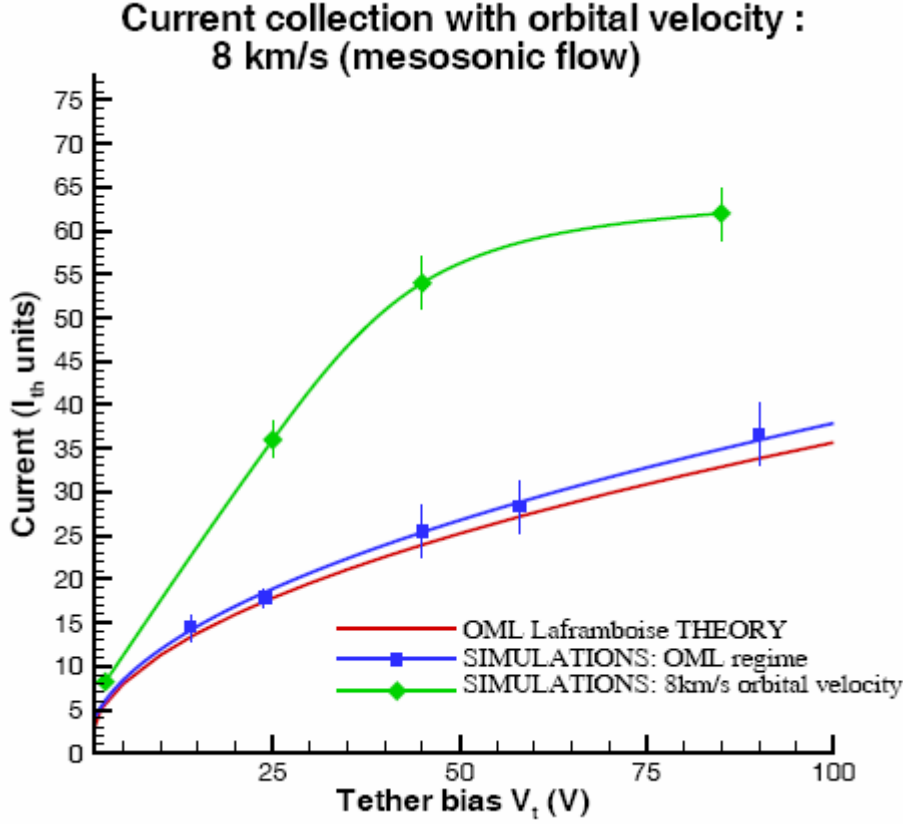
Figure 2-9: The dependence of current collection on (positive) tether bias in the cases of the O.M.L. and orbital velocity. [3]

2.4.2 Sheath Radius

According to Choiniere and Gilchrist, the radius of the tether's sheath is governed by the ambient plasma, the potential bias on the surface of the tether, and the radius of the tether [4]:

$$\frac{e\Phi_T}{kT_e} = 2.554 \left(\frac{r_s}{\lambda_D}\right)^{1.325} \ln\frac{r_s}{r_T}$$

(2.26)

We already know that our tether will bear a potential bias of 1 megavolt on its surface, so $\Phi_T = 10^6$ V. λ_D is the Debye length of the plasma and depends upon the electron temperature and density of the plasma, and thus depends upon the altitude at which the satellite will operate.

$$\lambda_D = \sqrt{\frac{\varepsilon_0 kT_e}{e^2 n_e}}$$

(2.27)

The tether sheath thus depends upon electron temperature, which in turn depends upon altitude. The following graph dictates the ambient temperature of the radiation belts below 8000km.
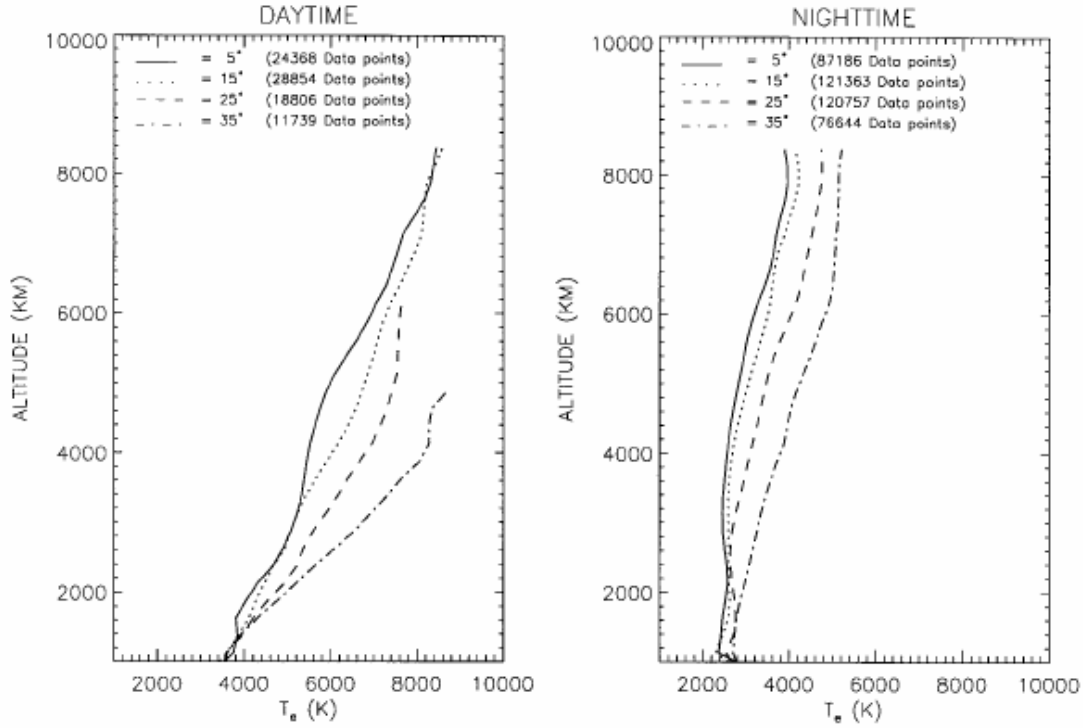
Figure 2-10: Variation of electron temperature with altitude and magnetic latitude. The data depicts the average temperatures from 1989 to 1995 recorded by the thermal electron distribution instrument on the EXOS-D satellite. [5]

The small temperature differential between the latitudes 5° and 15° indicate that we can roughly approximate the temperature in the equatorial plane (i.e. at 0°) using the data accumulated at 5°. Since the temperature varies dramatically between night and day, we approximate day-average temperatures for several altitudes, which will in turn be used to approximate their corresponding day-average sheath radii. This simply involves converting the previous equation to:

$$2.554\left(\frac{r_s}{\lambda_D}\right)^{1.325} \ln\frac{r_s}{r_T} - \frac{e\Phi_T}{kT_e} = 0$$

(2.28)

For a given altitude, we simply employ a computational zero-solver to find the radius sheath. We need not worry about the computer having to choose between multiple solutions, since the above equation increases monotonically with r_s.

Altitude (km)	Electron	Plasma	Sheath Radius	Sheath Radius

	Temperature	Debye Length	Negative Tether	Positive Tether
	(K)	(m)	(m)	(m)
2000	3400	0.040275	242.68	1.2346
4000	3900	0.043134	234.80	1.1959
6000	5100	0.049326	220.11	1.1237
8000	6200	0.054386	210.00	1.0739

Table 2-1: Sheath Radii, Positive and Negative Tethers

The negative tethers each bear a sheath radius of order 10^2m, while the positive tether's sheath is only on the order of 1m. In either case, tether length dwarfs the sheath radius by multiple orders of magnitude, allowing us to approximate the geometry of the entire sheath as a long cylinder.

2.5   Magnetic Field Effects

Our analysis of the deflection of particles by the tether necessitates an analysis of both electrodynamic and magnetic effects of particle scattering.

2.5.1   Self-Magnetic Field

As the tether collects current, the resulting magnetic field creates a series of closed field lines surrounding the tether. The intensity of this field reduces with distance until it merges with the Earth's locally open magnetic field lines. The planar projection of the field lines on the border between the open and closed field lines is called the separatrix. Since the separatrix is not circular, Khazanov et al stated that the separatrix and the circular induced field lines converge around radius where they share equal perimeters. Thus, the condition for reduced current collection due to self-magnetic field effect is as follows (in SI units) [6]:

$$2\pi r_s < P_{separatrix} = \frac{3.23}{\cos \alpha} r^*, \quad r^* = \frac{I}{2\pi \varepsilon_0 c^2 B}$$

(2.29)

r_s = plasma sheath radius

$P_{separatrix}$ = perimeter of separatix

$\alpha = \frac{\pi}{2}$ - (angle between tether and earth's magnetic field)

B = magnitude of earth's magnetic field

We've already determined the angle between the tether and the earth's magnetic field to be $\pi/2$, so $\alpha=0$, and $\cos\alpha=1$. The upper limit decreases with B, and our sheath radius increases with B. Since B increases with altitude, the inequality is most likely to be satisfied at the highest possible altitude, which for the scope of this study is 8000km above the earth's surface. Substituting the magnitude of the magnetic field at this altitude and the equation for OML current, the inequality in (2.29) can now be quantified:

$$2\pi r_s < 3.23\left(\frac{1}{2\pi\varepsilon_0 c^2 B}\right)2r_T en_\infty L\sqrt{\frac{-2e\Phi_T^-}{m_i}}$$

$$r_s < 3.23\frac{r_T n_\infty L}{\pi^2 \varepsilon_0 c^2 B}\sqrt{\frac{-e^3\Phi_T^-}{2m_i}} < 4.1821 mm$$

$$(2.30)$$

The separatrix radius measures only about eight times the radius of the tether itself, which is to be expected, given that the total current amounts to only a fraction of an ampere. Our sheath radius for both the positive and negative tethers exceed this upper limit by several orders of magnitude, so we deduce that self-magnetic field effects have negligible impact on current reduction and can be ignored when calculating deflection angles.

2.5.2   Magnetic Gyrations

The Earth's magnetic fields generate gyrations in the particles that must be considered when analyzing the electrostatic effects of the tether, so long as the Larmor radius (or gyroradius) is of a higher order of magnitude than the radius of the tether sheath. The Larmor radius is represented in CGS units thus [7]:

$$r_e = 2.38\frac{\sqrt{T_e}}{B}cm$$

$$(2.31)$$

$$T_e = \text{electron temperature (eV)}$$
$$B = \text{magnetic field (G))}$$

$$r_i = 1.02 \cdot 10^2 \frac{\sqrt{\gamma T_e}}{BZ}cm$$

$$T_i = \text{ion temperature (eV)} \qquad (2.32)$$

$$B = \text{magnetic field (G)}$$

$$Z = \text{charge state}$$

$$\gamma = \frac{m_{ion}}{m_{proton}}$$

Again, protons dominate the ion population above 1500km, making them the only ions whose Larmor radii we will consider, and for which Z=1 and γ=1. As stated before, the magnetic field is given by:

$$B = \frac{\mu_0}{4\pi} \frac{M_E}{R_{orbit}^3} Telsa = \frac{\mu_0}{4\pi} \frac{M_E}{R_{orbit}^3} \cdot 10^4 \, Gauss$$

$$(2.33)$$

Now we can substitute (2.33) into (2.31) and (2.32) to calculate the values of the magnetic field and Larmor radius for both ions and elections at various altitudes.

altitude (km)	T_e(K)	T_e(eV)	B(Tesla)	r_e (m)	r_i (m)
2000	3400	0.29	1.37×10^{-5}	0.094	4.024
4000	3900	0.34	7.22×10^{-6}	0.191	8.192
6000	5100	0.44	4.26×10^{-6}	0.371	15.895
8000	6200	0.53	2.72×10^{-6}	0.641	27.467

Table 2-2: Average Temperature and Larmor Radius in Ambient Plasma

The thermal Larmor radius of the ions is considerably less than the radius of the tether, but since the voltage on our tether is seven orders of magnitude larger than the average thermal energy of the particles, the particles greatly increase their energy by entering the sheath, thus increasing their Larmor radii. Let us assume that a particle enters the sheath and increases its thermal energy 2% of the tether's total potential bias (that is, 20 keV), its Larmor radius exceeds the radius of the negative sheath by one order of magnitude and the positive sheath by two orders.

Altitude	B(Tesla)	r_e (m)	r_i (m)
2000	1.37×10^{-5}	24.52	1050.94
4000	7.22×10^{-6}	46.60	1997.55

6000	4.26×10^{-6}	79.08	3389.30
8000	2.72×10^{-6}	123.94	5311.95

Table 2-3: Larmor Radii at 2% of Negative Tether Energy

Altitude	B(Tesla)	r_e (m)	r_i (m)
2000	1.37×10^{-5}	0.5727	24.546
4000	7.22×10^{-6}	1.0886	46.655
6000	4.26×10^{-6}	1.8471	79.161
8000	2.72×10^{-6}	2.8949	124.06

Table 2-4: Larmor Radii at 2% of Positive Tether Energy

Thus, the effect of magnetic gyrations in ions can be neglected in determining the deflection angle in both tethers. The same is not true for electrons, however, so any scattering calculations that neglect the effects of the Larmor radius will accurately apply only to ions.

Chapter 3

Scattering Theory

3.1   Electrostatic Scattering

To calculate the total dispersion rate of the tether, we analyze the effects of a single electrostatic tether on a single incoming particle. Defining the directional axes as we did when analyzing the loss cone, and assume a single tether of uniform potential parallel to the z-axis such that the origin lies in the center of the tether. Next, assume a particle barely inside the tether sheath, within the xy-plane, whose trajectory is radial inward. Since the sheath of our tether is considerably shorter than the total length of any one section of the series tether, we assume that the tether is infinitely long when calculating the electrostatic force on the particle. Under this assumption, the tether is symmetric in both the positive and negative z-directions, and thus exerts no force in the z-direction. Thus, we analyze the electrostatic force on the particle only in the xy-plane as we would a two-dimensional Coulomb collision.
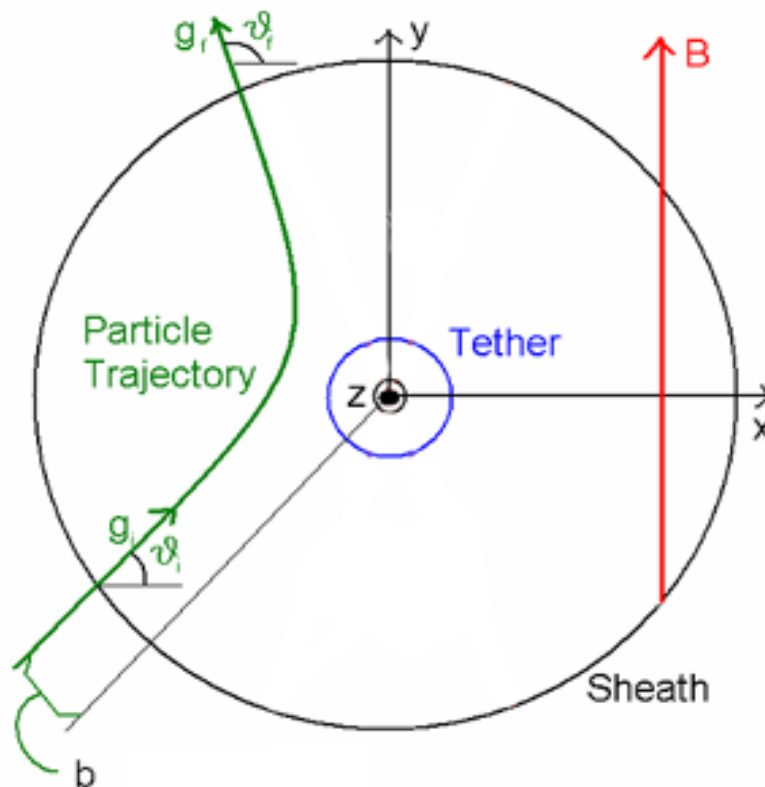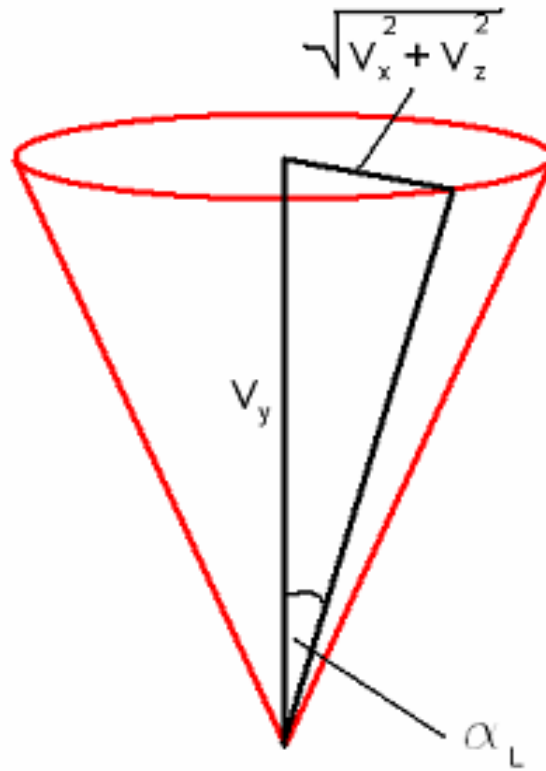

Figure 3-1: Repelling Tether

Figure 3-2: Loss Cone in Positive y-direction

Defining g as the particle's speed in the xy-plane just as it enters the particle's sheath, q as its charge, r as its radial distance from the tether, and φ as angular position, the energy and momentum equations defining a two-dimensional Coulombic interaction are as follows:

$$\frac{1}{2}m\left(\dot{r}^2 + r^2\dot{\varphi}^2\right) + q\phi(r) = \frac{1}{2}mg^2 \qquad g = \sqrt{v_x^2 + v_y^2} \qquad (3.1)$$

$$mr^2\dot{\varphi} = -mgb \qquad\qquad\qquad\qquad\qquad\qquad\qquad (3.2)$$

We obtain a formula for the rate of change in angle as a function of radius by rearranging the momentum equation as shown:

$$\dot{\varphi} = \frac{-mgb}{mr^2} = \frac{-gb}{r^2} \qquad\qquad (3.3)$$

Substituting (3.3) directly into the energy equation (3.1) produces an expression for rate of change in radius as a function of radius.

$$\frac{1}{2}m\left(\dot{r}^2 + \frac{g^2b^2}{r^2}\right) + q\phi(r) = \frac{1}{2}mg^2$$

$$\dot{r}^2 = \left(\frac{dr}{dt}\right)^2 = g^2\left[1 - \frac{b^2}{r^2} - \frac{2q\phi(r)}{mg^2}\right]$$

$$\qquad\qquad\qquad\qquad\qquad\qquad\qquad\qquad (3.4)$$

Square both sides of (3.4) and divide by (3.3) to get:

$$\frac{\dot{r}^2}{\dot{\varphi}^2} = \left(\frac{dr}{d\varphi}\right)^2 = \frac{r^4}{b^2}\left[1 - \frac{b^2}{r^2} - \frac{2q\phi(r)}{mg^2}\right] \qquad (3.5)$$

Split the differential terms:

$$d\varphi = \frac{b}{r^2}\frac{dr}{\sqrt{1 - \frac{b^2}{r^2} - \frac{2q\phi(r)}{mg^2}}} \qquad (3.6)$$

To determine the total change in angle that results from the Coulomb collision, we integrate both sides. The left side is integrated from the initial angle to the final angle, and thus integrates to the total angle change. The limits of the radius for the integral on the right hand side are taken from r_m to r_∞, where r_m is the minimum radial distance from the tether that the particle reaches. Applying these limits of integration, we get:

$$\Delta\varphi = \int_{\varphi_i}^{\varphi_f} d\varphi = \int_{r_m}^{r_\infty} \frac{b}{r^2} \frac{dr}{\sqrt{1 - \frac{b^2}{r^2} - \frac{2q\phi(r)}{mg^2}}} \tag{3.7}$$

$$1 - \frac{b^2}{r_m^{\,2}} - \frac{2q\phi(r_m)}{mg^2} = 0$$

Iisregarding gravitational forces, if there were no electrostatic forces resulting from the tether, then the particle would travel in a straight line, and $\Delta\varphi$ would equal π. The angle by which the trajectory is deflected from the free flight path is denoted χ, and:

$$\chi = \pi - 2\Delta\varphi \tag{3.8}$$

By the definition of the tether sheath, the potential of the plasma outside of the sheath radius r_∞ is of the order $0.5kT_i << e\Phi_T$, and is thus neglected. We also neglect the potential change due to the space charge of the charged particles in transit through the sheath. Thus, we take the potential to be Coulombic for $r<r_\infty$ and zero for $r>r_\infty$, and our integral becomes:

$$\Delta\varphi = \int_{r_m}^{r_\infty} \frac{b}{r^2} \frac{dr}{\sqrt{1 - \frac{b^2}{r^2} - \frac{2q\phi(r)}{mg^2}}} + \int_{r_\infty}^{\infty} \frac{b}{r^2} \frac{dr}{\sqrt{1 - \frac{b^2}{r^2}}} \tag{3.9}$$

Now we must calculate the potential function in the Coulombic region. We employ LaPlace's equation to the electric potential.

$$\nabla^2\phi = \frac{1}{r}\frac{\partial}{\partial r}\left(r\frac{\partial\phi}{\partial r}\right) + \frac{1}{r}\frac{\partial^2\phi}{\partial\theta^2} + \frac{\partial^2\phi}{\partial z^2} = -\frac{\rho}{\varepsilon_0} \tag{3.10}$$

Assuming the potential field near the tether to be similar to that of the field around an infinite wire, the potential function varies only with r, eliminating the second and third

terms in the differential equation. Furthermore, we assume the tether to be surrounded by macroscopically neutral plasma, so the charge density in its vicinity is zero.

$$\nabla^2 \phi = \frac{1}{r} \frac{\partial}{\partial r} \left(r \frac{\partial \phi}{\partial r} \right) = 0$$

$$\frac{d}{dr} \left(r \frac{d\phi}{dr} \right) = 0$$

$$(3.11)$$

Thus, the content of the derivative is constant, or:

$$r \frac{d\phi}{dr} = A$$

$$\phi = A \ln r + B$$

$$(3.12)$$

Our boundary conditions dictate that the potential at the surface of the tether is Φ_T while the potential at the surface of the sheath is 0.

$$r = r_T : \quad \Phi_T = A \ln r_T + B \tag{3.13}$$

$$r = r_\infty : \quad 0 = A \ln r_\infty + B \tag{3.14}$$

Combine the two equations to get:

$$-\Phi_T = A \ln \frac{r_\infty}{r_T}$$

$$(3.15)$$

$$A = \frac{-\Phi_T}{\ln \dfrac{r_\infty}{r_T}} \qquad\qquad B = \frac{\Phi_T \ln r_\infty}{\ln \dfrac{r_\infty}{r_T}}$$

$$\phi = A \ln r + B = \frac{-\Phi_T}{\ln \dfrac{r_\infty}{r_T}} \ln r + \frac{\Phi_T \ln r_\infty}{\ln \dfrac{r_\infty}{r_T}} = \Phi_T \frac{\ln \dfrac{r_\infty}{r}}{\ln \dfrac{r_\infty}{r_T}}$$

Plug this into our integral to get:

$$\Delta\varphi = \int_{r_m}^{r_\infty} \frac{b}{r^2} \frac{dr}{\sqrt{1 - \frac{b^2}{r^2} - \frac{2q}{mg^2} \Phi_T \frac{\ln\frac{r_\infty}{r}}{\ln\frac{r_\infty}{r_T}}}} + \int_{r_\infty}^{\infty} \frac{b}{r^2} \frac{dr}{\sqrt{1 - \frac{b^2}{r^2}}}$$

(3.17)

The denominator of the first integral contains many factors independent of r which can be grouped for simplicity. Let us define:

$$\lambda = \frac{2q}{mg^2} \frac{\Phi_T}{\ln\frac{r_\infty}{r_T}}$$

(3.18)

Thus, our integral becomes:

$$\Delta\varphi = \int_{r_m}^{r_\infty} \frac{b}{r^2} \frac{dr}{\sqrt{1 - \frac{b^2}{r^2} - \lambda \ln\frac{r_\infty}{r}}} + \int_{r_\infty}^{\infty} \frac{b}{r^2} \frac{dr}{\sqrt{1 - \frac{b^2}{r^2}}}$$

(3.19)

We define $\eta = \frac{b}{r}$, and thus $\eta_\infty = \frac{b}{r_\infty}$, and substitute into both integrals to simplify:

$$\Delta\varphi = -\int_{\eta_m}^{\eta_\infty} \frac{d\eta}{\sqrt{1 - \eta^2 - \lambda \ln\frac{\eta}{\eta_\infty}}} - \int_{\eta_\infty}^{0} \frac{d\eta}{\sqrt{1 - \eta^2}}$$

$$= \int_{\eta_\infty}^{\eta_m} \frac{d\eta}{\sqrt{1 - \eta^2 - \lambda \ln\frac{\eta}{\eta_\infty}}} + \int_{0}^{\eta_\infty} \frac{d\eta}{\sqrt{1 - \eta^2}}$$

$$= \int_{\eta_\infty}^{\eta_m} \frac{d\eta}{\sqrt{1 - \eta^2 - \lambda \ln\frac{\eta}{\eta_\infty}}} + \sin^{-1}\eta_\infty$$

$$(3.20)$$

Substitute this into our equation for the deflection angle:

$$\chi = \pi - 2\Delta\varphi = \pi - 2\sin^{-1}\eta_\infty - 2\int_{\eta_\infty}^{\eta_m} \frac{d\eta}{\sqrt{1-\eta^2 - \lambda\ln\frac{\eta}{\eta_\infty}}}$$

$$(3.21)$$

3.2   Approximation Methods

3.2.1 Hard-body approximation

Fast, high-energy ions are naturally capable of penetrating deeper into the sheath of the positive tether than slower, lower-energy ions. If an incoming ion possesses significantly less energy than the tether possesses potential, it may be overwhelmed by the tether's repelling force as soon almost immediately after entering the sheath. When such an ion is repelled, it appears to almost bounce off the edge of the sheath as though it were a hard body collision. We can thus approximate our expression for the deflection angle for large, positive values of λ and expect to derive a solution similar to that of an elastic hard body collision between a tiny object and a cylinder.

We start with the definition for the η_m:

$$1 - \eta_m{}^2 - \lambda\ln\frac{\eta_m}{\eta_\infty} = 0$$

$$(3.22)$$

Now we convert the logarithm to an exponential expression which we can then approximate via first-order Taylor expansion:

$$\eta_m = \eta_\infty \cdot e^{\frac{1-\eta_m{}^2}{\lambda}} \approx \eta_\infty\left(1 + \frac{1-\eta_m{}^2}{\lambda}\right) = \eta_\infty + \eta_\infty\frac{1-\eta_m{}^2}{\lambda}$$

$$(3.23)$$

Substituting this expression back into the limit in our integral yields

$$\chi \cong \pi - 2\sin^{-1}\eta_\infty - 2\int_{\eta_\infty}^{\eta_\infty\left(1+\frac{1-\eta_m^2}{\lambda}\right)} \frac{d\eta}{\sqrt{1-\eta_\infty^2 - \lambda\ln\frac{\eta}{\eta_\infty}}} \tag{3.24}$$

Now we expand the term in the radical of the integral's denominator via a Taylor expansion around η_∞:

$$Rad = 1 - \eta^2 - \lambda\ln\frac{\eta}{\eta_\infty} \cong (Rad)_{\eta_\infty} + \left(\frac{dRad}{d\eta}\right)(\eta - \eta_\infty)$$

$$= 1 - \eta_\infty^2 + \left(-2\eta_\infty - \frac{\lambda}{\eta_\infty}\right)(\eta - \eta_\infty) \tag{3.25}$$

Assuming $\lambda \gg 1$, we can approximate:

$$-2\eta_\infty - \frac{\lambda}{\eta_\infty} \approx -\frac{\lambda}{\eta_\infty} \tag{3.26}$$

This gives us the following approximation for the radical:

$$Rad = 1 - \eta_\infty^2 - \frac{\lambda}{\eta_\infty}(\eta - \eta_\infty)$$

$$\chi \cong \pi - 2\sin^{-1}\eta_\infty - 2\int_{\eta_\infty}^{\eta_\infty\left(1+\frac{1-\eta_m^2}{\lambda}\right)} \frac{d\eta}{\sqrt{1-\eta_\infty^2 - \frac{\lambda}{\eta_\infty}(\eta - \eta_\infty)}}$$

$$\tag{3.27}$$

To solve, we substitute:

$$R = 1 - \eta_\infty^2 - \frac{\lambda}{\eta_\infty}(\eta - \eta_\infty) \qquad dR = -\frac{\lambda}{\eta_\infty}d\eta$$

$$\eta = \eta_\infty\left(1 + \frac{1-\eta_m^2}{\lambda}\right) \to R = 0 \qquad \eta = \eta_\infty \to R = 1 - \eta_\infty^2$$

$$\chi \cong \pi - 2\sin^{-1}\eta_\infty - 2\int_{1-\eta_\infty^2}^{0} -\frac{\eta_\infty}{\lambda}\frac{dR}{\sqrt{R}}$$

$$\cong \pi - 2\sin^{-1}\eta_\infty - 2\frac{\eta_\infty}{\lambda}\int_{0}^{1-\eta_\infty^2}\frac{dR}{\sqrt{R}}$$

$$\cong \pi - 2\sin^{-1}\eta_\infty - 4\frac{\eta_\infty}{\lambda}\sqrt{1-\eta_\infty^2}$$

(3.28)

Since we are still assuming that $\lambda \gg 1$, then $\lambda^{-1} \ll 1$, and

$$b = r_\infty \cos\left(\frac{\chi}{2}\right)$$

(3.29)

This is the equation for a particle colliding with a hard cylinder, just as we expected.

3.2.2 Soft-body approximation

On the other side of the coin, if an ion possesses a very large amount energy in comparison to the tether's potential, such that $\lambda \ll 1$, it can pass almost straight through the sheath with only minimal influence from the tether. Such an approximation applies to only a small minority of the total number of ions, but it can apply to both attracting and repelling tethers.
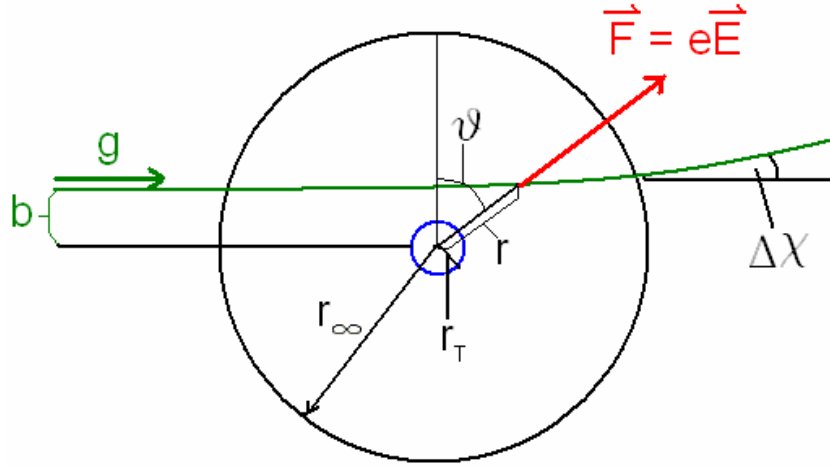
Figure 3-3: Soft-Body Approximation

Since the effect of the tether will be miniscule, we can approximate the entrance and exit angles of the ion to be nearly the same.

$$\theta_{MAX} = \cos^{-1} \frac{b}{r_\infty}$$

(3.30)

We use this to define the range of the particle's radius from the tether and its position along the x-axis with respect to b and θ:

(3.31)

$$r = \frac{b}{\cos\theta} \qquad -\theta_{MAX} < \theta < \theta_{MAX}$$

$$x = r\sin\theta = b\tan\theta$$

$$dx = \frac{b}{\cos^2\theta}\,d\theta$$

(3.32)

(3.33)

We define g as the ion's velocity component in the plane of the tether cross-section. If we assume that the electrostatic force is so weak that it accelerates the particle mostly in the direction perpendicular to the particle's initial velocity, we can approximate g to be constant, which we use to approximating change in time as directly proportional to change in the x-direction. Further substitution yields change in time with angle.

$$dt = \frac{dx}{g} = \frac{b}{g} \frac{d\theta}{\cos^2 \theta}$$

(3.34)

The electric field within the sheath is given by:

$$E = -\frac{d\phi}{dr} = -\frac{d}{dr} \left(\Phi_T \frac{\ln \frac{r_\infty}{r}}{\ln \frac{r_\infty}{r_T}} \right) = \frac{\Phi_T}{\ln \frac{r_\infty}{r_T}} \frac{1}{r} = \frac{\Phi_T}{\ln \frac{r_\infty}{r_T}} \frac{\cos \theta}{b}$$

(3.35)

Next we define the force on the particle in the normal direction to obtain a differential equation for the ion's normal velocity:

$$F_N = ma_N = m \frac{dv_N}{dt} = eE \cos \theta$$

(3.36)

Substituting our prior equations produces a

$$dv_N = \frac{eE}{m} \cos \theta dt = \frac{e\Phi_T}{m \ln \frac{r_\infty}{r_T}} \frac{\cos^2 \theta}{b} \frac{b}{g \cos^2 \theta} d\theta$$

$$\frac{dv_N}{g} = \frac{e\Phi_T}{mg^2 \ln \frac{r_\infty}{r_T}} d\theta = \frac{\lambda}{2} d\theta$$

(3.37)

Integrating over the total trajectory of the particle within the sheath, we deduce the total change in the normal velocity (that is, the final normal velocity) in terms of the total change in angle.

$$\int_0^{\Delta v_N} \frac{dv_N}{g} = \int_{-\theta_{MAX}}^{\theta_{MAX}} \frac{\lambda}{2} d\theta$$

$$\frac{\Delta v_N}{g} = \lambda \theta_{MAX} = \lambda \cos^{-1} \eta_\infty$$

$$(3.38)$$

Since the ion originally has no normal velocity, the deflection angle is simply the angle of the final velocity vector, or:

$$\chi = \frac{\Delta v_N}{g} = \lambda \cos^{-1} \eta_\infty$$

$$(3.39)$$

This approximation is only valid for very low values of λ, and since the result itself must be not much greater than λ.

Chapter 4

Numerical Implementation

4.1   Flux Integral

Since we are primarily interested in the scattering of high-energy particles, we shall restrict our focus to the high-energy populations, whose mean energy is 1 MeV. Low-energy particles are collected and scattered by the tether as well, but their primary effect lies in their collection rates which in turn determine the tether and sheath radii. Since such effects have already been calculated in the previous chapters, the low-energy particles can now be regarded as a separate population and ignored as we calculate the scattering rates of the high-energy particles at mean temperature $T = 10^6 \cdot 11600$ K

4.1.1   Distribution Function

Now that we have a computationally feasible expression for the deflection angle of a given particle, we will implement it to determine what percentage of incoming particles will be depleted. A tether in orbit will be attracting ions from many different directions and velocities, and using the equation for the deflection angle, we can determine the percentage of these ions that are properly deflected into the loss cone. However, before we can do anything, we must first determine what distribution the ion velocities will obey.

4.1.1.1 Loss Cone Correction

We start with a Maxwellian distribution of particle velocities in the magnetosphere plasma, dependent only upon the velocity magnitude and normalized to integrate over all velocities to the density n.

$$f\left(v_x, v_y, v_z\right) = n\left(\frac{m}{2\pi kT}\right)^{\frac{3}{2}} e^{-\frac{m(v_x{}^2+v_y{}^2+v_z{}^2)}{2kT}}$$

(4.1)

$$\iiint\limits_{All\,Velocities} f\left(v_x, v_y, v_z\right) dv_x dv_y dv_z = \int_{v_z=-\infty}^{v_z=\infty}\int_{v_y=-\infty}^{v_y=\infty}\int_{v_x=-\infty}^{v_x=\infty} f\left(v_x, v_y, v_z\right) dv_x dv_y dv_z = n$$

(4.2)

However, we are assuming that all charged particles whose velocities fall into the loss cone exit the magnetosphere, so our distribution function must not include such ions. This exclusion depends solely upon the direction of the ions' velocity vectors, not their

magnitude, while the Maxwellian distribution function depends upon velocity magnitude, not direction. Thus, if we exclude a certain fraction of velocity directions from our calculation, then the contribution of each velocity magnitude to the normalizing integral will be reduced by that same fraction, as will the integral's total value. To determine the fraction by which the normalizing integral is reduced, we simply determine the solid angle fraction not encompassed by the loss cone. Remembering that the loss cone is projected in both directions along the y-axis, we calculate this fraction κ of the total solid angle 4π to be:

$$\kappa = 1 - \frac{\Omega_{Loss}}{4\pi} = 1 - \frac{2 \cdot 2\pi(1 - \cos\alpha_L)}{4\pi} = \cos\alpha_L$$

(4.3)

If we restrict the limits of our normalizing integral to only those velocity vectors whose directions lie outside the loss cone, yet maintain our original Maxwellian distribution function, our result is reduced by a factor of κ:

$$\iiint\limits_{\substack{Outside \\ Loss\,Cone}} f(v_x, v_y, v_z)\,dv_x dv_y dv_z = n\kappa = n\cos\alpha_L$$

(4.4)

Since we want the normalizing integral to equal n, we divide the distribution function by the extra factor, thus converting the normal Maxwellian distribution into a normal loss-cone distribution:

$$f_{LC}(v_x, v_y, v_z) = \frac{n}{\cos\alpha_L} \left(\frac{m}{2\pi kT}\right)^{\frac{3}{2}} e^{-\frac{m(v_x^2 + v_y^2 + v_z^2)}{2kT}}$$

(4.5)

$$\iiint\limits_{\substack{Outside \\ Loss\,Cone}} f_{LC}(v_x, v_y, v_z)\,dv_x dv_y dv_z = n$$

(4.6)

This makes sense because constricting the limits of the normalization integral reduces the result, and we compensate by increasing the distribution function.

4.1.1.2 Change to Cylindrical Coordinates

Our two-dimensional calculations on scattering theory were derived in polar coordinates rather than Cartesian coordinates, so it makes sense to convert our three-dimensional distribution function from Cartesian coordinates to cylindrical coordinates.

We split up the velocity vector into three components: the velocity component parallel to the tether (v_z), the velocity component within the perpendicular xy-plane (g), and the angle at which the latter component lies from the x-axis (θ). In other words:

$$v_x = g \cos\theta \qquad\qquad g = \sqrt{v_x^2 + v_y^2}$$

$$v_y = g \sin\theta \qquad\qquad \theta = \tan^{-1}\frac{v_y}{v_x}$$

$$\tag{4.7}$$

We similarly convert the differential terms in the integral:

$$dv_x dv_y = g\,dg\,d\theta \tag{4.8}$$

Our loss-cone distribution is now defined:

$$f_{LC}(v_z, g, \theta) = \frac{n}{\cos\alpha_L}\left(\frac{m}{2\pi kT}\right)^{\frac{3}{2}} e^{-\frac{m(g^2 + v_z^2)}{2kT}} \tag{4.9}$$

$$\iiint\limits_{\substack{\text{Outside}\\\text{Loss Cone}}} g \cdot f_{LC}(v_z, g, \theta)\,dg\,d\theta\,dv_z = n$$

$$\tag{4.10}$$

4.1.1.3 Flux and Impact Parameter

Now that we have our distribution function, we can calculate the particle flux per square meter per second through a surface area in the magnetosphere's plasma, assuming the radial direction to be perpendicular to the surface.

$$\Gamma = \iiint\limits_{\substack{\text{Outside}\\\text{Loss Cone}}} g^2 \cdot f_{LC}(v_z, g, \theta)\,dg\,d\theta\,dv_z\, m^{-2} s^{-1} \tag{4.11}$$

To calculate the actual number of particles passing through, we have to determine the area through which the ions are passing. However, we cannot simply multiply the per-square-meter flux equation by the area of the tether sheath because not all particles which penetrate the sheath do so at a perfect right angle. This problem can be circumvented by working in terms of the impact parameter b.

Starting with a cross-sectional diagram of the tether sheath, define a velocity vector **v** such that g is greater than zero and θ any single value. Isolate all incoming particles with said velocity. Define a Gaussian surface directly between these incoming particles and the tether sheath, as shown, such that the ram end is flat, precisely the length of the sheath diameter, and perpendicular to the radial direction.
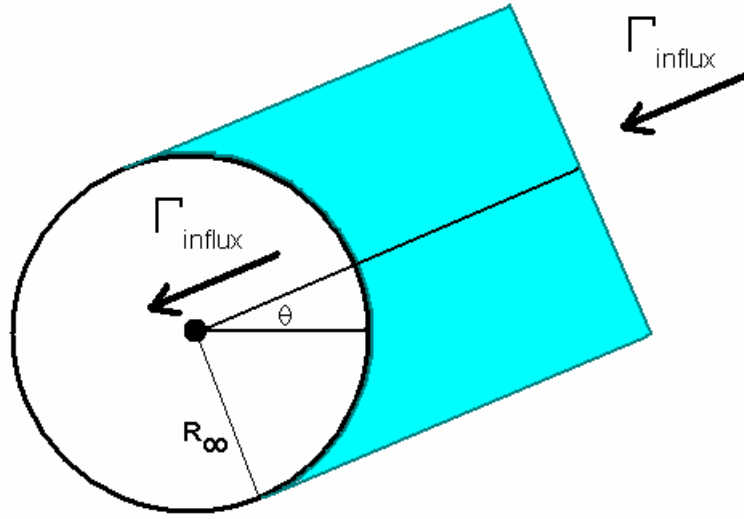

Figure 4-1: Gaussian Surface Around Sheath

Since there are no sources or sinks of ions, the flux of ions of this given velocity out of the surface's rounded end (and into the sheath) must equal the flux into the plate from outside, which we can much more easily calculate. The incoming particles have no impetus to pass through any portion of the plate any more than any other part because the flat-plate portion of the surface exists outside the tether sheath, resulting in equal distribution across this plate. For ions of any given velocity vector with a non-zero radial component, the flux area is simply twice the sheath radius multiplied by the length of the tether. This holds true for all such velocity vectors, so the entire flux integral is also multiplied by this factor, as shown:

$$\Gamma_{\inf lux} = \iiint_{\substack{Outside \\ Loss\,Cone}} g^2 \cdot f_{LC}(v_z, g, \theta) \cdot 2R_\infty L_T \cdot dg d\theta dv_z s^{-1} \tag{4.12}$$

However, when we calculate the rate at which particles are scattered into the loss cone, not all impact parameters result in the incident ion hitting its target. This is not only a limiting factor to the range of impact parameters which we sum into the integral but also

a function of the velocity vector itself. This term for the impact parameter's acceptable width, which we shall call w_b, must be completely nested within the flux integral.

$$\Gamma_{scatter} = \iiint_{\substack{Outside \\ Loss\,Cone}} g^2 \cdot f_{LC}(v_z, g, \theta) \cdot w_b(v_z, g, \theta) \cdot L_T \cdot dg\,d\theta\,dv_z\,s^{-1} \tag{4.13}$$

4.1.2 Scattering Limits

Before we leave the integral as is, we must realize that w_b is not non-zero for all velocity vectors. That is particles incident at certain velocities have no chance at being scattered into the loss cone. To minimize the computational requirements for this calculation, there is no sense in spending processing time towards ions which do not contribute toward the scattering flux. We continue with our two-dimensional plate diagram, identifying and excluding all such "hopeless" ions from the integral limits to manageable levels. Our goal is to isolate the permutations of initial velocities and impact parameters such that any particle bearing those initial conditions upon entering the tether sheath will be scattered into the loss cone upon exiting the sheath.

4.1.2.1 Axial Velocity Component v_z

We start with the v_z parameter and allow it to take any value. Placing no restrictions leaves the limits of v_z the same as in the normalizing integral:

$$-\infty < v_z < \infty \tag{4.14}$$

To shorten our calculations, we remember that we are assuming the particles to act as though our tether were infinitely long, thus resulting in the same deflection in the equatorial plane regardless of the sign of the z-velocity component. Thus, we cut the limits to our integral in half due to symmetry:

$$0 < v_z < \infty \tag{4.16}$$

This change is accommodated by multiplying the total flux integral by 2.

4.1.2.2 Radial Velocity Component g

Next up is the g parameter. Remember that for a particle with a given velocity, the scattering tether can alter the particle's velocity vector only by rotating it about the tether's parallel axis. Thus, if v_z is sufficiently large compared to g, then the total vector cannot be rotated into the loss cone no matter how it is scattered:

Thus, for a given value of v_z, g much be at least sufficiently large that, if the velocity vector were to exist entirely within the y-z plane, it would lie parallel to the edge of the cone. Larger values of g place the vector further inside the loss cone, while smaller values of g cause it to exit the loss cone. Thus, only values of g within this limit have an opportunity to enter the loss cone, and no other values of g do not factor into our scattering flux. That is:

$$\frac{v_z}{\tan \alpha_L} < g < \infty$$

(4.17)

4.1.2.3 Incident angle θ

Next, we analyze the incoming particle angle θ with respect to both v_z and g. If we assume that the ions will be approaching the tether sheath independent of incident angle, then the behavior of the particles is symmetric across both the x-axis and y-axis. To simplify our calculations, we multiply the flux integral by four and limit our integral to one-quarter of the total range of θ:

$$0 \le \theta \le \frac{\pi}{2}$$

(4.19)

These limits must be further constricted so as not to include any incoming particles whose velocities fall into the loss cone. The condition for an ion's velocity vector to lie outside a loss cone is:

$$\tan \alpha_L \le \frac{\sqrt{v_x^2 + v_z^2}}{|v_y|}$$

(4.20)

Since we are assuming that no incoming particles lie within the loss cone, we substitute the initial polar velocity components into the above equation and deduce which values of θ satisfy and thus may be excluded from our calculations.

$$\tan^2 \alpha_L \le \frac{v_x^2 + v_z^2}{v_y^2} = \frac{g^2 \cos^2 \theta + v_z^2}{g^2 \sin^2 \theta}$$

$$g^2 \sin^2 \theta \tan^2 \alpha_L \le g^2 \cos^2 \theta + v_z^2 = v^2 - g^2 \sin^2 \theta$$

$$g^2 \sin^2 \theta \left(1 + \tan^2 \alpha_L\right) = g^2 \sin^2 \theta \left(\frac{1}{\cos^2 \alpha_L}\right) \le v^2$$

$$\theta_{lim} = \pm \sin^{-1} \left(\frac{v \cos \alpha_L}{g}\right)$$

<div align="right">(4.21)</div>

Since we restrict θ to the first quadrant, the integral limit becomes:

$$0 \le \theta \le \sin^{-1} \left(\frac{v \cos \alpha_L}{g}\right)$$

<div align="right">(4.22)</div>

4.1.2.4 Impact Parameter b

Now, given an ion with velocity vector components v_z, g, θ, we must determine which values of b allow for loss scattering. This is accomplished by determining which values of χ produce such results, from which we determine the corresponding values of b. As displayed in the following figure, we define χ such that a positive deflection angle corresponds to a deflected particle whether the impact parameter is positive or negative:
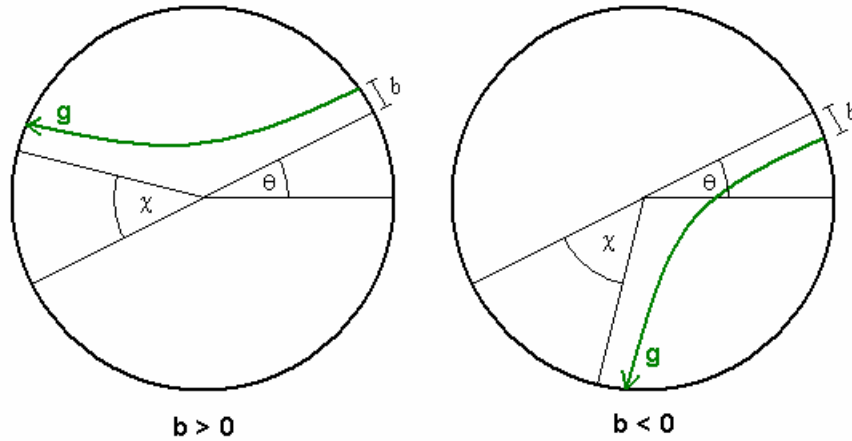

Figure 4-2: Deflection Angles for Positive and Negative Impact Parameter

We first identify the initial velocity components in terms of v_z, g, θ.

$$
\begin{aligned}
v_x &= -g \cos \vartheta \\
v_y &= -g \sin \vartheta \\
v_z &= v_z
\end{aligned}
$$

$$(4.23)$$

We then define the exit velocity components in terms of the initial velocity and the deflection angle:

$$
\begin{aligned}
v_x' &= g \cos(\theta + \pi - \chi) = -g \cos(\theta - \chi) \\
v_y' &= g \sin(\theta + \pi - \chi) = g \sin(\theta - \chi) \\
v_z' &= v_z
\end{aligned}
$$

$$(4.23)$$

$$v_x' = g\cos(\theta + \pi + \chi) = -g\cos(\theta + \chi)$$
$$v_y' = g\sin(\theta + \pi + \chi) = g\sin(\theta + \chi)$$
$$v_z' = v_z \tag{4.23}$$

In other words:

$$v_x' = -g\cos(\theta \mp \chi)$$
$$v_y' = g\sin(\theta \mp \chi)$$
$$v_z' = v_z \tag{4.23}$$

$$\mp = \begin{cases} -\text{ for } b > 0 \\ +\text{ for } b < 0 \end{cases}$$

Next, we plug the components of the exit velocity vector into the loss-cone condition.

$$\tan^2 \alpha_L \geq \frac{\sqrt{v_x'^2 + v_z'^2}}{|v_y'|} \geq \frac{g^2\cos^2(\theta \mp \chi) + v_z^2}{g^2\sin^2(\theta \mp \chi)}$$

$$g^2\sin^2(\theta \mp \chi)\tan^2 \alpha_L \geq g^2\cos^2(\theta \mp \chi) + v_z^2$$

$$g^2\sin^2(\theta \mp \chi)(1 + \tan^2 \alpha_L) \geq g^2 + v_z^2$$

$$\frac{\sin^2(\theta \mp \chi)}{\cos^2 \alpha_L} \geq 1 + \frac{v_z^2}{g^2}$$

$$\sin^2(\theta \mp \chi) \geq \cos^2 \alpha_L\left(1 + \frac{v_z^2}{g^2}\right)$$

$$\tag{4.24}$$

Isolate the angular terms to obtain our limit for χ in terms of θ:

$$\sin^{-1}\left(\sqrt{\frac{1+v_z^2}{g^2}}\cos\alpha_L\right) \le \left|\chi \mp \vartheta\right| \le \pi - \sin^{-1}\left(\sqrt{\frac{1+v_z^2}{g^2}}\cos\alpha_L\right)$$

$$\sin^{-1}\left(\frac{v}{g}\cos\alpha_L\right) \le \left|\chi \mp \vartheta\right| \le \pi - \sin^{-1}\left(\frac{v}{g}\cos\alpha_L\right)$$

$$\mp = \begin{cases} - \text{ for } b > 0 \\ + \text{ for } b < 0 \end{cases} \qquad v = \sqrt{g^2 + v_z^2} \qquad\qquad (4.25)$$

From here we can determine which values of χ result in an ion of velocity vector **v** being scattered. After that, we can computationally determine which values of b correspond to each deflection angle limit, and the sum w_b would equal the difference between each pair of impact parameter limits.
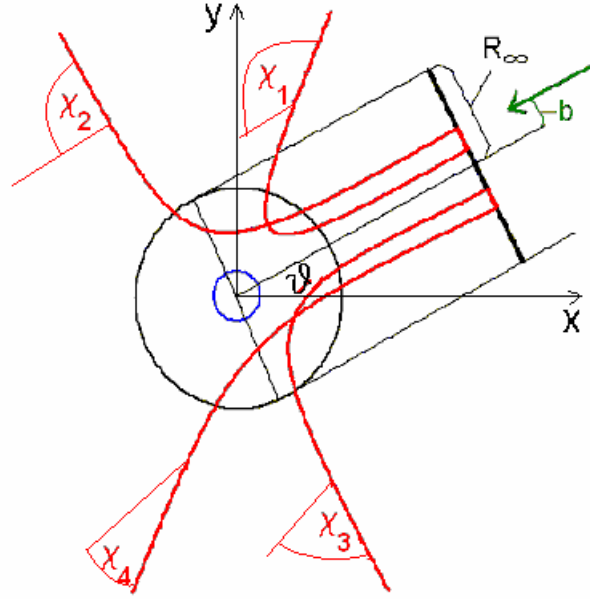

Figure 4-3: Deflection Angles Dependant upon Impact Parameter

That is, if each of the limit deflection angles χ_1, χ_2, χ_3, χ_4, and determining their corresponding impact parameters b_1, b_2, b_3, b_4:

$$w_b(v_z, g, \theta) = \left|b_1 - b_2\right| + \left|b_3 - b_4\right| \qquad\qquad (4.26)$$

4.1.3   Final Flux Equation

Going back to equation 3.1, we establish the distribution function by multiplying the interior term. After applying all of the above limits to our flux equation this turns into the following for our scattering flux:

$$\Gamma_{scatter} = 8 \cdot \int_0^\infty \int_0^\infty \int_0^{\sin^{-1}\left(\frac{v\cos\alpha_L}{g}\right)} g^2 \cdot f_{LC}\left(v_z, g, \theta\right) \cdot w_b\left(v_z, g, \theta\right) \cdot L_T \cdot d\theta dg dv_z s^{-1}$$

(4.26)

4.2   Computational Approximation

We have already derived an expression which, for a given velocity, accepts an impact parameter and returns the deflection angle. For this integral, however, our task is to accept a deflection angle and return an impact parameter. The deflection angle expression cannot be simplified analytically, so instead we will develop a reference table from which we can interpolate values.

We construct a 2-dimensional matrix such that each column index corresponds to a given value of b, and each row index corresponds to a given value of λ. The matrix elements themselves are the values of χ corresponding to the values of b and λ corresponding to that element's indices. In the deepest layer of the flux integral, we can determine the limits of χ as defined by v_z, g, and θ, and use the reference matrix to determine the corresponding values of b.

The integral in this expression cannot be determined analytically, so for the purpose of our calculations, we will be employing quadratic approximations via Matlab. One problem that arises is that quadratic integral approximations substitute the integration limits directly into the expressions; doing so with the upper limit produces an infinite number since, by our definition of r_m:

$$\frac{1}{\sqrt{1 - \eta_m^2 - \lambda \ln\dfrac{\eta_m}{\eta_\infty}}} = \frac{1}{\sqrt{1 - \dfrac{b}{r_m}^2 - \lambda \ln\dfrac{r_\infty}{r_m}}} = \frac{1}{\sqrt{0}} = \infty$$

(4.27)

This singularity at η_m produces an error which we resolve by splitting the integral into two parts: the main body, and an addendum to approximate the area closest to the singularity.

Define ε as a value of η slightly smaller than η_m. We split up the integral thus:

$$\int_{\eta_\infty}^{\eta_m} \frac{d\eta}{\sqrt{1-\eta^2-\lambda\ln\dfrac{\eta_m}{\eta_\infty}}} = \int_{\eta_\infty}^{\eta_m-\varepsilon} \frac{d\eta}{\sqrt{1-\eta^2-\lambda\ln\dfrac{\eta_m}{\eta_\infty}}} + \int_{\eta_m-\varepsilon}^{\eta_m} \frac{d\eta}{\sqrt{1-\eta^2-\lambda\ln\dfrac{\eta_m}{\eta_\infty}}} \qquad (4.28)$$

The first expression on the right-hand side can be derived computationally because neither limit encompasses the singularity. The second expression can be approximated analytically by introducing a change of variables.

$$\eta'=\eta_m-\eta, \qquad 0\le\eta'\le\varepsilon, \qquad \varepsilon\ll\eta_m \qquad (4.29)$$

From here we expand the term within the denominator's square root.

$$1-\eta^2-\lambda\ln\frac{\eta}{\eta_\infty} = 1-(\eta_m-\eta')^2-\lambda\ln\frac{\eta_m-\eta'}{\eta_\infty}$$

$$=1-\eta_m^{\;2}+2\eta_m\eta'-\eta'^2-\lambda\ln\left[\frac{\eta_m}{\eta_\infty}\left(1-\frac{\eta'}{\eta_m}\right)\right]$$

$$=1-\eta_m^{\;2}+2\eta_m\eta'-\eta'^2-\lambda\ln\left(\frac{\eta_m}{\eta_\infty}\right)-\lambda\ln\left(1-\frac{\eta'}{\eta_m}\right)$$

$$=\underbrace{1-\eta_m^{\;2}-\lambda\ln\left(\frac{\eta_m}{\eta_\infty}\right)}_{=0}+2\eta_m\eta'-\eta'^2-\lambda\ln\left(1-\frac{\eta'}{\eta_m}\right)$$

$$=2\eta_m\eta'-\eta'^2-\lambda\ln\left(1-\frac{\eta'}{\eta_m}\right)$$

$$(4.30)$$

We approximate this expression with a second-order logarithmic Taylor series.

$$2\eta_m\eta'-\eta'^2-\lambda\ln\left(1-\frac{\eta'}{\eta_m}\right) \approx 2\eta_m\eta'-\eta'^2-\lambda\left(-\frac{\eta'}{\eta_m}-\frac{1}{2}\frac{\eta'^2}{\eta_m^2}\right)$$

$$\approx \eta'^2\left(\frac{\lambda}{2\eta_m^2}-1\right)+\eta'\left(\frac{\lambda}{\eta_m}+2\eta_m\right)$$

(4.31)

Next we substitute this approximate expression into the addendum integral.

$$\int_{\eta_m-\varepsilon}^{\eta_m}\frac{d\eta}{\sqrt{1-\eta^2-\lambda\ln\frac{\eta_m}{\eta_\infty}}} \approx \int_{\eta_m-\varepsilon}^{\eta_m}\frac{d\eta}{\sqrt{\eta'^2\left(\frac{\lambda}{2\eta_\infty^2}-1\right)+\eta'\left(\frac{\lambda}{\eta_\infty}+2\eta_m\right)}}$$

(4.32)

From our earlier definition, $\eta'=\eta_m-\eta$, we determine that $d\eta'=-d\eta$. Furthermore, while the limits of η are η_m-ε and η_m , the corresponding limits of η' are ε and 0, respectively. Substituting all of this into our integral yields:

$$\int_{\varepsilon}^{0}\frac{-d\eta'}{\sqrt{\eta'^2\left(\frac{\lambda}{2\eta_m^2}-1\right)+\eta'\left(\frac{\lambda}{\eta_m}+2\eta_m\right)}} = \int_{0}^{\varepsilon}\frac{d\eta'}{\sqrt{\eta'^2\left(\frac{\lambda}{2\eta_m^2}-1\right)+\eta'\left(\frac{\lambda}{\eta_m}+2\eta_m\right)}}$$

(4.33)

$$= \frac{1}{\sqrt{\left(\frac{\lambda}{\eta_m}+2\eta_m\right)}}\int_{0}^{\varepsilon}\frac{d\eta'}{\sqrt{\eta'}\sqrt{1+\eta'\frac{1}{2\eta_m}\frac{\lambda-2\eta_m^2}{\lambda+2\eta_m^2}}}$$

To make the integral a bit more feasible, we compute the first-order Taylor expansion of the term about $\eta'=0$.

$$\left(1+\eta'\frac{1}{2\eta_m}\frac{\lambda-2\eta_m^2}{\lambda+2\eta_m^2}\right)^{-\frac{1}{2}} \approx 1-\frac{1}{4\eta_m}\frac{\lambda-2\eta_m^2}{\lambda+2\eta_m^2}\eta'$$

(4.34)

Plug this into the integral to get

94

$$\frac{1}{\sqrt{\left(\dfrac{\lambda}{\eta_m}+2\eta_m\right)}}\int_0^\varepsilon \frac{d\eta'}{\sqrt{\eta'}\sqrt{1+\eta'\dfrac{1}{2\eta_m}\dfrac{\lambda-2\eta_m^{\;2}}{\lambda+2\eta_m^{\;2}}}}$$

$$\approx \frac{1}{\sqrt{\left(\dfrac{\lambda}{\eta_m}+2\eta_m\right)}}\int_0^\varepsilon \frac{1}{\sqrt{\eta'}}\left(1-\dfrac{1}{4\eta_m}\dfrac{\lambda-2\eta_m^{\;2}}{\lambda+2\eta_m^{\;2}}\eta'\right)d\eta'$$

$$\approx \frac{\varepsilon^{\frac{1}{2}}}{\sqrt{\left(\dfrac{\lambda}{\eta_m}+2\eta_m\right)}}\left[2-\dfrac{1}{6\eta_m}\dfrac{\lambda-2\eta_m^{\;2}}{\lambda+2\eta_m^{\;2}}\varepsilon\right]$$

(4.35)

Plugging this approximation back into our expression for the integral yields:

$$\int_{\eta_\infty}^{\eta_m}\frac{d\eta}{\sqrt{1-\eta^2-\lambda\ln\dfrac{\eta_m}{\eta_\infty}}}=\int_{\eta_\infty}^{\eta_m-\varepsilon}\frac{d\eta}{\sqrt{1-\eta^2-\lambda\ln\dfrac{\eta_m}{\eta_\infty}}}+\frac{\varepsilon^{\frac{1}{2}}}{\sqrt{\left(\dfrac{\lambda}{\eta_m}+2\eta_m\right)}}\left[2-\dfrac{1}{6\eta_m}\dfrac{\lambda-2\eta_m^{\;2}}{\lambda+2\eta_m^{\;2}}\varepsilon\right]$$

(4.36)

In turn, substituting this integral into the expression for the deflection angle yields:

$$\chi=\pi-2\Delta\varphi$$

$$=\pi-2\sin^{-1}\eta_\infty-2\int_{\eta_\infty}^{\eta_m-\varepsilon}\frac{d\eta}{\sqrt{1-\eta^2-\lambda\ln\dfrac{\eta_m}{\eta_\infty}}}-\frac{2\varepsilon^{\frac{1}{2}}}{\sqrt{\left(\dfrac{\lambda}{\eta_m}+2\eta_m\right)}}\left[2-\dfrac{1}{6\eta_m}\dfrac{\lambda-2\eta_m^{\;2}}{\lambda+2\eta_m^{\;2}}\varepsilon\right]$$

(4.37)

4.3   Reference Tables

Since we cannot invert the previous integral to obtain an impact parameter as a direct function of a given deflection angle, we produce reference tables containing values of χ for a range of values of both b and λ. During our calculations, given a value of both b and λ, we can interpolate the corresponding value of χ.

4.3.1   Positive Tether

For very low values of λ, the positive tether's sheath produces deflection angles similar to those predicted by the soft-angle approximation. For extremely low values of λ, however, the total value of the deflection angle is dwarfed by the error in the integral approximation, resulting in negative values, though of negligible order.
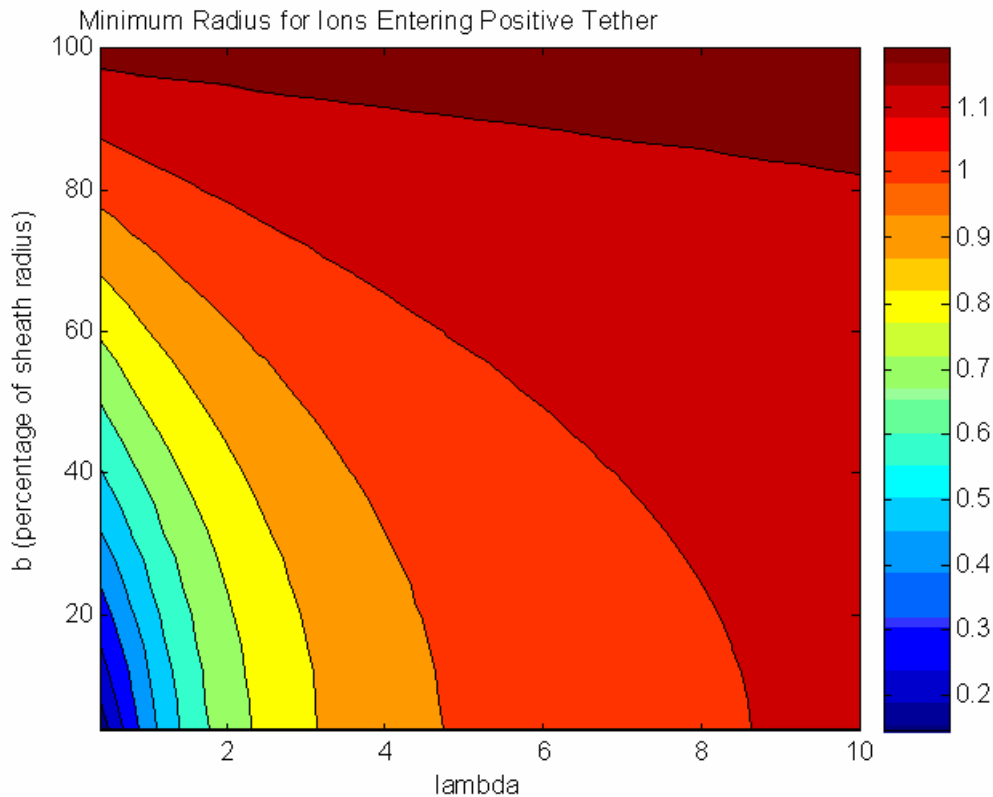
4.3.1.1 Positive Tether - Minimum Radius

Figure: 4-4: Minimum Radius, Positive Tether

For very low values of λ, the minimum distance approaches zero, as the incoming particles are deflected much more rapidly.
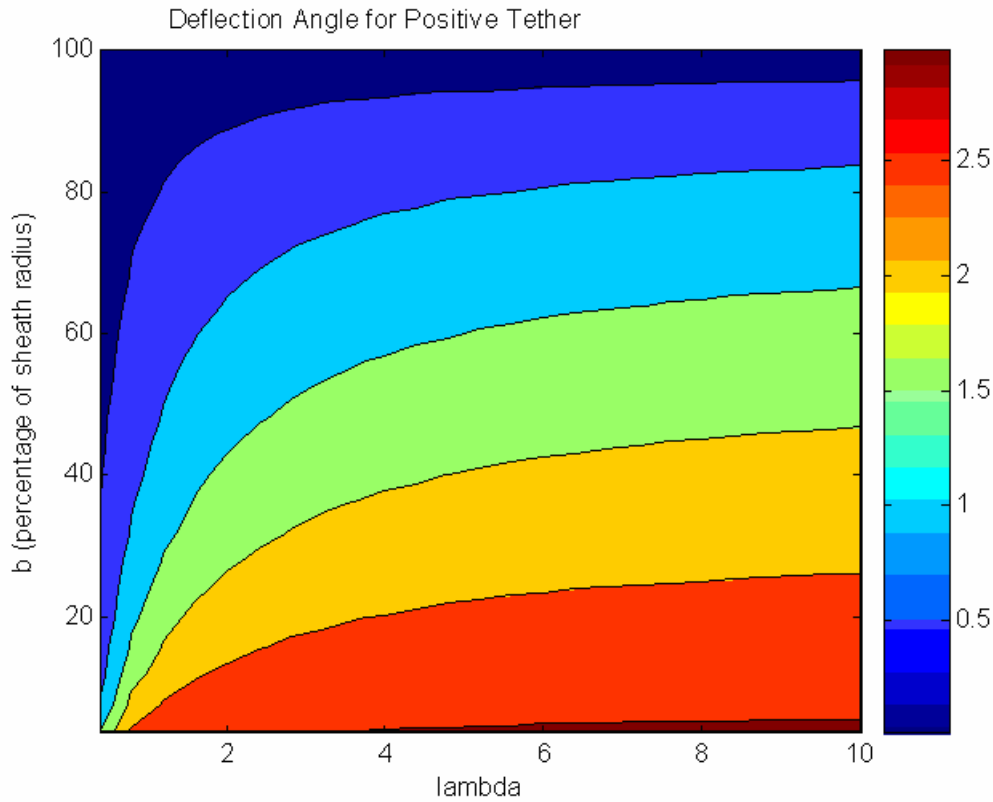
4.3.1.2 Positive Tether - Deflection Angle

Figure: 4-5: Deflection Angle, Positive Tether

For any given value of lambda, the smaller the impact parameter, the greater the deflection angle. This makes sense, since we expect the tether to produce a greater effect upon the ion when it makes a closer pass. For the further portions of the graph

4.3.1.3 Positive Tether - Deflection Angle Focused

The problem with this graph is that the high gradient of the deflection angle for low values of λ makes interpolation imprecise for low values of b and λ. Our solution is to adjust our sampling positions such that it is focused about the area of highest change. For b, we space our sampling points inverse-exponentially from b=0:
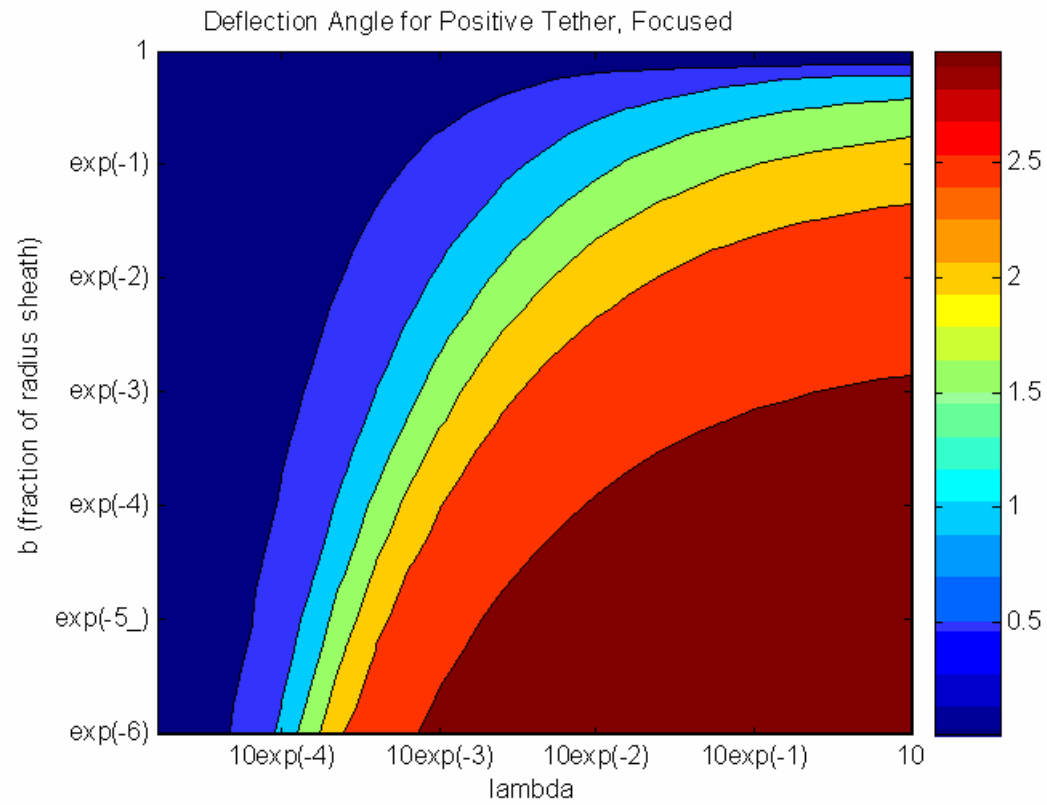
Figure: 4-6: Deflection Angle, Positive Tether, Focused

4.3.2   Negative Tether

4.3.2.1 Negative Tether – Minimum Radius

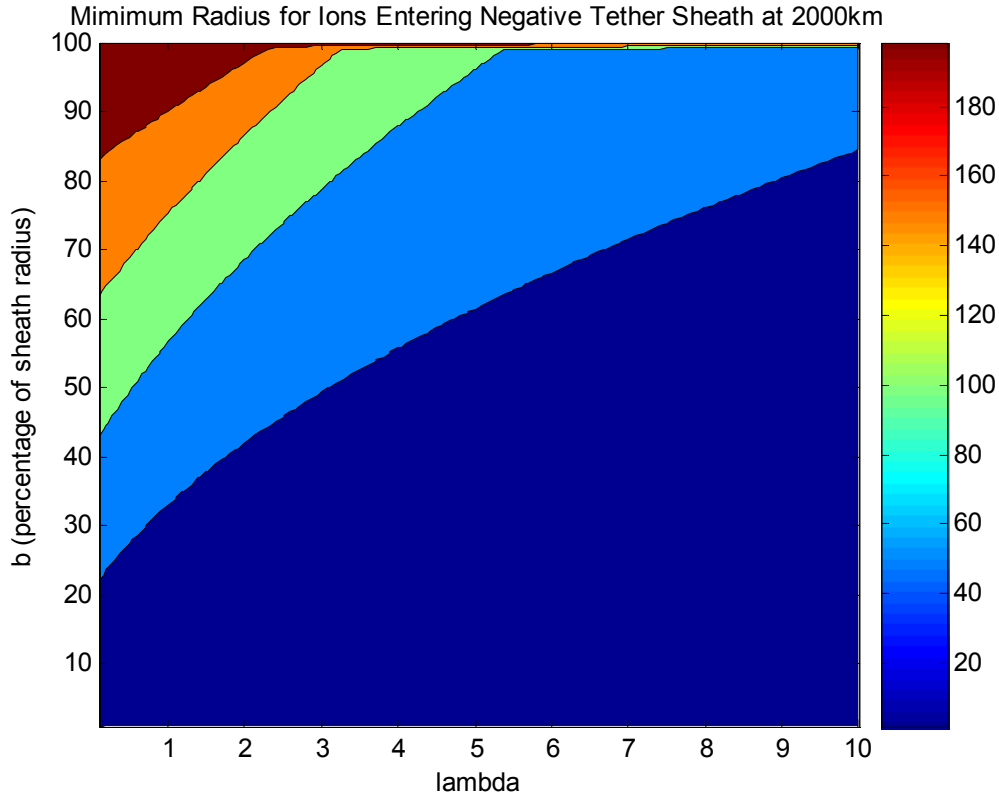First off, we look at the values of r_m:

Figure 4-7: Minimum Radius, Negative Tether

Naturally, since this is an attracting tether, the minimum radii will be much smaller than those for the positive tether. For very low values of λ (i.e. for ions with very high energy), the tether has little chance to exert a force on the ion, and thus the minimum radius approaches the initial impact parameter as λ approaches zero.

4.3.2.2 Negative Tether - Deflection Angle

When we attempt to replicate the data with the negative tether, we initially expect our results to be vaguely similar to our results to our positive tether, with smaller impact parameters resulting in deflection angles of larger magnitude, keeping in mind that the deflection angles will now be measured as negatives. However, when we calculate the deflection angle, we discover an unusual phenomenon: for any lambda, the deflection angle as a function of impact parameter is no longer monotonic.
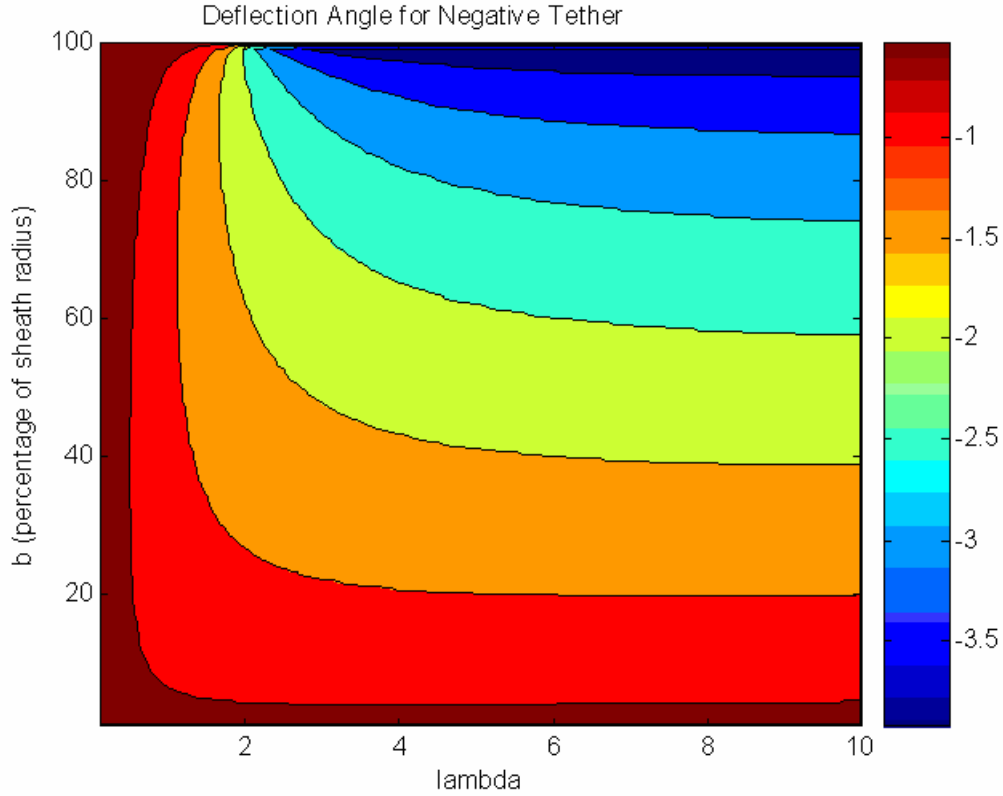
Figure 4-8: Deflection Angle, Negative Tether

For the lower values of λ, the deflection angle once again appears to obey the soft-body approximation and approach zero, yet it is apparent from the contour graph that the deflection angle magnitude first increases with increasing impact parameter and after some turning point starts decreasing again. This turning point appears to increase with λ. The scale of the graph makes the contour lines for high values of b difficult to read, but we know that for any finite value of lambda, the deflection angle must equal zero if the impact parameter equals the radius of the sheath. Assuming there are no discontinuities in the graph, that must mean that for every value of λ, there exists a value b_{max} such that the magnitude of the deflection angle is maximum for that value of λ. For low values of λ, this value is a fairly small fraction of the sheath radius. For larger values, the distance between this value and the sheath radius is tiny.

4.3.2.3 Negative Tether - Deflection Angle Focused

For computational purposes, we take an exponential-scale sample of the data to zoom in on the impact parameters closest to the radius sheath.
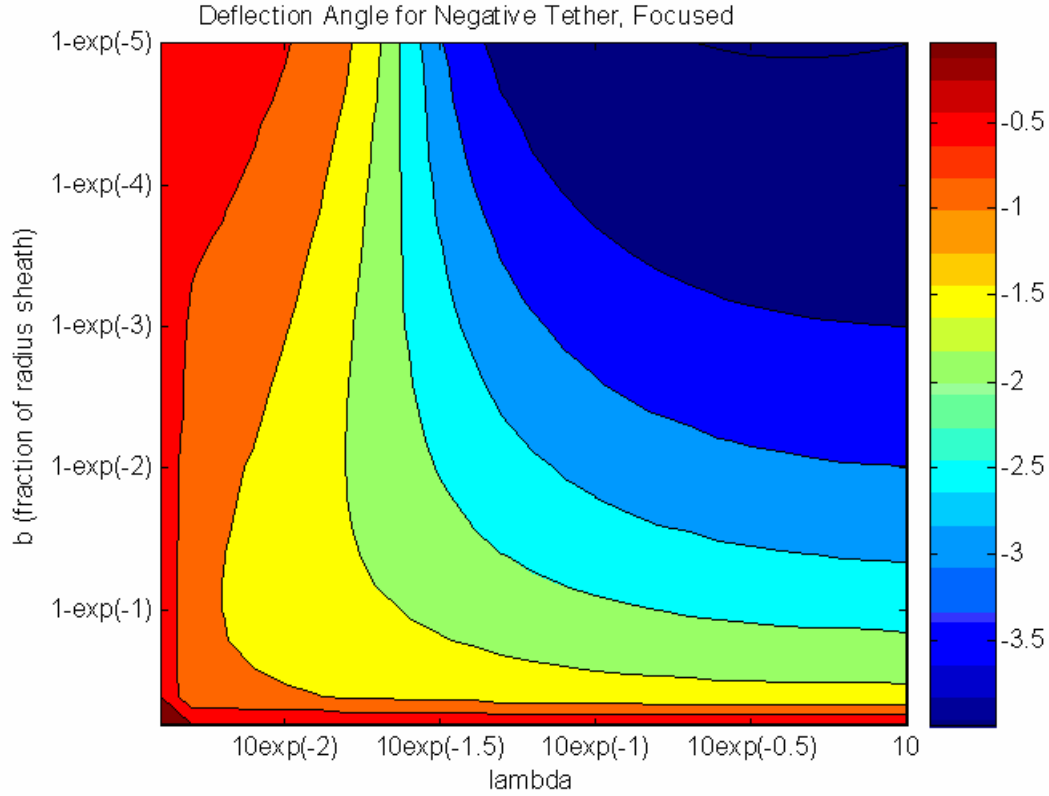
Figure 4-9: Deflection Angle, Negative Tether, Focused

The exponential close-up verifies our previous analysis, as we can now more clearly define the values of b_{max} for the lower values of λ. For high values of λ, even though we know b_{max} exists, it is even greater than our sampling increment closest to the sheath radius. When we compute the ranges for the tether, the range of b greater than b_{max} becomes negligible.

In order to determine the source of this odd behavior, we compare the above graphs of minimum radius and deflection angle. For a given λ, there exists some value b_{max} such that the maximum possible deflection angle is achieved. For $b_{low} < b_{max}$, the ion makes a closer pass to the tether, but the pass doesn't last as long. What appears to be happening is that because the ion has a lower value of b, more of the force exerted upon it by the tether is directed in the direction parallel to its velocity until it passes very close to the tether. For b_{max}, the tether potential exerts more force in the radial direction, translating into a weaker but longer-lasting centripetal force.

If you could position an ion directly into the sheath such that its velocity vector was exactly perpendicular to the radial direction, there would exist a value λ such that the force on the ion would be precisely equal to the centripetal force required for a stable orbit, and the ion's deflection angle would be infinite. We know this to be an impossible scenario for the ions in question because the only way an incoming ion can enter the sheath at precisely 90° would be if the impact parameter equaled the sheath radius, at

which point no deflection occurs at all. However, such a trajectory can be partly mimicked if the ion approaches the sheath at an angle and speed that maximizes angular acceleration while minimizing linear acceleration.
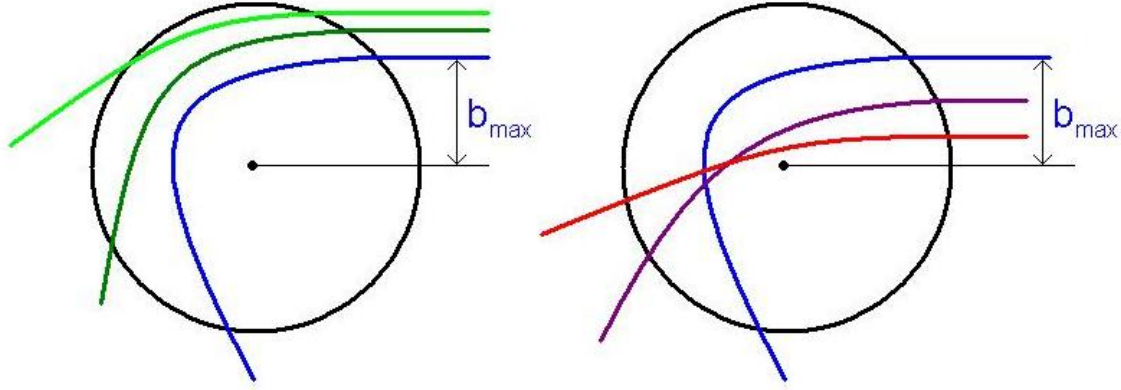

Figure 4-10: Maximum Impact Parameter

With this in mind, let us examine the integral for the deflection angle itself. Of particular note is the integral defining the angle transversed by the ion while within the sheath:

$$\Delta \varphi = \int_{r_m}^{\infty} \frac{b}{r^2} \frac{dr}{\sqrt{1 - \frac{b^2}{r^2} - \lambda \ln \frac{r_\infty}{r}}} \tag{4.38}$$

$$1 - \frac{b^2}{r_m^{\,2}} - \lambda \ln \frac{r_\infty}{r_m} = 1 - \frac{b^2}{r_m^{\,2}} + |\lambda| \ln \frac{r_\infty}{r_m} = 0$$

The larger this integral becomes, the greater the magnitude of the deflection angle becomes. Thus, let us examine how increases in b and λ affect the size of this integral.

The limits of the integral are r_m and ∞. Set λ as a constant. We already know that as b increases, r_m increases, and thus the range of integration decreases. However, if we look at the content of the integral, we see that an increase in b causes an increase in the integral's interior. Our adjustments in b thus produce two counteracting effects on the integral. Below b_{max}, the increasing effects dominate, and the integral increases with b. Above b_{max}, the limit restriction dominates, and the integral decreases with b.

Chapter 5

Results and Discussion

5.1   Tether Scattering Flux

For each of the tether altitudes, we have been able to calculate not only the total scattering flux per unit length of tether, but also the total influx of particles into the sheath per unit length. Thus we are able to compute not only the scattering flux of the entire tether, but also the efficiency of the tether. Note once again that we will be focusing specifically on the population of high-energy ions, as low-energy ions are of little concern to us, and our calculations cannot be used to determine electron fluxes accurately.

The first term we will evaluate will be the total flux of particles entering the sheath, which we shall call the sheath influx. We take our particle influx equation from 4.12 and obtain:

$$\Gamma_{\inf lux} = 8n \cdot \int_0^\infty \int_0^\infty \int_0^{\sin^{-1}\left(\frac{v\cos\alpha_L}{g}\right)} g^2 \cdot \frac{1}{\cos\alpha_L} \left(\frac{m}{2\pi kT}\right)^{\frac{3}{2}} e^{-\frac{m(g^2+v_z^2)}{2kT}} \cdot R_\infty \cdot L_T \cdot d\theta dg dv_z s^{-1}$$

(5.1)

Since we restricting our focus to only the population of high-energy particles, we set the temperature T to correspond to particles of the energy 1MeV, such that $T = 10^6 \cdot 11600$. The ambient density term in the distribution function could easily be extracted from the flux integral before calculation:

$$f_{LC}(v_z, g, \theta) = \frac{n}{\cos\alpha_L} \left(\frac{m}{2\pi kT}\right)^{\frac{3}{2}} e^{-\frac{m(g^2+v_z^2)}{2kT}}$$

(5.2)

Since separating the term proves useful for our analysis later, we display the particle influx as a product of the ambient density and the remaining integral, which is now just the volume influx, or γ:

$$\gamma_{\inf lux} = 8\int_0^\infty \int_0^\infty \int_0^{\sin^{-1}\left(\frac{v\cos\alpha_L}{g}\right)} g^2 \cdot \frac{1}{\cos\alpha_L} \left(\frac{m}{2\pi kT}\right)^{\frac{3}{2}} e^{-\frac{m(g^2+v_z^2)}{2kT}} \cdot R_\infty \cdot L_T \cdot d\theta dg dv_z m^3 s^{-1}$$

(5.3)

Substituting the sheath radii for each altitude at each tether potential yields the following volume influxes:

Altitude (km)	Volume Influx (m^3s^{-1})	Volume Influx(m^3s^{-1})
	Positive Tether	Negative Tether
2000	1.5153×10^{11}	2.9786×10^{13}
4000	1.4678×10^{11}	2.8819×10^{13}
6000	1.3792×10^{11}	2.7016×10^{13}
8000	1.3181×10^{11}	2.5775×10^{13}

Table 5-1: Volume Influx, Positive and Negative Tethers

As we increase the tether's altitude, the loss cone angle decreases, the effects of which are twofold. First, since we assume the velocities of all particles in the magnetosphere lie outside the loss cone, decreasing the loss cone angle increases the range of radial velocity g for the incoming ions. Since the flux incorporates an extra g term into the normalized distribution integral, the increased range of g makes for a greater range of angles for the ions to penetrate the sheath, thus increasing the flux. However, this effect is counteracted by the fact that the tether has to redirect incoming ions into a much smaller loss-cone, which it misses more frequently. That is, even though the total number of incoming particles increases with altitude, the total number that is actually scattered into the loss cone decreases.

To calculate the particle scattering flux, we similarly split up the integral into a product of the ambient density and the volume scattering flux:

$$\Gamma_{scatter} = \iiint_{\substack{Outside \\ Loss\,Cone}} g^2 \cdot f_{LC}(v_z, g, \theta) \cdot w_b(v_z, g, \theta) \cdot L_T \cdot dg\, d\theta\, dv_z\, s^{-1}$$

$$= n_\infty \iiint_{\substack{Outside \\ Loss\,Cone}} g^2 \cdot \frac{1}{\cos\alpha_L}\left(\frac{m}{2\pi kT}\right)^{\frac{3}{2}} e^{-\frac{m(g^2+v_z^2)}{2kT}} \cdot w_b(v_z, g, \theta) \cdot L_T \cdot dg\, d\theta\, dv_z\, m^3 s^{-1}$$

$$\Gamma_{scatter} = n_\infty \gamma_{scatter}$$

(5.4)

From this we derive our volume scattering fluxes:

Altitude (km)	Volume Scattering Flux Positive Tether (m^3s^{-1})	Volume Scattering Flux Negative Tether (m^3s^{-1})
2000	8.6978×10^9	1.8130×10^{12}
4000	3.9829×10^9	8.6175×10^{11}
6000	1.3792×10^{11}	4.4095×10^{11}
8000	1.3181×10^{11}	1.5059×10^{10}

Table 5-2: Volume Scattering Flux

We can also calculate the tether "efficiencies" by dividing the volume influx by the volume scattering flux for each altitude at each tether:

Altitude (km)	Efficiency (%) Positive Tether	Efficiency (%) Negative Tether
2000	5.74	6.09
4000	2.71	2.99
6000	1.45	1.63
8000	0.02	0.06

Table 5-3: Tether Efficiency

The most obvious result from our analysis is the rate at which tether efficiency is reduced as we increase altitude.

5.2   Remediation Time

To determine how long the tether would take to deplete a certain region of space, we first observe that its scattering flux is directly proportional to the ambient plasma density.

Assume we wish to thin a certain region of the magnetosphere by a factor of β (that is, reducing the magnetosphere's population to one-tenth its original value would translate to $\beta=10$). Say that the tether has a scattering flux of γn. Within a single unit of time, the

tether thus scatters γn ions. Now suppose we isolate the tether within a given volume V, which initially contains a total number of particles N, such that the ambient density is n. To calculate the depletion rate, we first calculate the factor by which the ambient density is reduced over a unit of time Δt. We start by defining the density before and after this unit of time:

$$n_i = \frac{N}{V}, \qquad n_f = \frac{\left(N - n\gamma_{scatter}\Delta t\right)}{V} \tag{5.5}$$

Now obtain Δn by subtracting the initial density from the final density:

$$\Delta n = n_f - n_i = \frac{\left(N - n\gamma_{scatter}\Delta t\right)}{V} - \frac{N}{V} = -\frac{\gamma \cdot n}{V}\Delta t \tag{5.6}$$

Divide by the given unit of time to obtain a differential equation defining the density:

$$\frac{dn}{dt} = \frac{\Delta n}{\Delta t} = -\frac{\gamma \cdot n}{V} \tag{5.7}$$

Integrate both sides to obtain

$$n = n_0 e^{-\frac{\gamma}{V} \cdot t} \tag{5.8}$$

Thus, we can define a target density we wish to achieve for this region, and the following tells us how long this goal will take:

$$e^{-\frac{\gamma}{V} \cdot t} = \frac{n_{final}}{n_0}$$

$$t = \frac{V}{\gamma}\ln\left(\frac{n_0}{n_{final}}\right)$$

$$\tag{5.9}$$

Now to define the region we wish to isolate. Since we are attempting to deplete the radiation belts via a tether traveling in the equatorial plane at a certain altitude, we limit our space to those magnetic field lines which intersect the equatorial plane near the

altitude of our satellite. We approximate the magnetic field lines of a given strength and altitude to form a torus around the Earth.

The volume of a torus is given by:

$$V_{torus} = 2\pi^2 R r^2 \qquad (5.10)$$

R is the radial distance from the torus center to its circular axis, and r is the radius about the circular axis. To approximate the shape of the magnetic field lines, we take both R and r equal to half the radius to the magnetic field line in question, or:

$$V_{torus} = \frac{1}{4}\pi^2 R_{eq}{}^3 \qquad (5.11)$$

If we want to determine the volume encompassed by the magnetic field lines that intersect the equatorial plane within a certain radial distance form our tether's orbit, we calculate the volume of the torus with the larger radius and subtract the volume of that of the smaller radius.

$$V_{mag} = \frac{1}{4}\pi^2 (R_{eq,outer}{}^3 - R_{eq,inner}{}^3) \qquad (5.12)$$

When we substitute (5.8) into our equation for mission time, we discover that density by itself plays no role in the total mission time, while the desired fraction depletion does.

$$t = \frac{1}{4\gamma}\pi^2 (R_{eq,outer}{}^3 - R_{eq,inner}{}^3)\ln(\beta) \qquad (5.13)$$

For a given altitude of tether orbit, let us define our target volume by the area covered by the magnetic field lines which intersect the equatorial plane at altitudes within a distance D of the tether orbit. Or:

$$R_{eq,outer} = R_{orbit} + D \qquad (5.14)$$
$$R_{eq,inner} = R_{orbit} - D$$

Substitute this into our time equation to get:

$$t = \frac{1}{4\gamma} \pi^2 ((R_{orbit} + D)^3 - (R_{orbit} - D)^3)\ln(\beta) \qquad (5.15)$$

Furthermore, the satellite possesses both positive and negative tethers, each of cumulative length 10 km. Thus, the term for the scattering rate is actually the sum of the rates from each tether, or:

$$t = \frac{1}{4(\gamma_+ + \gamma_-)} \pi^2 ((R_{orbit} + D)^3 - (R_{orbit} - D)^3)\ln(\beta) \qquad (5.16)$$

Let us suppose we restrict our toroidal space such that it covers only those magnetic field lines whose equatorial altitudes are directly intersected by the tether's orbital path; that is, we take D to equal 10km. If we wish to reduce the density within this isolated range to one-tenth of its original value (i.e. set β=10), we get the following times at various altitudes:

Altitude	T (sec)	T (years)
2000	1.3135×10^7	0.4165
4000	6.0330×10^7	1.9130
6000	2.0643×10^8	6.5458
8000	1.5722×10^{10}	498.54

Table 5-4: Mission Time: D = 10km

At low altitudes, the mission time falls to within approximately one year, so depleting this section of the magnetosphere seems a plausible task. At high altitudes, however, the mission time increases to outrageous proportions, so we might be better off setting out sights a bit lower.

Of course, these results are unrealistic in that we cannot cordon off the area of space surrounding those we have designated to be part of V without particles from the surrounding areas randomly scattering into it and repopulating it. Thus, let us expand our borders by a factor of 10 and define D = 100km. Our results are now:

Altitude	T (sec)	T (years)
2000	1.3135×10^8	4.1652
4000	6.0331×10^8	19.131

6000	2.0643×10^9	65.459
8000	1.5722×10^{11}	4985.5

Table 5-5: Mission Time: D = 100km

Expanding it to D = 1000km:

Altitude	T (sec)	T (years)
2000	1.3140×10^9	41.847
4000	6.0461×10^9	191.72
6000	2.0669×10^{10}	655.39
8000	1.5730×10^{12}	49878.

Table 5-6: Mission Time: D = 1000km

The volume increases roughly linearly as a result of our range expansion, so naturally the depletion time is also linearly increased as a result.

Chapter 6

Conclusion and Recommendations

6.1   Conclusion

The prospects of a single tether satellite depleting a substantial portion of the radiation belts now is temporally feasible for low altitudes around 2000km, but not for higher altitudes around 8000km. When designing missions for magnetospheric remediation of high-energy ions, a single tether should suffice for the low altitudes, but an array of several dozen satellites might be required for the higher altitudes.

However, even for the lower altitudes, the tether satellite can sustain depletion only for short spans of altitude. To deplete a range of altitude on the order of 1000km, one would need an array of satellites constantly functioning at varying altitudes. Note that we have yet to consider the effects of natural replenishment from cosmic neutrons, so our estimates would appear to be best-case scenarios which must be tempered with future research.

Regarding the implausibility of remediation missions at higher altitudes, on of the greatest hindrance is the loss cone angle, which gets terribly narrower as we increase altitude, resulting in reduced efficiency, especially above 6000km. At the higher altitudes, even if every particle to interact with the tether satellite were to be deflected into the loss cone, the number of particles to be deflected would still require at least decades for the remediation requirements missions we wish to fulfill. Also, while our calculations do not consider possible influx rate increases as a result of our tether's orbital velocity, yet any increase of influx on the ram end would likely be offset at least in part by a wake on the tail end, so any net gain in scattering rate would not in itself deem feasible any high-altitude missions.

One method of rendering high-altitude tethers more efficient would be to increase the sheath size, which would necessitate increasing either the sheath radius or the sheath length. Increasing the latter is a simple matter of increasing the overall length of the tether, but the resulting increase in ion influx would be linear. If we wanted to increase the ion influx by two orders of magnitude, we would increase the tether length similarly, from a 10-km tether to a 1000-km tether. Since the tether radius term is logarithmic while the tether potential term is not, changes in the latter overshadow changes in the former. Furthermore, the added tether length would also result in increases in charge collection, which would increase the deforming Lorentz forces and reduce the tether radius.

If we choose to increase the sheath radius, we still encounter problems when considering the power and structural limitations. Increasing the tether potential by several orders of magnitude would easily increase the sheath radius to a more acceptable size, but the tether radius would have to be reduced by an even greater factor to compensate for the power limitation:

$$r_T \leq \frac{P_{\max}}{n_\infty L} \sqrt{\frac{m_i}{-2\left(e\Phi_T{}^-\right)^3}} \tag{6.1}$$

Increasing the tether potential by a factor of 100 thus decreases the tether radius by a factor of 1000, making our tether radius roughly 0.5μm. Our design for a 0.5mm tether was tenuous enough as was, even if our design employed tungsten steel, but if our tether is meant to connect two 100-kg power supplies, 0.5-μm is much, much more likely to snap. We could increase the tether radius by also decreasing the length of the tether, but that would linearly reduce the size of the sheath, and the ion influx, thus defeating our intended purpose.

6.2   Recommendations

For future research, we would recommend several avenues for increasing the efficiency of scattering tether mission designs. If one were to employ the series tether design outlined in this thesis and expect a feasible mission plan, one would be required to analyze different models for tether arrays in various orbits and maximize their cumulative depletion rates. One should also analyze and compare various other designs, including tether-clusters and tape tethers, to determine the most efficient and effective scattering methods. Further research is also required to determine the effects of each of these tether designs upon the natural replenishment rates of the radiation belts.

Whichever tether design one should settle upon, one must also determine the feasibility of its design with regards to structural mechanics. Our analysis of Lorentz forces upon the series tether concludes that non-negligible forces are exerted lengthwise on either end of the tether, and whatever material is used to construct the satellite must be able to hold its shape under these forces for consistent scattering operation. We calculated our scattering rates on the assumption that a 0.5-mm tether could survive collisions with heavy ions and cosmic debris, but this assumption must be verified before we can cast away the concern that the tether may snap too easily once deployed. We also assumed that attaching two 100-kW power supplies to the series tether was a plausible design, yet this electronic configuration must too be verified for feasibility over long periods of time.

Bibliography

[1] J.E. Allen, "Probe Theory – The Orbital Motion Limited Approach", *Physica Scripta*, vol. 45, 1992, pp. 497-503.

[2] P.A. Webb, *Electron Density Measurements of the Plasmasphere – experimental observations and modeling studies*, tech. report, Cooperative Research Centre for Satellite Systems, La Trobe Univ., 2000.

[3] J.M Deux, *Kinetic Modeling of Electrodynamic Space Tethers*, master's thesis, Dept. Aeronautics and Astronautics, Massachusetts Institute of Technology, 2004.

[4] Choiniere, Theory and Experimental Evaluation of a Consistent Steady-State Kinetic Model for 2-D Conductive Structures in Ionospheric Plasmas, 1999

[5] M.H. Denton, G.J. Bailey, Y.Z. Su, K.I. Oyama, T. Abe, "High altitude observations of electron temperature and a possible north-south asymmetry," *Journal of Atmospheric and Solar-Terrestrial Physics*, vol. 61, 1999, pp. 775-788.

[6] G. V. Khazanov, N. H. Stone, E. N. Krivorutsky, K. V. Gamayunov, and M.H. Liemohn, "Current-induced magnetic field effects on bare tether current collection: A parametric study," *Journal of Geophysical Research*, vol. 106, no. A6, June 2001, pp. 10565-10579.

[7] J.D. Huba, *2004 revised NRL plasma formulary*, The Office of Naval Research, 2004.

APPENDIX 3: PITCH DIFFUSION BY RESONANT INTERACTION WITH WHISTLERS

Radiation Belt Remediation methods

In order to reduce the density of energetic particles inside the radiation belts we have to make them enter their loss cone. There are three ways of doing so, or any combination of them:

- To increase their parallel energy / momentum.

- To reduce their perpendicular energy / momentum.

- To reduce their incidence, rotating their velocity without any change in their energy.

The use of space tethers for modifying the particles' trajectories has already been considered. We can distinguish between two main approaches.

The first is using high voltage electrostatic tethers. The electric potential around the tether deviates the particles, making some of them enter their loss cone. The tether's orbital motion allows it to cover a significant volume inside the magnetosphere. A preliminary study for such a system has already been done [*Christopher F. Zeineh*], and it shows how the characteristic time for remediation is of the order of the year for a 10 kW system at an altitude of L=2. For higher values of L the effectiveness of the system decreases quite dramatically.

The second, which is the main objective of this preliminary study, is to use space tethers as VLF/ELF antennas. These antennas emit whistler waves which can perturb the motion of the energetic trapped particles, creating a net diffusion towards their loss cone and thus removing them from the radiation belts. We expect the characteristic remediation times to be significantly smaller, since such a system does not act at a local but at a global scale.

Theoretical Background

In this chapter we will analyze the wave-particle interaction process and explain what will be the theoretical frame used to solve the problem and obtain the characteristic precipitation time.

<u>**Electron cyclotron waves**</u>

The first idea that comes to our mind to perturb the energetic particles' motion is to emit waves at the resonant frequency of their Larmor motion. In doing so, the electric and magnetic fields seen by the particles will be quasi-static and there will be a significant energy exchange between both of them. But, since this frequency is independent of the particle's energy, this is not a good idea. Using these waves, the background plasma, with a density several orders of magnitude higher and energies of the order of 0.4 eV, will absorb them, and such a system will do nothing but heating this plasma.

To verify the importance of this dumping, we've taken this dispersion relation, given by the kinetic theory of plasma perturbations

$$n^2 = 1 + \frac{\omega_{pe}^2}{\omega k v_e} Z\left(\frac{\omega - \Omega_e}{k v_e}\right) \tag{2.1}$$

and, being the background plasma non relativistic, we can consider their mean velocity as

$$v_e \cong \sqrt{\frac{2k_B T_e}{m_e}} \tag{2.2}$$

The plasma dispersion function can be approached by the following development, because we are near the cyclotron frequency

$$\omega \approx \Omega_e \rightarrow \varsigma = \frac{\omega - \Omega_e}{k v_e} \ll 1 \rightarrow Z(\varsigma) \approx i\sqrt{\pi} - 2\varsigma \tag{2.3}$$

and the dispersion relation can thus be written

$$1 - \frac{\omega \cdot \omega_{pe}^2}{\left(k^2 c^2 - \omega^2\right) k v_e}\left(i\sqrt{\pi} - 2\frac{\omega - \Omega_e}{k v_e}\right) = 0 \tag{2.4}$$

To obtain an estimate of the penetration distance of the waves inside the background plasma, we consider complex solutions for the equation (2.4). The inverse of the

imaginary part of the wave number corresponds to a characteristic penetration length. Solving equation (2.4) is equivalent to obtaining the roots of the following complex polynomial.

$$\xi^4 - v^2\xi^2 - i\sqrt{\pi}\left(\frac{\omega_{pe}}{\Omega_e}\right)^2\left(\frac{c}{v_e}\right)v\xi + \left(\frac{\omega_{pe}}{\Omega_e}\right)^2\left(\frac{c}{v_e}\right)v(v-1) = 0 \qquad (2.5)$$

where the variables are

$$\xi = \frac{kc}{\Omega_e}, \quad v = \frac{\omega}{\Omega_e} \qquad (2.6)$$

Obtaining the roots for L=2 and frequencies near the cyclotron one, we've plot the results and we see that after some tens of meters, the waves are absorbed by the background plasma.
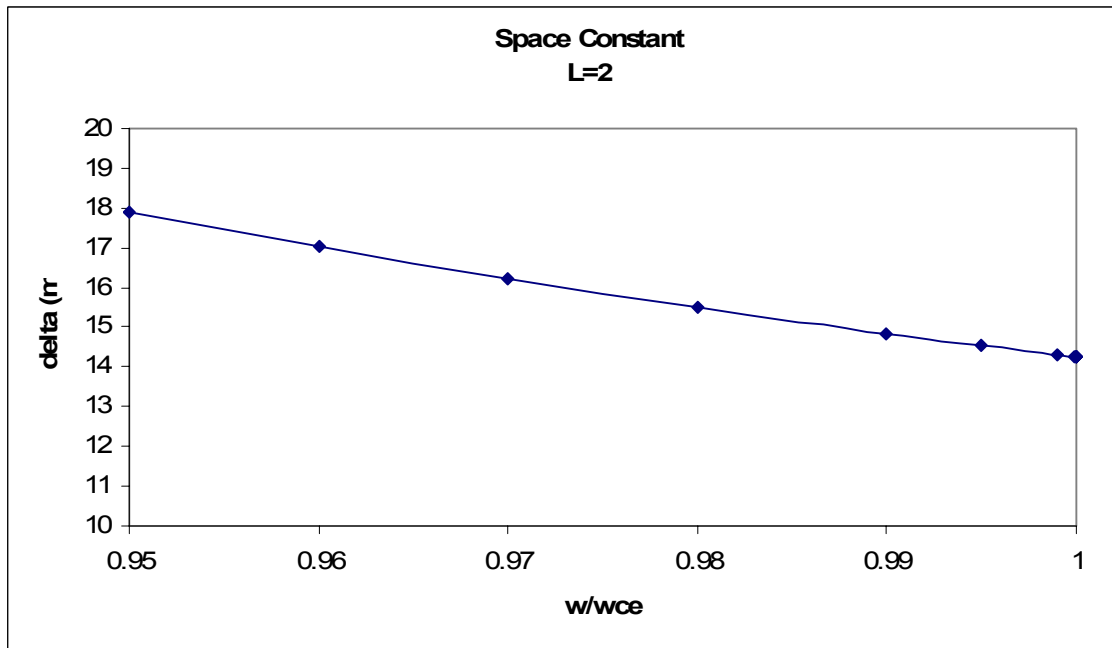
Figure 2-1. Characteristic penetration distance for an electron cyclotron wave as a function of its frequency for L=2

The use of such waves is of no interest at all, because all the power is used to heat the background plasma, instead of perturbing the motion of the more energetic particles.

VLF/ELF emissions

Low frequency modes, like the whistlers, can induce particles' precipitation. In nature, these modes can be excited by lightning, but we can emit such waves with antennas of the proper length. The influence of this and other low frequency modes on the magnetospheric particles' distribution, and its possible use for radiation belt remediation, has already been considered in several studies like [*Abel & Thorne, 1998*] and [*Inan, Bell, Bortnik & Albert, 2003*]. We will see now how to calculate the effects of such waves on the energetic populations of the ionosphere.

Cyclotron resonance

The wave particle interaction at low frequencies can be explained by the existence of Doppler resonances. To obtain the resonance condition, we can start by writing the motion equations for an electron under the influence of the electric and magnetic fields of an electromagnetic wave. The electrons considered are relativistic because their energies are of the order of 1 MeV. Once we take into account the magnetic moment conservation

$$\frac{p_\perp^2}{B_0} = cste \tag{2.7}$$

and if we take the z axis as the direction of the Earth's magnetic field, we obtain

$$
\begin{aligned}
\frac{dp_\parallel}{dt} &= -\frac{eB_w}{m_e\gamma}p_\perp \sin\varphi + \frac{p_\perp^2}{2\Omega_e m_e\gamma}\frac{\partial\Omega_e}{\partial z} \\
\frac{dp_\perp}{dt} &= \frac{eB_w}{m_e\gamma}\left(p_\parallel - \frac{\omega}{k}m_e\gamma\right)\sin\varphi - \frac{p_\perp p_\parallel}{2\Omega_e m_e\gamma}\frac{\partial\Omega_e}{\partial z} \\
\frac{d\varphi}{dt} &= \frac{\Omega_e}{\gamma} - \omega + k\frac{p_\parallel}{m_e\gamma} + \frac{eB_w}{m_e\gamma}\left(p_\parallel - \frac{\omega}{k}m_e\gamma\right)\frac{\cos\varphi}{p_\perp}
\end{aligned}
\tag{2.8}
$$

here, the angle between the perpendicular momentum and the wave's magnetic field , B_w , is $\pi - \varphi$.

If the electrons' motion is to be modified significantly by the wave's fields, their effect must cumulate for a certain period of time, and the resonance condition must be

$$\dot{\varphi} \cong 0 \tag{2.9}$$

so that the electron does not see rapid oscillating fields, which mean effect is negligible. The last term of the third equation in (2.8), which gives the change in the phase angle, is negligible for the conditions given in the Earth's magnetosphere. Therefore

$$\omega - k\frac{p_\parallel}{m_e\gamma} = \frac{\Omega_e}{\gamma} \tag{2.10}$$

and (2.10) will we used as resonance condition for all our calculations.

Cyclotron waves whose frecuency is small in comparison with the electron gyrofrequency, Ω_e, can thus resonate with the energetic particles, perturbing their motions in a significant way. The particles' pitch angle will change stochastically, some times it will increase and other it will decrease, depending on the phase angle value at the moment of the interaction. Nonetheless, given the fact that the distribution is a hollow one, because of the loss cone, there are more particles with higher values of pitch angle, and there will be a net diffusion towards the loss cone.

Quasilinear Theory

The instabilities' saturation process inside a plasma can be described as a continuous diffusion in the velocity space, in which a zero order distribution function evolves slowly. The diffusion rate is proportional to the sum of the squares of the modes obtained by the linear theory, thus the name of quasilinear theory. When applying this theory we are making implicitly two assumptions:

First, the amplitudes of the perturbations must be small enough. For small enough we understand that the results obtained for the zero order distribution function given by the linear theory must be correct. We will average this distribution function in space $f_0(\vec{v},t) = \langle f_0(\vec{r},\vec{v},t) \rangle$.

Second, the wave spectrum must be dense enough so that any coherence between the different modes is destroyed by phase mixing in the time scale of the plasma parameters variation.

If we start from the Vlassov equation for the plasma

$$\frac{\partial f}{\partial t} + \vec{v}\cdot\nabla f + \frac{q}{m}\nabla_{\vec{p}}\cdot\left[\left(\vec{E}+\frac{\vec{v}\times\vec{B}}{c}\right)f\right]=0 \tag{2.11}$$

we can average it over a certain number of periods in space and time, and also we can average it over the gyro motion around the Earth's magnetic field, $\vec{B}_0$. Doing so, we can rewrite (2.11) under this new form [*Kennel & Engelmann, 1966*]

$$\frac{\partial f_0}{\partial t} = \lim_{V\to\infty}\int\frac{d^3\vec{k}}{(2\pi)^3 V}\frac{\pi q^2}{m^2}\sum_{n=-\infty}^{\infty}\left[\hat{G}_k+\frac{\omega_k-k_\parallel v_\parallel}{\omega_k v_\perp}\right]\delta(k_\parallel v_\parallel+n\Omega-\omega_k)|\theta_{nk}|^2\hat{G}_k f_0$$

$$\hat{G}_k = \frac{\partial}{\partial v_\perp}-\frac{k_\parallel}{\omega_k}\left(v_\parallel\frac{\partial}{\partial v_\perp}-v_\perp\frac{\partial}{\partial v_\parallel}\right) \tag{2.12}$$

$$\theta_{nk} = \frac{E_{k,R}J_{n+1}+E_{k,L}J_{n-1}}{\sqrt{2}}+\frac{v_\parallel}{v_\perp}E_{k,\parallel}J_n$$

And after some math, we arrive to a diffusion equation for $f_0(E,L,t,\alpha_0)$. Because of the conditions given in our case of interest, the energy exchange between waves and particles is negligible, and the diffusion equation simplifies into a pure diffusion equation for pitch angle.

$$\frac{\partial f_0}{\partial t}=\frac{1}{\sin 2\alpha_0 T(\alpha_0)}\frac{\partial}{\partial\alpha_0}\left(\sin 2\alpha_0 T(\alpha_0)D_{\alpha\alpha}(\alpha_0)\frac{\partial f_0}{\partial\alpha_0}\right) \tag{2.13}$$

In (2.13) we cannot see any source of particles. That is the case for an artificial radiation belt, created for instance by means of a nuclear detonation at high altitude. If we wanted to study the dynamics of the natural radiation belts, the Van Allen belts, we would need to model the particles' sources, but this is out of the scope of this study. But for the case of the inner Van Allen belt, equation (2.13) could be taken as an approximation, for the dynamics of its sources are very slow.

To solve (2.13), the easiest way is to assume that we can separate both variables, time and pitch angle

$$f_0(t,\alpha_0)=N(t)g(\alpha_0) \tag{2.14}$$

N represents the equatorial electron density, for a given value of L and E, and g gives us the shape of the distribution in pitch angle. We consider the density to be constant along

the field lines, and g constant along the time evolution of the distribution, or at least that the shape of the distribution changes very slowly in comparison with the density

$$\frac{1}{N(t)}\frac{dN(t)}{dt} = \frac{1}{\sin 2\alpha_0 T(\alpha_0)g(\alpha_0)}\frac{d}{d\alpha_0}\left(\sin 2\alpha_0 T(\alpha_0)D_{\alpha\alpha}(\alpha_0)\frac{dg(\alpha_0)}{d\alpha_0}\right) = \frac{-1}{\tau} \quad (2.15)$$

here τ is the characteristic time scale for the equation, at it is representative of the time needed to clean the L shell in which we find our antenna

$T(\alpha_0)$ is an approximate function which gives us the bounce period as a function of the equatorial pitch angle, taking the Earth's magnetic field as dipolar.

$$T(\alpha_0) = 1.3802 - 0.3198\left(\sin\alpha_0 + \sqrt{\sin\alpha_0}\right) \quad (2.16)$$

Several authors [*Lyons & Thorne, 1972*], [*Abel & Thorne, 1998*], solve (2.15) using iterative methods. Nevertheless, these methods can give some convergence problems if the diffusion coefficient approaches zero for certain pitch angle values.

That is why we have decided to rewrite the problem under the form of an eigenvalue problem.

$$M \cdot g = \frac{-1}{\tau}g$$

$$M = \left[\left(\frac{2D_{\alpha\alpha}}{\tan 2\alpha_0} + \frac{dT}{d\alpha_0}\frac{D_{\alpha\alpha}}{T} + \frac{dD_{\alpha\alpha}}{d\alpha_0}\right)\frac{d}{d\alpha_0} + D_{\alpha\alpha}\frac{d^2}{d\alpha_0^2}\right] \quad (2.17)$$

The operator's matrix dimension is equal to the number of pitch angles chosen to discretize the electrons' distribution function. In principle, the negative eigen value which yields the shortest precipitation time is the one we are looking for, and its corresponding eigen vector, the distribution in pitch angle, g.

But numerical instabilities can make more difficult the identification of the eigen value we are looking for. In this case, easily identifiable if the corresponding g does not satisfy the conditions, we have to verify each one of the eigen values, in a process that can be very time consuming.

We have to impose two boundary conditions to g. The first one is that the distribution function must be zero at the loss cone. The second one is that the distribution function must be symmetrical with respect to $\dfrac{\pi}{2}$

$$g\left(\alpha_{0,LC}\right) = 0$$

$$\left. \frac{dg}{d\alpha_0} \right|_{\alpha_0 = \frac{\pi}{2}} = 0 \tag{2.18}$$

Diffusion Coefficients

To solve (2.16) we need to know the diffusion coefficient as a function of the equatorial pitch angle. This coefficient will be the sum of the coefficients for each resonance.

$$D_{\alpha\alpha}(\alpha_0) = \sum_r D_r(\alpha_0) \qquad r = 0,\pm1,\pm2,... \tag{2.19}$$

Here $r = 0$ corresponds to the Landau resonance. The value of the bounce averaged Landau coefficient can be obtained trough

$$D_0(\alpha_0) = \frac{A}{T(\alpha_0)\cos^2\alpha_0} \int_0^{\lambda_m} \frac{\sqrt{\pi}}{2} \frac{B_w^2}{B^2} \frac{\Omega_e^2}{\gamma^2\omega} W_0 \cos\alpha \cdot \sin^4\alpha \cdot \cos^7\lambda \, d\lambda \tag{2.20}$$

A is a normalization constant that can be calculated if we take the energy of the wave to be distributed in frequency and propagating angle following a Gaussian.

$$B_w^2 \propto e^{-\left(\frac{\omega-\omega_m}{\delta\omega}\right)^2} \cdot e^{-\left(\frac{\tan\theta-\tan\theta_m}{\tan\delta\theta}\right)^2} \tag{2.21}$$

We call θ the angle between the wave vector, $\vec{k}$, and the local magnetic field. The rest of the parameters needed to determine the Gaussians are defined by the emitter properties.

The value for this constant is

$$A = \frac{\omega_m}{\delta\omega} \left[\int_1^\infty \exp\left[-\left(\frac{\sqrt{x^4-1}-\tan\theta_m}{\tan\delta\theta} \right)^2 \right] dx \right]^{-1} \left[1 + erf\left(\frac{\omega_m - \omega_{LC}}{\delta\omega} \right) \right]^{-1} \tag{2.22}$$

where we have introduced a new variable, $x = \tan\theta$, and an low frequency cut off at ω_{LC}.

W_0 is the weighting function for the Landau resonance.

$$W_0 = \int_0^{x_{max}} \exp\left[-\left(\frac{\omega - \omega_m}{\delta\omega} \right)^2 \right] \Psi(\theta)\Phi_0(\theta)\sin\theta\sqrt{\cos\theta} \, dx \tag{2.23}$$

where

$$\Psi(\theta) = \exp\left[-\left(\frac{x - \tan\theta_m}{\tan\delta\theta}\right)^2\right]$$

$$\Phi_0(\theta) = \left(\cos\theta \cdot J_1 - \frac{\omega}{\Omega_e}\cot\alpha\sin\theta \cdot J_0\right)^2$$

(2.24)

and J_i are Bessel functions of the first kind, whose argument is $\left[\gamma\dfrac{\omega}{\Omega_e}\tan\alpha \cdot x\right]$

The integration limit is

$$x_{max} = \tan\left[\arccos\left[\gamma^2\left(\frac{\omega_{LC}}{\omega_m}\right)\left(\frac{P_{\parallel,m}}{P_\parallel}\right)^2\left(\frac{\omega_m}{\Omega_e}\right)^2\right]\right]$$

(2.25)

and this limit allows us to avoid all the frequencies under de cut off. All these expressions depend on two different linear momenta. The first is the particles' linear momentum parallel to the local magnetic field

$$P_\parallel = P\cos\alpha$$

(2.26)

The second is the parallel momentum required for the first order resonance, $P_{\parallel,m}$. We can obtain the latter trough the general resonance condition

$$\omega - k_\parallel v_\parallel = -\frac{r\Omega_e}{\gamma}$$

(2.27)

For the first order resonance, r = -1

$$\omega_m - \frac{n\omega_m}{c}\cos\theta_m\frac{P_{\parallel,m}}{\gamma m_e} = \frac{\Omega_e}{\gamma} \rightarrow P_{\parallel,m} = \frac{(\Omega_e + \gamma\omega_m)\cdot m_e c}{n\omega_m\cos\theta_m}$$

(2.28)

Finally, all the expressions that must be integrated in W_0 should be evaluated for a frequency obtained from the Landau resonance condition

$$\frac{P_\parallel}{P_{\parallel,m}} = \gamma\left(\frac{\omega_m}{\Omega_e}\right)\sqrt{\frac{\omega}{\omega_m}}\sqrt{\frac{\cos\theta_m}{\cos\theta}}$$

(2.29)

For the rest of the resonances, the bounce averaged diffusion coefficient can be obtained as follows

$$D_r(\alpha_0) = \frac{A}{T(\alpha_0)\cos^2\alpha_0} \int_0^{\lambda_m} \frac{\sqrt{\pi}}{2} \frac{B_w^2}{B^2} \frac{\Omega_e}{\gamma} \frac{P_{\parallel,m}}{P_\parallel} W_r \cos\alpha \cos^7\lambda \, d\lambda \qquad (2.30)$$

And the weighting functions are slightly different from their Landau's counterpart

$$W_r = \int_{x_{min}}^{\infty} \sqrt{\frac{\omega}{\omega_m}} \exp\left[-\left(\frac{\omega-\omega_m}{\delta\omega}\right)^2\right] \Psi(\theta)\Phi_r(\theta)\sin\theta \, dx \qquad (2.31)$$

where

$$\Phi_r(\theta) = \frac{1}{4}\left[(1+\cos\theta)\cdot J_{r+1} + (1-\cos\theta)\cdot J_{r-1}\right]^2 \qquad (2.32)$$

the argument of the Bessel functions is now $[r\tan\alpha\cdot x]$, and to avoid taking into account the effect of frequencies below the cutoff, we have to limit the integration from

$$x_{min} = \tan\left[arc\sec\left[\frac{\omega_{LC}}{\omega_m}\left(\frac{P_\parallel}{P_{\parallel,m}}\right)^2\frac{1}{r^2}\right]\right] \qquad (2.33)$$

Finally, all the parameters involved in the integration of the weighting function W_r must be evaluated for the corresponding resonant frequency.

Modeling

In this chapter we will analyze the different models used to implement the theoretical expression given in the preceding chapter in a computational code.

Environment

Earth's Magnetic Field

For the sake of simplicity we have considered the Earth's magnetic field in the radiation belt region as that of a centered magnetic dipole aligned with the Earth's rotation axis so that the magnetic South Pole is located on the Earth's geographical North Pole.

$$\vec{B} = \frac{\mu_0}{4\pi} \cdot \frac{1}{r^3} \cdot \left(3 \cdot \left(\vec{M}_T \cdot \vec{u}_r\right) \cdot \vec{u}_r - \vec{M}_T\right) \tag{3.1}$$

here $\vec{M}_T$ is the Earth's magnetic dipole. The strength of the field is

$$B = \frac{\mu_0}{4\pi} \frac{M_T}{r^3} \sqrt{1 + 3\sin^2 \lambda} \tag{3.2}$$

where λ is the latitude. Using polar coordinates, where the latitude acts as the polar angle, we obtain the polar equation for the force lines

$$r = R_0 \cos^2 \lambda \tag{3.3}$$
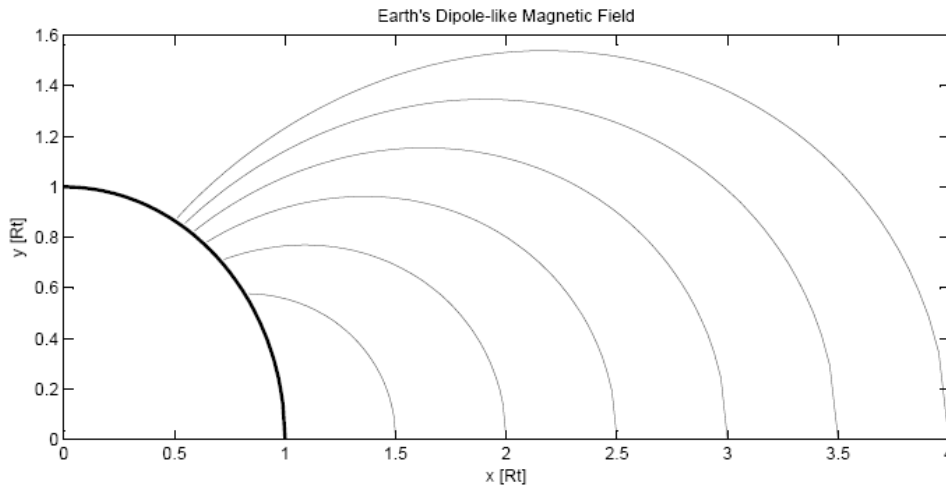
Figure 0-1. Near Earth's magnetic field topology, according to the dipolar approximation considered.

R_0 is the radial distance at the equator. Using this relationship, we find a more convenient expression for the field strength, in which we will introduce the McIlwain's shell parameter, L, which at the magnetic equator corresponds to the radial distance from the Earth's center expressed in units of Earth radii, and labels the dipole field lines (in a multipole field that is no longer the case).

$$B = \frac{\mu_0}{4\pi} \frac{M_T}{L^3} \frac{\sqrt{4 - 3\cos^2 \lambda}}{\cos^6 \lambda} \tag{3.4}$$

And this one will be the expression used within our calculation, with $M_T = 8.05 \cdot 10^{22} \ Am^2$.

Background Plasma

We will consider the ionospheric background plasma to be cold and with only two components, electrons and protons.

Density

It is hardly possible to give an analytical expression for the background plasma density as a function of its dependences on the various parameters. It is necessary therefore to use empirical values or numerical models, specifying the different conditions under their use. As we are working with a quasi-analytical model, we've tried to model the plasma density as simple as possible. Nevertheless, the modular structure of the code makes it easy to use different models instead, and compare the different results obtained with them.

We've taken the density to be constant along field lines, which is consistent with diffusive equilibrium, at least not far from the equator. The equatorial density has been obtained trough.

$$N(z) = N_0 \frac{z_0}{z} \exp\left[\frac{g_0 M_0 z_0}{2kT_0} \left(\frac{1}{1 + R_T/z} - \frac{1}{1 + R_T/z_0} + \ln \frac{1 + R_T/z}{1 + R_T/z_0} \right) \right] \tag{3.5}$$

where z is the altitude, k is the Boltzmann constant, M_0 is the ion mass (in this case the proton mass) and the subscript 0 in the other quantities refers to their value at a reference altitude of $z_0 \cong 10^3 \ km$.
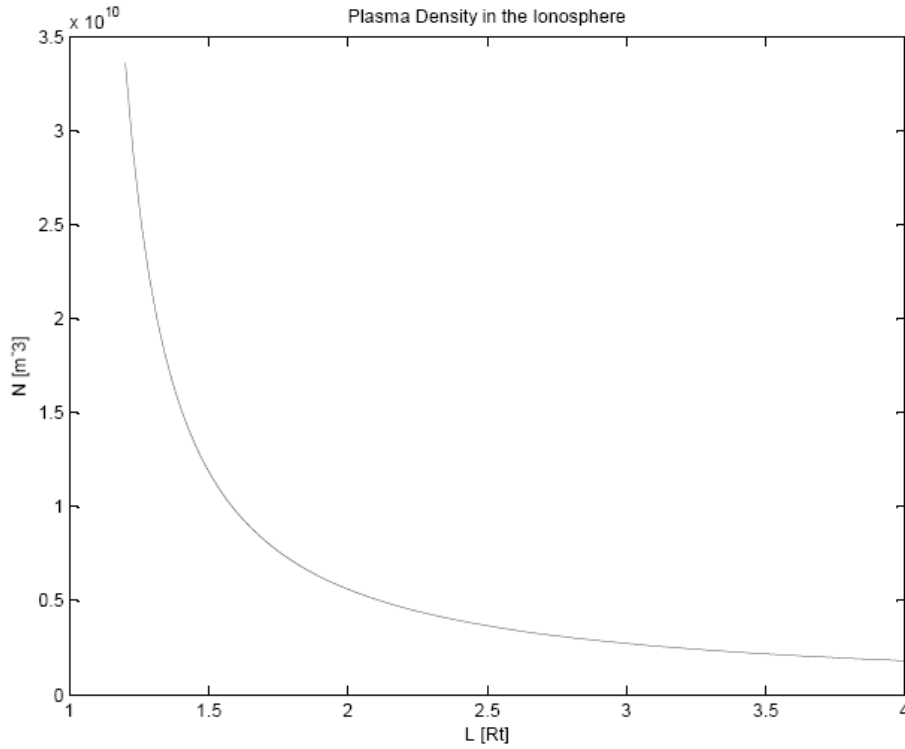
Figure 0-2. Plasma density as a function of the distance to the Earth's center.

Index of Refraction

For obtaining the index of refraction of the background plasma we'll use the Appleton-Hartree dispersion relation, that is, we consider the plasma to be cold, neglecting the ion motions but considering their inertial effects.

$$n^2 = \frac{B \pm F}{2A} \tag{3.6}$$

The definition of the parameters involved is

$$F^2 = B^2 - 4AC$$

$$A = S\sin^2\theta + P\cos^2\theta$$

$$B = RL\sin^2\theta + PS\left(1 + \cos^2\theta\right)$$

$$C = PRL$$

And they are functions of the elements of the dielectric tensor, which for a 2 component cold plasma are:

$$S = \frac{1}{2}(R + L)$$

$$D = \frac{1}{2}(R - L)$$

$$P = 1 - \frac{\omega_{pe}^2}{\omega^2} - \frac{\omega_{pp}^2}{\omega^2}$$

$$R = 1 - \frac{\omega_{pe}^2}{\omega \cdot (\omega - \Omega_e)} - \frac{\omega_{pp}^2}{\omega \cdot (\omega + \Omega_p)}$$

$$R = 1 - \frac{\omega_{pe}^2}{\omega \cdot (\omega - \Omega_e)} - \frac{\omega_{pp}^2}{\omega \cdot (\omega + \Omega_p)}$$

These terms depend solely on the wave frequency and the characteristic frequencies of the plasma, the electron and proton cyclotron frequencies.

$$\Omega_e = \frac{eB}{m_e} \qquad \Omega_p = \frac{eB}{m_p}$$

and the plasma frequencies

$$\omega_{pe} = \sqrt{\frac{Ne^2}{m_e \varepsilon_0}} \qquad \omega_{pp} = \sqrt{\frac{Ne^2}{m_p \varepsilon_0}}$$

Emitter

We have to define the characteristics of the waves we emit in frequency, propagation angle and intensity. To do so we have first to determine what kind of emitter we will use.

Our emitter will be a space tether. The easiest and more effective way of using a space tether as an emitter is making it work as a half-wave electric dipole antenna.

The orientation of such an antenna must be perpendicular to the local magnetic field to maximize the emissions. In addition, the stiffness of the tether is very small, making it

necessary to look for a stable configuration from a dynamical point of view to avoid attitude control issues.

We have chosen as configuration that of a tether in a circular equatorial orbit, an stabilized by gravity gradient (gravity acts as a restoring force). The orientation following the vertical in an equatorial plane keeps the tether perpendicular to the local magnetic field, and the circular orbit is the only one with a stable equilibrium position for the tether. If we consider the Earth's magnetic field to be dipole-like, the antenna will work at constant L, because of the symmetry.
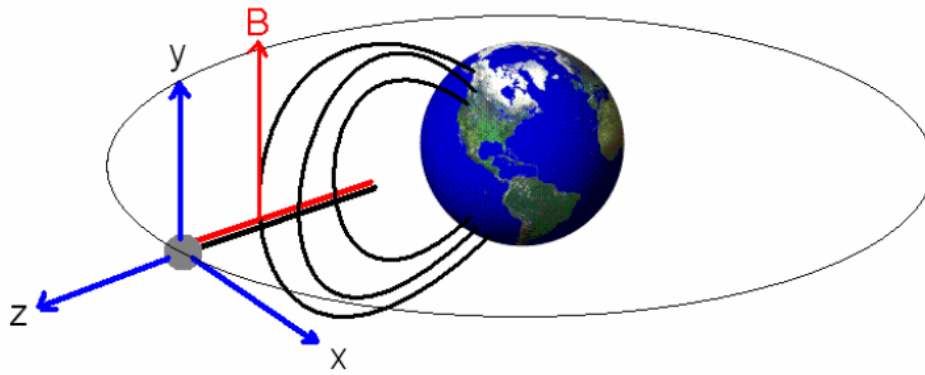
Figure 0-3. Tether's configuration during the mission

Now, the properties of an electric dipole inside a plasma will define the wave parameters needed for computation of the diffusion coefficient, and latter the characteristic precipitation time.

The frequency employed is a design parameter. We will determine it among the permitted frequencies trough an optimization process, being the optimization criteria the minimization of the precipitation time. Once we define the frequency, we can easily obtain the rest of the parameters.

The first one is the tether length. The antenna efficiency is the highest when its length equals half the wavelength of emission. In that case, the efficiency is of the order of $\approx 70 - 80\%$. The tether length is thus a function of the frequency, the propagation angle and the background plasma conditions.

$$L = \frac{1}{2}\lambda = \frac{\pi c}{n\omega} \tag{3.7}$$

The propagation angle dependence appears in the refractive index of the background plasma.

According to [*Wang & Bell*], the propagation angle value for a perfect electric dipole inside a magnetized plasma is only a function of the frequency

$$\theta_m \cong \arccos\left(2\frac{\omega}{\Omega_e}\right) \tag{3.8}$$

and this will be the value we use in our calculations.

Finally, the emission is nothing but perfectly monochromatic, and the propagation angle can also have some variation around the value given by (3.8). We will use typical values for their dispersion, the same we can find in the literature.

$$\delta\omega = 2\pi \cdot 5 \qquad \delta\theta = 10^\circ \tag{3.9}$$

and we will introduce a cut-off at low frequencies

$$\omega_{LC} = \omega_m - \delta\omega \tag{3.10}$$

Now we only need to define the magnetic field intensity of the wave, $B_w(\lambda)$. If we consider an electron cyclotron wave, circularly polarized and monochromatic, which propagates along the Earth's magnetic field lines, we can apply the WKB theory, because all the magnetospheric parameters change in distances very large in comparison with the wavelength. Under this assumptions, the magnetic field intensity can we expressed like this.

$$\vec{B}_w(\lambda,t) = B_w(\lambda)\left[\vec{i}\cos\left(\omega t - \int_0^\lambda k(\lambda)rd\lambda\right) + \vec{j}\sin\left(\omega t - \int_0^\lambda k(\lambda)rd\lambda\right)\right] \tag{3.11}$$

We want to know how does $B_w(\lambda)$ evolves. On one hand, it varies with the square root of the refraction index of the background plasma. On the other hand, if the waves are ducted, which is another assumption we are doing, the intensity varies inversely with the surface of the magnetic duct. Taking into account both effects, we have

$$B_w(\lambda) = B_{w,0}\sqrt{\frac{\Omega_e(\lambda)n(\lambda)}{\Omega_{e,0}n_0}} \tag{3.12}$$

The factor that multiplies the intensity of the magnetic field at the equator is of order unity, slightly bigger than 1 and in all our calculations smaller than 2. We can then assume the intensity of the wave's magnetic field to be constant, and equal to its equatorial value. Such a hypothesis is conservative, because it assumes a smaller value for the intensity, which yields a higher precipitation time.

If B_w^2 does not change, it is just a multiplicative constant for the diffusion coefficient and the diffusion equation. Since this square is proportional to the antenna's emission power, we see that the power of the antenna acts solely as a scale factor. Doubling the power of the system, through an increase in the power of the satellites or an increase of their number, will cut the remediation time in half.

To find an expression of the magnetic field intensity as a function of the emitted power is quite delicate. Following the scale arguments used by Inan and Bell, we have taken an intensity of 15 pT for an onboard power supply of 10 kW. We will use this value for our calculations, but we should not forget the role of the emitted power as a scale factor.

Numerical Model

Our first objective is to obtain, for a field line and energy given, the diffusion coefficient as a function of the particles' equatorial pitch angle.

We have discretized the pitch angle interval between the loss cone and $\frac{\pi}{2}$ with 100 points, which is enough for all the cases we have studied at a reasonably good computational cost.

To discretize the problem in latitude, we have taken into account the fact that, for a certain equatorial pitch angle, the weighting functions W_i are zero everywhere but in a small region around the resonance point. Therefore, we have calculated first for each pitch angle the resonance latitude, and afterwards we've discretized in latitude in a small interval around this value. The amplitude of the interval depends on the case. After each simulation we have verified that the amplitude considered was enough (zero value at the boundaries, unless the equator is one of them), if not, it was widened. The number of points used depends on the dimension of the latitude interval, ranging from 100 to 200.

The language employed to code the program is Matlab®, and we have used when possible Matlab functions to speed up the calculations.

Once calculated the diffusion coefficient as a function of the particles' equatorial pitch angle, we can solve the diffusion equation. We have transformed it in an eigen value problem, with matrix

$$M = \left[\left[\left(\frac{2D_{\alpha\alpha}}{\tan 2\alpha_0} - \frac{0.3198 \cdot \cos\alpha_0 \left(1 + \frac{1}{2\sqrt{\sin\alpha_0}}\right)}{1.3802 - 0.3198\left(\sin\alpha_0 + \sqrt{\sin\alpha_0}\right)} D_{\alpha\alpha} + \frac{dD_{\alpha\alpha}}{d\alpha_0}\right) \frac{d}{d\alpha_0} + D_{\alpha\alpha} \frac{d^2}{d\alpha_0^2}\right]\right]$$

(3.13)

We have discretized this matrix using finite differences. Before choosing the type of scheme to be used, we need to have a look at the order of magnitude of the different terms of the matrix. If the second derivative is the most important term, then the way we discretize the first derivatives is unimportant from the numerical stability point of view. But if there are values of the equatorial pitch angle for which the diffusion coefficient tends to zero, which is our case, the first derivatives become dominant, and we can no longer neglect their influence in the scheme stability.

The stability of our numerical algorithm depends on the direction taken by the derivatives. To decide what finite differences scheme to use, we have done a boundary layer analysis to evaluate the perturbations evolution. Through this analysis we have decided to employ right hand finite differences for the first derivatives. For the second derivative we have used a centered scheme of second order.

The problem to solve is then

$$\begin{bmatrix} 1 & 0 & \cdots & \cdots & \cdots & \cdots & 0 \\ & \ddots & & & & & \\ 0 & \cdots & m_{i-1} & m_i & m_{i+1} & \cdots & 0 \\ & & & & \ddots & & \\ 0 & \cdots & \cdots & \cdots & 0 & -1 & 1 \end{bmatrix} \cdot \begin{bmatrix} g_1 \\ \vdots \\ g_i \\ \vdots \\ g_n \end{bmatrix} = [\lambda_i] \cdot \begin{bmatrix} g_1 \\ \vdots \\ g_i \\ \vdots \\ g_n \end{bmatrix}$$

(3.14)

where

$$m_{i-1} = \frac{D_{\alpha\alpha}{}^{i-1}}{\Delta^2}$$

$$m_i = \frac{-1}{\Delta}\left[\frac{2D_{\alpha\alpha}{}^i}{\tan 2\alpha_0{}^i} - \frac{0.3198 \cdot \cos\alpha_0{}^i\left(1 + \dfrac{1}{2\sqrt{\sin\alpha_0{}^i}}\right)}{1.3802 - 0.3198\left(\sin\alpha_0{}^i + \sqrt{\sin\alpha_0{}^i}\right)}D_{\alpha\alpha}{}^i + \frac{D_{\alpha\alpha}{}^{i+1} - D_{\alpha\alpha}{}^i}{\Delta}\right] - \frac{2D_{\alpha\alpha}{}^i}{\Delta^2}$$

$$m_{i+1} = \frac{1}{\Delta}\left[\frac{2D_{\alpha\alpha}{}^i}{\tan 2\alpha_0{}^i} - \frac{0.3198 \cdot \cos\alpha_0{}^i\left(1 + \dfrac{1}{2\sqrt{\sin\alpha_0{}^i}}\right)}{1.3802 - 0.3198\left(\sin\alpha_0{}^i + \sqrt{\sin\alpha_0{}^i}\right)}D_{\alpha\alpha}{}^i + \frac{D_{\alpha\alpha}{}^{i+1} - D_{\alpha\alpha}{}^i}{\Delta}\right] + \frac{D_{\alpha\alpha}{}^{i+1}}{\Delta^2}$$

(3.15)

here n is the number of points of the pitch angle discretization and $\Delta = \dfrac{\dfrac{\pi}{2} - \alpha_{0,LC}}{n-1}$ is the

integration step. This scheme does not give any numerical problem in all cases studied. We have to consider also $\lambda_1 = \lambda_n = 0$ because of the boundary conditions.

Once we solve this problem, the eigen values give the characteristic precipitation time and the eigen vectors the form of the equatorial pitch angle distribution for the electrons, $g(\alpha_0)$.

132

Results

In this chapter we will analyze several cases, so as to decide whether or not such a system for RBR is feasible. First of all we will decide which frequency among all the possible is the best option for cleaning the radiation belts the fastest way. Then, we will analyze the influence of the distance to the Earth in the performance of the system

<u>Frequency optimization</u>

The formalism employed, that of the quasilinear theory, is valid in a certain range of frequencies. The upper frequency is limited by the absorption (Landau damping) due to the background plasma, as seen in §2.1. We have taken as a boundary 25% of the cyclotron resonance frequency. The lower limit corresponds to the low hybrid resonance.

$$\omega_{LH} = \sqrt{\Omega_e \Omega_p \frac{\omega_{pe}^2 + \Omega_e \Omega_i}{\omega_{pe}^2 + \Omega_e^2}} \qquad (4.1)$$

And we have taken as a boundary twice this frequency. Both limits define a range in the frequencies we can use, which depends on the distance to the Earth.
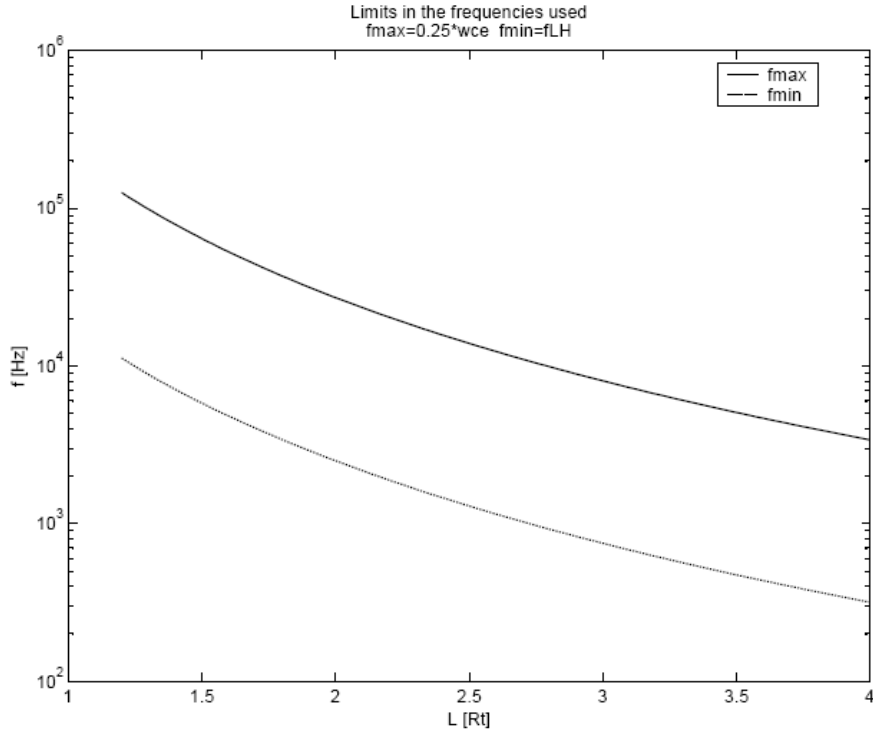
Figure 0-4. Possible antenna emitting frequencies

To analyze the influence of the frequency on the precipitation time, and decide which one is the optimal choice, we have run four simulations with different frequencies. The rest of the parameters remain the same. The basic conditions for all of them are L=1.5 and an energy of 1 MeV per electron.

The two dominant resonances are the first one and that of Landau. We have plot the diffusion coefficients corresponding to these resonances, together with the latitude of resonance as a function of the equatorial pitch angle. The four frequencies chosen are 5 kHz, 10 kHz, 15 kHz and 25 kHz, and they cover the whole range between the low hybrid resonant frequency and the cyclotron frequency.
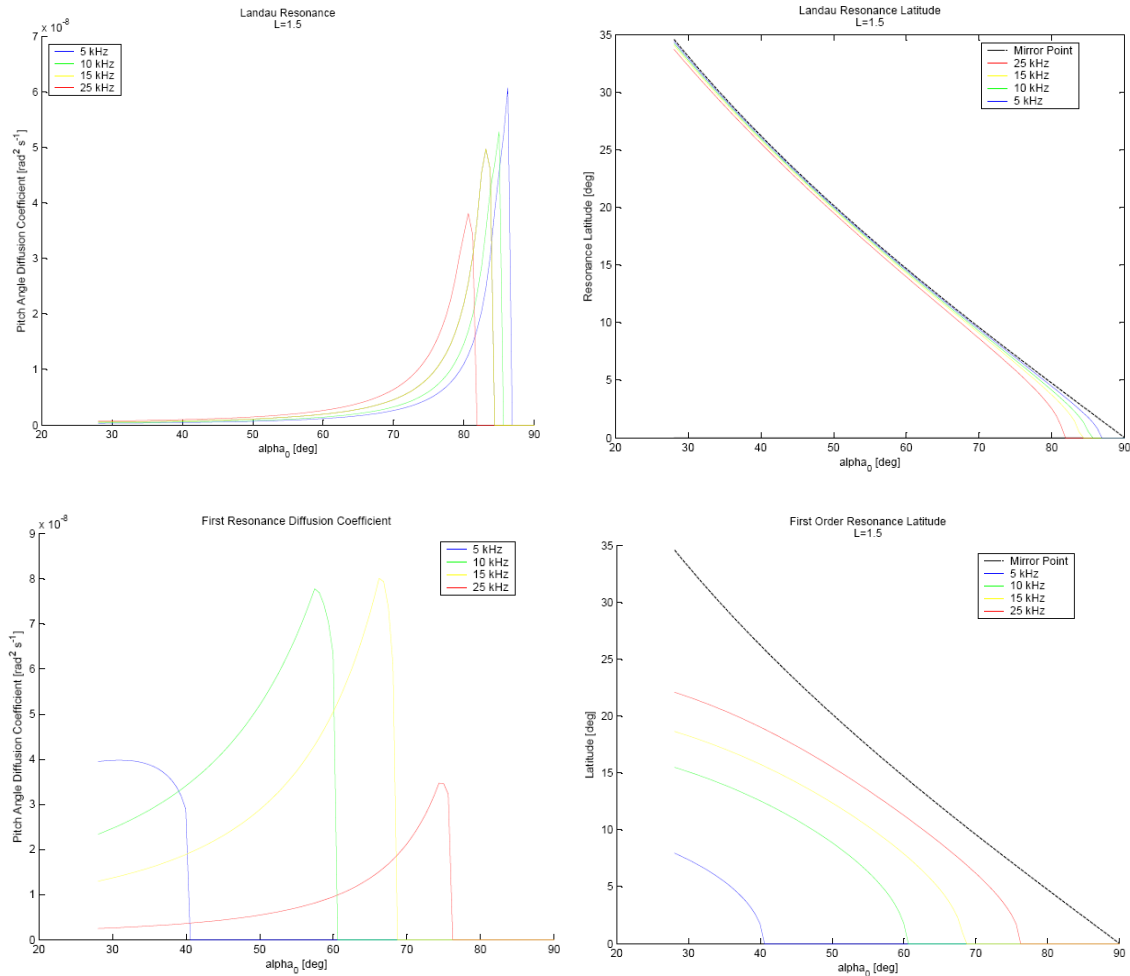
Figure 0-5. Left: emission frequency influence on the diffusion coefficients. Right : emission frequency influence on the latitude of resonance

The most dramatic changes take place within the first order resonance. The more we reduce the frequency, less particles enter in resonance with the wave, but the higher the diffusion coefficient value in at the loss cone boundary. The shape of the diffusion coefficient tends to become more flat at the same time. If we plot the total diffusion coefficient as a function of the equatorial pitch angle for the four frequencies, we obtain
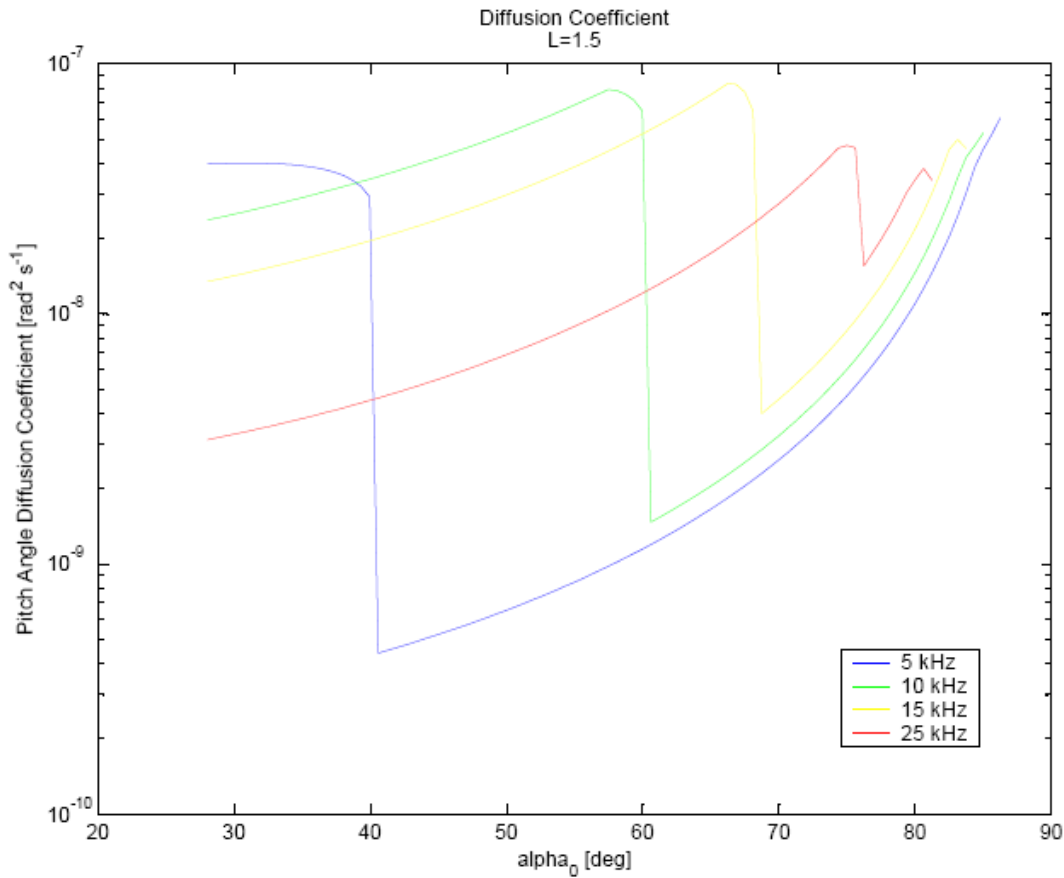
Figure 0-6. Bounce averaged diffusion coefficients as a function of the equatorial pitch angle for different values of the emission frequency. In all cases the particles' energy is 1 MeV and L=1.5

Now we are going to obtain the precipitation time, taking into account all resonances. In fact, we've taken into account just the first 5 resonances, because the influence of the rest is negligible. The results we have obtained by solving the eigen value problem are the following
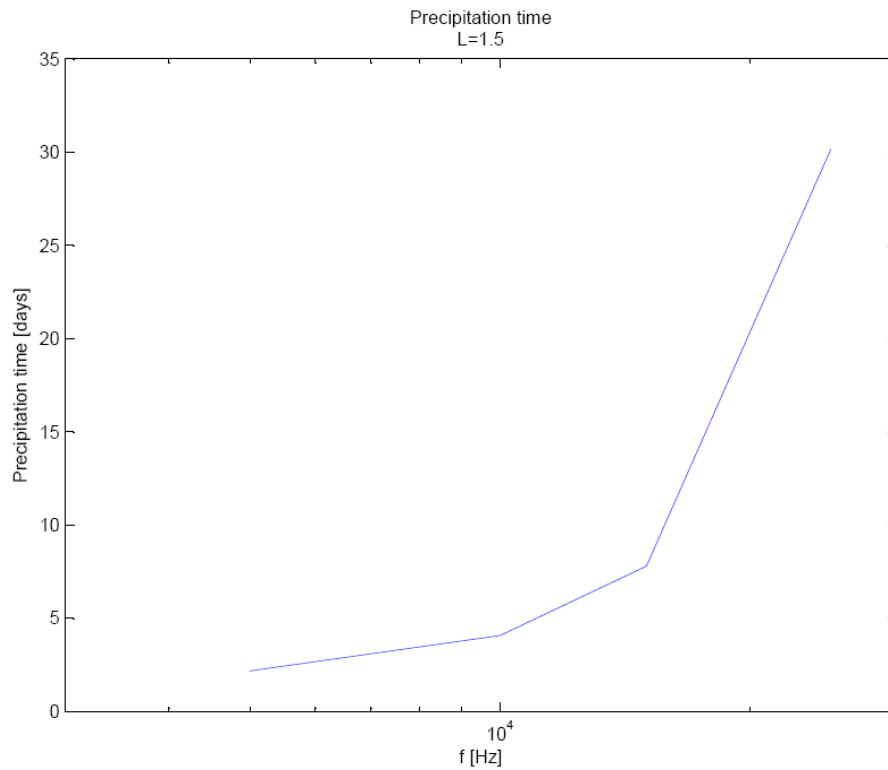
Figure 0-7. Characteristic precipitation time for the electrons, as a function of the emission frequency

The characteristic precipitation time has a strong dependence on the emission frequency. We will then try to use frequencies near the lower limit in order to reduce the mission time.

Distance to Earth influence

We will now analyze the influence of the distance to Earth on the characteristic precipitation time. To avoid absorption near the low hybrid resonance, we consider frequencies equal to twice the low hybrid resonant frequency. We have calculated this time for three different field lines and for a frequency near twice the low hybrid resonant frequency.

L	f [kHz]
1.5	10

2.0   5

2.5   2.5

Table 4-1. Frequencies employed for different distances to Earth

First, we will see the effect on each resonance independently
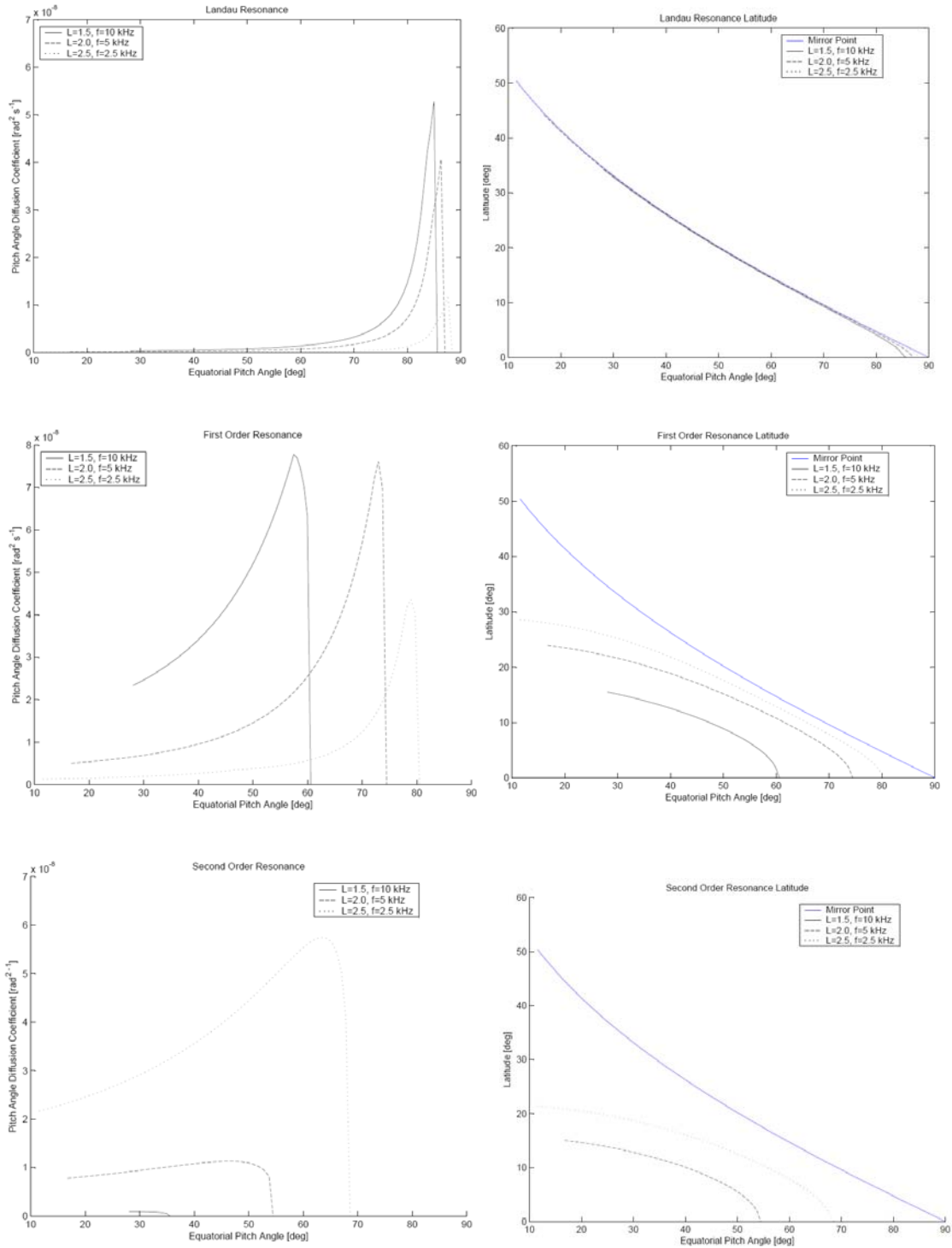
Figure 0-8. Left : influence of the distance to Earth on the diffusion coefficients, for the Landau, first and second order resonances, for three different distances. Right : influence of the distance to Earth on the resonance latitude, for three different distances and the Landau, first and second order resonances.

The further the system is to the Earth, the resonances take place nearer the mirror points and the diffusion acts for particles until higher values for the equatorial pitch angle. As for the magnitude of the diffusion coefficients, it depends on the resonance we consider.
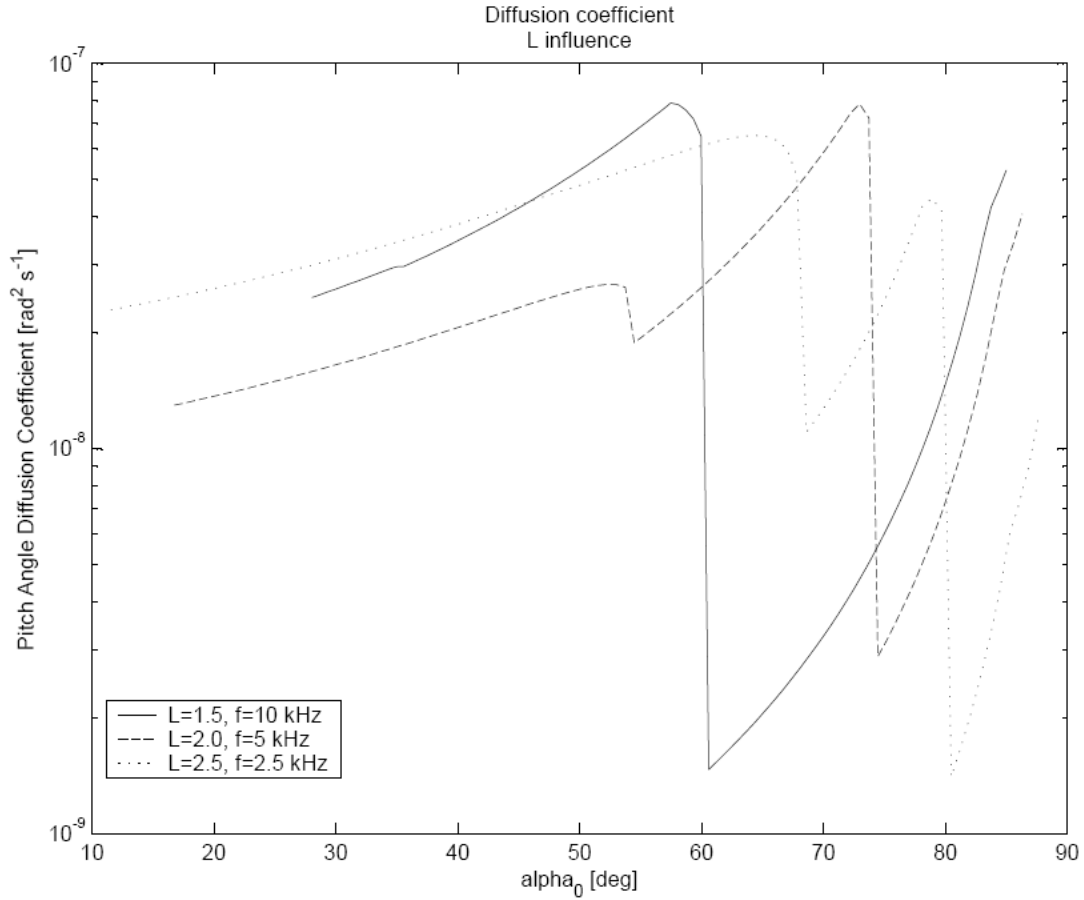
Figure 0-9. Diffusion Coefficients for three different distances, a frequency approximately equal to twice the low hybrid frequency and particles of 1 MeV.

The second resonance becomes more important as the distance to Earth increases. The characteristic times obtained when solving the diffusion equation are
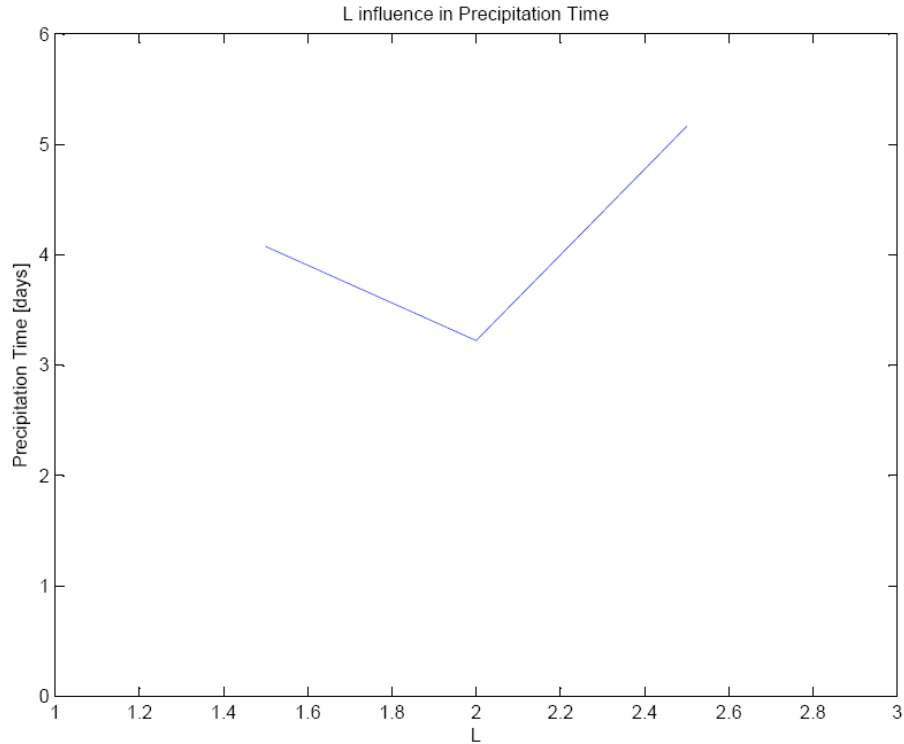
Figure 0-10. Characteristic time obtained for each one of the three cases studied previously

There is no evident tendency, but all of them are of the same order of magnitude, and what is more important, they are short enough so that we can expect this to a be a promising RBR method.

Some additional antenna considerations

Taking into account the environment conditions, and the propagation angle, we can easily obtain the antenna length needed for each situation using (3.7). The results are

L	Longitude [m]
1.5	164.3
2.0	235.7
2.5	293.4

Table 4-2. Antenna length needed for three different distances to Earth.

As we can see, the lengths needed are large enough to make unpractical the use of conventional dipole antennas. The use of tethers can solve this problem. However, they are short enough so that there won't be any specific production or control problems. The differences in length are significant, thus, if we wish to use the same tether to clean different L shells, we will have to design it so as to have a variable length, to avoid severe efficiency losses when we deviate from the initial design point. The adaptability of the system depends on the range of L shell each tether will work, which depends on the number of tethers and the area to be cleaned. There is then a trade off between number of satellites and complexity of each one of them and the design will be chosen in terms of cost and mission time (the more satellites we have, the less time it takes to clean a specific area).

Since the tether length is small, there won't be any concerns about its strength and for the sake of simplicity we can consider a design with constant cross section.

The tension generated through gravity gradient is
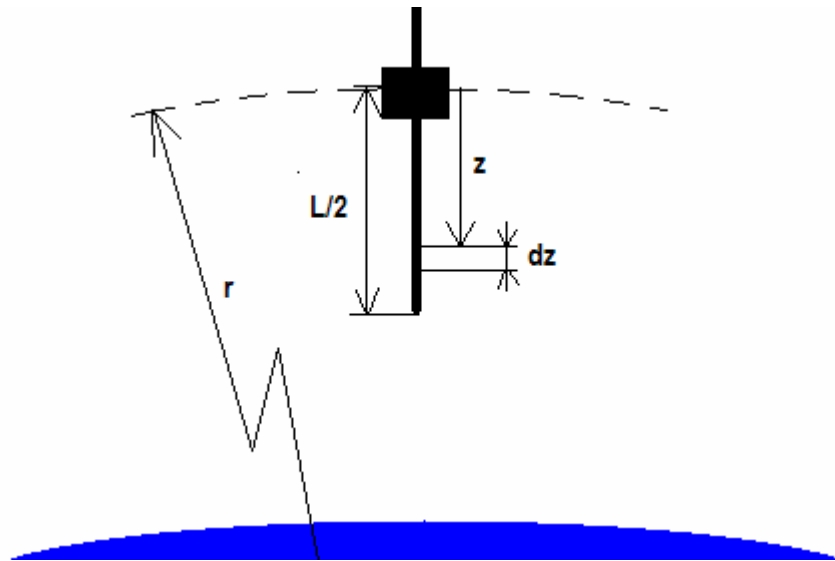
Figure 0-11. Tether configuration and nommenclature for the calculation ot the tether tension.

$$dT(z) = \rho S dz \left(\frac{\mu_T}{r^2} - \frac{\mu_T}{(r-z)^2} \right)$$

$$\frac{L}{2} << r$$

$$dT(z) \cong \frac{2\rho S \mu_T}{r^3} z dz$$

$$T_{max} = T(z=0) = \frac{\rho S L^2 \mu_T}{4r^3}$$

(4.2)

And if we take an aluminum tether at L=2 this yields

$$\frac{T_{max}}{S} = 7.2 \ Pa$$

This value is negligible in comparison with the mechanical strength of the material. We do not have, then, any concern about the system construction.

From the dynamical point of view, without doing a deep study of the cable dynamics, its first frequency is approximately that of a string under tension

$$f_1 \cong 2 \frac{1}{2L} \sqrt{\frac{T}{\rho S}} \approx 2 \cdot 10^{-4} \ Hz$$

(4.3)

which is very far from the excitation frequency, which is that of the waves, because the perturbation forces are basically due to the interaction between the Earth's magnetic field and the currents in the tether. Thus, there should not be any attitude control problems for the system.

Finally, according to Edelman's research, there are no specific sputtering problems due to the ions bombardment.

Synthesis

If we take as a characteristic remediation time three times the time constant, the results that we have obtained are

L	Remediation time [days]	Tether length [m]
1.5	12	164

2.0	9	236
2.5	15	293

Table 4-3. Results for the different distances to Earth

In this analysis we have just considered the effect of VLF/ELF waves. There are other effects that affect the mean life of a trapped particle. This other effects make that the mean precipitation time for a 1 MeV particle at the distances we are considering is a year [*Edelmann*]. Since our decay times are small in comparison with those obtained without the effect of VLF/ELF waves, we can infer that the effect of the latter is dominant, and that the results we have obtained are accurate.

The fact that the decay times are reduced by an order of magnitude or more, means this is a promising approach to Radiation Belt Remediation.

We have not taken into account the effect of possible wave reflections in the ionosphere. Data from natural whistlers indicate that there can be as many reflections as 20 or 30. We could therefore expect further reductions in the remediation time, by a factor of 10.

To take into account the effect of reflections, we would need an in depth study of VLF/ELF waves propagation in the ionosphere, which is out of the scope of this study.

Conclusion and recommendations

<u>Conclusion</u>

The cleaning of a thin L shell by a 10 kW system is feasible in a few days if there are no particles' sources involved. For cleaning significant areas of the ionosphere we need a variable length system, a system made of several satellites, or a combination of the two, depending of the mission time and cost we are targeting. If we stay relatively near the Earth, the RBR time stays more or less constant.

This method appears to be more promising than the one studied by [*Zeineh, 2005*], which consisted in a high voltage tether dispersing the ions as it orbits around the Earth. The remediation times obtained by Zeineh were one to two orders of magnitude higher. It is true that for comparing both methods we should apply the Zeineh method to electrons, but this needs significant modifications of the prior work

The results obtained depend on the emitter power. If we multiply the power of the system by a factor, either increasing the power of each satellite, or increasing the number of satellites, the total remediation time will be reduced by the same factor.

Finally the accuracy of the results can be improved by using better models for the Earth's magnetic field (IGRF, …), the ionospheric plasma density (SLIM, …), and taking into account more resonances. The modifications needed are minor, but we lose many analytical expressions.

<u>Recommendations</u>

Our recommendations for future research are the following

- Development of a code for calculating the ray trajectory of VLF/ELF waves in the ionosphere. This code would allow us to better know the area of influence of the antenna, and take into consideration the effect of multiple reflections near the mirror points. Whistlers can reflect several times, increasing the effect over the particles' trajectories. This effect, that we have neglected in our analysis could reduce even more the remediation time, and should be studied in detail. Such a code could be based on the WKB optical approximation and should be able to use several different ionospheric models.

- Numerical simulation of the VLF/ELF emissions by an electrodynamic tether. A PIC code specially designed for the study of electrodynamic tethers has already been developed inside SPL. This code should be modified to allow an increase in the numerical domain without increasing the computational cost. It is also necessary to introduce boundary conditions that allow waves to cross the boundaries without reflection. Such radiation like boundary conditions may be similar to those used in CFD codes for aeroacoustic simulations. This code should allow us to know better the properties of the waves generated by the tether, improving then our results.

- Numerical study of the wave-particle interaction. The region in which the resonance takes place is small in comparison with the particles' trajectories (under 6 degrees in latitude) but too large to simulate the resonance phenomenon through a PIC code. If we consider that the wave is not perturbed by the particles, we can assume they are not coupled and we can try a "test particle" approach to the problem. Then using statistical Monte Carlo techniques, we can obtain the average pitch angle scattering and the precipitating particle fluxes, comparing the results with those obtained with the quasilinear theory with a reasonably computational cost.

- Study of the influence of ions other than protons inside the ionosphere and of other kinds of wave (EMIC, Chorus).

All these studies and simulations should allow us to know better the behaviour of such a system before starting with flight models.

Bibliography

Abel, B., and R. M. Thorne, Electron scattering loss in the Earth's inner magnetosphere: 1. Dominant physical processes, J. Geophys. Res., 103, 2385, 1998a. (Correction, J. Geophys. Res., 104, 4627, 1999).

Abel, B., and R. M. Thorne, Electron scattering loss in the Earth's inner magnetosphere: 2. Sensitivity to model parameters, J. Geophys, Res., 103, 2397, 1998b. (Correction, J. Geophys. Res., 104, 4627, 1999).

Al'pert, Ya. L., The near-Earth and interplanetary plasma, Cambridge University Press, Cambridge, 1962.

Edelman, N., Environment parameters for radiation belt remediation with a high voltage tether, MIT, 2006.

Kennel, C. F., Engelmann, F., Phys. Fluids, 9, 2377, 1966.

Inan, U. S., T. F. Bell, J. Bortnik, and J. M. Albert, Controlled precipitation of radiation belt electrons, J. Geophys. Res., 108(A5), 1186, 2003

Redfern, D., C. Campbell, The Matlab 5 Handbook, Springer, 1998.

Spitzer, Lyman Jr, Physics of fully ionized gases, Interscience Publishers, 1962.

Stix, T. H., The Theory of Plasma Waves, McGraw-Hill, New York, 1962.

Wang, T. N. C., and T. F. Bell, Electric dipole radiation at VLF in a uniform warm magneto-plasma, Rev. Phys. Apppl., 7, 11, 1972b.

Wang, T. N. C., and T. F. Bell, VLF/ELF Radiation patterns of arbitrarily oriented electric and magnetic dipoles in a cold lossless multicomponent magnetoplasma, J. Geophys. Res., 77, 1174, 1972.

Zeineh, C. F., Applications of an electrostatic high-voltage tether to radiation belt remediation, MIT MSc Thesis, 2005.

Emission of Whistler Waves from an ionospheric tether

May 26, 2008

1 Equations

An electromagnetic wave in plasma is formulated by application of Maxwell's equations and the equations of motion of the particles. In our problem, we use Maxwell's equations and the electron equation of motion. We neglect the ion motion because the frequencies of interest are above the lower hybrid frequency.

Maxwell's equations (Neglecting displacement current):

$$\nabla \times \vec{E}_{(\vec{r})} = -\frac{\partial \vec{B}_{(\vec{r})}}{\partial t} \tag{1}$$

$$\nabla \times \vec{B}_{(\vec{r})} = \mu_0 \vec{j}_{(\vec{r})} \tag{2}$$

Electron equation of motion

$$m_e \frac{\partial \vec{v}_e}{\partial t} = -e(\vec{E}_{(\vec{r})} + \vec{v}_e \times \vec{B}_{0(\vec{r})}) - m_e \nu_e \vec{v}_e \quad (\ \nu_e : \text{collision frequency}) \tag{3}$$

From Eq.(1) andEq.(2),

$$\nabla^2 \vec{E}_{(\vec{r})} - \nabla(\nabla \cdot \vec{E}_{(\vec{r})}) = -\mu_0 e n_{e0} \frac{\partial \vec{v}_e}{\partial t} + \mu_0 \frac{\partial \vec{j}_s}{\partial t} \tag{4}$$

147

2 Fourier Transformation

We can solve those equations using Fourier transformation. In this problem, we analyse the wave propagation with fixed frequency ω.

One of the space-time Fourier components can be expressed as

$$\vec{E}_{(\vec{r})} = \vec{\tilde{E}}_{(\omega,\vec{k})} \exp i(\omega t - \vec{k} \cdot \vec{x}) \tag{5}$$

From Eq.(4),

$$-k^2 \vec{\tilde{E}} + \vec{k}(\vec{k} \cdot \vec{\tilde{E}}) = -i\mu_0 e n_{e0} \omega \vec{\tilde{v}}_e + i\mu_0 \omega \vec{\tilde{j}}_s \tag{6}$$

From Eq.(3),

$$m_e(i\omega + \nu_e)\vec{\tilde{v}}_e = -e(\vec{\tilde{E}} + \vec{\tilde{v}}_e \times \vec{B}_0) \tag{7}$$

Then, from Eq.(6) and Eq.(7),

$$\vec{\tilde{E}}\left[1 - \frac{ik^2}{\mu_0\omega}\frac{m_e(i\omega + \nu_e)}{e^2 n_{e0}}\right] - \frac{ik^2}{\mu_0 n_{e0}\omega e}\vec{\tilde{E}} \times \vec{B}_0 + (\vec{k} \cdot \vec{\tilde{E}})i\left[\frac{\vec{k}}{\mu_0\omega}\frac{m_e(i\omega + \nu_e)}{e^2 n_{e0}} + \frac{\vec{k} \times \vec{B}_0}{\mu_0 e n_{e0}\omega}\right]$$
$$= \frac{-m_e(i\omega + \nu_e)}{e^2 n_{e0}}\vec{\tilde{j}}_s - \frac{\vec{\tilde{j}}_s \times \vec{B}_0}{e n_{e0}} \tag{8}$$

Define

$$\vec{b_0} = \vec{B}_0/B_0 \tag{9}$$

$$\delta = \frac{\nu_e}{\omega_{ce}} \tag{10}$$

$$\nu = \frac{\omega}{\omega_{ce}} \tag{11}$$

$$l = \sqrt{\frac{m_e}{e^2 n_{e0}\mu_0}} \tag{12}$$

$$K = kl \tag{13}$$

$$\sigma_{ce} = \frac{e^2 n_{e0}}{m_e \omega_{ce}} \tag{14}$$

Assuming that $B_0 = 10^{-5}$ Tesla and electron temperature is 1 eV, the plasma skin depth l, σ_{ce} and δ for $n = 10^{10}$ [/m^3] and $n = 10^8$ [/m^3] are estimated as shown in Table 2. ($\omega_{ce} \sim 1.7 \times 10^6$ [rad/sec])

148

Table 1: Estimated l, σ_{ce} and δ

n [/m³]	l [m]	σ_{ce} [Si/m]	δ
10^10	50	1.6×10^{-4}	4×10^{-8}
10^8	500	1.6×10^{-6}	4×10^{-10}

Then,Eq.(8) becomes

$$\vec{E}\left(1 + K^2 - i\frac{K^2\delta}{\nu}\right) - i\frac{K^2}{\nu}\vec{E} \times \vec{b_0} + \left(\vec{K} \cdot \vec{E}\right)\left(-\vec{K} + i\frac{\vec{K} \times \vec{b_0}}{\nu} + i\frac{\delta}{\nu}\vec{K}\right)$$

$$= -\frac{(i\nu + \delta)\vec{\tilde{j_s}} + \vec{\tilde{j_s}} \times \vec{b_0}}{\sigma_{ce}} \tag{15}$$

The configuration is such that $\vec{k}$ is along x-axis,and $\vec{B_0}$ makes an angle θ to $\vec{k}$ and is in the x-y plane (Fig.(1)).
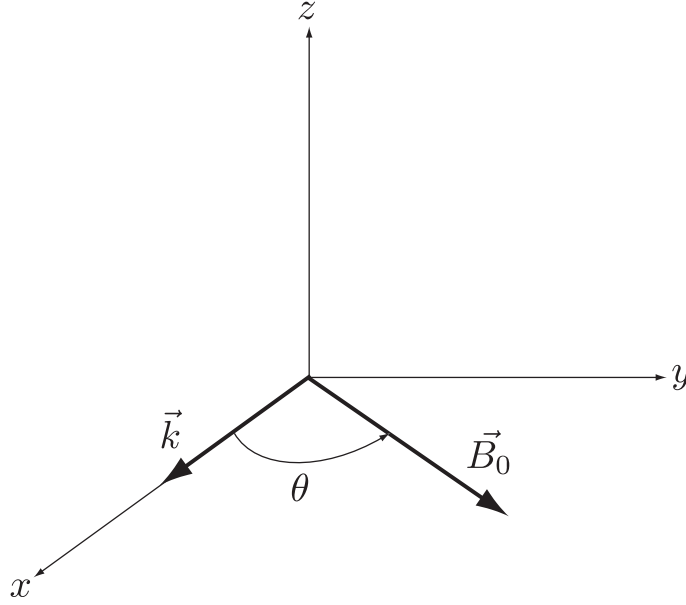
Figure 1: $\vec{k}$ and $\vec{B_0}$ configuration

Then,

$$\vec{b_0} = \cos\theta\hat{x} + \sin\theta\hat{y}$$

$$\vec{\hat{E}} \times \vec{b_0} = -\sin\theta\hat{E}_z\hat{x} + \cos\theta\hat{E}_z\hat{y} + \left(\sin\theta\hat{E}_x - \cos\theta\hat{E}_y\right)\hat{z}$$

$$\vec{K} \times \vec{b_0} = K\sin\theta\hat{z}$$

$$\vec{\hat{j}_s} = -\sin\theta\hat{j}_{sz}\hat{x} + \cos\theta\hat{j}_{sz}\hat{y} + \left(\sin\theta\hat{j}_{sx} - \cos\theta\hat{j}_{sy}\right)$$

$$(\hat{x}, \hat{y}, \hat{z}: \text{unit vectors on x, y, z axes})$$

Thus, Eq.(15) becomes the system

$$\hat{E}_x + i\frac{K^2}{\nu}\sin\theta\hat{E}_z = -\frac{(i\nu + \delta)\hat{j}_{sx} - \sin\theta\hat{j}_{sz}}{\sigma_{ce}} \tag{16}$$

$$\left(1 + K^2 - i\frac{K^2\delta}{\nu}\right)\hat{E}_y - i\frac{K^2}{\nu}\cos\theta\hat{E}_z = -\frac{(i\nu + \delta)\hat{j}_{sy} - \cos\theta\hat{j}_{sz}}{\sigma_{ce}} \tag{17}$$

$$i\frac{K^2}{\nu}\cos\theta\hat{E}_y + \left(1 + K^2 - i\frac{K^2\delta}{\nu}\right)\hat{E}_z = -\frac{(i\nu + \delta)\hat{j}_{sz} + \sin\theta\hat{j}_{sx} - \cos\theta\hat{j}_{sy}}{\sigma_{ce}} \tag{18}$$

$\hat{E}_y$ and $\hat{E}_z$ are decoupled from $\hat{E}_x$ (along $\vec{k}$), but $\hat{E}_x$ is tied to $\hat{E}_z$ by Eq.(16).

3 Dispersion relation

The determinant of Eq.(16),(17),(18) is same as the determinant of Eq.(17),(18). For a valid $\hat{E}_x$, $\hat{E}_y$, $\hat{E}_z$, we need this determinant to be zero.

$$\left(1 + K^2 - i\frac{K^2\delta}{\nu}\right)^2 - \frac{K^4}{\nu^2}\cos^2\theta = 0 \tag{19}$$

And the roots are

$$K_u = \pm\sqrt{\frac{\nu}{\cos\theta - \nu + i\delta}} \tag{20}$$

$$K_d = \pm i\sqrt{\frac{\nu}{\cos\theta + \nu - i\delta}} = \pm\sqrt{\frac{\nu}{\cos(\pi - \theta) - \nu + i\delta}} \tag{21}$$

These are the dispersion relations. As in Fig.(2), for $\theta < \cos^{-1}\nu$, K_u represents slightly damped waves, and K_d represents heavily damped waves. For

$\cos^{-1}\nu < \theta < \pi - \cos^{-1}\nu$, K_u and K_d represent heavily damped waves. For $\theta > \pi - \cos^{-1}\nu$, K_u represents heavily damped waves, and K_d represents slightly damped waves. So, the K_u wave propagates when $\theta < \cos^{-1}\nu$, and the K_d wave propagates when $\theta > \pi - \cos^{-1}\nu$.
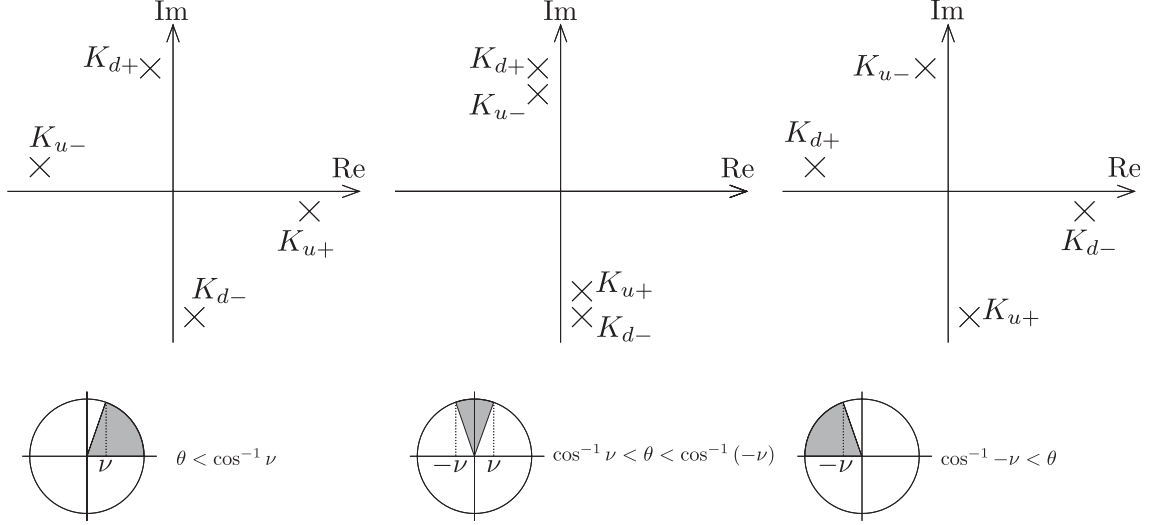
Figure 2: K_u and K_d pole position

4 Matrix form of Ohm's law

Eq.(16),(17),(18) can be solved as follows

$$\vec{\hat{E}} = \begin{bmatrix} \hat{E}_x \\ \hat{E}_y \\ \hat{E}_z \end{bmatrix} = Z\vec{\hat{j}}_s = Z \begin{bmatrix} \hat{j}_{sx} \\ \hat{j}_{sy} \\ \hat{j}_{sz} \end{bmatrix} \tag{22}$$

$$Z = -\frac{1}{\sigma_{ce}\triangle} \begin{bmatrix} i\nu\left(1+K^2\right)^2 - i\frac{K^2}{\nu}\left(K^2+\sin^2\theta\right) & i\frac{K^2}{\nu}\sin\theta\cos\theta & -(1+K^2)\sin\theta \\ i\frac{K^2}{\nu}\sin\theta\cos\theta & i\nu\left(1+K^2\right) - i\frac{K^2}{\nu}\left(\cos^2\theta\right) & \cos\theta \\ (1+K^2)\sin\theta & -\cos\theta & i\nu\left(1+K^2\right) - i\frac{K^2}{\nu}\left(\cos^2\theta\right) \end{bmatrix} \tag{23}$$

151

$$\triangle = \left(1 + K^2 - i\frac{K^2\delta}{\nu}\right)^2 - \frac{K^4}{\nu^2}\cos^2\theta \tag{24}$$

5 Antenna related axes

For the computation of the inverse Fourier transformation, we will need to vary $\vec{k}$ in all possible ways. Thus, it is better to change the coordinates to ones which do not change in the inverse Fourier transformation process. Now, $\vec{k}$ is on the x-axis. We will change the coordinates by defining axes(X_B, Y_B, Z_B) such that $\vec{B_0}$ is on the z-axis (B-frame) as in Fig.(3). The antenna is in the $X_B - Z_B$ plane and has an angle α to $\vec{B_0}$. $\vec{k}$ is oriented according to the polar angles (θ, ϕ).

Any vector can be expressed in the old coordinates $\vec{V} = (V_x, V_y, V_z)$ and in the new coordinates $\vec{V_B} = (V_{xB}, V_{yB}, V_{zB})$ and the two representations are related as

$$\vec{V_B} = R\vec{V} \tag{25}$$

R is a rotation matrix and has components as follows

$$R = \begin{bmatrix} \sin\theta\cos\phi & -\cos\theta\cos\phi & \sin\phi \\ \sin\theta\sin\phi & -\cos\theta\sin\phi & -\cos\phi \\ \cos\theta & \sin\theta & 0 \end{bmatrix} \tag{26}$$

$R^{-1} = R^T$, so $\vec{V} = R^T\vec{V_B}$.

From Eq.(22), the current to field relationship is $\vec{\tilde{E}} = Z\vec{\tilde{j}_s}$. Transforming to the B-frame gives

$$RZ\vec{\tilde{j}_s} = R\vec{\tilde{E}} = \vec{\tilde{E}_B} = Z_B\vec{\tilde{j}_{sB}} = Z_B R\vec{\tilde{j}_s} \tag{27}$$

and, therefore

$$Z_B = RZR^T \tag{28}$$

152
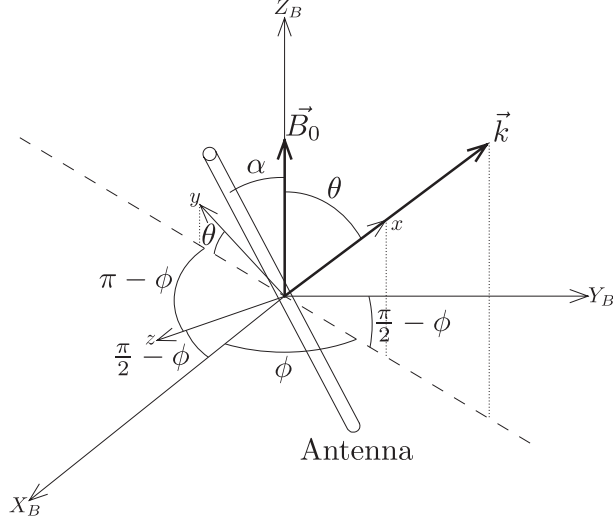
Figure 3: Antenna Related Axes

Explicitly, Z_B has components as follows

$$
Z_B = -\frac{1}{\sigma_{ce}\triangle}
\begin{bmatrix}
\begin{array}{c}
-p + K^2 \sin^2\theta \left(-p\cos^2\phi + \frac{i}{\nu}\sin^2\phi\right) \\
- \left(1 + K^2\sin^2\theta\right) - iK^2\left(1 + K^2\right)\left(\frac{1}{\nu} - \nu\right)\sin^2\theta\sin\phi\cos\phi \\
-K^2\left(p\cos\phi + \sin\phi\right)\sin\theta\cos\theta
\end{array} \\[2mm]
\begin{array}{c}
- \left(1 + K^2\sin^2\theta\right) - iK^2\left(1 + K^2\right)\left(\frac{1}{\nu} - \nu\right)\sin^2\theta\sin\phi\cos\phi \\
- \left(p - i\frac{K^2}{\nu}\sin^2\theta\right)\cos^2\phi - p\left(1 + K^2\sin^2\theta\right)\sin^2\phi \\
K^2\left(-p\sin\phi + \cos\phi\right)\sin\theta\cos\theta
\end{array} \\[2mm]
\begin{array}{c}
K^2\sin\theta\cos\theta\left(\sin\phi - p\cos\phi\right) \\
-K^2\sin\theta\cos\theta\left(p\sin\phi + \cos\phi\right) \\
-pK^2\cos^2\theta + i\nu\left(1 + K^2\right)
\end{array}
\end{bmatrix}
\tag{29}
$$

where

$$
p = i\frac{K^2}{\nu} - i\nu\left(1 + K^2\right)
\tag{30}
$$

153

6   The antenna model

For an antenna source current distribution $\vec{j}_s(\vec{x})$, the Fourier transformation is

$$\vec{\tilde{J}}_s(\vec{x}) = \frac{1}{(2\pi)^3} \int \int \int \vec{j}_s(\vec{x}) e^{i\vec{k}\cdot\vec{x}} d^3x \tag{31}$$

and,

$$\vec{j}_s(\vec{x}) = \begin{cases} \frac{I_s(z_a)}{\pi a^2}\vec{1a} & \text{inside wire} \\ 0 & \text{outside wire} \end{cases} \tag{32}$$

a is the radius of the antenna, $\vec{1a}$ is the unit vector along the antenna, I_s is the current, z_a is distance along the antenna. So, if I_0 is $I_s(z_a = 0)$, Eq.(31) becomes

$$\vec{\tilde{j}}_s(\vec{x}) = \frac{1}{(2\pi)^3}\frac{I_0}{\pi a^2}\vec{1a} \int \int \int_{\text{antenna}} \frac{I_s(z_a)}{I_0} e^{i\vec{k}\cdot\vec{x}} d^3x \tag{33}$$

Let $\vec{k_\perp}$ be the projection of $\vec{k}$ on the plane perpendicular to the antenna,
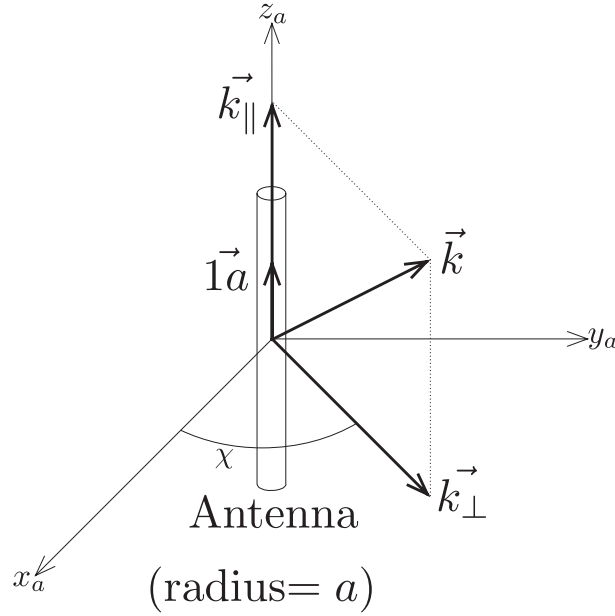
Figure 4: Antenna and $\vec{k}$

and $\vec{k_\parallel}$ be the projection of $\vec{k}$ on the antenna. Then if $\vec{k_\perp}$ makes an angle χ to

154

the x_a axis (which is on the $X_B Y_B$ plane), and $\vec{x}$ has cylindrical components (R, ψ, z_a) in (x_a, y_a, z_a),

$$\vec{k} \cdot \vec{x} = k_\perp R \cos(\psi - \chi) + k_\| z_a \tag{34}$$

The integration volume element is $d^3 x = R dR d\psi dz_a$. Using Bessel functions $\left(J_{n(x)} = \frac{1}{2\pi} \int_{-\pi}^{\pi} e^{ix \sin\theta - in\theta} d\theta \right)$, the integral on ψ is

$$\int_0^{2\pi} e^{ik_\perp R \cos(\psi - \chi)} d\psi = 2\pi J_0(k_\perp R) \tag{35}$$

and the integral on R is,

$$\int_0^a 2\pi J_0(k_\perp R) R dR = \frac{2\pi}{k_\perp^2} (ak_\perp) J_1(ak_\perp) \tag{36}$$

Then, we can get

$$\vec{j}_s\left(\vec{k}\right) = \frac{1}{(2\pi)^3} \frac{I_0}{\pi a^2} \vec{1a} \frac{2\pi a}{k_\perp} J_1(ak_\perp) \int_{-L/2}^{L/2} \frac{I_s(z_a)}{I_0} e^{ik_\| z_a} dz_a \tag{37}$$

Integrate by parts and assume $I_s(z_a = \pm L/2) = 0$, and $I_{s(z_a)} = I_{s(-z_a)}$

$$\int_{-L/2}^{L/2} \frac{I_s(z_a)}{I_0} e^{ik_\| z_a} dz_a = -\frac{2}{k_\|} \int_0^{L/2} \sin(k_\| z_a) \frac{d}{dz_a} \left(\frac{I_s}{I_0} \right) dz_a \tag{38}$$

We next assume a triangular current distribution for $I_s(z_a)$:

$$\frac{I_s}{I_0} = 1 - \frac{2|z_a|}{L} \tag{39}$$

Then,

$$\int_{-L/2}^{L/2} \frac{I_s(z_a)}{I_0} e^{ik_\| z_a} dz_a = \frac{4}{k_\|^2 L} \left(1 - \cos\left(k_\| \frac{L}{2} \right) \right) \tag{40}$$

Substituting this in Eq.(37),

$$\vec{j}_s\left(\vec{k}\right) = \frac{8a I_0 J_1(ak_\perp)}{(2\pi)^3 L a^2 k_\perp k_\|^2} \left(1 - \cos\left(k_\| \frac{L}{2} \right) \right) \vec{1a} \tag{41}$$

155

In general, $ak_\perp \ll 1$, so $J_1(ak_\perp) \simeq \frac{1}{2}ak_\perp$, and then

$$\vec{j_s}\left(\vec{k}\right) = \frac{4I_0L}{(2\pi)^3}\frac{1-\cos\left(k_\parallel L/2\right)}{k_\parallel^2 L^2}\vec{1a} \tag{42}$$

For long waves $\left(\frac{k_\parallel L}{2} \ll 1\right)$

$$\vec{j_s}\left(\vec{k}\right) = \frac{1}{2}\frac{I_0L}{(2\pi)^3}\vec{1a} \tag{43}$$

This is the Fourier transformed delta function at the origin with strength $\frac{1}{2}I_0L$.

7 Inverse Fourier transformation

We now have explicit expressions for Z and $\vec{j_s}$, and the Fourier transformed $\vec{E}$ field is $\hat{\vec{E}} = Z_B\vec{j_s}$. Then, the inverse Fourier transformation is

$$\vec{E}\left(\vec{x}\right) = \int\int\int \hat{\vec{E}}\left(\vec{k}\right)e^{-i\vec{k}\cdot\vec{x}}d^3\vec{k} \tag{44}$$

$$\hat{\vec{E}} = Z_BA\vec{j_s} \text{ with } A = \begin{bmatrix} \sin\alpha \\ 0 \\ \cos\alpha \end{bmatrix} \tag{45}$$

Z_B is shown in Eq.(29)

$$d^3\vec{k} = k^2dk\sin\theta d\theta d\phi$$

The process for integration is as follows.

1. Fix θ, ϕ, and integrate on k from 0 to ∞. Integration on k is effected in the complex k plane.

2. For θ and ϕ integration, we will use the stationary point method (explanation in [10 Stationary point method]). After k integration, for large kr (far field) identify the values (θ, ϕ) that make the phase $(\vec{k} \cdot \vec{x})$ stationary for each observation point $\vec{x}$.

156

3. We can carry out the θ, ϕ integration by covering the vicinity of the stationary points only. At the stationary point, (θ_s, ϕ_s), we can take the $\vec{E}\left(\vec{k}\right)$ term out of the integral and also we can expand $(\vec{k} \cdot \vec{x})$ to quadratic order in $\theta - \theta_s$ and $\phi - \phi_s$.

4. Perform the integration of $e^{-i\vec{k}\cdot\vec{x}}$ ($\vec{k}\cdot\vec{x}$ has only zeroth and second order terms now). This completes the process for most observation points $\vec{x}$.

5. For certain observation points $\vec{x}$ where the second derivative of $\vec{k}\cdot\vec{x}$ is zero, the expansion must be carried out to the next order.
For observation points along $\vec{B}$, we need another treatment for the integration because the ϕ derivative of $\vec{k}\cdot\vec{x}$ is zero at that point.
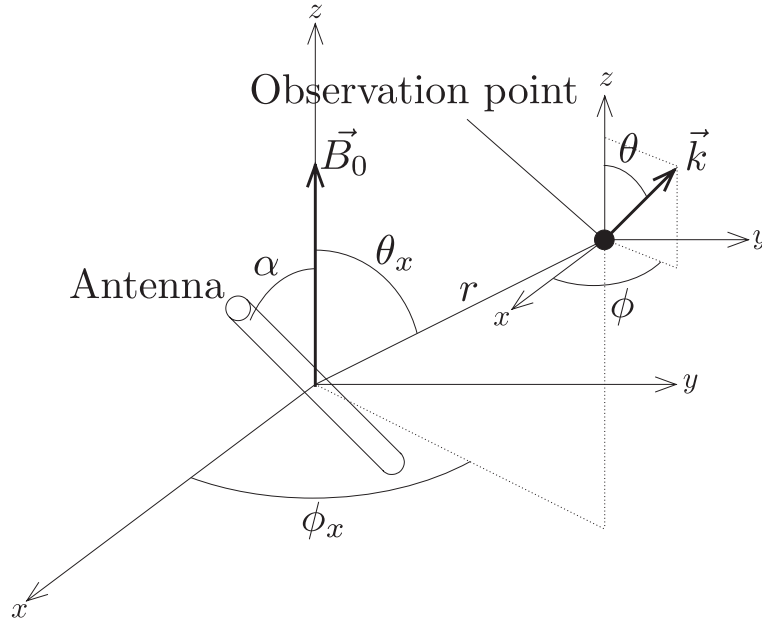
Figure 5: Antenna, observation point and $\vec{k}$

157

8 Causality considerations

At some distance from the antenna, information and power travel at the group velocity.

$$\vec{v_G} = \frac{\partial \omega}{\partial \vec{k}} \tag{46}$$

We define polar angles

θ, ϕ :polar angle of $\vec{k}$

θ_x, ϕ_x :polar angles of the vector to the observation point

θ_G, ϕ_G :polar angles of $\vec{v_G}$

The direction of $\vec{v_G}$ should be same as the direction of the observation point. So, for the waves to be observed from (θ_x, ϕ_x),

$$\theta_G = \theta_x, \phi_G = \phi_x \tag{47}$$

should be satisfied. For very small damping ($\delta \ll \nu$), the dispersion relations (Eq.(20) and Eq.(21))become

$$K_u^2 = \frac{\nu}{\cos\theta - \nu} \left(\text{or} \quad \nu = \frac{K_u^2 \cos\theta}{1 + K_u^2} \right) \tag{48}$$

$$K_d^2 = \frac{-\nu}{\cos\theta + \nu} \left(\text{or} \quad \nu = -\frac{K_d^2 \cos\theta}{1 + K_d^2} \right) \tag{49}$$

So, we define

$$K_{u+} = \sqrt{\frac{\nu}{\cos\theta - \nu}}$$

$$K_{u-} = -\sqrt{\frac{\nu}{\cos\theta - \nu}}$$

$$K_{d+} = \sqrt{\frac{-\nu}{\cos\theta + \nu}} \tag{50}$$

$$K_{d-} = -\sqrt{\frac{-\nu}{\cos\theta + \nu}}$$

158

K_u propagates only for $\theta < \cos^{-1}\nu$, K_d propagates only for $\theta > \pi - \cos^{-1}\nu$, where $\nu = \frac{\omega}{\omega_{ce}}$. Using $K_x = K\sin\theta\cos\phi$, $K_y = K\sin\theta\sin\phi$, $K_z = K\cos\theta$, so for K_u wave,

$$V_{Gxu} = \frac{v_{Gx}}{\omega_{ce}l} = \frac{\partial\omega}{\partial K_x}\frac{1}{\omega_{ce}l} = K_z\frac{1-K^2}{(1+K^2)^2}\frac{K_x}{K}$$

$$V_{Gyu} = \frac{v_{Gy}}{\omega_{ce}l} = \frac{\partial\omega}{\partial K_y}\frac{1}{\omega_{ce}l} = K_z\frac{1-K^2}{(1+K^2)^2}\frac{K_y}{K} \tag{51}$$

$$V_{Gzu} = \frac{v_{Gz}}{\omega_{ce}l} = \frac{\partial\omega}{\partial K_z}\frac{1}{\omega_{ce}l} = \frac{K}{1+K^2}\left(1 + \frac{1-K^2}{1+K^2}\cos^2\theta\right)$$

and for the K_d wave,

$$V_{Gxd} = -K_z\frac{1-K^2}{(1+K^2)^2}\frac{K_x}{K}$$

$$V_{Gyd} = -K_z\frac{1-K^2}{(1+K^2)^2}\frac{K_y}{K} \tag{52}$$

$$V_{Gzd} = -\frac{K}{1+K^2}\left(1 + \frac{1-K^2}{1+K^2}\cos^2\theta\right)$$

From Eq.(50), Eq.(51), and Eq.(52),

$$\cos\theta_{Gu+} = \frac{2\cos\theta\,(\cos\theta - \nu) + \sin^2\theta}{\sqrt{4\,(\cos\theta - \nu)^2 + \sin^2\theta}}$$

$$\cos\theta_{Gu-} = -\frac{2\cos\theta\,(\cos\theta - \nu) + \sin^2\theta}{\sqrt{4\,(\cos\theta - \nu)^2 + \sin^2\theta}}$$

$$\cos\theta_{Gd+} = -\frac{2\cos\theta\,(\cos\theta + \nu) + \sin^2\theta}{\sqrt{4\,(\cos\theta + \nu)^2 + \sin^2\theta}} \tag{53}$$

$$\cos\theta_{Gd-} = \frac{2\cos\theta\,(\cos\theta + \nu) + \sin^2\theta}{\sqrt{4\,(\cos\theta + \nu)^2 + \sin^2\theta}}$$

There are three methods to visualize the wave propagation:

1. $\vec{V_G}$ graph

2. $\vec{k}$ tip graph

159

3. θ vs θ_x graph

The $\vec{V}_G$ graph is a locus of the components of $\vec{V}_G$ along $\vec{B}_0$ and perpendicular to $\vec{B}_0$, with the $\vec{k}$ direction θ as a running parameter. Fig.(6) is the $\vec{V}_G$ graph for $\nu = 0.1$. For the K_u wave, $\vec{V}_G$ is on the $\hat{z}$ axis for $\theta = 0$, then θ_G increases until it reaches a maximum, then it decreases to zero at $\theta = \cos^{-1}(2\nu)$ and goes to negative. When $\theta = \cos^{-1}\nu$, the K_u wave is resonant. The K_u wave doesn't propagate for $\theta > \cos^{-1}\nu$, so that branch ends at this point.

Figure 6: $\vec{V}_G$ graph

160
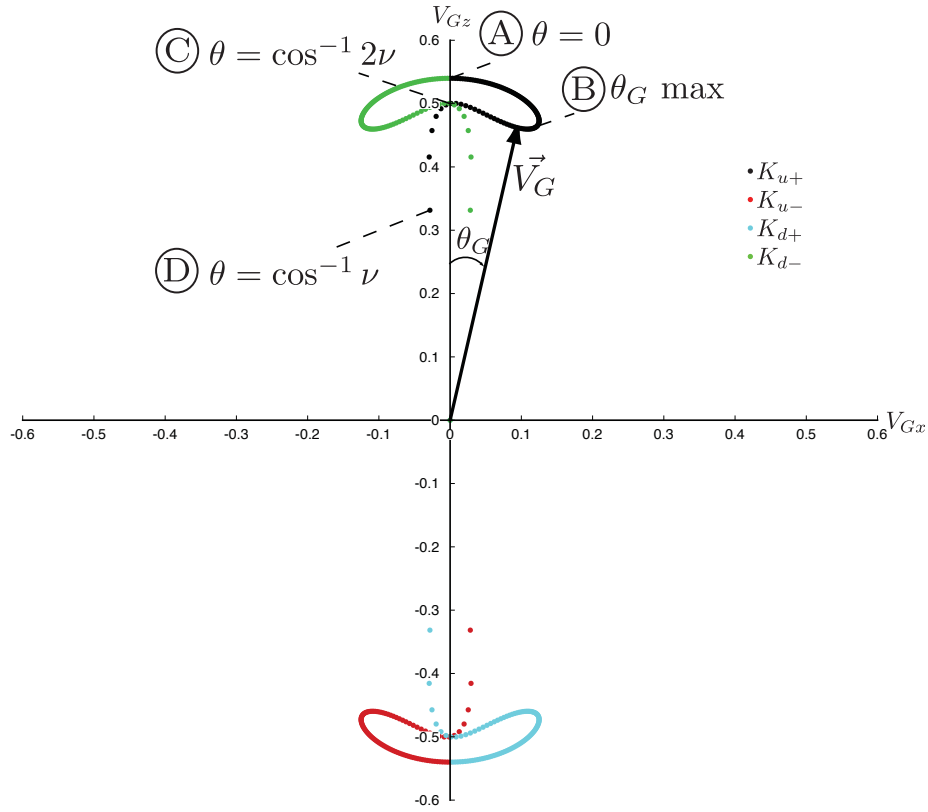
The $\vec{k}$ tip graph is a locus of $\vec{k}$ with θ as a running parameter. $\vec{V_G}$ is perpendicular to the locus of $\vec{k}$ at each point. Fig.(7) is the $\vec{k}$ tip graph for $\nu = 0.1$. For the K_u wave, θ cannot be larger than $\cos^{-1}\nu$, so the $\vec{k}$ tip curve for K_u goes to the asymptotes $\theta = \cos^{-1}\nu$.
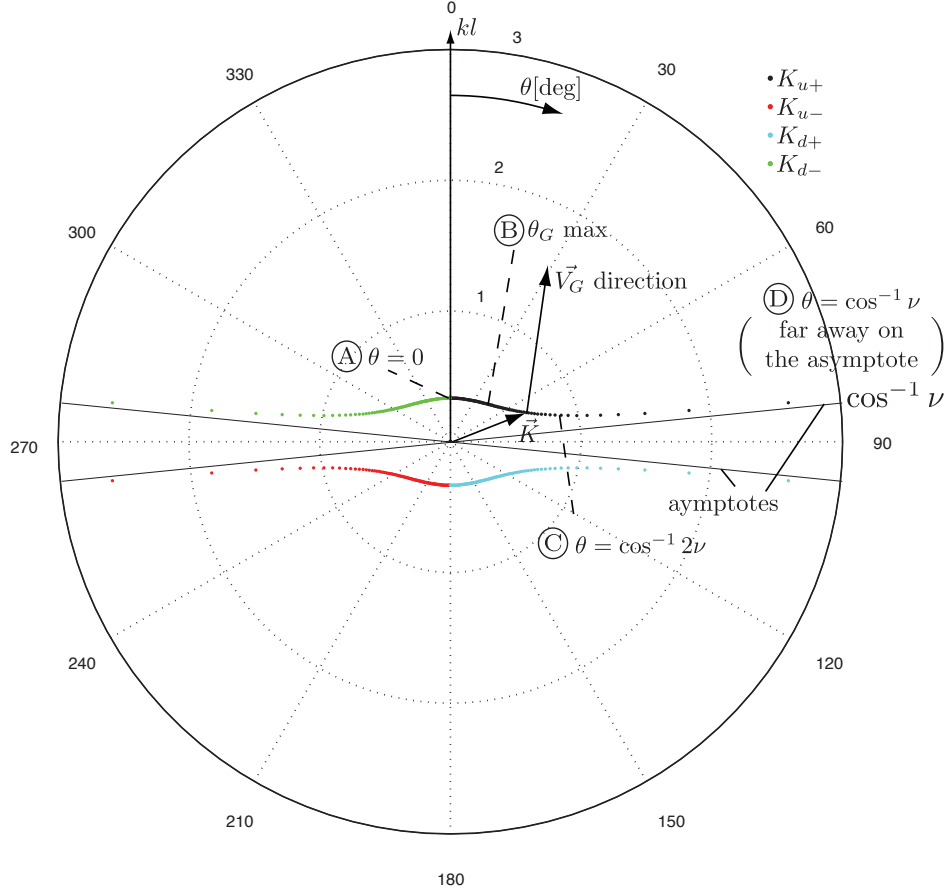
Figure 7: $\vec{k}$ tip graph

161

Using Eq.(53), we can draw the θ vs θ_x graph because for the wave to propagate, θ_x should be equal to θ_G. Fig.(8) is the θ vs θ_x graph for $\nu = 0.1$. For one observation point with θ_x, only the waves with θ on those curves in the graph can propagate. In Fig.(7), Fig.(8) and Fig.(8), Ⓐ, Ⓑ, Ⓒ and Ⓓ corresponds to

Ⓐ:$\theta = 0$, Ⓑ:θ_G max, Ⓒ:$\theta = \cos^{-1} 2\nu$, Ⓓ:$\theta = \cos^{-1} \nu$

Figure 8: θ vs θ_x graph

162
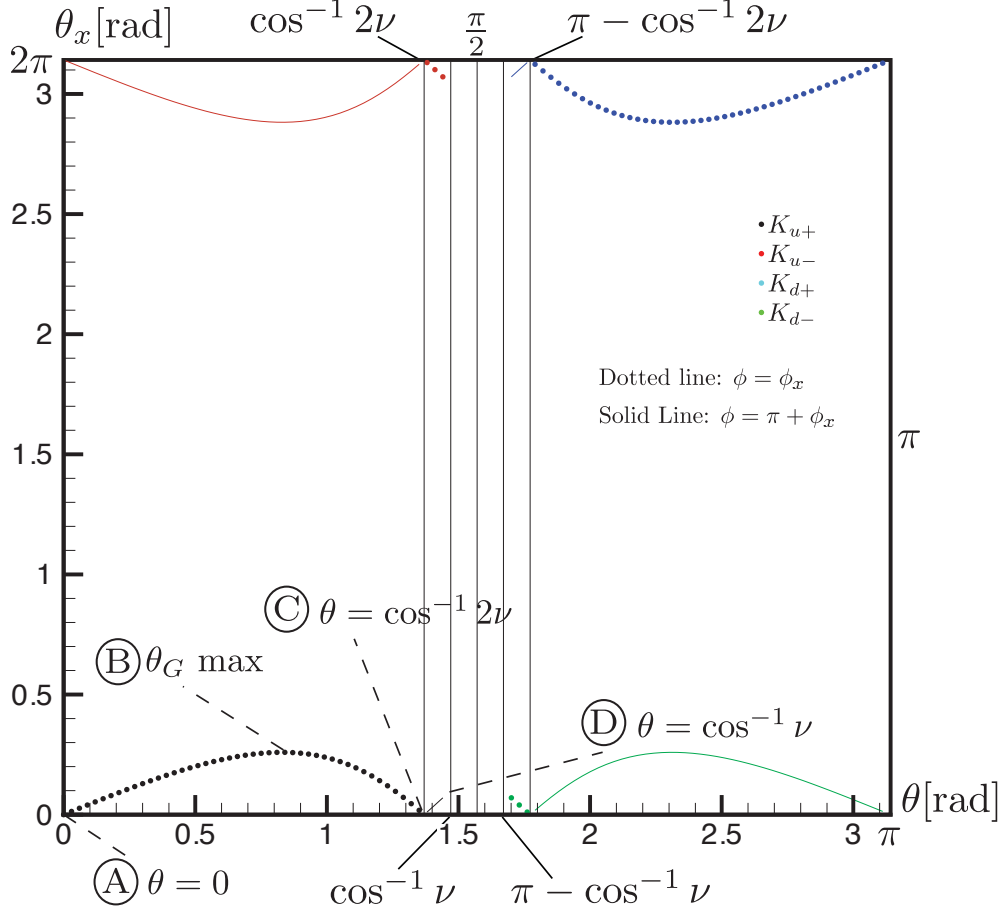
The branch that is observed, as well as the particular $\vec{k}$ within that branch, changes as the observation point angle θ_x changes. First, if the observation point is very near to the $\hat{z}$ axis, which means $\theta_x \approx 0$ but positive, three waves (2 K_{u+} waves and 1 K_{d-} wave) propagate as in Fig.(9), Fig.(10), and Fig.(11) at $\phi = \phi_x$. Also three waves (2 K_{d-} waves and 1 K_{u+} wave) propagate to the points very near to the $\hat{z}$ axis at $\phi = \pi + \phi_x$, only "behind" $\vec{B_0}$.
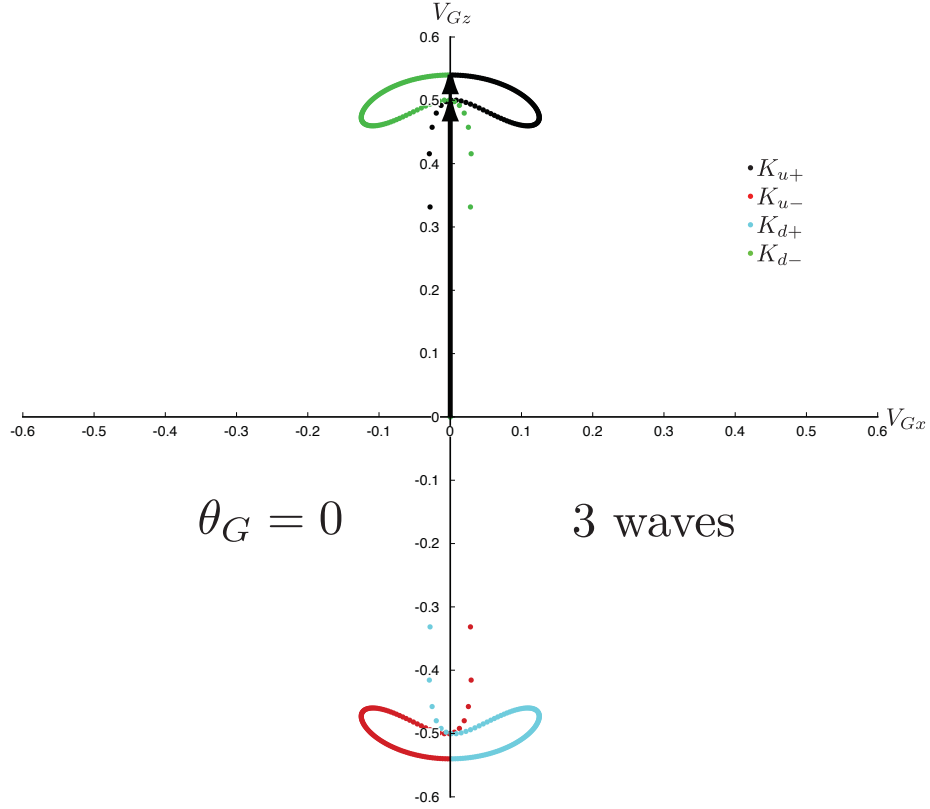
Figure 9: Region 1 $\vec{V_G}$ graph (Propagation along $\vec{B_0}$)

163
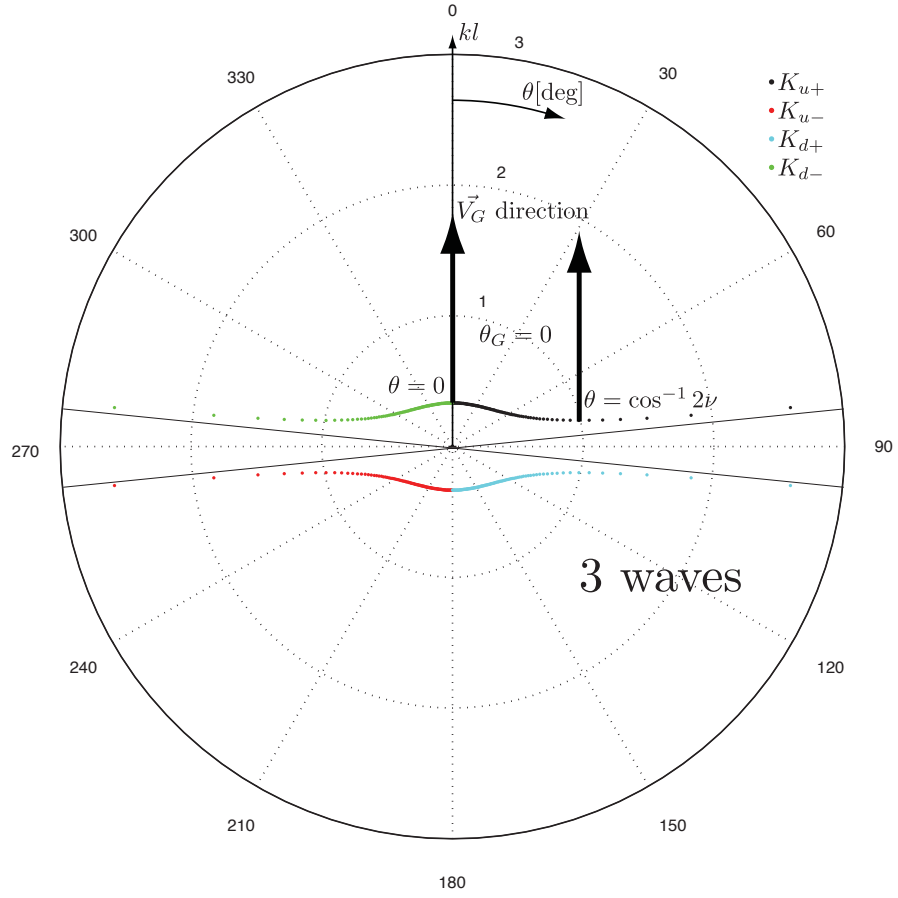
Figure 10: Region 1 $\vec{k}$ tip graph (Propagation along $\vec{B_0}$)
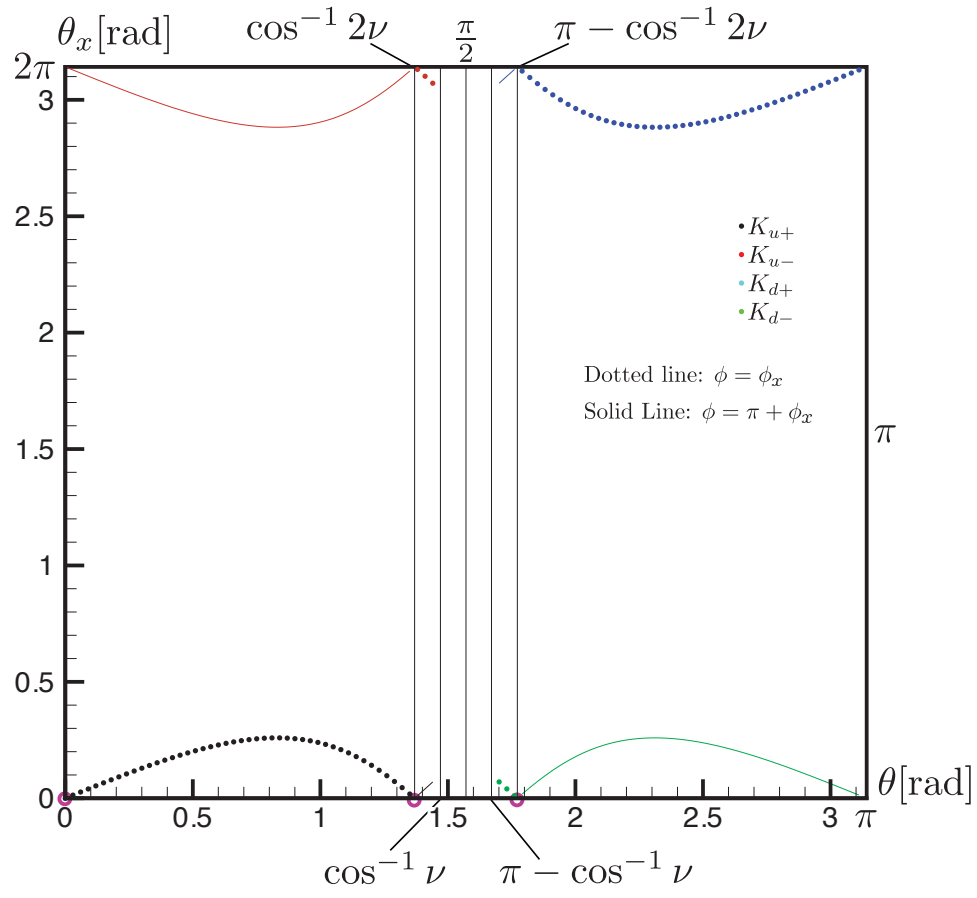
Figure 11: Region 1 θ vs θ_x graph (Propagation along $\vec{B}_0$)

In region 2, where $0 < \theta_x < \sin^{-1}\nu$, three waves (2 K_{u+} waves and 1 K_{d-} wave) propagates as in Fig.(12), Fig.(13), and Fig.(14). Again, there are three other waves observable from the (nearby) symmetric direction behind $\vec{B}_0$.
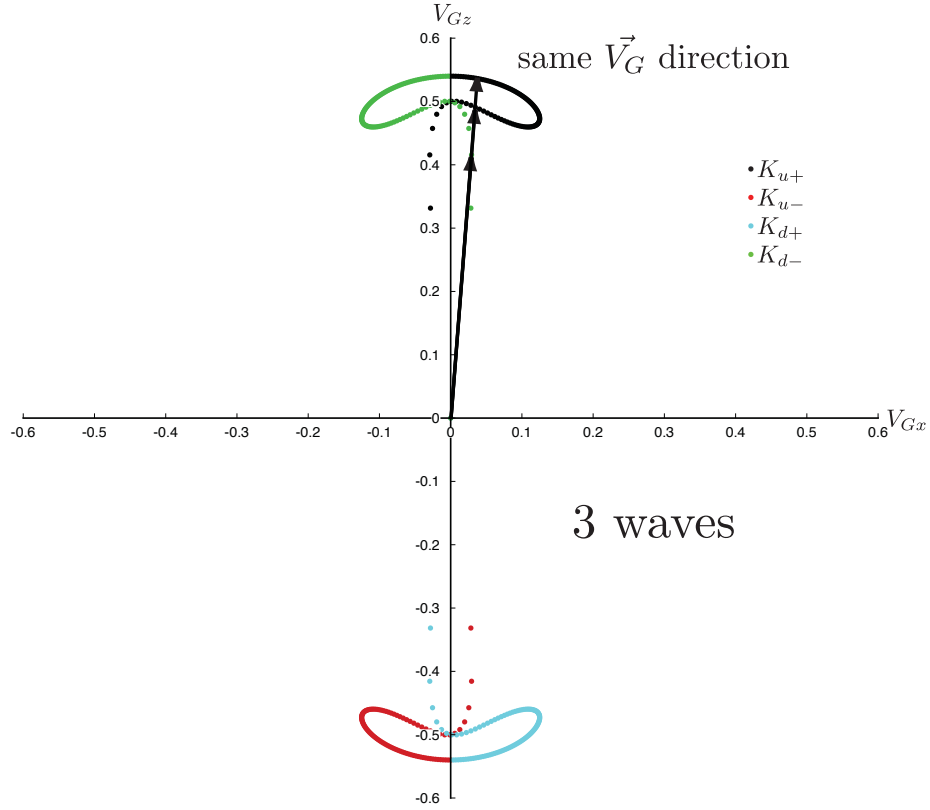
Figure 12: Region 2 $\vec{V}_G$ graph (very near $\vec{B}_0$)

166
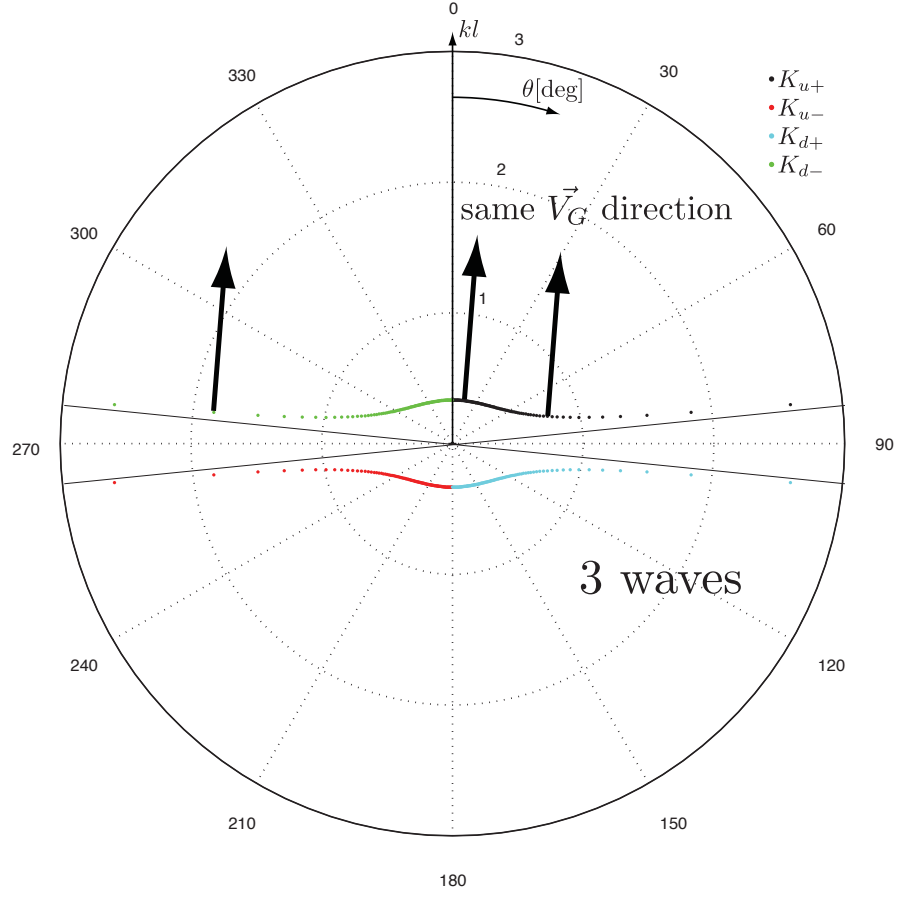
Figure 13: Region 2 $\vec{k}$ tip graph (very near $\vec{B_0}$)
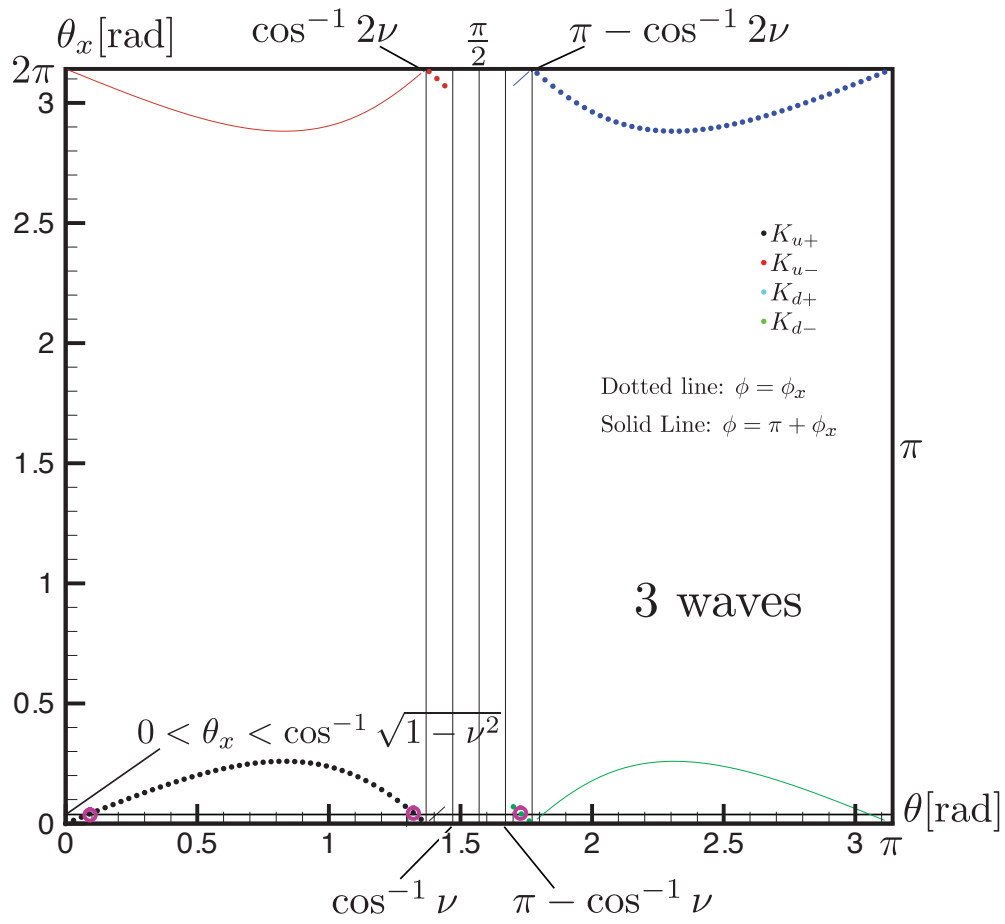
Figure 14: Region 2 θ vs θ_x graph (very near $\vec{B}_0$)

On the point where $\theta_x = \sin^{-1} \nu$, three waves (2 K_{u+} waves and 1 K_{d-} wave) propagates, of which the K_{d-} wave is resonant as in Fig.(15), Fig.(16), and Fig.(17). From Fig.(16), we can easily know that θ_x at the resonant point is $\theta_x = \frac{\pi}{2} - \cos^{-1} \nu = \sin^{-1} \nu$
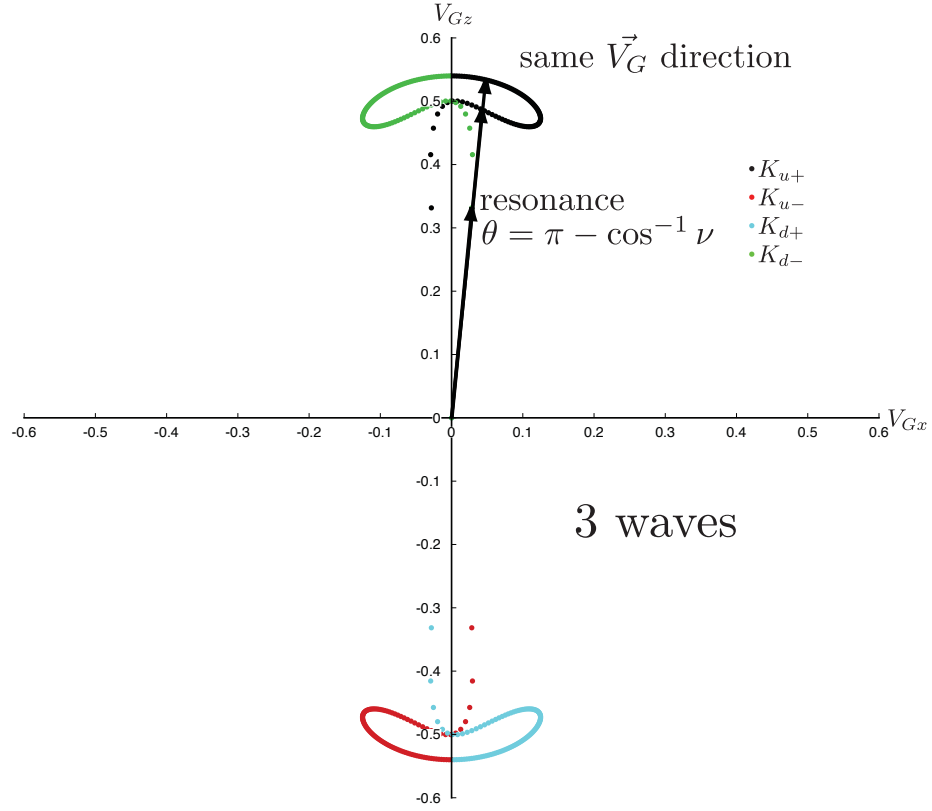
Figure 15: Region 3 $\vec{V_G}$ graph (on the resonance cone)

169
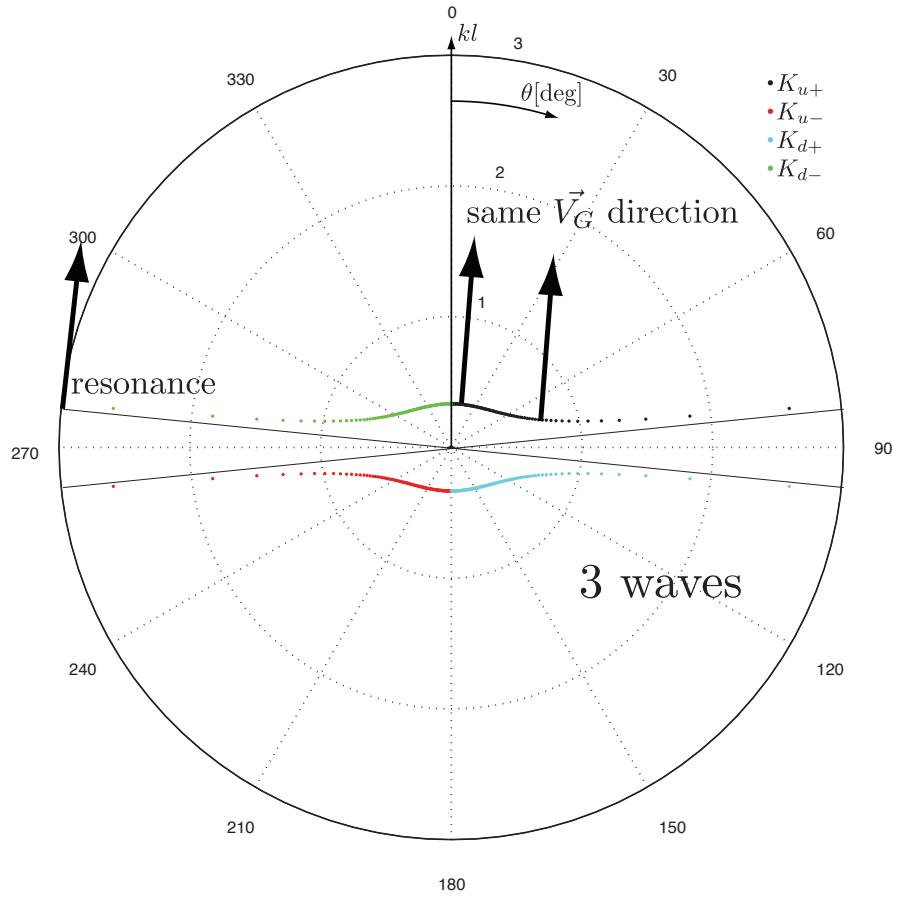
Figure 16: Region 3 $\vec{k}$ tip graph (on the resonance cone)
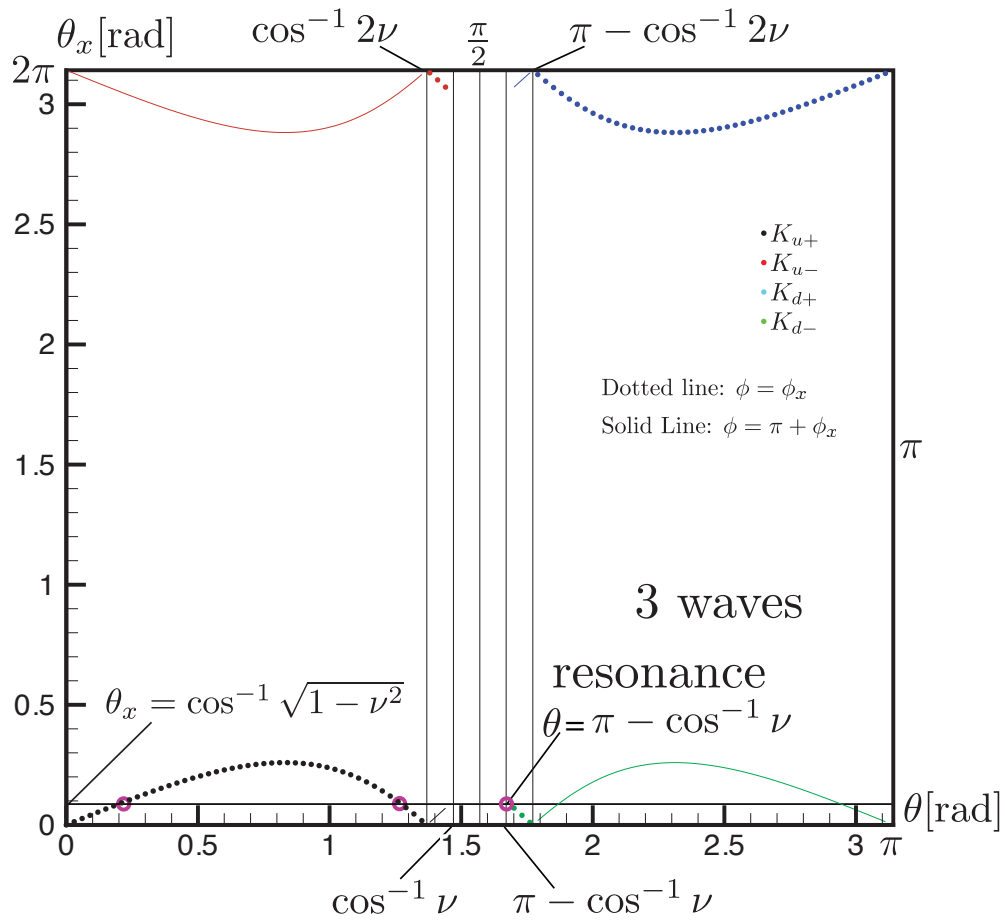
Figure 17: Region 3 θ vs θ_x graph (on the resonance cone)

In region 4, where $\sin^{-1} \nu < \theta_x < \cos^{-1} \dfrac{4\left(1-\nu^2\right)}{3\sqrt{2\left(1-\nu^2\right)-2\nu\sqrt{\frac{1-\nu^2}{3}}}}$, two waves (2

K_{u+} waves) propagates as in Fig.(18), Fig.(19), and Fig.(20).
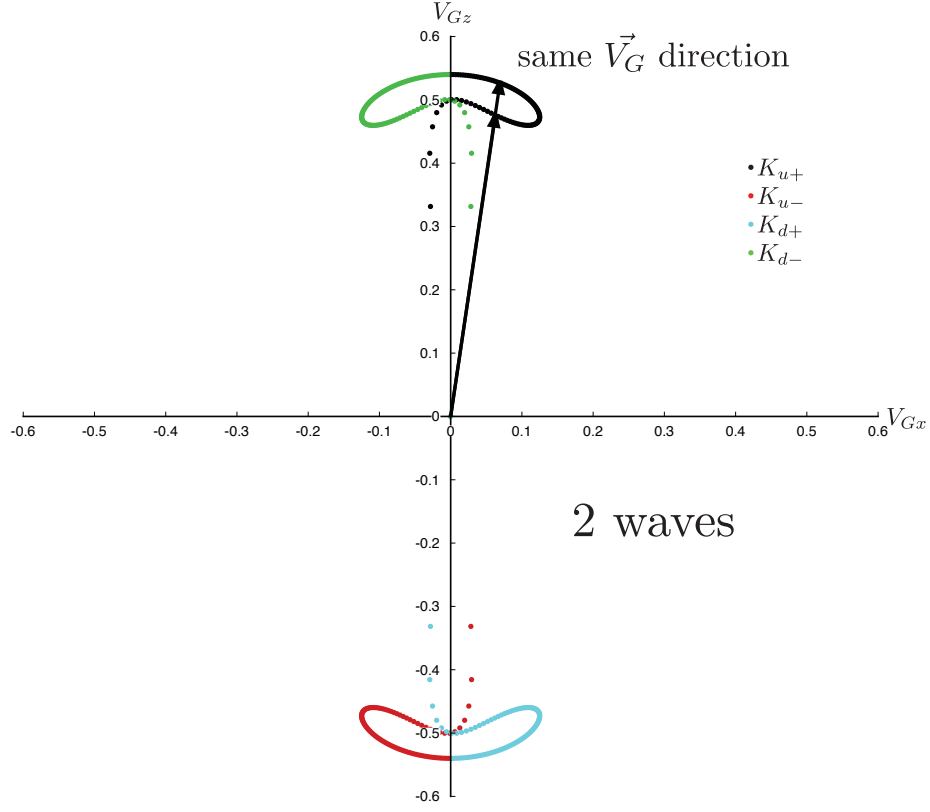
Figure 18: Region 4 $\vec{V_G}$ graph (outside resonance cone, but within propagation cone)
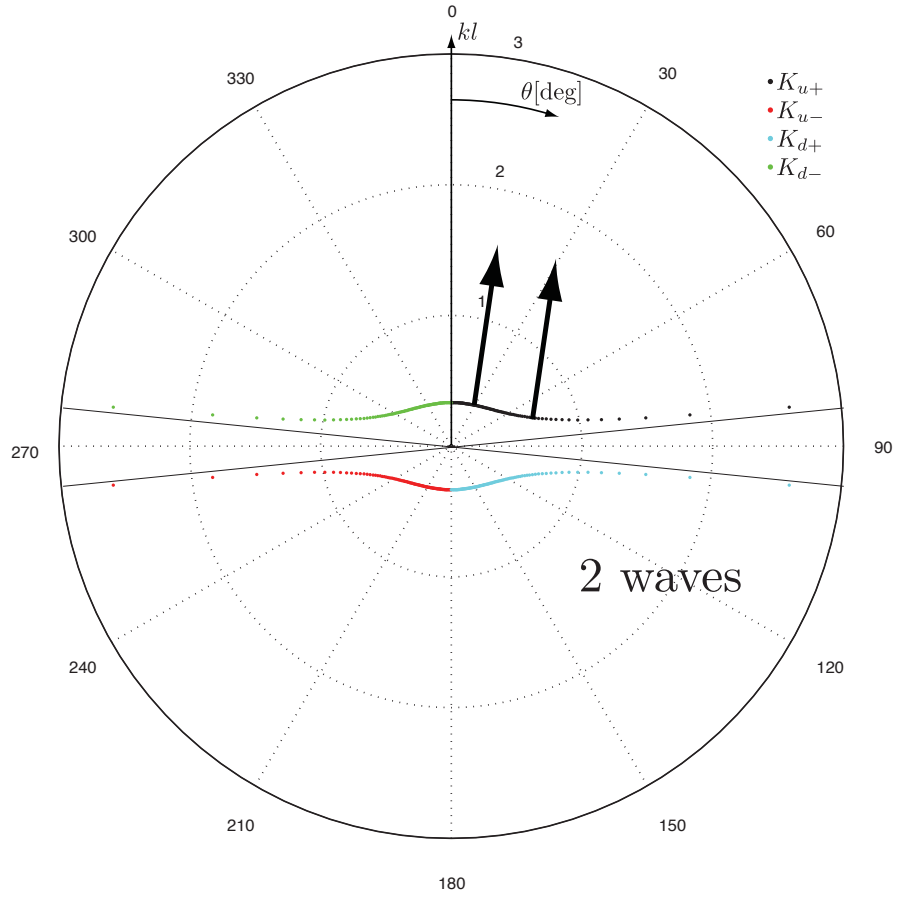
Figure 19: Region 4 $\vec{k}$ tip graph (outside resonance cone, but within propagation cone)
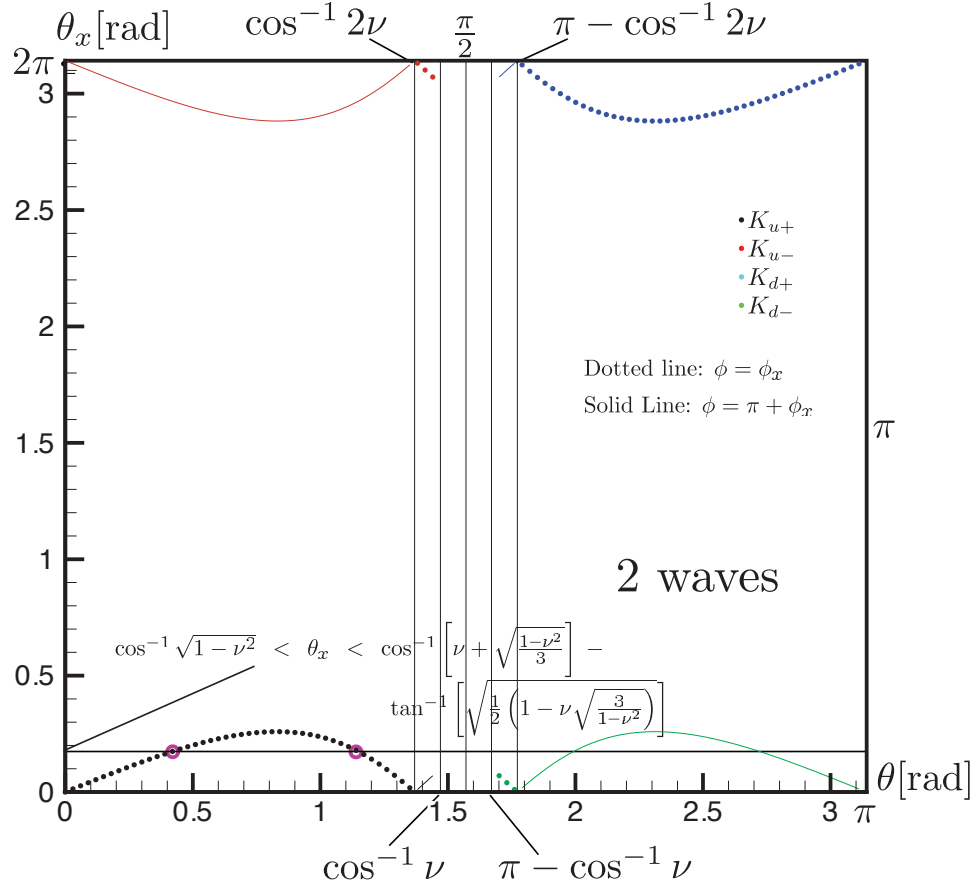
Figure 20: Region 4 θ vs θ_x graph (outside resonance cone, but within propagation cone)

174

On the cone where $\theta_x = \theta_{x\text{MAX}} = \cos^{-1}\left[\dfrac{4\left(1-\nu^2\right)}{3\sqrt{2(1-\nu^2)-2\nu\sqrt{\frac{1-\nu^2}{3}}}}\right]$, only one

wave (1 K_{u+} wave) propagates as in Fig.(21), Fig.(22), and Fig.(23). θ_G reaches its maximum and no wave can propagate in the region where $\theta_x >$

$\cos^{-1}\left[\dfrac{4\left(1-\nu^2\right)}{3\sqrt{2(1-\nu^2)-2\nu\sqrt{\frac{1-\nu^2}{3}}}}\right]$. From Fig.(23), $\frac{\partial^2 \Phi}{\partial \theta^2} = 0$ on this point. This yields

$$\cos\theta = \nu + \sqrt{\frac{1-\nu^2}{3}} \tag{54}$$

From Eq.(53),

$$\theta_G = \cos^{-1}\frac{4\left(1-\nu^2\right)}{3\sqrt{2\left(1-\nu^2\right)-2\nu\sqrt{\frac{1-\nu^2}{3}}}} \tag{55}$$
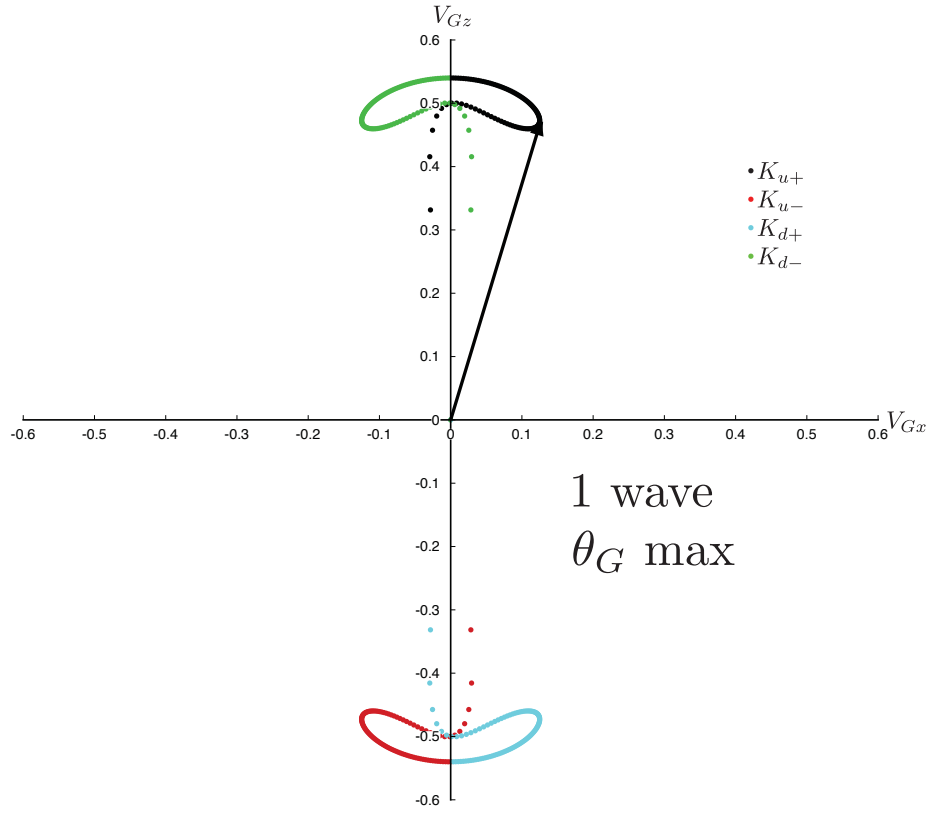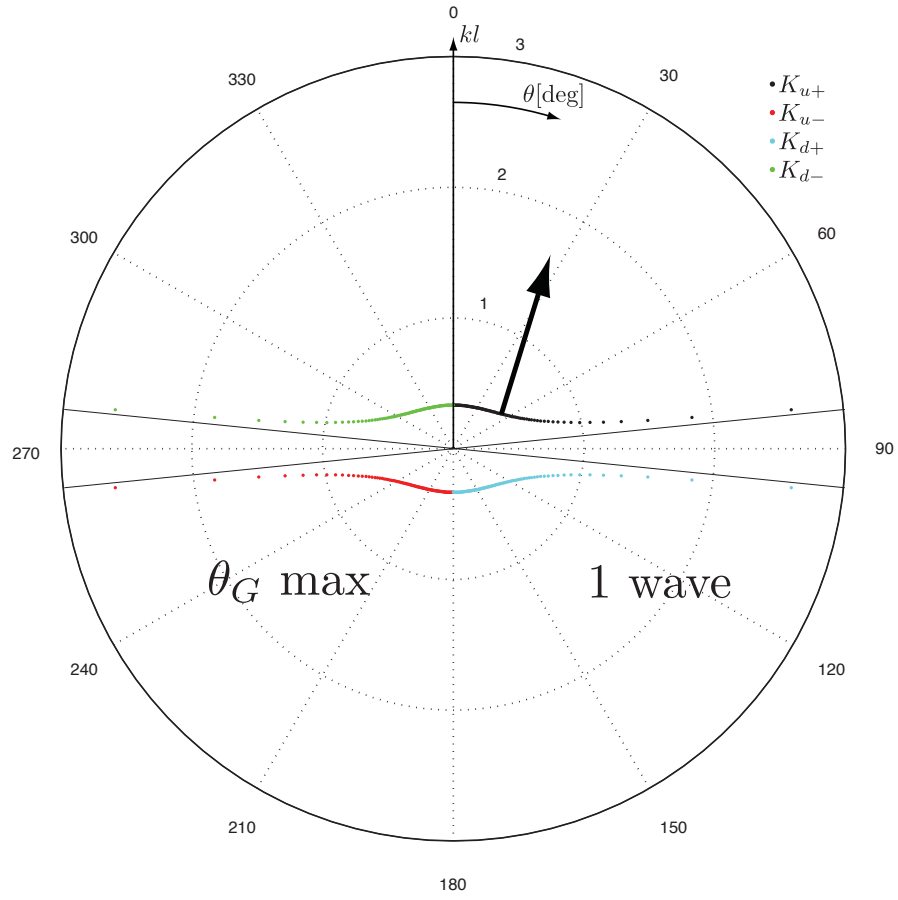
Figure 21: Region 5 $\vec{V_G}$ graph (on the edge of the propagation cone)

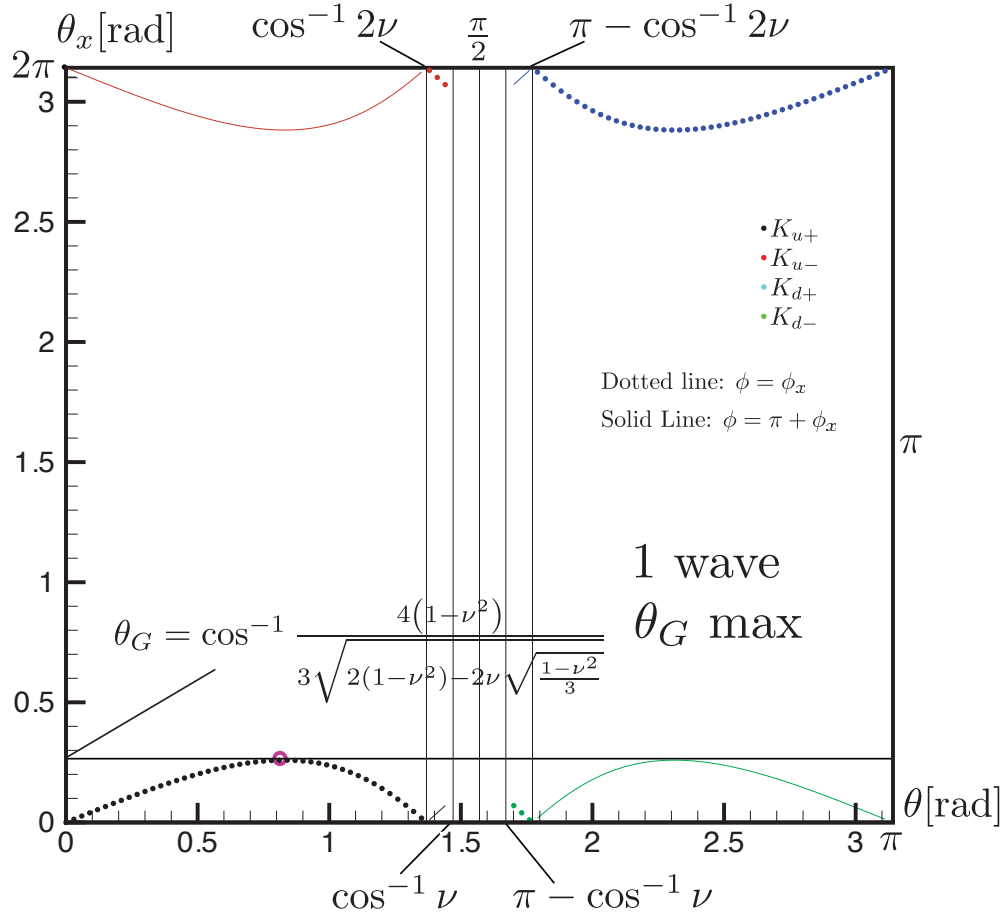Figure 22: Region 5 $\vec{k}$ tip graph (on the edge of the propagation cone)

Figure 23: Region 5 θ vs θ_x graph (on the edge of the propagation cone)

The same (symmetric) discussion applies in the vicinity of $\theta_x = \pi$, this time involving the K_{u-} and K_{d+} branches.

9 K integration

As a first step in computing the inverse Fourier transform (Eq.(44)), we fix the observation point $\vec{x}(r, \theta_x, \phi_x)$ and the wave direction (θ, ϕ) of $\vec{k} = \vec{K}/l$, then perform k integration. Now, allow K to be a complex variable and perform complex integration using the residue theorem, although the K integration is in principle along the real axis. In order to use the residue theorem, we need to close the path of integration around some of the poles of $\vec{\tilde{E}}(K)$, which are $K_{u\pm}$ and $K_{d\pm}$ as given by Eq.(20) and Eq.(21). This closure should be done in the half plane in which the $e^{i\vec{k}\cdot\vec{x}}$ does not diverge. Thus the imaginary part of $\vec{k} \cdot \vec{x}$ should be negative in this closure.
Now

$$\vec{k} \cdot \vec{x} = \frac{r}{l} K \left[\sin\theta \sin\theta_x \cos(\phi - \phi_x) + \cos\theta \cos\theta_x \right] \tag{56}$$

$$\equiv \frac{r}{l} K \cos\gamma \tag{57}$$

γ is the angle between $\vec{k}$ and $\vec{x}$, and $\cos\gamma$ is the bracket in Eq.(56). Thus, when $\cos\gamma > 0$, we must have $\text{Im}(K) < 0$, and vice versa. Since $\vec{v_G}$ should be along $\vec{x}$, γ is also the angle between $\vec{k}$ and $\vec{v_G}$.
We limit discussion to K_{u+} and K_{d-}, because the K_{u-} and K_{d+} case follows by symmetry. From the $\vec{k}$ tip graphs in the causality considerations section, the angle between $\vec{k}$ and $\vec{v_G}$ is always less than 90°. So, $\cos\gamma$ is always positive. Then, the integration path and relevant poles are shown circled in Fig.(24). With the residue theorem, the inverse Fourier transform is now reduced to a double integral as follows.

$$\vec{E}_{(\vec{r})} = \frac{1}{2} \int_\theta \int_\phi 2\pi i \text{Res} \left[k^2 \vec{\tilde{E}}_{(\vec{k})} e^{i\vec{k}\cdot\vec{x}} @ \text{pole} K_{u,d} \right] \sin\theta d\theta d\phi \tag{58}$$

(the $\frac{1}{2}$ is because the original K integration is in $(0, \infty)$, not $(-\infty, \infty)$). Poles are from $\frac{1}{\triangle}$ in Eq.(29)(K_u and K_d are the roots of $\triangle = 0$). Thus, the
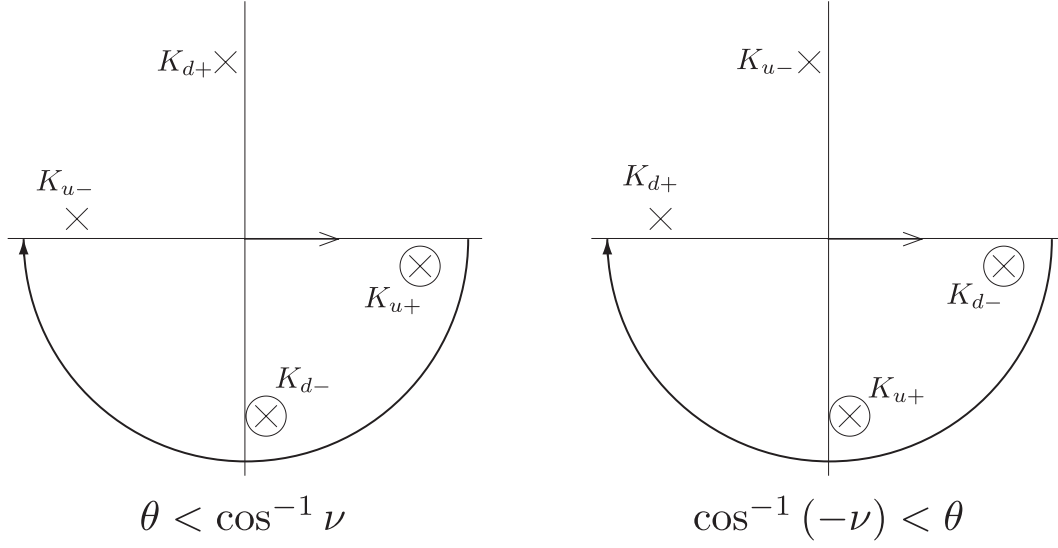
179

$$\theta < \cos^{-1} \nu \qquad\qquad \cos^{-1}(-\nu) < \theta$$

Figure 24: K and integration path

residue of $\frac{1}{\triangle}$ is

$$\text{Res}\left(\frac{1}{\triangle}\right) = \left.\frac{K - K_{u\pm}}{-\frac{\cos^2\theta - \nu^2}{\nu^2}\left(K^2 - K_d^2\right)\left(K^2 - K_u^2\right)}\right|_{K=K_{u\pm}} = \frac{\mp\sqrt{\nu\left(\cos\theta - \nu\right)}}{4\cos\theta} \tag{59}$$

for $K_{u\pm}$, and

$$\text{Res}\left(\frac{1}{\triangle}\right) = \left.\frac{K - K_{d\pm}}{-\frac{\cos^2\theta - \nu^2}{\nu^2}\left(K^2 - K_d^2\right)\left(K^2 - K_u^2\right)}\right|_{K=K_{d\pm}} = \frac{\pm\sqrt{\nu\left(-\cos\theta - \nu\right)}}{4\cos\theta} \tag{60}$$

for $K_{d\pm}$.

We can get $\text{Res}\left[\vec{E}_{(\vec{k})}e^{i\vec{k}\cdot\vec{x}}@\text{pole}K_{u,d}\right]$ using Eq.(59), Eq.(60), and substituting K_u and K_d into Eq.(44) and Eq.(45). Then, considering the direction of the integration paths, the integration is

$$\vec{E}_{(\vec{x})} = \int_\theta \int_\phi 2\pi i \left(\sum_{\text{valid waves}} Z_B\right) A_\alpha \vec{\hat{j}}_s e^{i\frac{r}{l}\sqrt{\nu}\Phi_{(\theta,\phi,\theta_x,\phi_x)}} \sin\theta d\theta d\phi \tag{61}$$

$$A_\alpha = \begin{bmatrix} \sin\alpha \\ 0 \\ \cos\alpha \end{bmatrix} \tag{62}$$

$$\Phi_{(\theta,\phi,\theta_x,\phi_x)} = \frac{\sin\theta\sin\theta_x\cos(\phi-\phi_x) + \cos\theta\cos\theta_x}{\sqrt{\cos\theta-\nu}} \tag{63}$$

$Z_{B(K_{u\pm})}$

$$= -\frac{\sqrt{\nu(\cos\theta-\nu)}}{4\sigma_{ce}\cos\theta} \left[\begin{array}{c} -p + K^2\sin^2\theta\left(-p\cos^2\phi + \frac{i}{\nu}\sin^2\phi\right) \\ -\left(1+K^2\sin^2\theta\right) - iK^2\left(1+K^2\right)\left(\frac{1}{\nu}-\nu\right)\sin^2\theta\sin\phi\cos\phi \\ -K^2\left(p\cos\phi+\sin\phi\right)\sin\theta\cos\theta \\[6pt] -\left(1+K^2\sin^2\theta\right) - iK^2\left(1+K^2\right)\left(\frac{1}{\nu}-\nu\right)\sin^2\theta\sin\phi\cos\phi \\ -\left(p - i\frac{K^2}{\nu}\sin^2\theta\right)\cos^2\phi - p\left(1+K^2\sin^2\theta\right)\sin^2\phi \\ K^2\left(-p\sin\phi+\cos\phi\right)\sin\theta\cos\theta \\[6pt] K^2\sin\theta\cos\theta\left(\sin\phi - p\cos\phi\right) \\ -K^2\sin\theta\cos\theta\left(p\sin\phi+\cos\phi\right) \\ -pK^2\cos^2\theta + i\nu\left(1+K^2\right) \end{array} \right]_{K=K_{u\pm}} \tag{64}$$

$Z_{B(K_{d\pm})}$

$$= -\frac{\sqrt{\nu(-\cos\theta-\nu)}}{4\sigma_{ce}\cos\theta} \left[\begin{array}{c} -p + K^2\sin^2\theta\left(-p\cos^2\phi + \frac{i}{\nu}\sin^2\phi\right) \\ -\left(1+K^2\sin^2\theta\right) - iK^2\left(1+K^2\right)\left(\frac{1}{\nu}-\nu\right)\sin^2\theta\sin\phi\cos\phi \\ -K^2\left(p\cos\phi+\sin\phi\right)\sin\theta\cos\theta \\[6pt] -\left(1+K^2\sin^2\theta\right) - iK^2\left(1+K^2\right)\left(\frac{1}{\nu}-\nu\right)\sin^2\theta\sin\phi\cos\phi \\ -\left(p - i\frac{K^2}{\nu}\sin^2\theta\right)\cos^2\phi - p\left(1+K^2\sin^2\theta\right)\sin^2\phi \\ K^2\left(-p\sin\phi+\cos\phi\right)\sin\theta\cos\theta \\[6pt] K^2\sin\theta\cos\theta\left(\sin\phi - p\cos\phi\right) \\ -K^2\sin\theta\cos\theta\left(p\sin\phi+\cos\phi\right) \\ -pK^2\cos^2\theta + i\nu\left(1+K^2\right) \end{array} \right]_{K=K_{d\pm}} \tag{65}$$

10 The stationary point method

For the θ and ϕ integrations, we will use the stationary point method. For the integration Eq.(61), if r is large, which means the observation point is far from the antenna, the exponential term $e^{i\frac{r}{l}\sqrt{\nu}\Phi_{(\theta,\phi,\theta_x,\phi_x)}}$ oscillates much more

181

than the other terms $\left(2\pi i Z_{(K_{u,d})} A \vec{\hat{j}}_s \sin\theta\right)$. However, at some points where $\frac{\partial \Phi}{\partial \theta} = \frac{\partial \Phi}{\partial \phi} = 0$, the exponential term does not vary rapidly. These points are called stationary points. For example, Fig.(25) is the real part of the integrand (x component) with $r = 1000$km. There are two stationary points in this graph (red dots). For wave orientation (θ, ϕ) not near these stationary
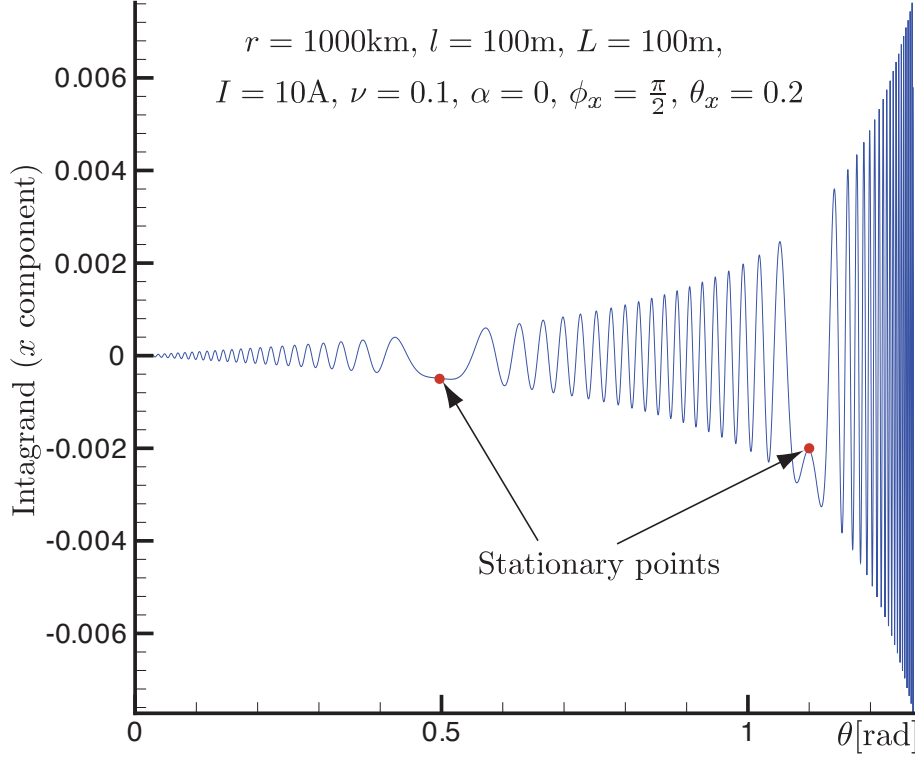

Figure 25: Integrand

points, the integrand $(\vec{E}\left(\vec{k}\right) e^{-i\vec{k}\cdot\vec{x}})$ contribution to the integration is small, because $e^{-i\vec{k}\cdot\vec{x}}$ term oscillates rapidly, and cancellations occur in the integration.

So, near the stationary point (θ_s, ϕ_s), we can take $\left(2\pi i Z_{(K_{u,d})} A \vec{\hat{j}}_s \sin\theta\right)$ terms out of the integral and we only have to integrate the exponential term. In addition, since only the vicinity of (θ_s, ϕ_s) contributes, the exponent can be expanded in a Taylor series about this point, where the first derivatives

182

are zero, and terms higher than second order in $(\theta - \theta_s)$, $(\phi - \phi_s)$ can be neglected. Fig.(26) is the plot of the stationary points $\left(\frac{\partial \Phi}{\partial \theta} = \frac{\partial \Phi}{\partial \phi} = 0\right)$ for observation direction θ_x, ϕ_x. The propagating wave lines in Fig.(8) are exactly on these stationary points lines. So, in the stationary phase method, the waves which do not propagate to the observation point are cancelled mathematically, and only the waves which propagate to the observation point (they are stationary points) contribute to the integration.
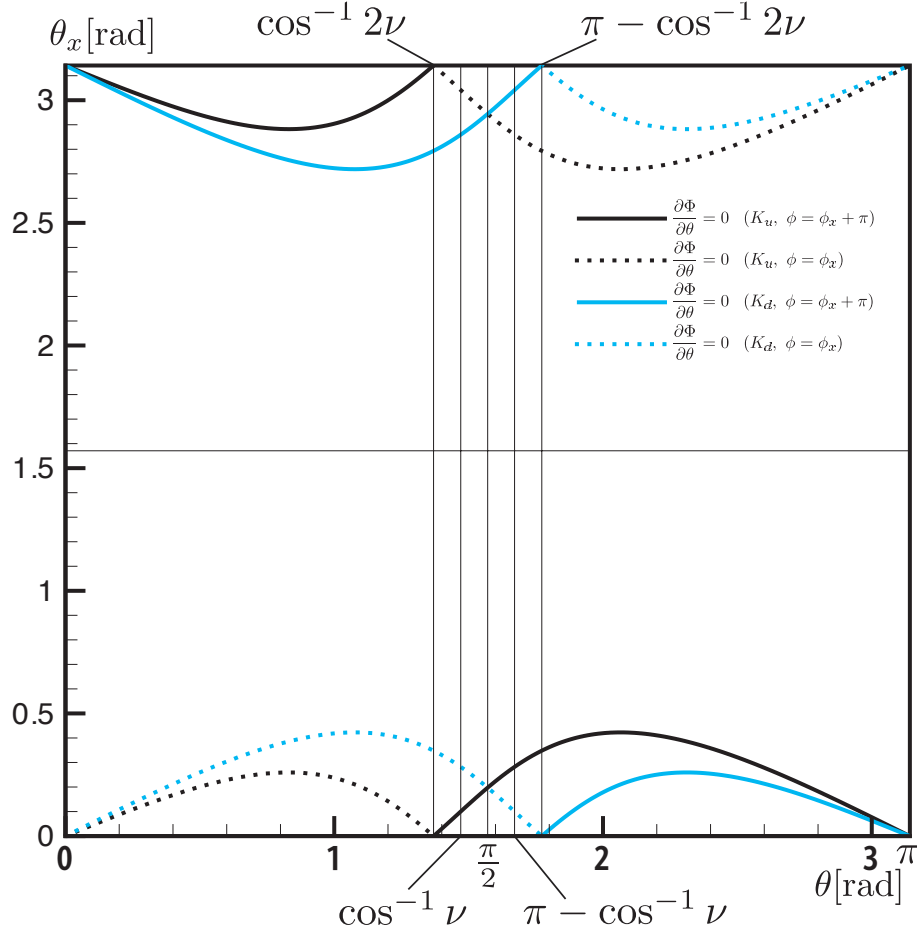
Figure 26: Stationary points

183

11 Propagation near $\vec{B}$

If the observation point is very near the magnetic field line from the antenna, there is a interesting phenomenon about wave proapagation. For this analysis, θ_x in Fig.(27) needs to be very small. After K integration, Eq.(61) can
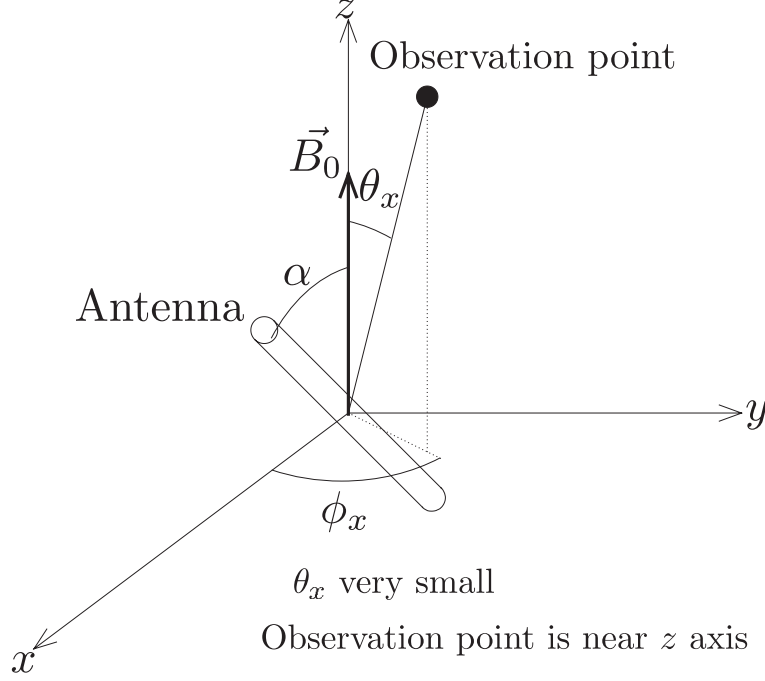

Figure 27: Observation point near $\vec{B}$ line

be written as

$$\vec{E} = 2\pi i G_{(\theta_s,\phi_x)} \int_\theta e^{-iA\frac{\cos\theta\cos\theta_x}{\sqrt{\cos\theta-\nu}}} \sin\theta d\theta \int_0^{2\pi} e^{-iA\frac{\sin\theta\sin\theta_x}{\sqrt{\cos\theta-\nu}}\cos(\phi-\phi_x)} d\phi \qquad (66)$$

with

$$G_{(\theta_s,\phi_x)} = \text{Res}\left[\vec{\tilde{E}}\right], A = \frac{r}{l}\sqrt{\nu}$$

And, using a Bessel function,

$$\vec{E} = 4\pi^2 i G_{(\theta_s,\phi_x)} \int_\theta J_0\left(A\frac{\sin\theta\sin\theta_x}{\sqrt{\cos\theta-\nu}}\right) e^{-iA\frac{\cos\theta\cos\theta_x}{\sqrt{\cos\theta-\nu}}} \sin\theta d\theta \qquad (67)$$

184

If the J_0 function can be moved out of the integral (this is valid only when $\theta_x \ll 1$, see discussion below) we obtain

$$
\begin{aligned}
\vec{E} &= 4\pi^2 i G_{(\theta_s,\phi_x)} J_0 \left(A \frac{\sin\theta_s \sin\theta_x}{\sqrt{\cos\theta - \nu}} \right) \int_\theta e^{-iA\frac{\cos\theta\cos\theta_x}{\sqrt{\cos\theta-\nu}}} \sin\theta d\theta \\
&= 4\pi^2 i G_{(\theta_s,\phi_x)} J_0 \left(A \frac{\sin\theta_s \sin\theta_x}{\sqrt{\cos\theta - \nu}} \right) \int_\theta e^{-iA\Phi'} \sin\theta d\theta \quad (68)
\end{aligned}
$$

$$
\Phi' = \frac{\cos\theta\cos\theta_x}{\sqrt{\cos\theta - \nu}}
$$

The stationary points for Φ' are $\theta \simeq 0$, $\cos^{-1} 2\nu$ from $\frac{\partial\Phi'}{\partial\theta} = 0$. However, because of the $\sin\theta$ term in Eq.(68), $\theta = 0$ has no contribution to the integral, so we only have to include a stationary point $u = \cos\theta = 2\nu$. Taylor expansion of Φ' around $\theta = \cos^{-1} 2\nu$ with $u = \cos\theta \simeq 2\nu$ is (to second order) gives

$$
\begin{aligned}
\Phi' &= \frac{u\cos\theta_x}{\sqrt{u - \nu}} \\
&\simeq \left[\Phi|_{u=2\nu} + \left.\frac{\partial\Phi}{\partial u}\right|_{u=2\nu}(u-2\nu) + \frac{1}{2}\left.\frac{\partial^2\Phi}{\partial u^2}\right|_{u=2\nu}(u-2\nu)^2 \right]\cos\theta_x \quad (69) \\
&= \cos\theta_x \left[2\sqrt{\nu} + \frac{1}{4}\frac{1}{\nu^{3/2}}(u-2\nu)^2 \right]
\end{aligned}
$$

Then, Eq.(68) becomes

$$
\vec{E} = 4\pi^2 i G_{(\theta_s,\phi_x)} J_0 \left(A\sqrt{\frac{1-4\nu^2}{\nu}}\sin\theta_x \right) \int_{2\nu}^\infty e^{-iA\cos\theta_x\left(2\sqrt{\nu}+\frac{(u-2\nu)^2}{4\nu^{3/2}}\right)} du \quad (70)
$$

And finally we can get

$$
\vec{E} = 4\pi^{5/2} i^{1/2} G_{(\cos^{-1} 2\nu,\phi_x)} \sqrt{\nu} \frac{J_0\left(\frac{r}{l}\sqrt{1-4\nu^2}\sin\theta_x\right)}{\sqrt{\frac{r}{l}\cos\theta_x}} e^{-2i\nu\frac{r}{l}\cos\theta_x} \quad (71)
$$

$$
\left(\text{using } \int_{2\nu}^\infty e^{-iA\cos\theta_x\left(\frac{(u-2\nu)^2}{4\nu^{3/2}}\right)} du = \frac{2\nu^{3/4}}{\sqrt{iA\cos\theta_x}}\frac{\sqrt{\pi}}{2} \right)
$$

This equation shows that, if $\theta_x \simeq 0$, then the wave propagates as $\vec{E} \sim \left(\frac{l}{r}\right)^{1/2}$ (from $J_0 \simeq 1$), whereas if θ_x is sufficiently large to make the argument of J_o

185

large, then $\vec{E} \sim \frac{l}{r}$ $\left(\text{from} \ J_0 \simeq \sqrt{\frac{l}{r \sin \theta_x}} \right)$. The transition occurs at $\theta_x \simeq \frac{l}{r}$ from the term inside of J_0 function in Eq.(71). This means that the region of weaker decay, $E \sim \left(\frac{l}{r} \right)^{1/2}$ is a cylinder of radius $r \sin \theta_x \simeq l$ about $\vec{B}_0$. So, there is a duct along the $\vec{B}$ line as in Fig.(28). The wave propagates intensely inside this duct. However, the word "duct" may be misleading, because the radiating power carried inside it is still decaying with r. The Poynting's vector will scale as $E^2 \sim \frac{l}{r}$ inside the "duct", and since its area remains constant (πl^2), the power it carries decays as $\frac{l}{r}$. Of course, outside this duct the Poynting's vector decays as $\left(\frac{l}{r} \right)^2$, much faster. Now we need
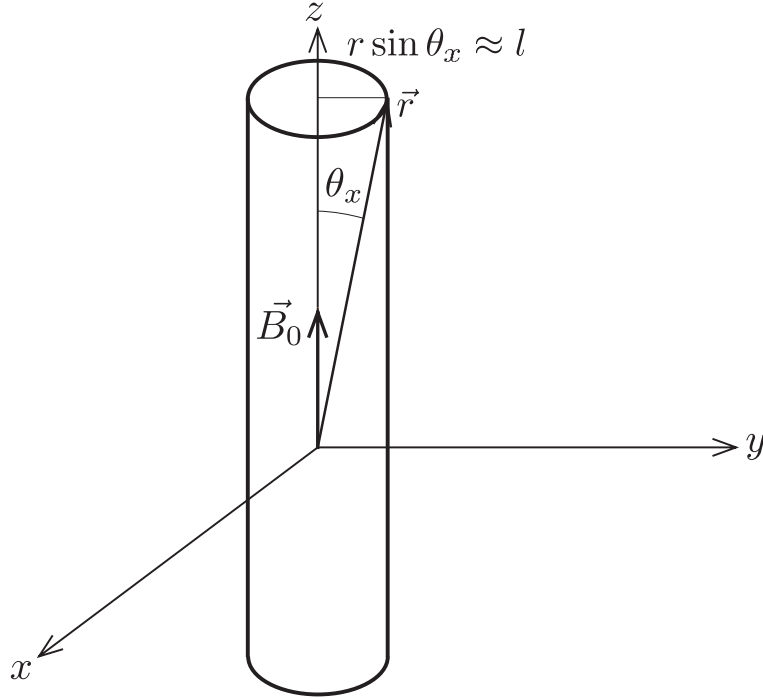

Figure 28: A "duct" along $\vec{B}$ line

to evaluate whether we can move the J_0 term out of the integral in Eq.(67). The J_0 term can be moved out if its argument $y = A \frac{\sin \theta \sin \theta_x}{\sqrt{\cos \theta - \nu}} = A \frac{\sin \theta \sqrt{1 - u^2}}{\sqrt{u - \nu}}$ varies little in an interval Δu of u about $u = 2\nu$ such that the exponent $A\Phi'$

changes by about one unit. From Eq.(69),

$$\Delta A\Phi' = A\cos\theta_x \frac{1}{4}\frac{1}{\nu^{3/2}}\Delta u^2 = 1 \tag{72}$$

Then,

$$\Delta u = \frac{2\nu^{3/4}}{\sqrt{A\cos\theta_x}} \tag{73}$$

Now,

$$\frac{dy}{du} = -\frac{u^2 - 2u\nu + 1}{\sqrt{1-u^2}\,(u-\nu)^{3/2}}\frac{A}{2}\sin\theta_x \tag{74}$$

And, in order to move the J_0 term out, the condition below should be satisfied:

$$\frac{dy}{du}\bigg|_{u=2\nu}\Delta u = \frac{\sqrt{A}}{\nu^{3/4}\sqrt{1-4\nu^2}}\frac{\sin\theta_x}{\sqrt{\cos\theta_x}} \ll 1 \tag{75}$$

Then, the condition for θ_x (assumed to be small) is

$$\theta_x \ll \frac{\nu^{3/4}}{\sqrt{A}} = \sqrt{\frac{\nu l}{r}} \tag{76}$$

The two limitations on θ_x can be visualized as in Fig.(29). Above OC (red line), the field decays as $\frac{l}{r}$ (outside of the "duct"), whereas below OC, $E \sim \sqrt{\frac{l}{r}}$.

Above OABD (blue line), the J_0 function varies too rapidly and must be kept inside the integral, whereas below OABD it can be moved outside.

For the far field $\left(r > \frac{l}{\nu}\right)$, there is therefore a significang region (OABO) outside the high-flux duct where the J_0 function can be moved out of the integral, and where Eq.(71) gives a good representation of the angular dependence of the field. Notice that this could include conditions where the argument of J_0 is large, and therefore its oscillatory behavior is visible. This then overlaps with the region where an asymptotic expansion of J_0 is valid, which turns out to be equivalent to an expansion of the exponent to second order in $\phi - \phi_s$, namely, the full stationary phase method.
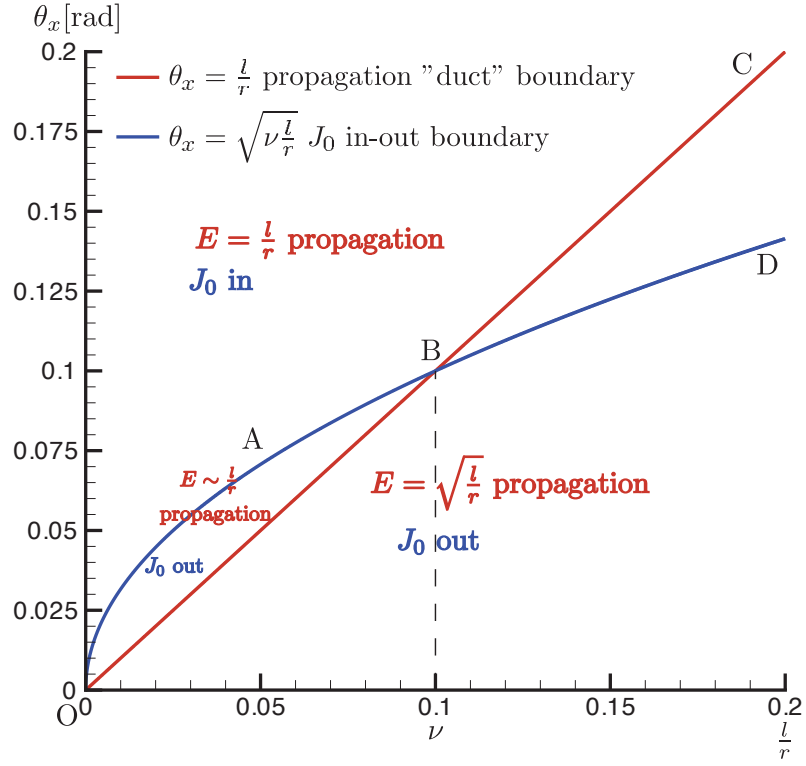
Figure 29: J_0 in-out and propagation "duct" limitation on θ_x

MODIFICATION OF THE EARTH's RADIATION BELTS

by Manuel Martínez Sánchez

ETSIA, November 2007

Outline

- Nature of the Belts. Effects on satellites.
- High altitude nuclear explosions.
- Basic Physics: energetic particles and background plasma.
- Mechanisms for depletion.
- Potential for human intervention. Possible approaches.
- Electrostatic scattering:
    - Basics, geometry
    - Formulation
    - Some results.
- Induced pitch diffusion:
    - Electron resonance with whistler waves
    - Diffusion in pitch and energy
    - Some results
    - Proton diffusion by EMIC waves
    - Antenna thory and antenna sizing
- Summary

The Earth´s Magnetic Field
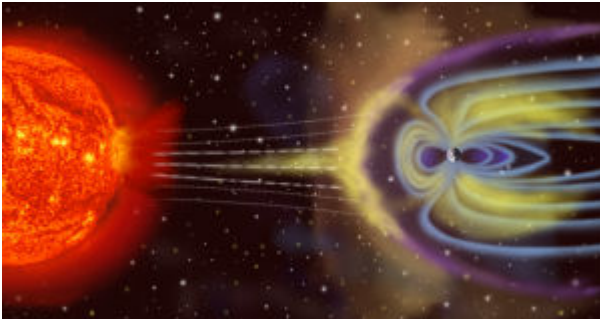
At a large scale, The **magnetosphere** shields the surface of the Earth from the charged particles of the **solar wind**. It is compressed on the day (Sun) side due to the force of the arriving particles, and extended on the night side. (Image not to scale.)

magnetic dipole axis

rotational axis (geographic)

$\sim 11\frac{1}{2}°$

N

S

On a scale of a few Earth radii, the field approximates that of a **Magnetic Dipole**, slightly tilted with respect to the Earth´s axis.
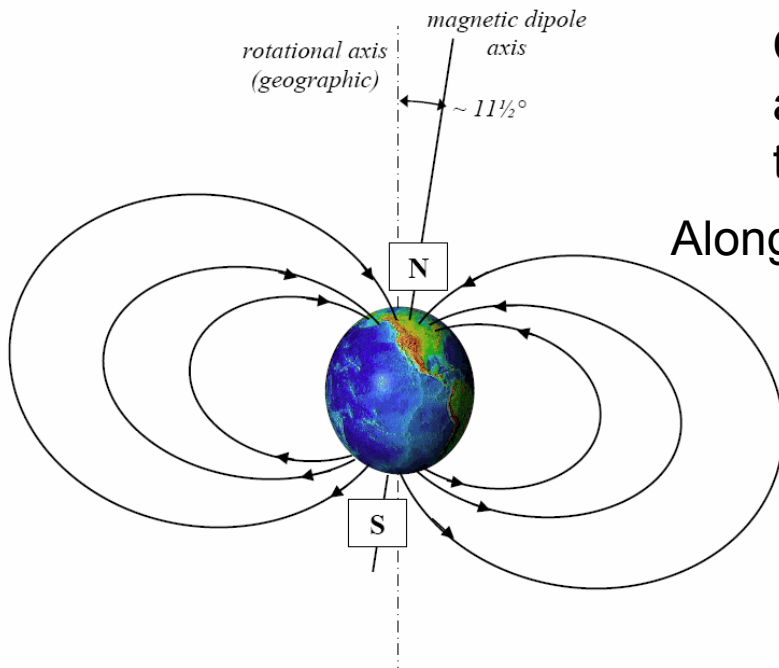
Along the **magnetic shell** crossing the equator at $R_{Equator}$

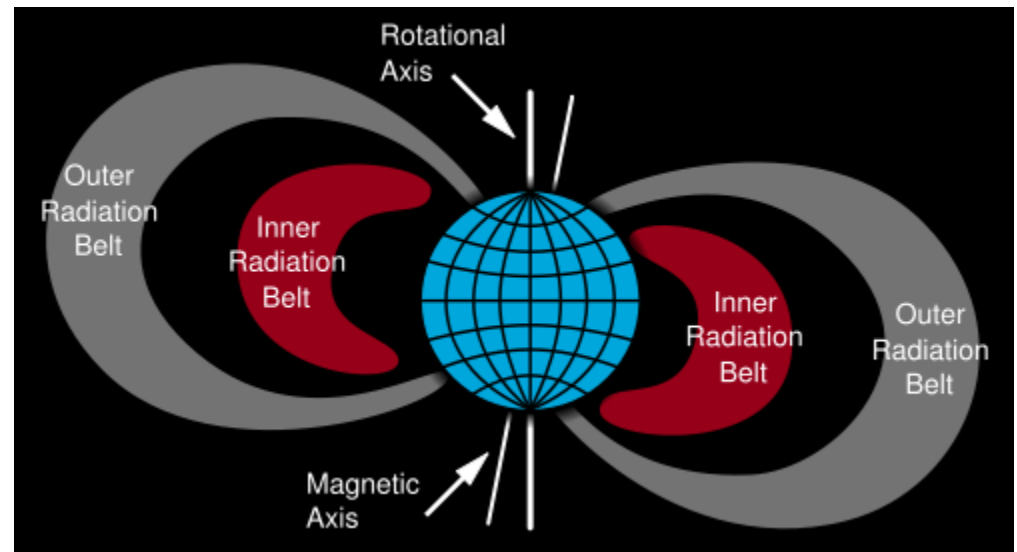$$R = R_{Equator} \cos^2 \lambda \qquad \text{and then}$$

$$B = B_E \left(\frac{R_E}{R_{Equatorial}}\right)^3 \frac{\sqrt{4 - 3\cos^2 \lambda}}{\cos^6 \lambda}; \quad B_E \cong 3.1 \times 10^{-5} Tesla;$$

$$R_E \cong 6,730 km$$

The L-Shell parameter is $R_{Equatorial} / R_E$ for a particular magnetic shell.

The Van Allen Radiation Belts

A fraction of the high energy particles from the solar wind, plus others generated from cosmic rays, are **trapped** in the **magnetic bottle** formed by the local magnetic tube.

The **outer belt** contains mainly electrons of 0.1-10 MeV (energetic ions have too large Larmor radii at these weak B-fields).
Te **inner belt** contains electrons of up to 1 MeV, plus ions (mainly protons) of energies up to 400 MeV.
The so-called **safe gap** in between is formed by natural precipitation of particles Through pitch angle diffusion.

In addition, there is a **low-energy plasma background**, with much higher density, but much lower energy. This plasma is **quasi-neutral.**

Effects on satellites

The bombardment by energetic trapped particles damages **solar cells, integrated circuits** and **sensors** on board satellites. Geomagnetic storms, during which teh radiation intensifies, often disrupts electronics on board spacecraft.

These effects are intensified in modern **miniaturized** devices, which may have Charge levels comparable to that of the bombarding ion and its trail.

Missions that need to reside for long periods in the Belts need to

(a) Use special, defect-free components (**"Class S electronics"**) that are very expensive and hard to find, as electronic manufacturers dislike their low production volume.
(b) Use **radiation hardening** measures, that increase weight and cost. A 3mm aluminum shield still allows exposure to 2500 rem/year (1mrem is the dose due to a medical X-ray exam)

Manned missions are particularly critical in this respect. Apollo crews passed through teh Belts quickly, but high altitude orbiting missions are essentially precluded.

High altitude nuclear explosions

Another possible source of trapped radiation is that generated in a nuclear blast above the atmosphere. Neutrons in fission fragments (or free neutrons) can then beta-decay to protons, ejecting high-energy electrons.

Crazy as it may seem, both the US and the former USSR did test high altitude nuclear devices:

US "Starfish", July 9, 1962. A 1.4 Mton device exploded at 400 km altitude (L=1.2)
USSR, October 22, 1962 . A sub-Mton device, exploded at L=2.

Both created intense new radiation belts near the detonation L-shells, that took About one year to decay. About 173 of all orbiting satellites were damaged.

The fear of another such occurrence, especially with many new nuclear nations and many more and more valuable satellites, has prompted research on possible remedies.
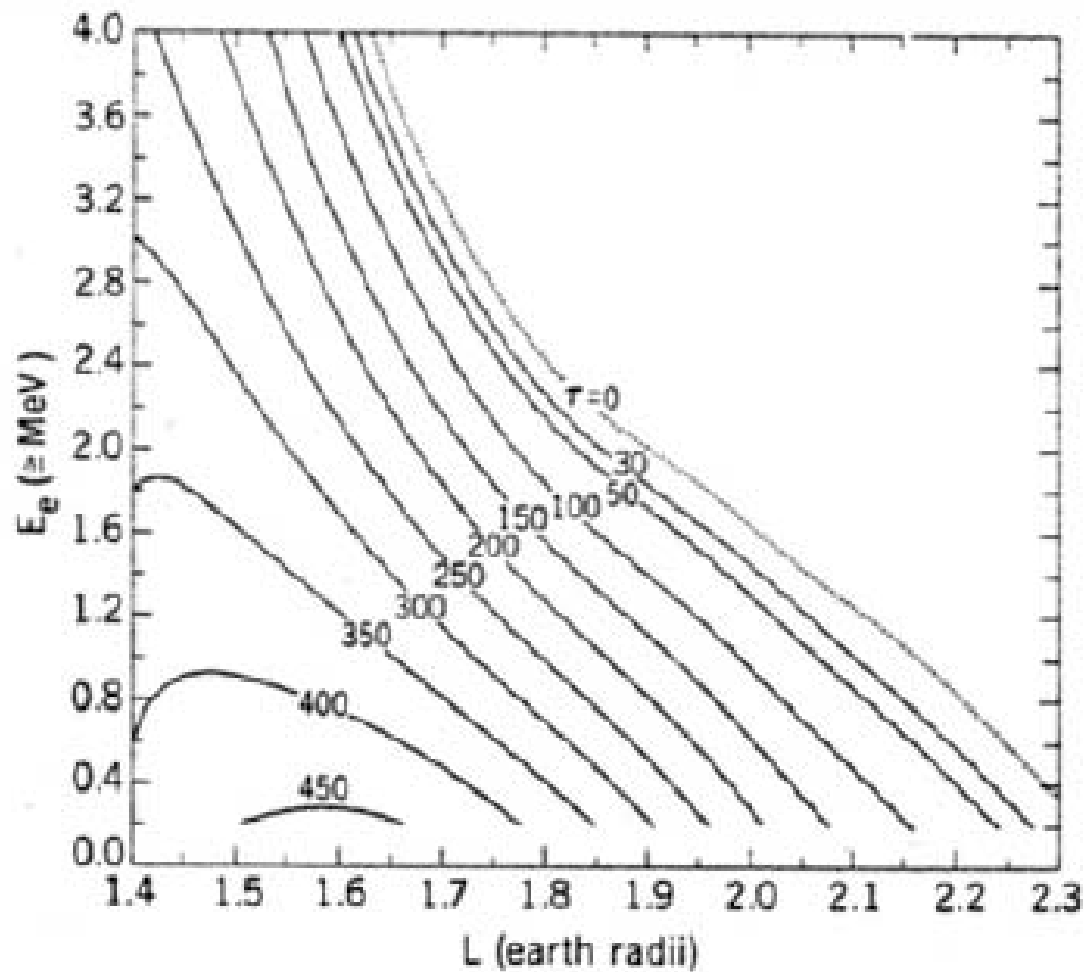
STARFISH decay times

Figure 2.12: Decay lifetimes (days) for Starfish electrons ($E > 0.2MeV$) as determined by the data from the 1963-38C satellite [9].
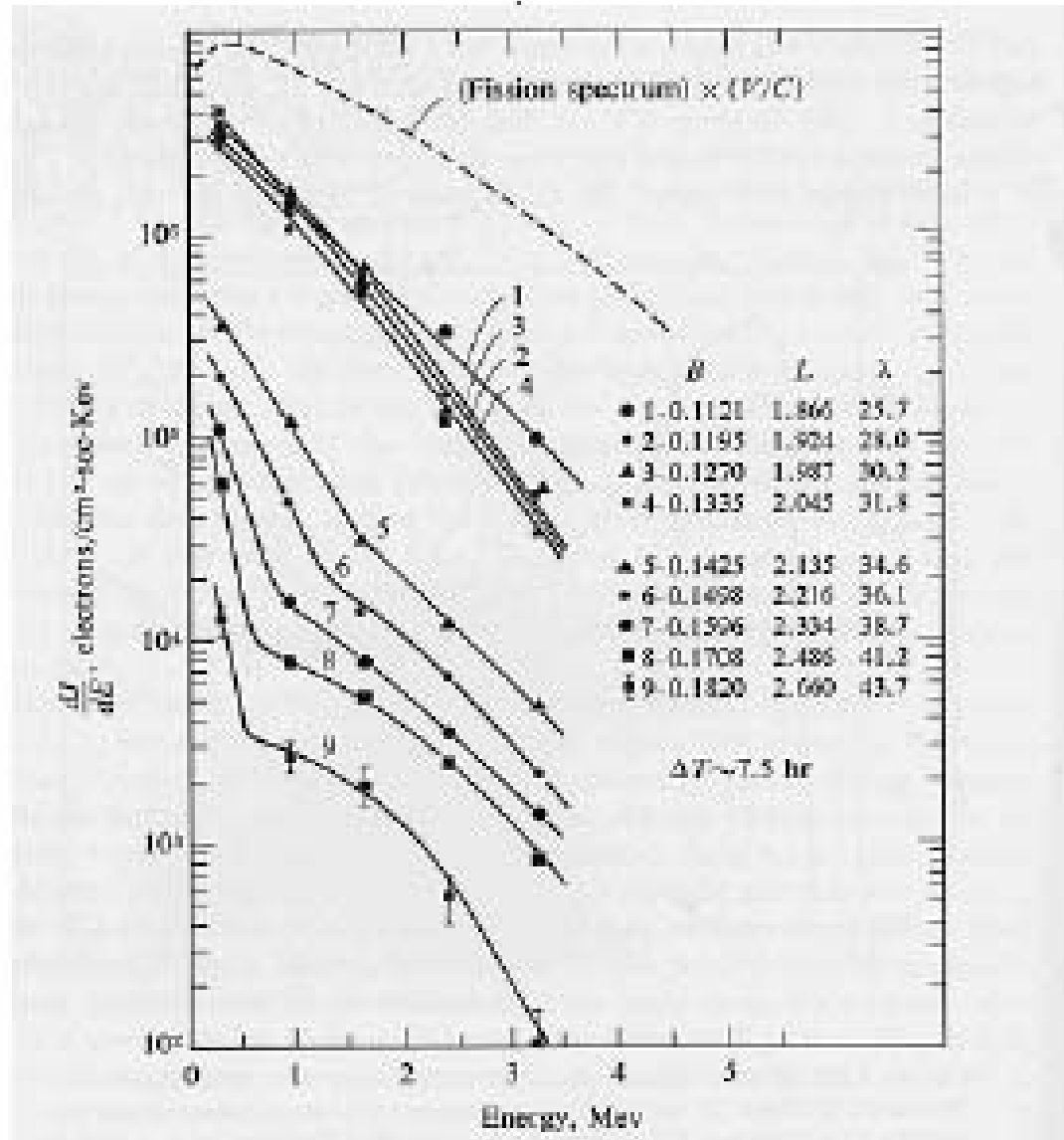
Particle spectrum from Soviet nuclear test

Figure 1.1: Trapped electron spectrum at various L-values following the October 28, 1962 Soviet nuclear detonation [15].
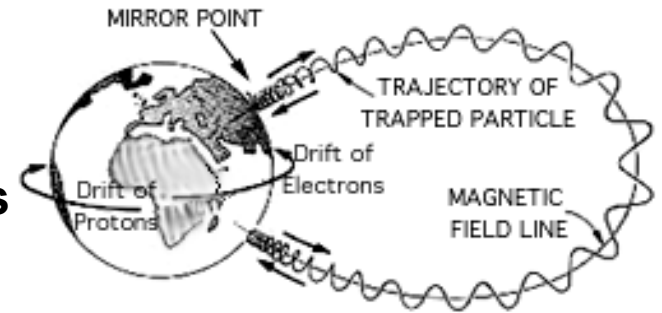
Dynamics of trapped particles

Each trapped particle executes three types of periodic motion:

Fast **Larmor motion** about **B**
Intermediate **bounce motion** between **conjugate points**
Slow **drift motion** about the magnetic axis.

Larmor:
$$\tau_{Larmor} = \frac{2\pi}{\omega_L}; \quad \omega_L = \frac{qB}{m} \approx 10^6 \, rad \, / \, s \; (electrons) \; or \; 5,000 \, rad \, / \, s \; (ions)$$

$$Hence \; \tau_L \approx 10^{-5} \, s \; (electrons) \; or \; 0.02 \, s \; (ions)$$

Bounce:
$$V_{parallel} = V \cos\alpha \approx 10^8 \, m \, / \, s \; (relativistic) \; ; \; L \approx 40,000 km$$

$$Hence \; \tau_B = \frac{L}{V_{par}} \approx 0.4 \, s$$

Drift:
$$V_{drift} = \frac{V_{par}^2}{\omega_L R_{curvature}} \approx \frac{(10^8)^2}{10^6 \times 10^7} = 10^3 \, m \, / \, s \; ; \; L \approx 80,000 \, km$$

$$Hence \; \tau_{drift} \approx 8 \times 10^4 \, s \approx 1 \, day$$

Sample background plasma parameters

In the middle of the inner belt, para L=1.5 (some 3,000km at the Equator)

| Characteristics of Natural Plasma Environment	
Magnetic Field	$B = 9.815 \times 10^{-2}$ Gauss
Plasma temperature (daytime)	$T = 0.4$ eV
Plasma temperature nighttime	$T = 0.2$ eV
Plasma density	$n = 10^4 \text{cm}^{-3}$
Ion composition	$H^+ = 5 \times 10^3 \text{cm}^{-3}$ $He^+ = 10^3 \text{cm}^{-3}$ $O^+ = 10^2 \text{cm}^{-3}$
Neutral density	$n = 10^4 \text{cm}^{-3}$
Neutral composition	$H = 10^4 \text{cm}^{-3}$ $He = 10^4 \text{cm}^{-3}$ $O = 10^3 \text{cm}^{-3}$
Larmor Radius	$r_e = 15.3 \text{cm}$ $r_i = 6.57 \times 10^2 \text{cm}$
Debye Length	$\lambda_D = 4.70 \text{cm}$
Collisionality (mean free path)	$\lambda_e = 135 \text{km}$ $\lambda_i = 192 \text{km}$

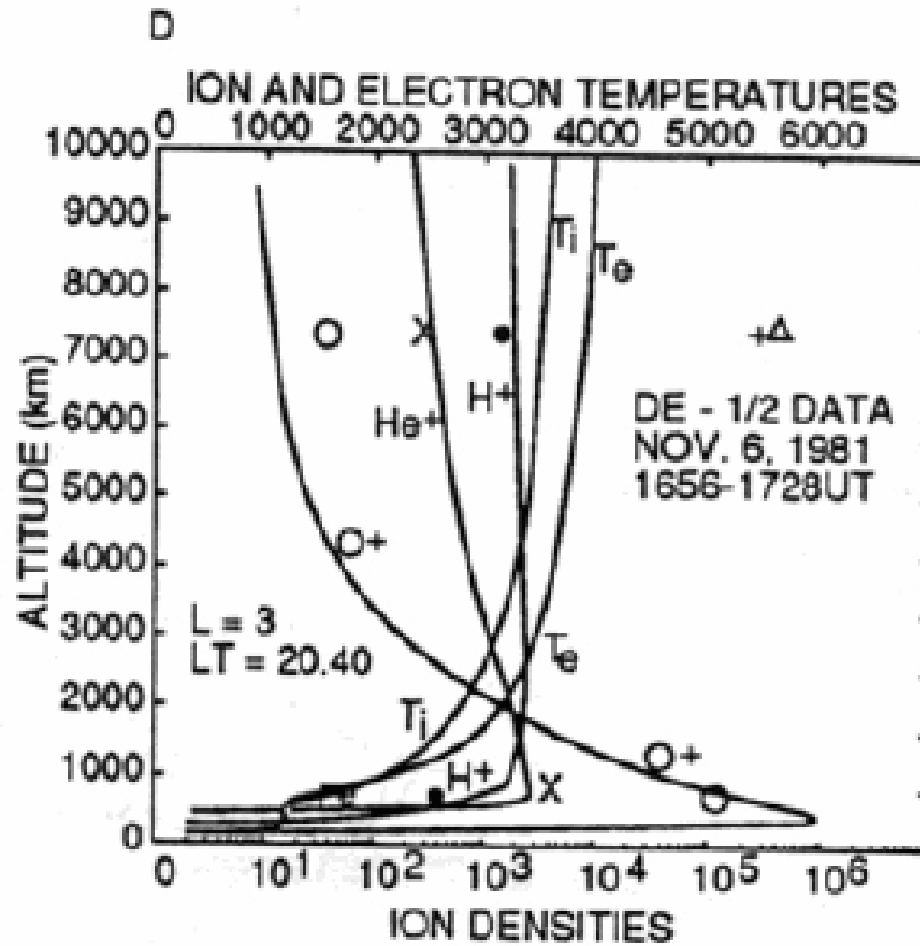# Variations with altitude: density
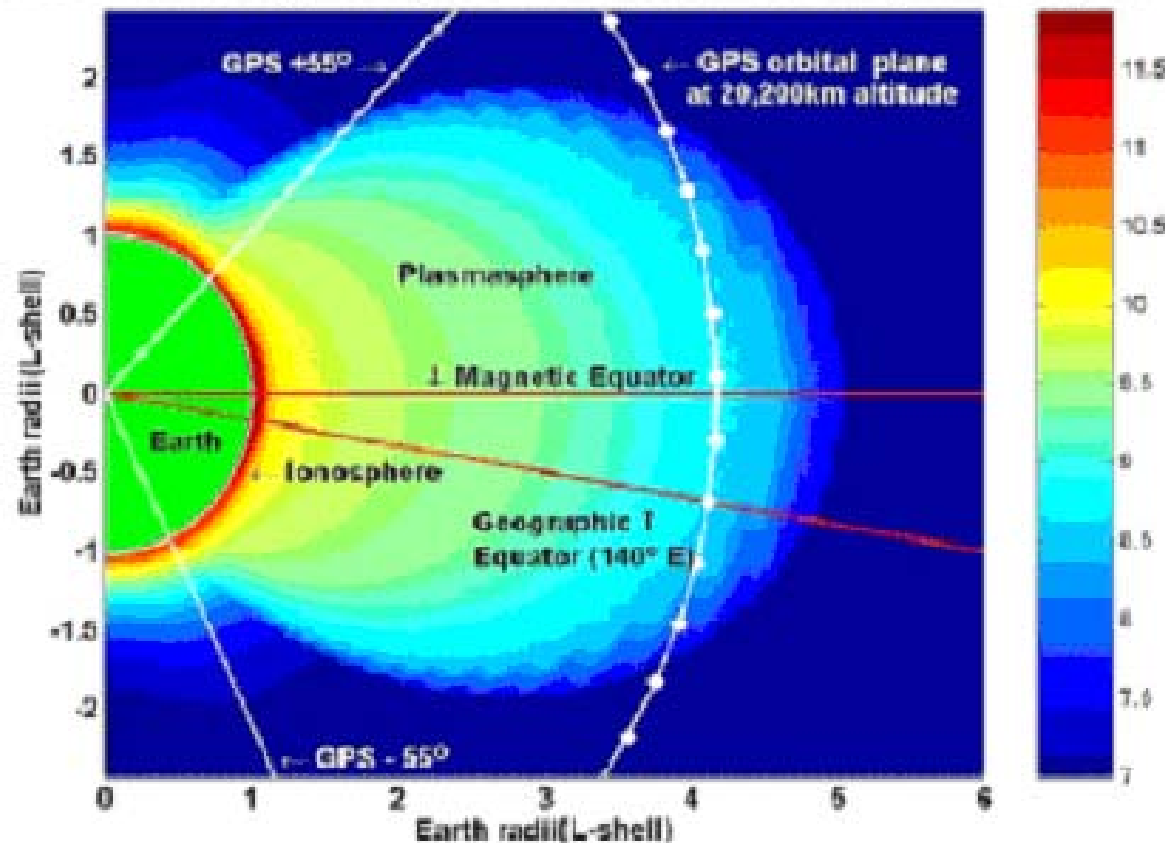
Figure 2.5: Electron densities (m^{-3}) described as a function of distance from the earth. Densities were calculated by the Global Plasmasphere Ionosphere Density (GPID) model [4].

Variations of the background Te (inner ring)
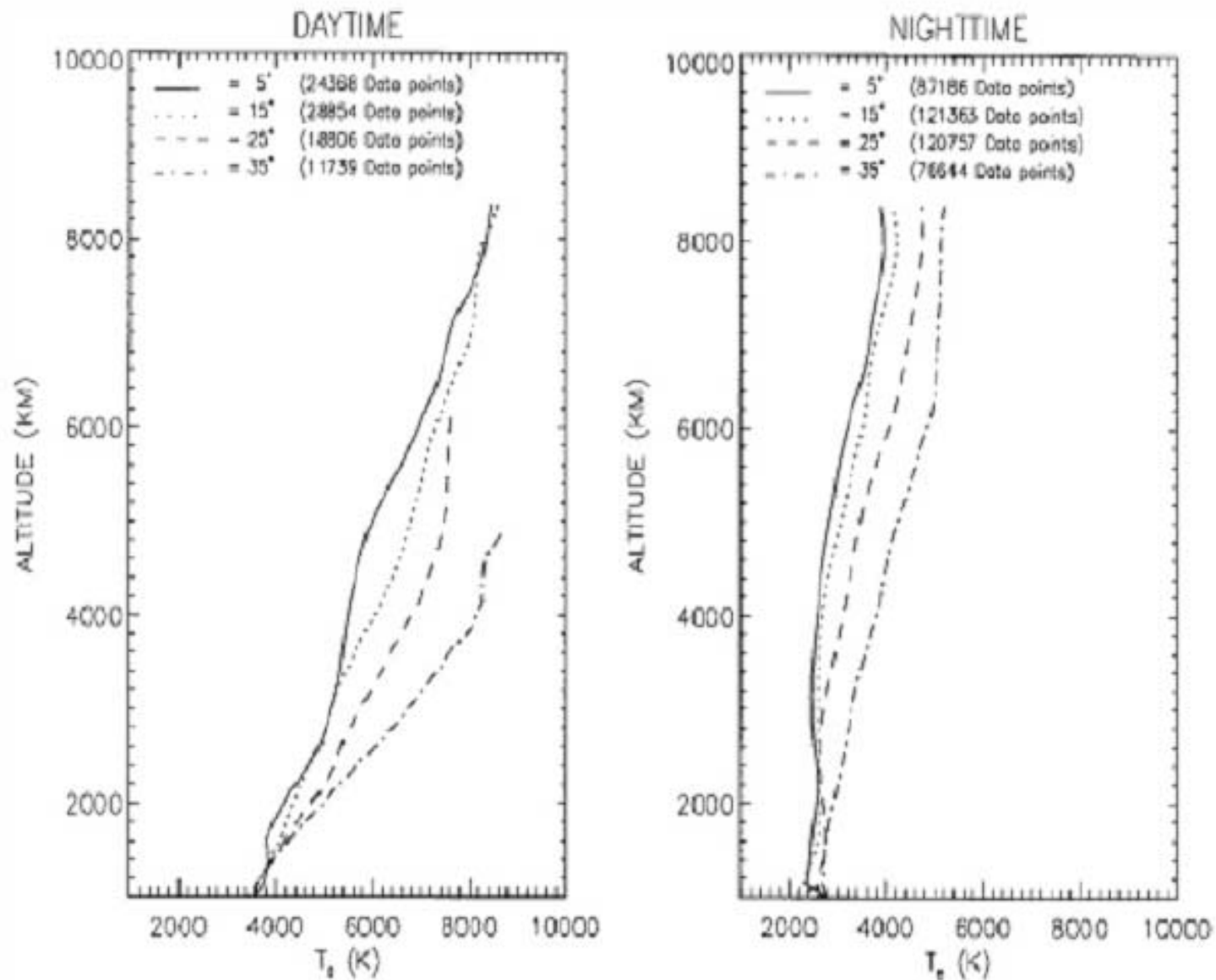
Outer ring variations (L=3)

Energetic electron fluxes

Electrons crossing per cm2, per second. Divide by velocity to get particle density. $Ve \approx c = 3 \times 10^{10} \, cm/s$
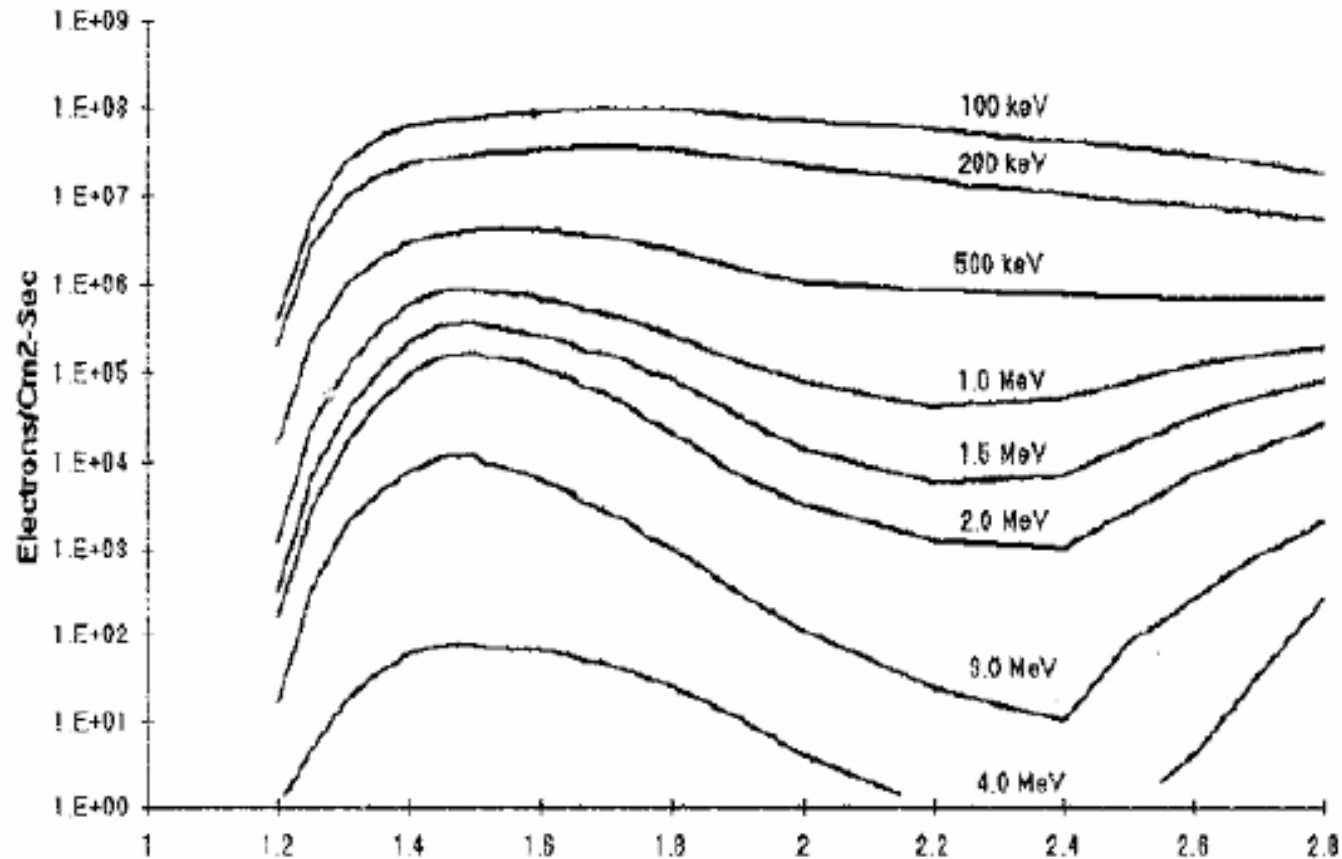

Figure 2.4: High energy electron fluxes and energies as a function of L-value. The data reflects Vampola's update of the AE-8 model using data from the Combined Release and Radiation Effects Satellite (CRRES) [3].

Energetic proton fluxes

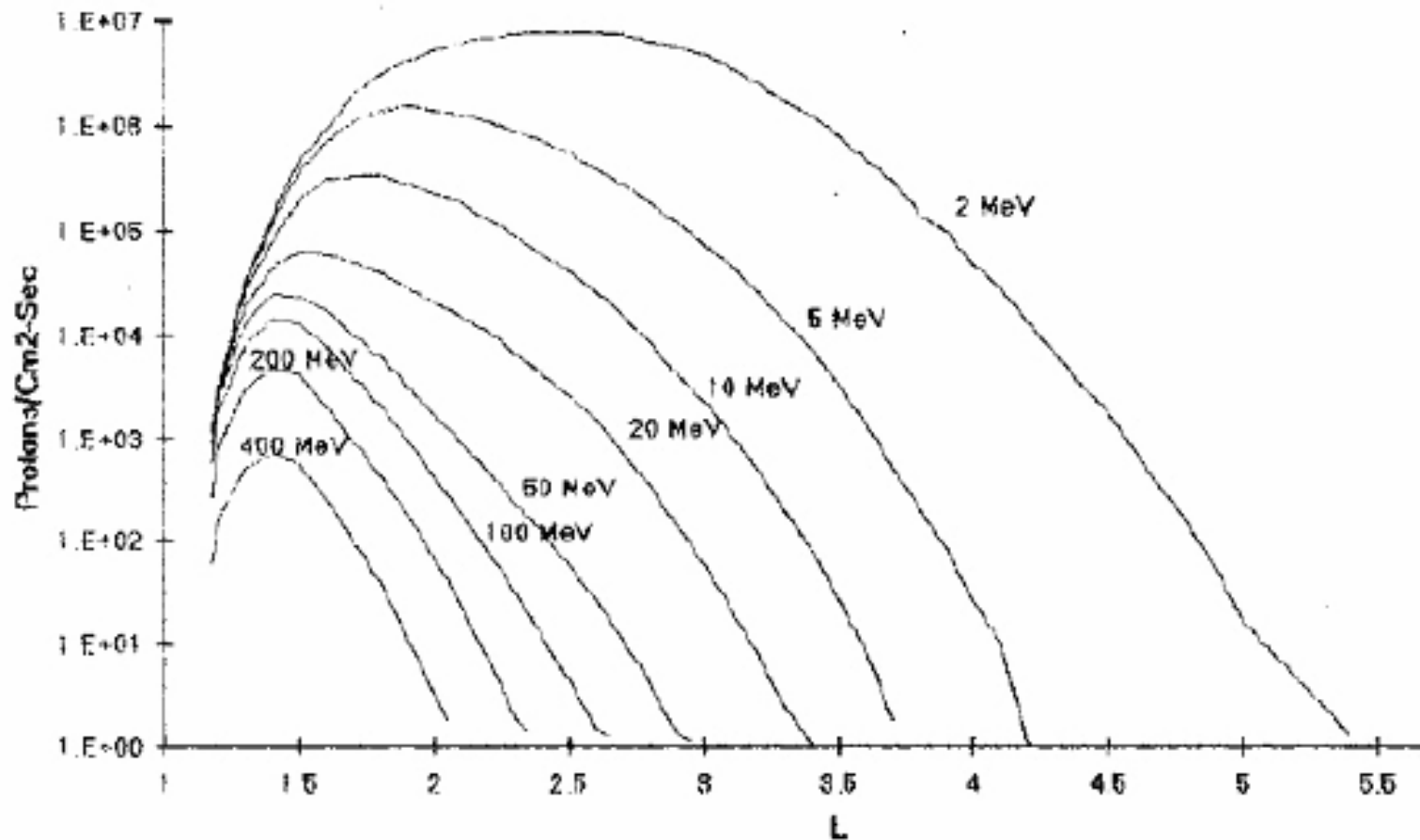Again, divide by velocity to get density, but ions not relativistic.

Figure 2.3: High energy proton fluxes and energies as a function of L-value from the AP8MIN model [3].

A note on relativistic energy and velocity

The energy in the previous data is only the kinetic energy of the particle, ie, it excludes the rest energy:

$$KE = E - m_0 c^2, \; with \quad E = \sqrt{p^2 c^2 + m_0 c^4}, \; and \; p^2 = \frac{m_0^2 c^2}{1 - v^2/c^2}$$

Solving for the velocity,

$$v = \sqrt{\frac{2KE}{m}} \; \frac{\sqrt{1 + 2\dfrac{KE}{m_0 c^2}}}{1 + \dfrac{KE}{m_0 c^2}}$$
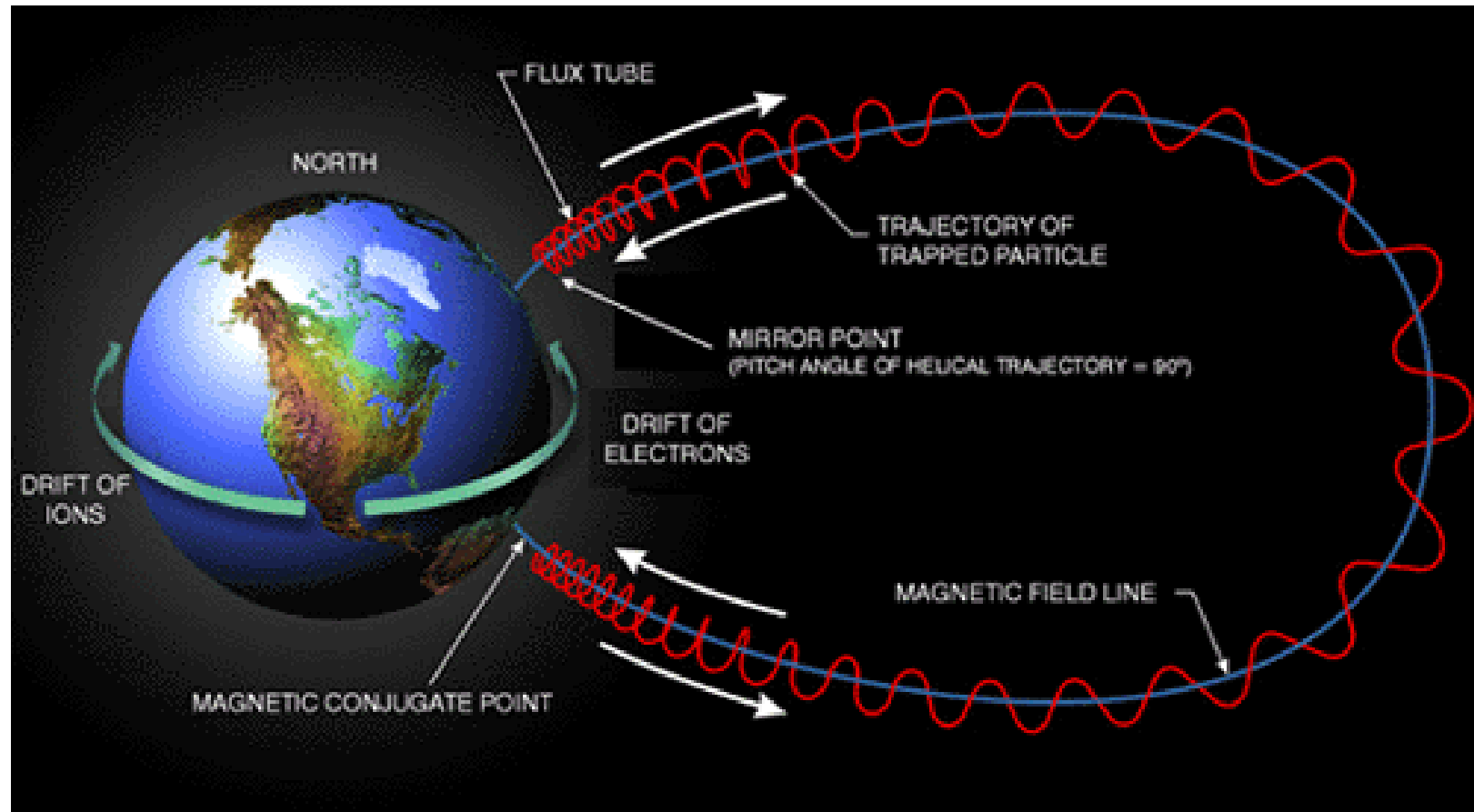
Which approaches c when $KE/m_0 c^2 \gg 1$ and $\sqrt{\dfrac{2KE}{m}}$ in the opposite limit.

For electrons, $\quad m_0 c^2 = 0.51 \, MeV$

For protons, $\quad m_0 c^2 = 940 \, MeV$

Thus, most belt electrons are relativistic, but most protons are classical.

204

Magnetic bottling-Schematic

Magnetic bottling-physics

When a charged particle rotates and slides along a non-uniform B-line, two quantities are conserved:

a) Full kinetic energy, $\qquad E = E_\perp + E_{\mathrm{II}}$

b) Adiabatic invariant, $\qquad \mu = \dfrac{E_\perp}{B}$

Solving for the parallel energy, $\qquad E_{\mathrm{II}} = \dfrac{1}{2} m v_{\mathrm{II}}^2 = E - \mu B$

Starting from a region of low B, where $\quad E_{\mathrm{II}} > 0 \quad$ the parallel velocity decreases

as B increases, and becomes zero at the point where $\qquad B = B_{bounce} = E / \mu$

Define the initial **pitch angle** $\quad \alpha_0 = \tan^{-1}(\dfrac{v_{\perp 0}}{v_{\mathrm{II} 0}})$

Then $\quad B_{bounce} = \dfrac{B_0}{\sin \alpha_0}$

Particles with a large initial pitch angle bounce early (at high B), while particles with small initial pitch angle penetrate deep into the higher B values.

Conditions for trapping

Trapped particles are characterized by having a **bounce point above about 120 km**., below which there are enough collisions with the neutral atmosphere to neutralize or scatter the particle.

From $\quad R = R_{Eq} \cos^2 \lambda = LR_E \cos^2 \lambda \quad$ and $\quad R_{Bounce} \approx R_E \quad$ we get $\quad \cos \lambda_{Bounce} = \dfrac{1}{\sqrt{L}}$

Substituting into $\quad \dfrac{B}{B_{Eq}} = \dfrac{\sqrt{4 - 3\cos^2 \lambda}}{\cos^6 \lambda} = \dfrac{1}{\sin^2 \alpha_{Eq}}$

we then find the pitch angle $\quad \alpha_{Eq} \quad$ corresponding to a given L-shell:

$$\alpha_{Eq} = \sin^{-1}\left(\frac{1}{L^{3/2}(4 - 3/L)^{1/4}}\right)$$

This gives 27.2 deg for L=1.5, and 8.4 deg for L=3. Particles with a smaller equatorial pitch angle are quickly lost to the atmosphere at the bounce point **("Loss Cone")**.

Any mechanism that scatters a trapped particle into an equatorial pitch angle smaller than the above limit will therefore remove that particle from the radiation belts.

Mechanisms for particle precipitation

Several **natural** effects have been identified that do scatter particles into their Loss Cone:

Coulomb Scattering: Although the background density is very low, it is not zero, and some electrons are scattered through Coulomb collisions with other bound and free electrons. This dominates at the lower altitudes, were densities are higher.

Scattering by Plasmaspheric Hiss: This is a low frequency (about 1 kHz) broadband incoherent radiation apparently due to cyclotron resonance of newly injected electrons.

Scattering by VLF Whistler waves from lightning: These are somewhat higher frequency waves (1 to 20 kHz) that enter the ionosphere near the polar regions and then propagate along **B** lines and resonate with the gyrating electrons.

In addition, it has been realized since the 1970's that VLF **radiation from high-power ground antennas**, at discrete frequencies in the 10-30 kHz range, can at night excite magnetospheric Whistler waves as well. The experimental evidence is still only episodic, though.

Some model calculations of precipitation lifetime

From Abel&Thorne, 1998, with data from decay of STARFISH:

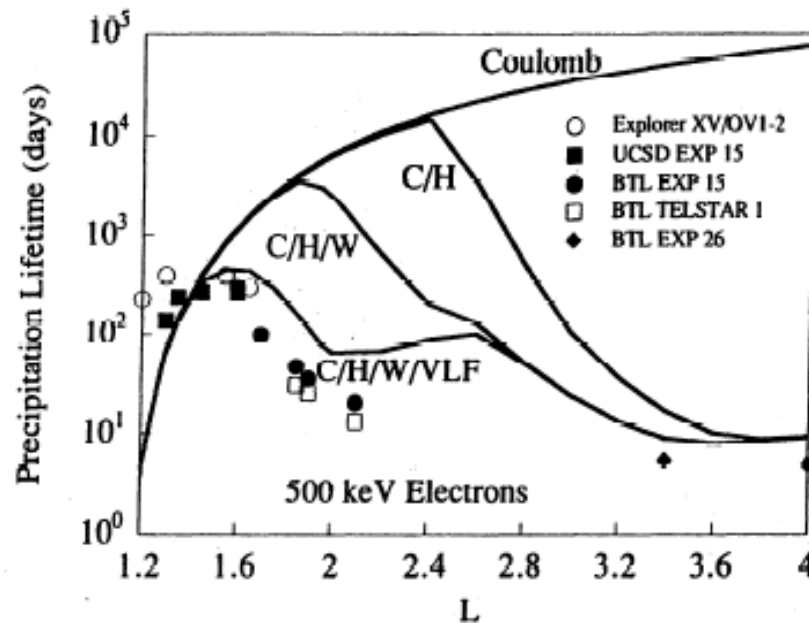**Figure 9.** Precipitation lifetime calculations for 500 keV electrons for scattering due to Coulomb collisions (C), Coulomb and plasmaspheric hiss (C/H), Coulomb, plasmaspheric hiss and lightning-generated whistlers (C/H/W), and with all scattering mechanisms included (C/H/W/VLF). Observed decay rates are included for comparison.

Note that the man-made VLF radiation effect is already very strong

Potential for human intervention

Since the number of energetic particles involved is relatively small, there is potential for **artificially enhancing the precipitation rate**.

The drift around Earth (in hours) should spead any disturbance in longitude. Also, radial particle diffusion between L-shells is slow, so one could in principle "clean up" relatively thin shells for specific needs.

Methods that have been proposed include:

Electrostatic scattering of charges by orbiting thin bodies (Tethers) biased to potentials of the same order as the particles to be scattered. With proper geometry, some of the scattered particles will go into the Loss Cone.

VLF ground antennas distributed strategically so as to pump Whistler radiation into the desired L-shells. This would systematize the already observed effects of operational (mainly military) VLF installations.

Orbiting VLF or ULF antennas, placed in the specific targeted orbital regions to be cleaned up. Since the wavelengths tend to be hundreds of meters to many km, a very attractive implementation would use **tethers** as antennas.

Electrostatic scattering of radiation belt particles

We next discuss some of the details of the electrostatic scattering method, using as the main source the MS Thesis of C. Zeineh at MIT (2005).

A **vertical tether** in an **equatorial orbit** is a suitable geometry. It is dynamically stable due to a Gravity Gradient restoring torque, and it cuts **B** lines almost perpendicularly, so that at least some of the scattering events can direct the particles towards **B**, as desired.
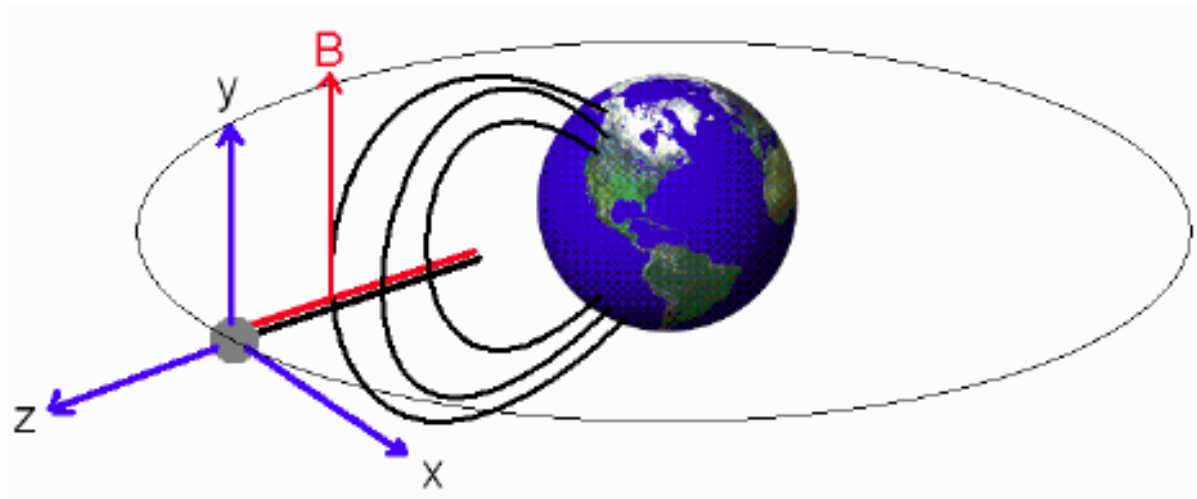
The tether must be at a potential similar to the energy of the particles to be Affected. For most of the study we assume a **1MV bias**.

Tether potentials

In order to have a tether biased at some potential, some sort of **counter-electrode** is required. This can be a separate segment of the same tether, or a separate tether.

Thin thethers will collect current in the **Orbital Motion Limit (OML)**:

$$\frac{dI}{dz} = qn\sqrt{\frac{2q\Delta V}{m}}$$

For electrons, $m = m_e = 0.91 \times 10^{-30}\ kg$ while protons are 1840 times heavier

Thus, to have equal current collected per unit length, $\left|\Delta V\right|$ must be 1840 times smaller for electrons (positive ΔV) than for ions (negative ΔV). Since what must be the same is really the total current, this ratio could vary somewhat by assigning different lengths to the two polarities. The result will be **a high negative potential** tether, ballasted by a **moderate positive potential** tether (or segment).

Tether architectures (a)

Single tether, no cathode:

Positive tether provides ballasting,
  automatically at low potential.

Problem: Net Loretz force
  will drift.
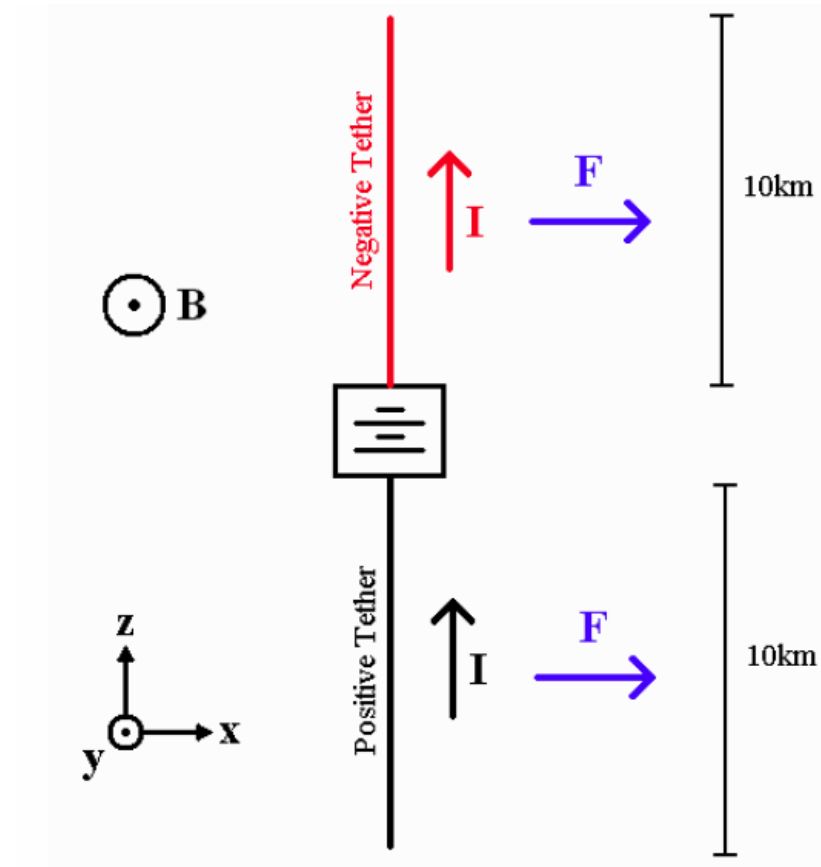
Tether architectures (b)

Single tether, with a cathode:

No net force, only a torque, can be counterd by a small angular deflection.

Problem: No counter-electrode, will float at a high positive potential, collect very high current.
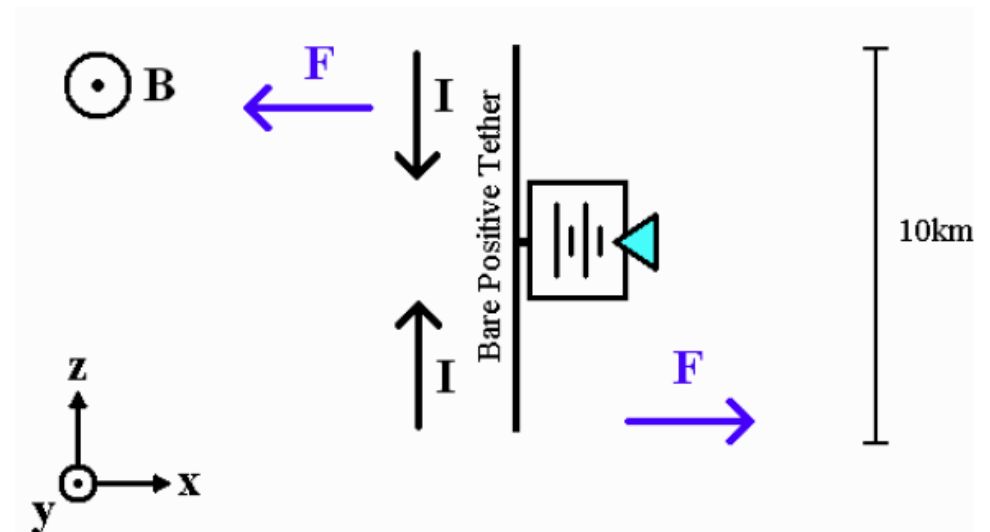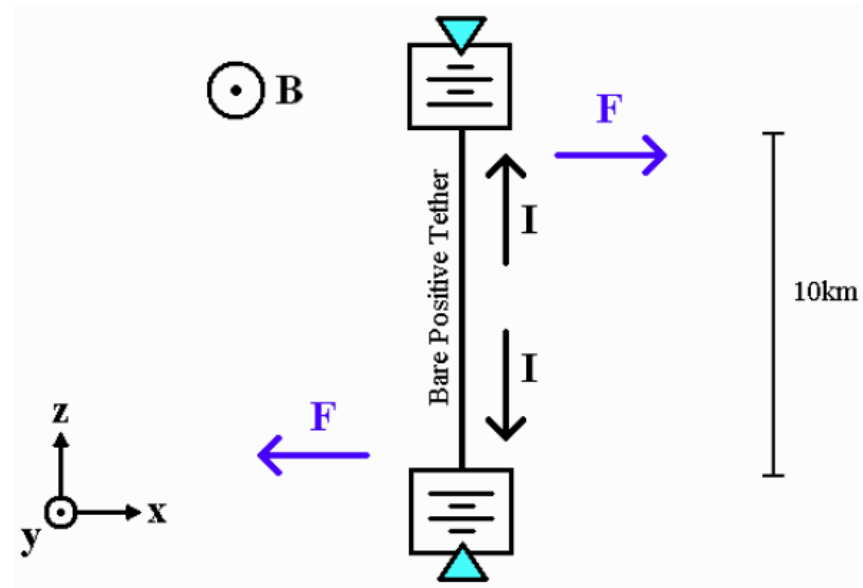
Tether architectures (c)

Parallel dual tethers:

No net force (some distortion only)
Positive tether automatically at
   low potential

Problem: The sheath about the
   negative tether is of the order of
   200m radius, difficult to avoid
   interference.
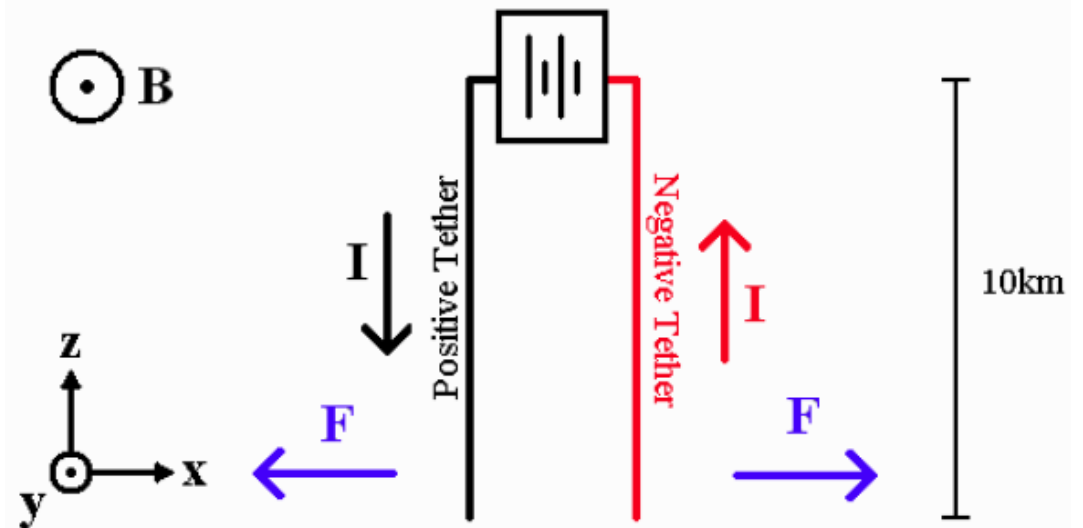
Tether architectures (d)

Symmetric series tether:

No net force, only a torque (some deflection)

No interference due to the sheaths on the negative (high potential) segments

Low potential ballasting by center tether

Longer length provides additional mechanical stability.

Selected design

216
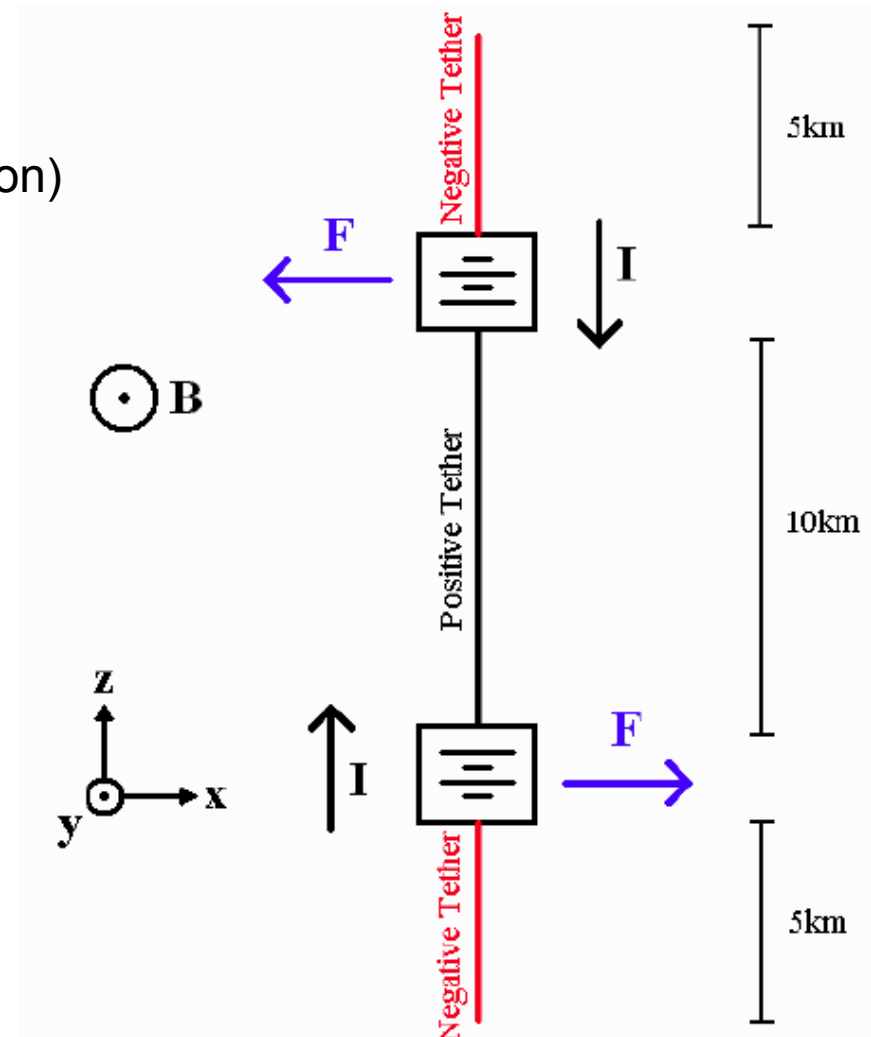
Tether deflection

Due to the distributed Lorentz forces, a torque appears about the cm of the assembly. This torque is proportional to the current I in the cable. Balancing against the restoring gg torque, the deflection angle is

$$\theta = \frac{IB}{3m\Omega^2}$$

The mass m of the tether is in turn proportional to the power:

$$m = \alpha P = \alpha I \Phi_{tether}$$

Substituting, the current cancels out, so the deflection ends up being **independent of tether thickness.** In addition, B and Ω^2 are both inversely proportional to R^3 so the deflection is also **independent of altitude.**

Using a 1MV bias and $\alpha = 20 \, kg/kW$ we calculate a very small deflection:

$$\theta = 0.02 \; \mathrm{deg}$$

Tether diameter

The current collected is a necessary evil, but it can be minimized by **reducing the tether diameter.** Assume we place an upper limit P_{MAX} on the power (product of tether current and voltage). Using the OML formula for current, then

$$r_T \leq \frac{P_{max}}{en_\infty L \Phi_T{}^+} \sqrt{\frac{m_e}{2e\Phi_T{}^+}} = \frac{P_{max}}{en_\infty L \Phi_T{}^-} \sqrt{\frac{m_i}{-2e\Phi_T{}^-}} = \frac{P_{max}}{n_\infty L} \sqrt{\frac{m_i}{-2(e\Phi_T{}^-)^3}}$$

$$r_T \leq 90.3 \frac{P_{max}}{n_\infty}$$

and for a plasma density $n_e = 10^4 cm^{-3} = 10^{10} m^{-3}$, $P_{MAX} = 100kW = 10^5 W$,

we find a tether radius of 0.9 mm, or a **diameter of 1.8 mm**. Even accounting for some extra current over and above OML, this appears manageable.

Ion sputtering

There is some concern about the very energetic ions that would bombard the negative tether. At energies of a few hundred to a few thousand eV, the **sputtering yield** (atoms removed from the metal per incident ion) can be of order unity.

However, and somewhat paradogically, the yield **becomes very small at energies above 100keV.** The lifetime of a 1mm tether due to sputtering turns out to be many centuries.

Size of the sheath

The very high negative potential about the end tethers will produce a region devoid of electrons, and where the background plasma is therefore non-neutral (a **sheath**). A smaller region devoid of ions will also appear about the posive middle tether.The radius r_s of the sheath can be calculated from the implicit formula

$$\frac{e\Phi_T}{kT_e} = 2.554 \left(\frac{r_s}{\lambda_D} \right)^{1.325} \ln \frac{r_s}{r_T}$$

that comes from numerical simulations of Choiniere, verified analytically by Sanmartín (2007). Here, r_T is the tether radius, and λ_D is de Debye shielding length, $\lambda_D = \sqrt{\varepsilon_0 kT_e/(e^2 n_e)}$ Results are shown below:

Altitude (km)	Electron Temperature (K)	Plasma Debye Length (m)	Sheath Radius Negative Tether (m)	Sheath Radius Positive Tether (m)
2000	3400	0.040275	242.68	1.2346
4000	3900	0.043134	234.80	1.1959
6000	5100	0.049326	220.11	1.1237
8000	6200	0.054386	210.00	1.0739

Scattering calculations

A given high negative potential tether can scatter both electrons (repelled species) and ions (attracted species). An example for repulsion is shown below:
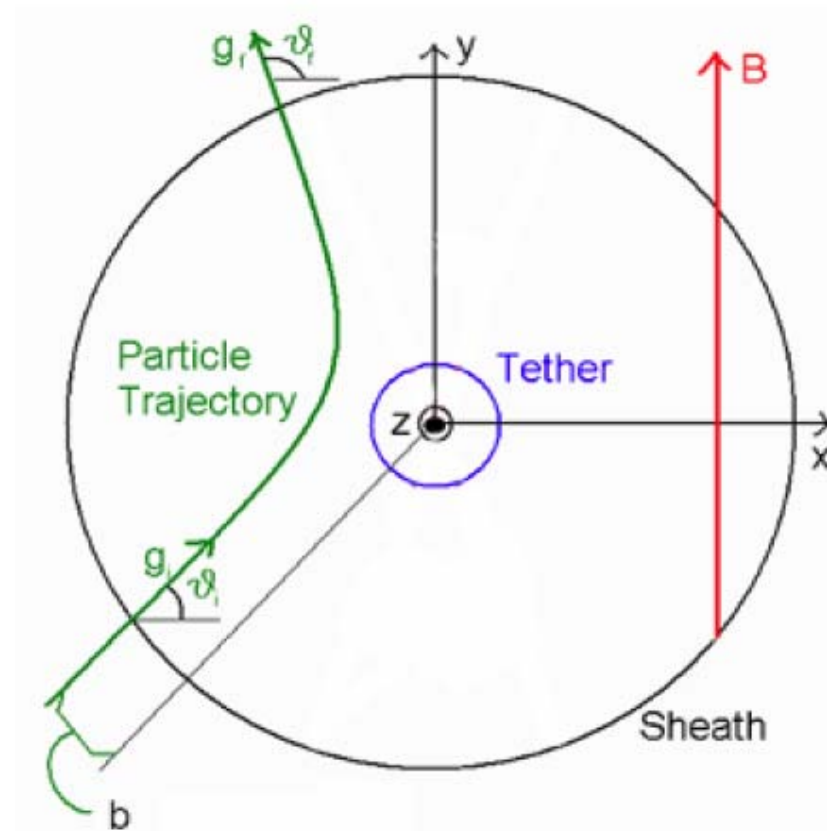
For attraction, the trajectory would instead "bend around" the tether, but the deflection would be analogous.

Scattering (continued)

Some trajectories that were originally outside the loss cone, and hence "trapped", will after deflection enter the loss cone,and the particle will be counted as instantaneously lost. The **loss cone** in velocity space is shown below:
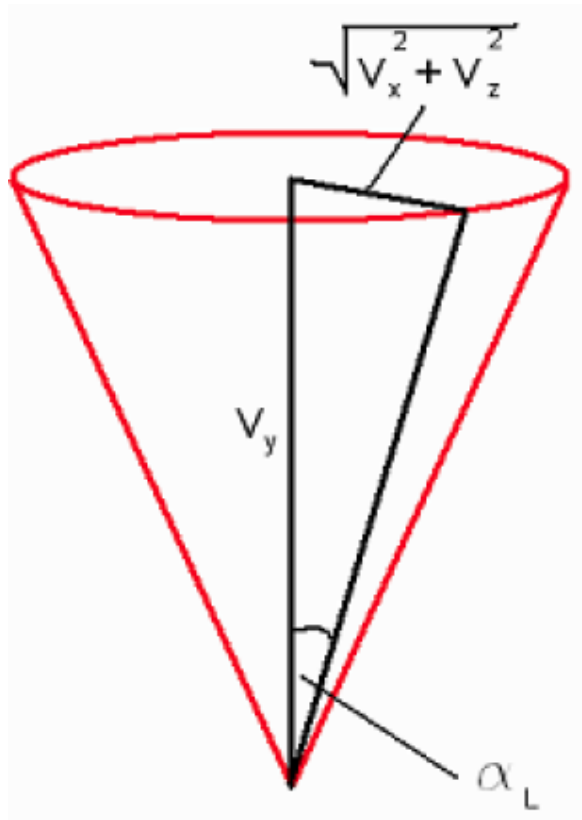
Classical scattering theory (in 2D)

By using conservation of energy and angular momentum, classical theory predicts a deflection (given the incoming miss distance b and velocity g) of

$$\chi = \pi - 2\Delta\varphi \; ; \quad \Delta\varphi = \int_{\varphi_i}^{\varphi_f} d\varphi = \int_{r_m}^{r_\infty} \frac{b}{r^2} \frac{dr}{\sqrt{1 - \dfrac{b^2}{r^2} - \dfrac{2q\phi(r)}{mg^2}}}$$

where $\phi(r)$ is the potential of the scattering center (the tether in cross-section)

and r_m is the radius of closest approach, which is the solution of the equation

$$1 - \frac{b^2}{r_m^2} - \frac{2q\phi(r_m)}{mg^2} = 0$$

In our case, we neglect the potential outside the sheath ($r > r_\infty$), and the effect of those ions that are in transit inside the sheath. The potential is then given by the classical electrostatic solution between two concentric cylinders:

$$\phi = \Phi_T \frac{\ln(r_\infty / r)}{\ln(r_\infty / r_T)} \; , \quad with \; \phi = 0 \; for \; r > r_\infty$$

223

Scattering (continued)

The deflection integral must then be split in two:

$$\Delta\varphi = \int_{r_m}^{r_\infty} \frac{b}{r^2} \frac{dr}{\sqrt{1 - \dfrac{b^2}{r^2} - \dfrac{2q}{mg^2}\Phi_T \dfrac{\ln\dfrac{r_\infty}{r}}{\ln\dfrac{r_\infty}{r_T}}}} + \int_{r_\infty}^{\infty} \frac{b}{r^2} \frac{dr}{\sqrt{1 - \dfrac{b^2}{r^2}}}$$

which can be put into the more compact form

$$\chi = \pi - 2\Delta\varphi = \pi - 2\sin^{-1}\eta_\infty - 2\int_{\eta_\infty}^{\eta_m} \frac{d\eta}{\sqrt{1 - \eta^2 - \lambda\ln\dfrac{\eta}{\eta_\infty}}}$$

with $\qquad \lambda = \dfrac{2q}{mg^2} \dfrac{\Phi_T}{\ln\dfrac{r_\infty}{r_T}} \qquad$ and $\qquad \eta = \dfrac{b}{r}$

Some simple limits

Hard body: An electron with an energy much less than the tether potential (specifically with $\lambda \gg 1$ almost "bounces off" the edge of the sheath. This gives the simple limiting deflection

$$\chi = \cos^{-1}(\frac{b}{r_\infty})$$

Soft body: In the opposite limit, a particle of either polarity with very high energy can penetrate deep into the sheath and suffer a small deflection only. Using the condition $\lambda \ll 1$ we now obtain

$$\chi = \lambda \cos^{-1} \eta_\infty = \frac{2q}{mg^2} \frac{\Phi_T}{\ln(r_\infty / r_T)} \cos^{-1}(\frac{b}{r_\infty})$$

For all other cases, numerical integration is necessary.

Selection of the impact parameter b

First of all, no incoming trajectories can lie within the loss cone:

$$0 \leq \theta \leq \sin^{-1}\left(\frac{v \cos\alpha_L}{g}\right)$$

Also, not every deflection places the outgoing trajectory inside one of the two loss cones (along +Y or –Y). The condition on χ is

$$\sin^{-1}\left(\frac{v}{g}\cos\alpha_L\right) \leq \left|\chi \mp \vartheta\right| \leq \pi - \sin^{-1}\left(\frac{v}{g}\cos\alpha_L\right)$$

$$\mp = \begin{cases} - \text{ for } b > 0 \\ + \text{ for } b < 0 \end{cases} \qquad v = \sqrt{g^2 + v_z^2}$$

And the values of b that satisfy it must be found from the scattering calculation. They are found to lie in the ranges (b1,b2) and (b3,b4), and we define the total range

$$w_b(v_z, g, \theta) = \left|b_1 - b_2\right| + \left|b_3 - b_4\right|$$
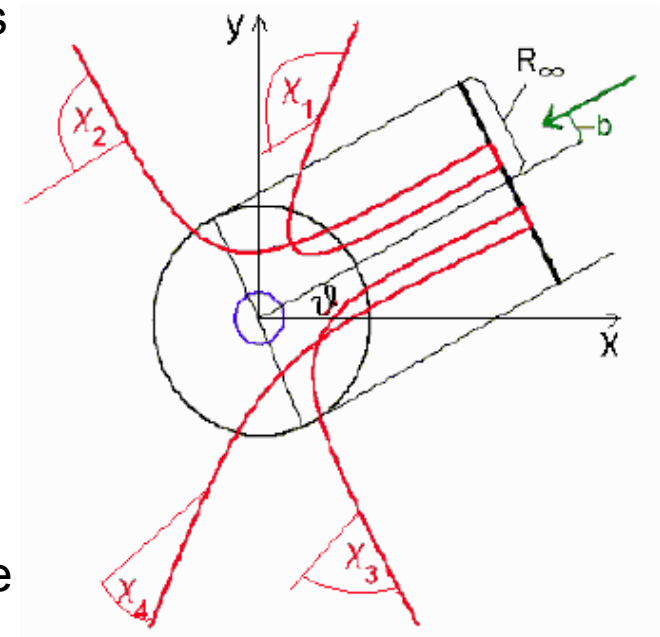
The total removal rate

We now have all the elements to construct the desired removal rate. For a tether length L_T , and using a "Hollow Cone" distribution (a Maxwellian with the particles within the loss cone removed), we have for the number of particles removed per second:

$$\Gamma_{scatter} = 8 \cdot \int_0^\infty \int_0^\infty \int_0^{\sin^{-1}\left(\frac{v\cos\alpha_L}{\varepsilon}\right)} g^2 \cdot f_{LC}(v_z, g, \theta) \cdot w_b(v_z, g, \theta) \cdot L_T \cdot d\theta dg dv_z$$

The calculations are done numerically by discretizing the ranges of integration. C. Zeineh´s thesis* explais the details and gives interesting intermediate results.

For reporting, these rates are divided by the number density of the energetic particles, yielding a quantity γ with units of $m^3 s.^{-1}$

Applications of an Electrostatic High-Voltage Tether to Radiation Belt Remediation
M.S. Thesis, Depatment of Aeronautics/Astronautics, MIT. September 2005

Results for a 1MV tether (a)

One first quantity of interest is the the _influx_ of particles (of either polarity) into the
sheaths of the positive or the negative tether.

Altitude (km)	Volume Influx (m^3s^{-1}) Positive Tether	Volume Influx(m^3s^{-1}) Negative Tether
2000	$1.5153 \cdot 10^{11}$	$2.9786 \cdot 10^{13}$
4000	$1.4678 \cdot 10^{11}$	$2.8819 \cdot 10^{13}$
6000	$1.3792 \cdot 10^{11}$	$2.7016 \cdot 10^{13}$
8000	$1.3181 \cdot 10^{11}$	$2.5775 \cdot 10^{13}$

Of course, the main interest is in the negative tether, which has the high potential
and therefore the higher flux.

Results for a 1MV tether (b)

Next we report the volumetric scattered fluxes, and the ratio of scattered to incoming flux, or "scattering efficiency":

Altitude (km)	Volume Scattering Flux Positive Tether (m^3s^{-1})	Volume Scattering Flux Negative Tether (m^3s^{-1})
2000	$8.6978 \cdot 10^9$	$1.8130 \cdot 10^{12}$
4000	$3.9829 \cdot 10^9$	$8.6175 \cdot 10^{11}$
6000	$1.3792 \cdot 10^{11}$	$4.4095 \cdot 10^{11}$
8000	$1.3181 \cdot 10^{11}$	$1.5059 \cdot 10^{10}$

Altitude (km)	Efficiency (%) Positive Tether	Efficiency (%) Negative Tether
2000	5.74	6.09
4000	2.71	2.99
6000	1.45	1.63
8000	0.02	0.06

The higher efficiencies at the lower altitudes reflect the fact that the loss cone is wider at these altitudes.

"Remediation" time

The rate of decrease of particle density being proportional to the density itself, the evolution of this density (or of the associated flux) turns out to be exponential:

$$n = n_0 e^{-\frac{\gamma}{V} \cdot t}$$

where V is the volume of the region being "remediated". The time to achieve a particular decrease ratio follows as

$$t = \frac{V}{\gamma} \ln\left(\frac{n_0}{n_{final}}\right)$$

The volume V is <u>very roughly</u> estimated as that comprised between two toroids whose major and minor radii are both half the equatorial radius of the particular L-shells that bound the "remediation region":

$$V_{mag} = \frac{1}{4} \pi^2 (R_{eq,outer}{}^3 - R_{eq,inner}{}^3)$$

And further, we assume the "remediation region" is bounded by the orbital radius of the tether plus/minus a distance D, that we equate with the 10km teher length.

Remediation time results

Setting as the target a reduction to **1/10** of the original energetic particle flux, we obtain the following results :

Altitude	T (sec)	T (years)
2000	$1.3135 \cdot 10^7$	0.4165
4000	$6.0330 \cdot 10^7$	1.9130
6000	$2.0643 \cdot 10^8$	6.5458
8000	$1.5722 \cdot 10^{10}$	498.54

These results assume no diffusion from adjacent L shells. To see the possible effect of this diffusion, suppose we increase the distance D to 100 km above and below the ends of the tether. We no calculate the longer times

Altitude	T (sec)	T (years)
2000	$1.3135 \cdot 10^8$	4.1652
4000	$6.0331 \cdot 10^8$	19.131
6000	$2.0643 \cdot 10^9$	65.459
8000	$1.5722 \cdot 10^{11}$	4985.5

The mission appears feasible only for the lower L-shells, to about L=1.2-1.5

Conclusions for the electrostatic scattering method

- No apparent technology barrier

- Can work for either electrons or ions

- Restricted to the inner belts, probably to its lower edges

-Fairly high power required to maintain the tethers at high potential
    (of the order ot 100 kW for 1 mm diameter)

-Parametric studies needed for other geometries, multiple tethers, etc.

Methods based on induced pitch diffusion

The eletrostatic scattering method relies on deflecting a fraction of the affected particles into the loss cone **all in one very energetic encounter** with the charged tether.

The **difusion methods**, to be considered next, rely on a multiplicity of "gentle" deflections, that accumulate as the particle travels repatedly back and forth along its guiding magnetic line (actually surface, considering the drift).

These methods can work because the scattering agent is a wave field that can be made to essentially "fill" the same magnetic shell as the particles. However, the resonance conditions needed for efective interaction occur only over a few percent of the particle´s path.

The physics of this interaction is fairly complex in detail, and has been studied by space physicists over the past 40 or so years in order to explain a multitude of magnetospheric and ionospheric effects. Only recently however has the <u>artificial</u> excitation of these effects been seriously considered.

Wave fields

A wave propagating through the background plasma will carry oscillating electic and magnetic fields, **Ew** and **Bw**. Normally $B_w << B_0$, the background B field.

These fields are related to each other through one of Maxwell´s equations:

$$\frac{\partial \vec{B}_w}{\partial t} = -\nabla \times \vec{E}_w$$

For a planar wave, every perturbation quantity a will vary in the Fourier form

$$a(\vec{r},t) = \Re\{\tilde{a}(\vec{k},\omega)\exp(i(\vec{k}.\vec{r} - \omega t)]\}$$

where the frequency ω is a certain function of the components of the wave

vector **k** as determined by the properties of the plasma. The phase (the exponent) will be constant for an observer moving at the **phase velocity**,

$$\vec{v}_\phi = (\frac{\omega}{k})(\frac{\vec{k}}{k})$$

In Fourier components, we have $\omega\vec{B} = \vec{k} \times \vec{E}$ which shows

(a) **E** and **B** are perpendicular to each other, and
(b) In magnitude, $\dfrac{E}{B} = \dfrac{\omega}{k} = v_\phi$

234

Wave-particle interaction

The wave fields exert a force on a particle of velocity **v** and charge q

$$\vec{F} = q(\vec{E}_w + \vec{v} \times \vec{B}_w)$$

- Since the magnetic force is perpendicular to the velocity **it cannot add energy** to it, only deflect its trajectory.
- The ratio of the magnetic and electric forces is $\dfrac{F_B}{F_E} = \dfrac{vB_w \sin\varphi}{E_w} = \dfrac{v}{v_\phi}\sin\varphi$

where φ is the angle of the velocity and the wave B field.

- The velocity ratio $\dfrac{c}{v_\phi} = n$ is called the **index of refraction** of the plasma.

For the whistler waves of interest, n is of the order of 20 or more, meaning these waves are much slower than the **speed of light c** in vacuum. On the other hand, the particle velocity v is, at least for electrons, close to c, as we saw. Hence

(a) The main wave-particle interaction is magnetic deflection
(b) The energy of the particles is affected only weakly by tese waves

The need for a resonance

- The basic magnetic field B_0 changes the velocity direction appreciably in a time of

the order of $1/\Omega_e$; $\Omega_e = eB_0/m$ The wave field, being weaker by the ratio

$B_w/B_0 \approx 10^{-3}$ will require a time proportionally longer for a similar deflection.

- When the frequencies of the wave and of the gyrating particle are unrelated, the magnetic forces will change direction rapidly and more or less at random, with not much net effect. But when they coincide, or the wave frequency is a multiple of the gyration frequency, (**a resonant condition)** the effect can accumulate for a reasonably long time, and lead to measurable deflections. In addition,

   (a) The wave frequency must be **Doppler-shifted**, so that it is the frequency
        seen by the advancing particle.
   (b) The gyration time must be modified by the relativistic dilation.
   (c) The wave fields must rotate in the same sense as the particle

- The resonance condition is then: $\omega - k_\parallel v_\parallel = -\dfrac{r\Omega_e}{\gamma}$

   with r=0, -1, -2…., and $1/\gamma = \sqrt{1-v^2/c^2}$ As noted the wave frequency

   must be as corresponds to the parallel wavevector k_II

The Pitch Diffusion approximation

Even with the help of the resonance, the deflections will happen at random, depending on the phase difference at the start of the resonant interaction. As the particle bounces back and forth between conjugate points, these random deflections will produce a **diffusion** of the particle population in the pitch variable.

Following these ideas, theorists have constructed the formulas that determine the **diffusivity** in pitch. These are different for each of the resonances possible (r=0,-1,-2, …). They involve averaging along the guiding magnetic lines, as well as over each Larmor cycle, and they depend on the specific **equatorial pitch**, α_0

As an example, for the r<0 resonances, the pitch diffusivity (in rad^2/s) is

$$D_r(\alpha_0) = \frac{A}{T(\alpha_0)\cos^2\alpha_0} \int_0^{\lambda_m} \frac{\sqrt{\pi}}{2} \frac{B_w^2}{B^2} \frac{\Omega_e}{\gamma} \frac{P_{\parallel,m}}{P_\parallel} W_r \cos\alpha \cos^7\lambda \, d\lambda$$

The details are explained for instance by J. M. Zorrilla * in his report.

(*) J. Manuel Zorrilla Matilla, "Radiation Belt Remediation Methods". Graduating Report for Supaero, (done at MIT, Spring 2006).

The pitch diffusion equation

For a given particle energy E and magnetic shell, we can define the **distribution function in pitch**, $f_0(E, L, t, \alpha_0)$ as the number of particles per unit pitch width and unit volume, at time t for which the equatorial pitch is α_0

The distribution function is governed by the time-dependent **pitch diffusion equation**

$$\frac{\partial f_0}{\partial t} = \frac{1}{\sin 2\alpha_0 T(\alpha_0)} \frac{\partial}{\partial \alpha_0} \left(\sin 2\alpha_0 T(\alpha_0) D_{\alpha\alpha}(\alpha_0) \frac{\partial f_0}{\partial \alpha_0} \right)$$

The boundary conditions are (a) Symmetry about zero pitch, and (b) Zero population at the edge of the hollow loss cone. Since these are **homogeneous** conditions on a linear PDE, any non-trivial solution must be an **eigenfunction** of the problem.

For solution, separation of variables is used: $f_0(t, \alpha_0) = N(t) g(\alpha_0)$

and the **separation constant** $1/\tau$ plays the role of an eigenvalue:

$$\frac{1}{N(t)} \frac{dN(t)}{dt} = \frac{1}{\sin 2\alpha_0 T(\alpha_0) g(\alpha_0)} \frac{d}{d\alpha_0} \left(\sin 2\alpha_0 T(\alpha_0) D_{\alpha\alpha}(\alpha_0) \frac{dg(\alpha_0)}{d\alpha_0} \right) = \frac{-1}{\tau}$$

238

Numerical solution

Several authors have solved this separated equation by iteration. Zorrilla chose to **discretize** the variables and convert the formulation to a **matrix eigenvalue** problem. Some care had to be exercised to select the lowest eigenvalue, corresponding to the fastest depletion time.